Combustion Lean Limits Fundamentals and Their Application to a SI Hydrogen-Enhanced Engine Concept

by

Ferrán A. Ayala

B.S. Mechanical Engineering
University of Kansas, 1999

M.S. Mechanical Engineering
Massachusetts Institute of Technology, 2001

SUBMITTED TO THE DEPARTMENT OF MECHANICAL ENGINEERING IN PARTIAL FULFILLMENT OF THE REQUIREMENTS FOR THE DEGREE OF

DOCTOR OF PHILOSOPHY IN MECHANICAL ENGINEERING
AT THE
MASSACHUSETTS INSTITUTE OF TECHNOLOGY
[September 2006]
August 19, 2006

Signature of Author: _____
Department of Mechanical Engineering
August 19, 2006

Certified by: _____
John B. Heywood
Sun Jae Professor of Mechanical Engineering
Thesis Supervisor

Accepted by: _____
Lallit Anand
Chairman, Departmental Graduate Committee

(this page was intentionally left blank)

Combustion Lean Limits Fundamentals and Their Application to a SI Hydrogen-Enhanced Engine Concept

by

Ferrán A. Ayala

Submitted to the Department of Mechanical Engineering on August 19, 2006
in partial fulfillment of the requirements for the Degree of Doctor of
Philosophy in Mechanical Engineering

ABSTRACT:

Operating an engine with excess air, under lean conditions, has significant benefits in terms of increased engine efficiency and reduced emissions. However, under high dilution levels, a lean limit is reached where combustion becomes unstable, significantly deteriorating drivability and engine efficiency, thus limiting the full potential of lean combustion. Due to hydrogen's high laminar flame speed, adding a hydrogen-rich mixture with gasoline into the engine helps stabilize combustion, extending the lean limit. This work studies the fundamental behavior of lean combustion in a spark ignition (SI) engine, identifying the processes that determine the engine's efficiency curve, and studying practical solutions to extend the peak efficiency and the lean limit.

Lean and hydrogen-enhanced combustion data in a SI engine were generated covering a wide range of operating conditions including different compression ratios, loads, types of dilution, types and levels of hydrogen enhancement, and levels of turbulence. Combustion simulations were then performed to quantify the components that determine the efficiency vs. dilution curve. Results showed how burn duration is the primary driver of lean combustion, with a limiting 10-90% burn duration at peak efficiency and a limiting 0-10% burn duration at the onset of rapid combustion variability. These two burn durations, while correlated, are affected differently by laminar flame speed and turbulence. Consequently the effect of hydrogen enhancement on combustion will depend on operating conditions.

A flame entrainment combustion model was then used to fundamentally explain the observed criticalities in the experiments. The model properly captured the physics of the combustion process, accurately predicting the data and the basic trends. The model showed that the rapid increase in variability near the lean limit is due to the inverse dependence of the eddy-burning time on the laminar flame speed. This relationship causes the eddy-burning time to grow slowly and then rapidly with decreasing laminar flame speed, amplifying the baseline, normal, random variability associated with the flame initiation process. Due to the effect of initial conditions on combustion phasing, this increasing, but symmetric, variability during flame initiation will lead to asymmetrical variability in the main part of the combustion process.

Modeling studies show how by reducing the eddy-burning time, the full burn duration curve can be shifted, extending the location of peak efficiency and the lean limit. This can be done by increasing turbulence, effectively decreasing its microscale structure or by increasing the laminar flame speed through hydrogen enhancement. Hydrogen enhancement using reformate shows diminishing returns at high loads and high compression ratios due to the detrimental effect of high pressures on laminar flame speed. As suggested by the model, reducing the engine's baseline combustion variability during flame initiation can also extend the lean limit. These conclusions are confirmed through experimental results.

Thesis Supervisor: Professor John B. Heywood
Title: Sun Jae Professor of Mechanical Engineering

(this page was intentionally left blank)

Acknowledgements

The most difficult part about finishing the Ph.D. is leaving MIT. I look back at the four and a half years that I spent here, and would give anything to live it again, and have an even more enhancing experience. MIT helped me uncover a great deal of my potential; it provided me with the opportunity for tremendous personal growth, great friends and mentors, and a chance to work with world-known Professors. True, there were moments of deep frustration, but even these moments helped me mature. I came to MIT having very high expectations of this place, but what I found here always surpassed those expectations. MIT is a real meritocracy, which has opened doors beyond my comprehension. I leave MIT with my head high, satisfied and proud of the work I have done, but sad that time has gone by so fast.

I want to thank the people that helped make MIT such a special time in my life. I want to start by thanking Professor Heywood for giving me the opportunity to work with him both during my Masters and during my Ph.D. This was an honor. Without his support I would not have been able to follow the non-traditional yet valuable path that I pursued, taking a leave of absence after the qualifier exams to go work at McKinsey, and then coming back to work on my Ph.D. My interactions with him motivated me to strive for higher levels of excellence and rigor.

Professor Keck is another person to whom I am very grateful. He was always of great help, and I am happy that I got to know him on a more personal level. I still have fond memories of us working together during my Masters, re-designing the rapid compression machine. His insights on the research were very valuable, and they came at the moments when I most needed them. Without his timely help it would have been difficult to finish my Ph.D. this summer.

I also want to thank the members of my thesis committee for their valuable help and support. I thank Professor Cheng for his hands-on help throughout this project, giving me the same attention and priority as he gave his direct students when I asked for help; I want to thank Professor Ghoniem, for the valuable teachings in the three classes that I took from him while at MIT and for his insights and support throughout the various committee meetings; I thank Professor Green in particular for his contributions during the committee meetings, always asking practical questions that helped me narrow down my research path and helped me focus on the end product, finishing the Ph.D. I am also very grateful to Rudy Smaling and ArvinMeritor, for their generous support of this project.

I would like to thank the staff and my colleagues at the Sloan lab. I thank Thane Dewitt for his friendship and support throughout my time at MIT. I want to thank Karla Stryker, Leslie Regan, Nancy Cook, and Janet Maslow, for their patience in dealing with me, in particular with putting up with my tendency to do things at the last minute. I also thank my colleagues at the Sloan Lab who helped me when I most needed them and were good friends and mentors; these include Morgan Andreae, Craig Wildman, Robert Scaringe, Dongkun Lee, Alex Sappok, Steve Przesmitzki, Yong Li, and many others. I would especially like to thank Tian Tian for his friendship and support, and in particular for helping me realize that doing the Ph.D. was the right next step in my life, at the time when I most questioned what I was doing. Staying on for the Ph.D. was clearly the right choice. I also thank all my friends at MIT, in Boston and outside of Boston for all their support; in particular I thank Buddy and Mary.

And most important, I thank God for giving me the great opportunities that I have had so far in life, and I thank my parents, Alfonso and Patricia, and my brothers, Alfonso, Rodrigo, and Alvar, for their never-ending support, and for their trust in my capabilities.

(this page was intentionally left blank)

TABLE OF CONTENTS

(this page was intentionally left blank)

List of Figures

List of Tables

(this page was intentionally left blank)

Nomenclature and Symbols

NOx: Nitrogen Oxides

COV: Coefficient of Variation

$\lambda_{A/F}$: Relative air-fuel ratio

NIMEP: Net Indicated Mean Effective Pressure

EGR: Exhaust Gas Recirculation

RPM: revolutions per minute

MBT: Maximum Brake torque

mfb: mass fraction burned

0-10%: time to burn 0% to 10% of the engine charge

10-90%: time to burn 10% to 90% of the engine charge (main burning angle)

$\lambda_{A/F}$: turbulence microscale

CA: Crank Angle

CAD: Crank Angle Degree

τ_b: eddy burning time

S_L: laminar flame speed

u': turbulence intensity

V_{Pmean}: mean piston speed

(this page was intentionally left blank)

Chapter 1 – INTRODUCTION

1.1 Background and Motivation

In the context of recent high oil prices, increasing global warming effects from fossil fuel emissions, and the unavailability of better substitutes for the internal combustion engine for the next 20 years, increasing engine efficiency continues to be one of the most important topics in the auto industry. There is an ongoing emphasis on the traditional methods for obtaining higher engine efficiency such as boosting and increasing the compression ratio, as well as a growing interest in the development of newer approaches such as lean engine concepts.

Operating an engine under lean or dilute conditions means running with excess air or excess diluents, such as Exhaust Gas Recirculation (EGR), relative to stoichiometric conditions. Lean or diluted engine operation offers significant benefits in terms of higher break engine efficiency and lower emissions. Diluted mixtures have a higher ratio of specific heats, relative to stoichiometric mixtures. Like in a diesel engine, this allows the burned gases to expand through a higher temperature ratio prior to exhaust, increasing the expansion work. All else equal, as a larger mass of air is inducted under lean operation, the cylinder intake pressure must increase, reducing the pumping losses. Average combustion temperatures during dilute operation are lower than during stoichiometric conditions, decreasing heat transfer losses. Peak combustion temperatures during lean combustion are also lower than during stoichiometric conditions. Consequently, under sufficiently dilute conditions, the amount of Nitrogen Oxides (NOx) produced will be much lower than the NOx produced during regular stoichiometric operation. Some manufacturers have developed engines that run under mildly lean conditions [1], however, significant challenges have so far prevented them from uncovering the full potential of this concept, achieved in the ultra-lean regime.

Under highly dilute conditions, flame speeds decrease and combustion becomes unstable, increasing the coefficient of variation (COV) in net indicated mean effective pressure (NIMEP) and decreasing fuel conversion efficiency. One way to aid combustion is to inject small amounts of hydrogen to the gasoline-air mixture. With its high laminar flame speed, hydrogen increases the burn rate and helps extend the lean limit of combustion. If regular engines can operate under ultra lean conditions, fuel efficiency can potentially increase up to some 30%, with appropriate

design modifications [2], and NOx emission can decrease substantially, potentially eliminating the need for catalytic converters.

Although the concept of lean combustion in IC engines and the advantages of hydrogen enhancement have been around for over 30 years, the factors that determine lean combustion limits have not yet been quantified. Decent amounts of engine data have been generated under lean conditions, but a fundamental explanation for how lean an engine can be operated is still missing. It is not known what combination of burn duration, mixture laminar flame speed, burned gas temperature, and cyclic variability, among other variables, defines the maximum efficiency point. Consequently there is a lack of a well-behaved model that predicts the lean limit, and the operation regime of ultra-lean engines has not been properly mapped.

1.2 Challenges

The benefits and challenges of lean combustion can best be depicted in figure 1-1. As the air-fuel ratio increases, the indicated fuel conversion efficiency steadily increases. Around a relative air-fuel ratio (lambda, $\lambda_{A/F}$) of 1.6, the efficiency peaks at a maximum value, and then begins to decrease. As the mixture gets leaner, right after this lambda for peak efficiency the COV of NIMEP rapidly increases, reaching the industry drivability limit of 2% COV of NIMEP [3]. As the air-fuel ratio keeps increasing, efficiency continues to fall, and variability continues to increase, until the engine begins to misfire. On the same figure, the history of NOx emissions with relative air-fuel ratio is shown. As the amount of excess air in the engine increases, the higher concentration of oxygen results in a higher production of NOx. As the mixture becomes leaner, the peak combustion temperatures decrease substantially, slowing the rates of NOx production, and decreasing the total concentrations of NOx. By the time the engine has become unstable, NOx is fairly low, but not yet below current EPA requirements. This poses a problem as standard catalytic converters can not operate under lean conditions. Thus, even though the NOx levels are significantly lower than at stoichiometric conditions, they still need to be decreased further. This can be possible by using expensive lean catalytic converters (e.g., NOx traps), which are still under development, or by using EGR dilution together with standard catalytic converters. This last approach will still provide advantages, but it is not as attractive as using air dilution. Operating an engine under high EGR dilution will decrease the engine efficiency, and cause a faster increase in variability compared to air-dilution operation [4]. Thus,

in order to extract the benefits of running lean, it is desired to extend the limit of combustion variability beyond the point where the NOx are substantially reduced, meeting EPA emissions levels. Otherwise, operating lean will have a higher cost, whether through special catalytic technologies, or using EGR dilution.

To maximize the benefits of lean operation, it is necessary to understand the phenomena that limit the combustion process. Fundamental questions must still be answered. Why does peak efficiency increase steadily with dilution, but then reaches a peak and begins to fall? Why does combustion variability suddenly increase after having a low and stable value? How can the location of peak efficiency be extended? How can the lean variability limit be extended? How can variability in lean combustion be reduced?

1.3 Hydrogen Enhancement

A potential way in which the lean misfire limit can be extended is through hydrogen enhancement. Hydrogen-enhanced combustion refers to the addition of a pure hydrogen or hydrogen-rich mixture to an engine running on gasoline in order to improve the combustion characteristics. The pure hydrogen, or hydrogen-rich mixture, typically accounts for anywhere from 0 to 40% of the total energy flowing into the engine. The gasoline and the hydrogen-rich mixture can mix in the intake manifold, or in the combustion chamber prior to combustion. Hydrogen-rich mixtures are typically produced from reformed gasoline, and ideally consist of 25% H2, 26% CO, and 49% N2, on a molar basis. For the specific research described in this thesis, the concept for reforming the fuel is the plasmatron[1] (figure 1-3). Developed at MIT's plasma-fusion center [5], the plasmatron uses a plasma discharge to partially oxidize the fuel, producing a hydrogen-rich mixture, which is then injected into the engine. Fuel is reformed on-board, and on-demand, as shown in figure 1-4. Because the partial oxidation reaction undergone in the plasmatron is exothermic, and therefore some of the fuel energy is released as heat, this reforming method has thermodynamic losses on the order of 15-20% [5]. With its high laminar flame speed, hydrogen speeds up combustion and extends the location of the peak efficiency as well as the location of the lean limit. Figure 1-2 compares the location of the peak efficiency and the lean drivability limit for two hydrogen-enhanced cases and a baseline indolene case. The

[1] As described in the experimental setup (Chapter 2), experiments are done using bottled gases, not the actual plasmatron device

effect of adding plasmatron becomes clear, as it speeds up combustion and extends both the location of peak efficiency and the location of the lean limit.

1.4 Previous work

A considerable amount of work has been done in the area of lean and hydrogen-enhanced combustion. This work dates back to the late 70's and the most relevant research is summarized below:

- The effect of some engine variables on lean limits has been studied, and qualitative trends have been derived [6]
- Studies have focused on the extension of the lean limit through changes in the ignition system (e.g., spark plug design, spark energy and duration) [6]
- Effects of mixture turbulence, and other operating variables have also been studied [6]
- Quader looked at situations where lean combustion was limited by flame initiation and situations where combustion was limited by flame propagation [9]
- Hydrogen-enhanced combustion has been studied to some degree, and its benefits in extending lean limits have been acknowledged [10]
- Through modeling of the lean misfire limit, some authors interpret that the flame initiation process is the major factor determining/limiting lean combustion [11]
- Some OEM's have developed lean burn engines, which operate under a limited lean regimes (λ<1.4); [1]

Recent lean combustion research, including significant work done at MIT, has focused on extending the lean combustion limit through the addition of reformate. The most relevant work is summarized in the following points:

- MIT Plasma and Fusion center developed the plasmatron concept for vehicle on-board reforming of gasoline into Hydrogen and CO [5]
- For the last 5 years, MIT has been studying the effect of reformate addition and other variables (including turbulence, compression ratio, EGR, ignition system) on engine lean combustion [13, 14, 4, 15]
- Lean combustion characteristics for on-board reforming concept similar to MIT's plasmatron have been studied [16]

- An integrated system model of the plasmatron and engine has been developed [26]

Many questions still remain regarding the understanding of the main processes limiting lean combustion, and methods to improve these processes and extend the limits of lean and hydrogen-enhanced combustion

1.5 Objectives

The overall objectives of this research are to understand the fundamental processes that limit lean and hydrogen-enhanced combustion and to apply this understanding to extend the operating limits and improve the performance of lean and hydrogen-enhanced engine concepts. More specifically, and to reach the stated objectives, the following structure was followed during this research:

- Identify and quantify the variables and processes that define the maximum efficiency point in a lean regime, as well as the maximum stable lean operation point
- Develop a combustion model that accurately simulates the combustion process and behavior under lean conditions, predicting engine performance for different operating parameters
- Use the combustion model to understand the limitations of lean and hydrogen-enhanced engines, and suggest focused efforts to increase their performance

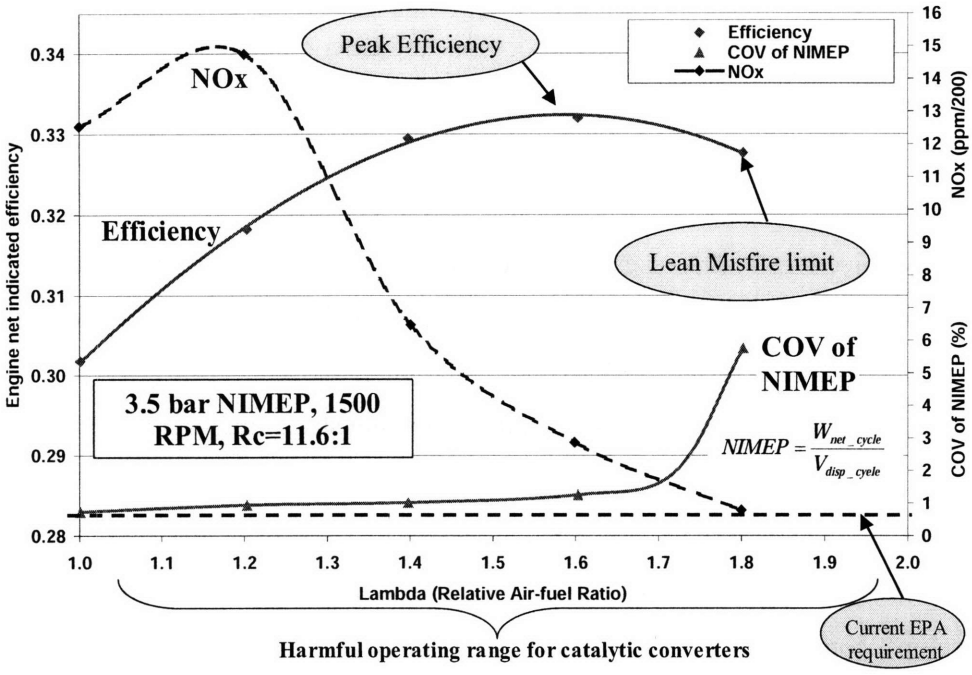

Figure 1-1 Overview of lean combustion benefits and challenges

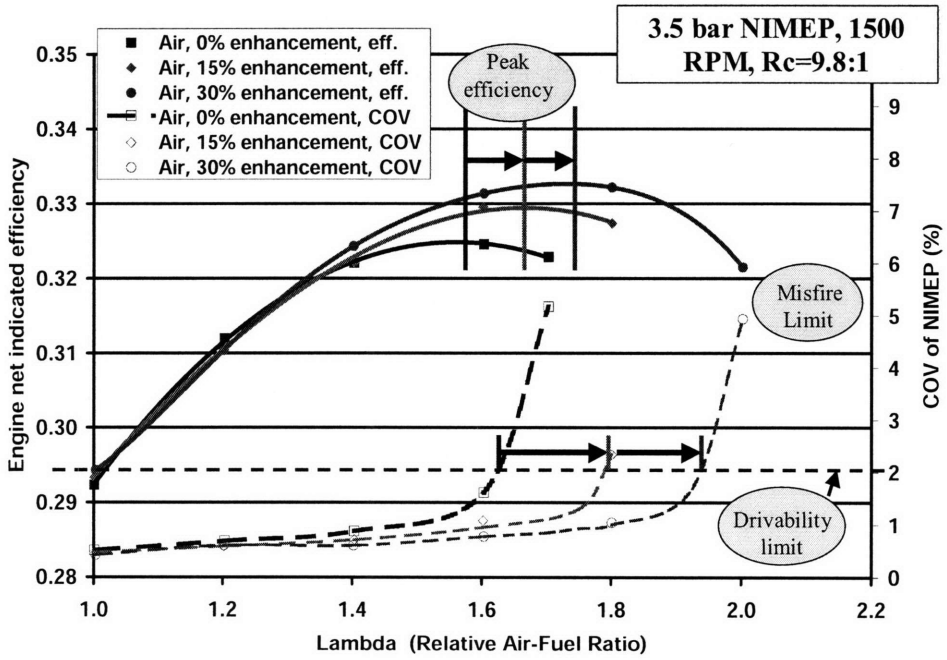

Figure 1-2 Comparison of hydrogen enhancement benefits for different levels of plasmatron, MBT, 3.5 Bar NIMEP, 1500 RPM, Rc=9.8:1

$$C_mH_n + \frac{m}{2}(O_2 + 3.773N_2) \rightarrow mCO + \frac{n}{2}H_2 + \frac{m}{2} * 3.773N_2$$

•Plasmatron Schematic

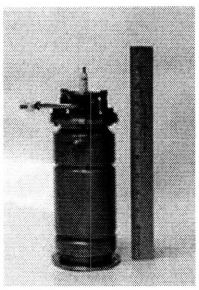

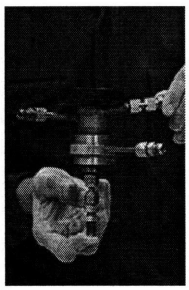

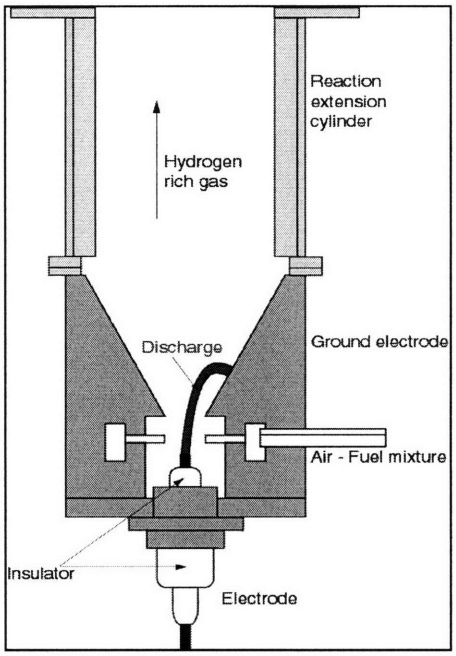

•Photos and schematic courtesy of MIT PSFC

Figure 1-3 Schematic of plasmatron concept

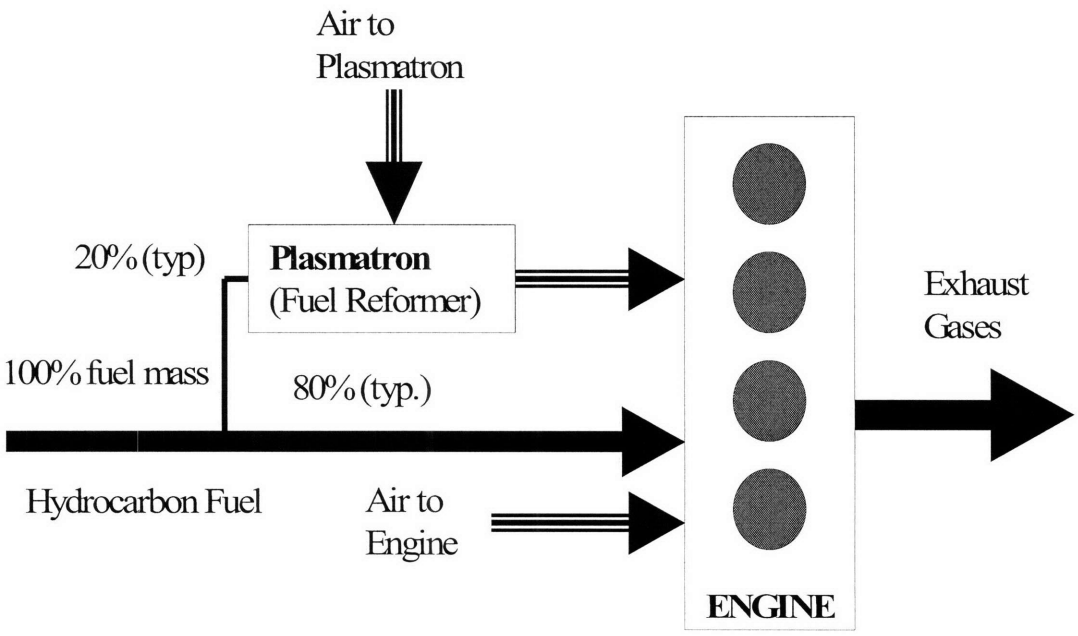

Figure 1-4: Schematic of plasmatron/engine interaction [4]

(this page was intentionally left blank)

Chapter 2 – EXPERIMENTAL APPARATUS AND PROCEDURES

2.1 Engine Setup

2.1.1 Engine specifications

The engine used for this study is a Ricardo Hydra MK III with baseline compression ratio of 9.8:1. The original head has been replaced with a B5254 Volvo head that has a modern 4-valve pentroof combustion chamber with a central spark plug. The engine has relatively low swirl and high tumble. Turbulence is increased with a charge motion control plate added to the intake manifold [14, 13]. The engine is naturally aspirated, and air supply from a compressor is used to simulate boost. Two other compression ratios were used with this engine, 11.6:1 and 13.4:1. Figure 2-1 shows a picture of the engine, and its details are shown in Table 2.1.

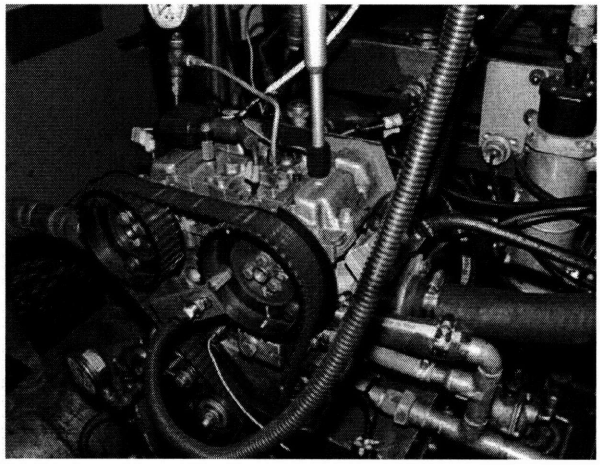

Figure 2-1 – Picture of Experimental Engine

Displaced Volume (cm^3)	487
Clearance Volume (cm^3)	46
Bore (mm)	83
Stroke (mm)	90
Connecting Rod Length (mm)	158
Piston 1 Clearance Vol. (cm^3)/Rc	55 / 9.8:1
Piston 2 Clearance Vol. (cm^3)/Rc	46 / 11.6:1
Piston 3 Clearance Vol. (cm^3)/Rc	39 / 13.4:1
Valve timing	IVC 60° ABDC IVO 0° ATDC
	EVO 8° ATDC EVO 68° BBDC

Table 2.1 – Engine Specifications

2.1.2 Air intake system and charge motion control devices

Figure 2-2 shows a simplified diagram of the intake system, starting with the throttle valve and ending at the intake port, right before the intake valves. The basic characteristic lengths are also indicated.

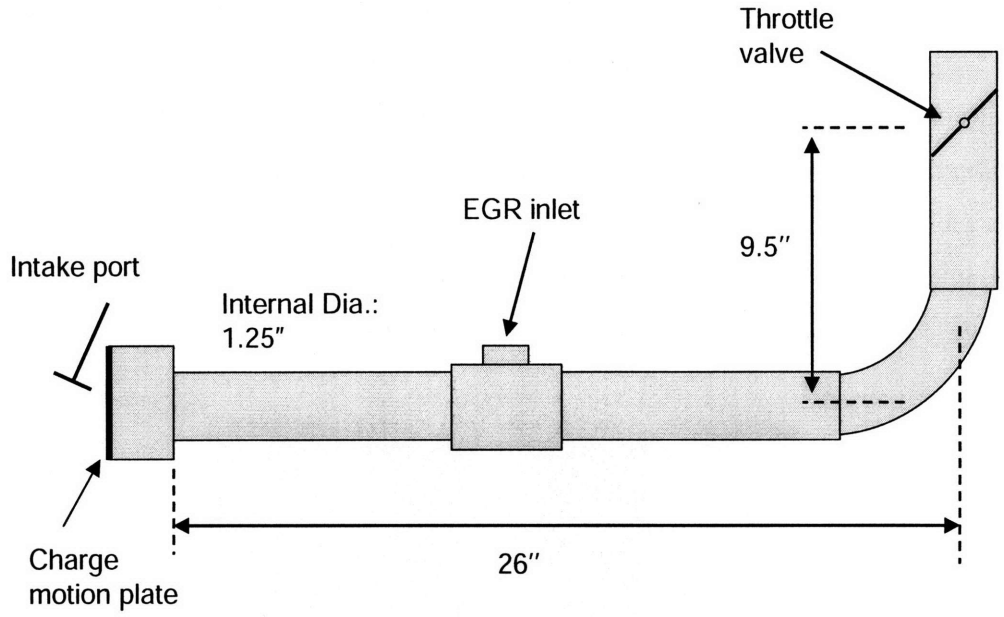

Figure 2-2 – Schematic of intake system

To speed up the intake flow, and increase the level of turbulence, a charge motion plate was inserted immediately before the intake port. This plate was part of the baseline engine configuration, and unless otherwise noted, it was used for all experiments. A picture of the specific "2/3 asymmetric" plate used is shown in figure 2-3. As the name indicates the plate blocks two thirds of the original intake port area. This has the effect of speeding up the flow and inducing tumble/swirl as previous experiments have shown [14].

Another method to induce charge motion, used for select experiments of this research, consists of inserting metal cones into the intake port, as shown in figures 2-4 and 2-5. This method was first used by Goldwitz, who showed how the different cones provided different flow characteristics that improved combustion. The two cones from Goldwitz, used in these experiments are the "deac" cone (Fig. 2-4) and the "moderate" cone (Fig. 2-5). The first cone was originally designed to simulate motion obtained through a valve deactivation scheme from a

real production engine, while the second cone was intended to generate moderate swirl and high tumble.

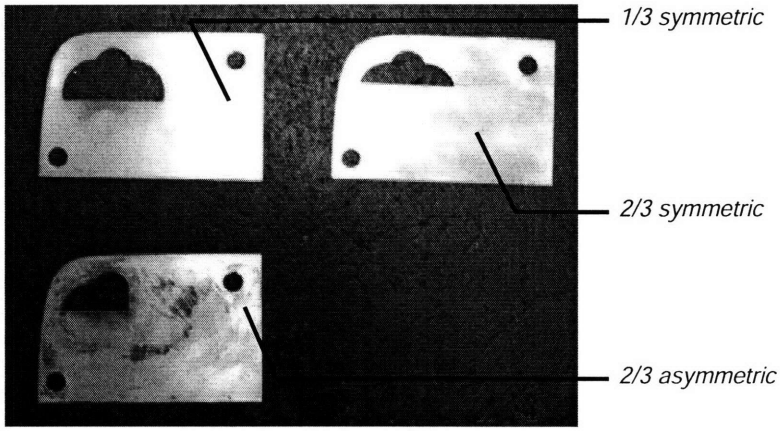

Figure 2-3 – Sample turbulence plates introduced before intake port [14]

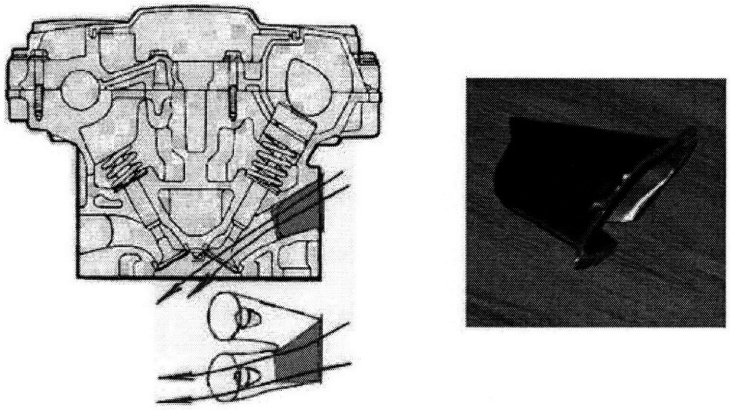

Figure 2-4 – Deactivation cone setup [14]

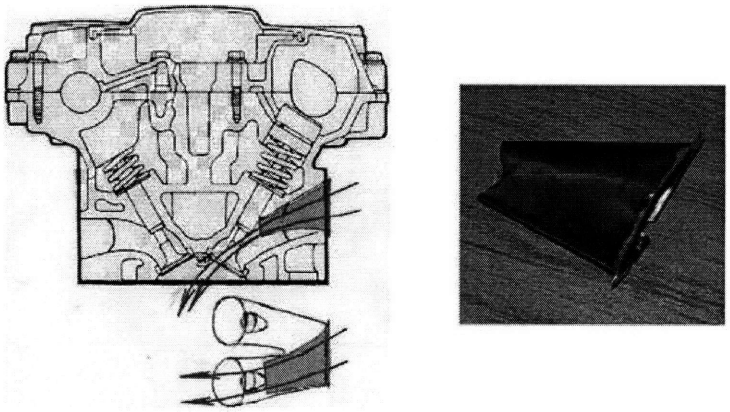

Figure 2-5 – Moderate cone setup [14]

2.1.3 Exhaust Gas Recirculation System

The engine is equipped with EGR capabilities. This system was implemented by Goldwitz and Ivanic [14]. The hot exhaust gases are taken from a location immediately after the exhaust manifold, and circulated back into the engine through the EGR inlet shown in figure 2-2. The EGR is not cooled.

2.2 Control System

The experimental engine was controlled by a Motec M4 engine controller. Spark timing, and fuel flow are varied through this system.

2.3 Data Acquisition system

LABVIEW was the system used to acquire data from the pressure transducer as well as the crank angle information/signal, produced by the shaft encoder.

2.4 Measurements

2.4.1 Relative Air-fuel Ratio

The relative air-fuel ratio was measured in the exhaust using a wideband Horiba MEXA-110 lambda sensor. This number would then be compared to the relative air-fuel ratio calculated by using the measured air flow and the measured fuel flow. The error ranged from 0.5% at stoichiometric conditions, to 3-4% for ultra-lean operation.

2.4.2 Air flow

Air mass flow was indirectly determined, by measuring the differential pressure across a laminar flow element. A Druck differential pressure sensor, built by GE sensing, measured the pressure difference and converted this number to an air volume flow. Together with the ideal gas law, the volume flow was then used to calculate the air mass flow.

2.4.3 Fuel Flow

Fuel is measured using two methods. The first measurement is provided by the Motec system, which controls the fuel injection; based on the selected pulse width, and the proper injection calibration, the amount of fuel injected can be calculated. This method provides

measurements within 2% error. The second and more accurate method, used for all efficiency measurements was using a scale. Fuel would be kept in a close container sitting on a pan scale. At any given time, the initial weight of the fuel would be recorded, and after 10 minutes the weight of the fuel left in the container would again be recorded, thus calculating the mass of the fuel that was consumed. The procedure would be repeated until a set of 2 to 3 consecutive measurements were within 0.5% of each other.

2.4.4 Pressure measurement

The pressure inside the cylinder was measured using a Kiestler 60125A piezoelectric pressure transducer.

2.4.5 EGR measurements

The same procedure described in [4] was followed to apply and measure EGR; both the exhaust gases, and the EGR going into the intake manifold were sampled, using a Horiba emissions analyzer, and the CO_2 concentration was measured. The percent of EGR was then calculated as the ratio of the measured engine-in CO_2 to the measured engine-out CO_2.

2.4.6 Emissions

NOx exhaust emissions were measured with a Chemiluminescent NO/NOx analyzer, model number 400 HCLD, made by California Analytical Instruments. To measure CO_2 concentration in the intake manifold and in the exhaust stream the Horiba Automotive Emission Analyzer, MEXA-554JU was used.

2.4.7 Reformate measurements

As explained in the procedures section, the same method used by [4] was used to measure the reformate going into the engine. This consisted of measuring the pressure difference across the critical flow used to choke the reformate prior to entering the engine. This pressure difference would then be used with the chocked-flow correlations for the specific orifice being used, to calculate the exact amount of reformate used.

2.5 Experimental Procedure

2.5.1 Air-fuel ratio sweeps

All experiments throughout this research were done at MBT spark timing. For each set of experiments the air-fuel ratio was set at stoichiometric conditions, and was then increased in increments of 0.2 lambda until the combustion process became unstable (COV of NIMEP>2%). The lambda sweeps were repeated for three different compression ratios, three different enhancement levels (using both plasmatron and hydrogen enhancement), and EGR and air dilution. To study the effect of changes in air-fuel ratio at higher loads, a lambda sweep was also done at a load of 6.0 bar NIMEP and the baseline compression ratio of 9.8. The fuel used for these experiments was Indolene, Phillips Chevron UTG-96 [8], in order to make direct comparisons with past publications; Table 2.2 provides the fuel's properties.

PROPERTY	
Research Octane Number	96.1
Motoring Octane Number	87
Lower Heating Value (MJ/kg)	43.1
Carbon Content (%)	86.5
Hydrogen content (%)	13.5
Antiknock index	92
H/C molar ratio	1.93

Table 2.2 – Fuel properties of Phillips Chevron UTG-96

2.5.2 Reformate Addition

Using the same definitions and procedures as defined in [4, 13], a H_2, CO, N_2 mixture that a plasmatron fuel reformer would produce from a fraction of the gasoline, to enhance combustion was used for select data points. On a molar basis, the plasmatron mixture consisted of 25% H_2, 26% CO and 49% N_2. Up to four enhancement levels were applied: 0%, 15%, 30%, and 45%. These enhancement numbers indicate the percentage of the total fuel energy going into the system that is used to produce plasmatron gases. For example, 30% enhancement means that 30% of the fuel flow was use to produce plasmatron. If the partial oxidation energy losses are taken into account (~20%), then the effective energy carried by the plasmatron would be 24% of the total fuel energy. Except where noted, however, the analyses were done assuming zero

thermodynamic losses. Therefore, the enhancement percentage indicates the total energy provided by plasmatron, as a percent of the total energy going into the engine.

2.5.3 Hydrogen Addition

Pure hydrogen was also use to speed up combustion, for a few points. The procedure used to inject hydrogen was similar to that of plasmatron gas. The hydrogen enhancement level was defined on an energy basis, relative to the total energy going into the engine. Thus, 15% enhancement meant 15% of the total energy going into the engine was provided by hydrogen.

(this page was intentionally left blank)

Chapter 3 – LAMINAR FLAME SPEED MODELING TOOLS AND CORRELATIONS

This research uses laminar flame speed calculations to understand the fundamentals of lean combustion, as well as the more practical considerations. Two methods were used to calculate laminar flame speeds: the Rhodes and Keck correlation [17], and CHEMKIN's laminar flame speed code. The Rhodes-Keck laminar flame speed correlation used is for indolene fuel, and does not include the effect of hydrogen enhancement. In the absence of well developed, and robust laminar flame speed codes for primary reference fuels, the CHEMKIN laminar flame speed calculations used methane (CH4) as the fuel to draw comparisons and analyze the data; Extensive laminar flame speed tests using methane have been conducted by several researchers, and well behaved CHEMKIN-compatible codes have also been developed to calculate methane's laminar flame speed.

3.1 Rhodes and Keck correlations

The laminar flame speed correlation from Rhodes and Keck is expressed as follows:

$$SSUBL = \left(SLINF \left(\frac{T}{298K} \right)^{\alpha} \left(\frac{P}{1atm} \right)^{\beta} \right) \left(4.70617(RES)^2 - 4.06185(RES) + 1 \right) \qquad (3\text{-}1)$$

where:

res = residual mass fraction

$SLINF = 30.5 - 54.9(1.21 - \phi)^n$

$\alpha = 2.4 - 0.271\phi^{3.51}$

$\beta = -0.357 + 0.14\phi^{2.77}$

The power n, in the term SLINF was originally published with a value of 2.0; however, as explained by Keck, this value is not totally fixed and there is some room to vary it and have a better fit with the data. A good value for n that matched the data reasonably well was 1.65. Keck's original correlation includes a residual fraction correction however the residual correction factor shown was obtained from a different reference [18] because it is valid over a wider range of residual, and can be used for high values of EGR.

When Rhodes and Keck developed their indolene flame speed correlations, using a combustion bomb, their experimental results encompassed relative air-fuel ratios of up to 1.4. For the applications presented in this thesis, a greater range of relative air-fuel ratios is of interest. Thus, the Rhodes-Keck correlation has been extrapolated to cover leaner conditions. The resulting values are still reasonable based on a comparison with laminar flame speed data for other fuels, under highly lean environments. Figure 3-1 shows this comparison. Published experimental data using Propane and Methane [19] at standard conditions (P=1 atm and T=298 K) are shown in this plot, along with a CHEMKIN-calculated methane curve, and two more curves produced with the Rhodes-Keck correlation. These last two curves are for the originally published power in the SLINF term, n=2.0, as well as the modified power, n=1.65. The relevant point from this comparison is how the slope of the n=1.65 curve for the extrapolated values ($\lambda_{A/F}$ >1,4) is similar to that of the experimental methane and propane data. The CHEMKIN-calculated curve shows differences in the slope compared to the other curves. For these sets of initial conditions, the CHEMKIN code could not be run successfully beyond $\lambda_{A/F}$=1.7.

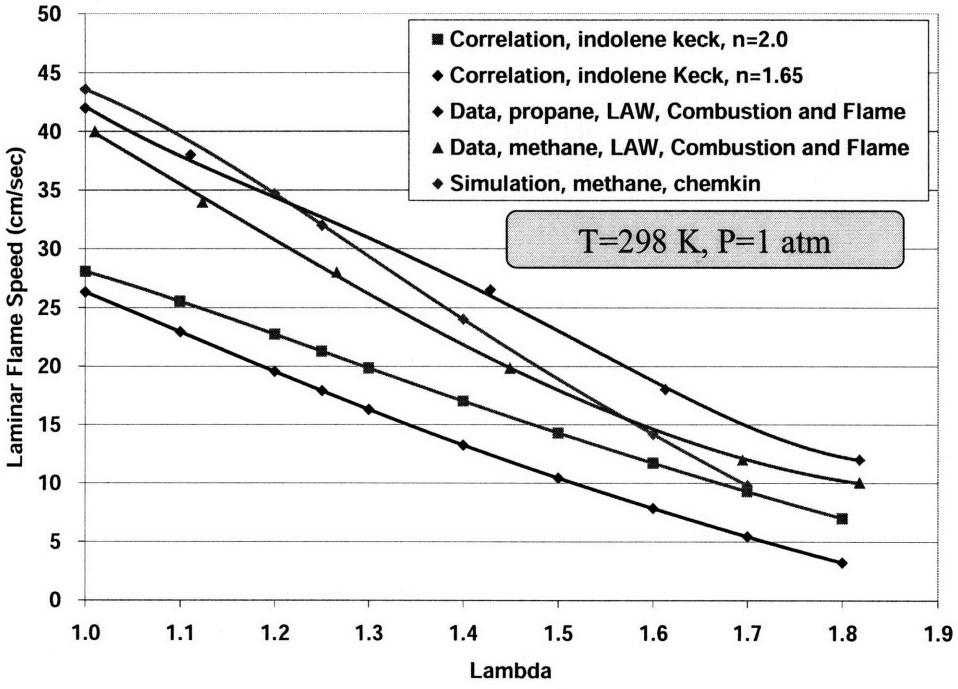

Figure 3-1 Comparison of laminar flame speed correlations and experimental data

The comparison from figure 3-1 validates the use of the Keck-Rhodes correlation to calculate laminar flame speeds for relative air-fuel ratios greater than 1.4 and at least until $\lambda_{A/F}$ =1.8. However, caution should be used when applying the Rhodes-Keck correlations for even more extreme lean conditions, $\lambda_{A/F}$ >1.9. As shown in figure 3-2, beyond these values of $\lambda_{A/F}$, the current form of the Rhodes-Keck correlation will force the laminar flame speed to cross the y-axis (SL=0), and become negative. The exact location of where the laminar flame speed becomes zero will depend on the value of n. This represents a criticality in the flame entrainment model, as discussed in section 6.12. In reality, a flammable mixture will quench before the laminar flame speed reaches a value of zero.

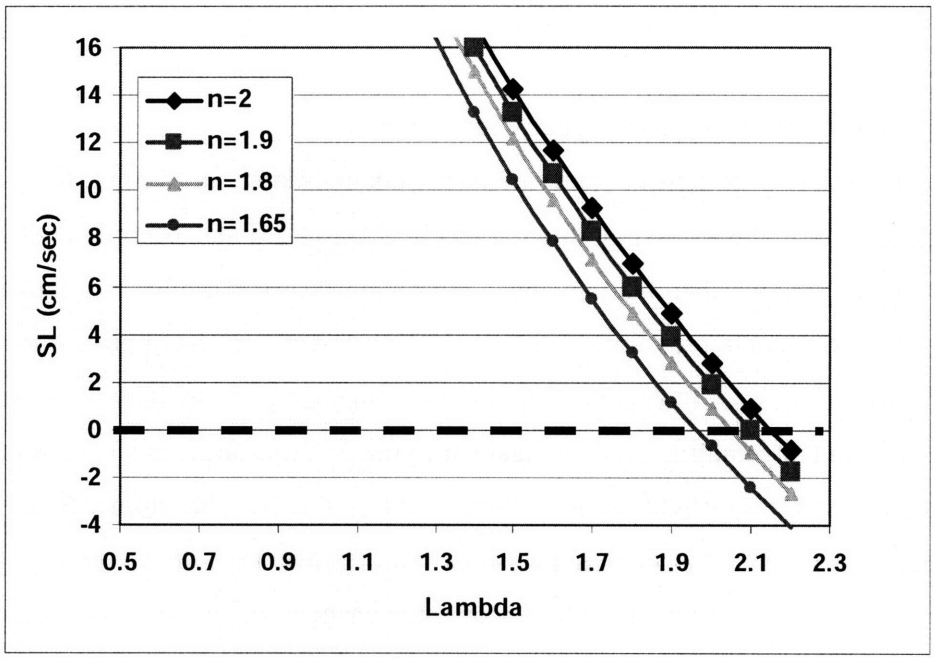

Figure 3-2 – Value of Relative air fuel ratio where laminar flame speed becomes zero in the Keck-Rhodes correlations.

3.2 CHEMKIN calculations

Laminar Flame speed calculations using CHEMKIN are particularly important to compare the effect of hydrogen enhancement using pure hydrogen and plasmatron. These calculations help understand the practical limitations and diminishing returns of using plasmatron, as will be explained in Chapter 5. The laminar flame speed code from CHEMKIN was use for these calculations, with the detailed GRI 2.11 mechanism for methane [20]. Laminar

flame speed calculations were done for pure methane, methane plus pure hydrogen, and methane plus plasmatron (25% H2, 25% CO, 49% N2 on molar basis). The level of hydrogen enhancement (pure hydrogen or plasmatron) varied from 0% to 45%. The level of dilution was also varied, along with the temperature and the pressure of interest.

Some of the results obtained with CHEMKIN have been put into correlation form to allow for correction factors for plasmatron and pure hydrogen enhancement that can be used directly with the Rhodes-Keck correlation. This is important, especially as one tries to study the effect of enhancement using the combustion flame entrainment model, as discussed in Chapter 6. CHEMKIN flame speed calculations for methane-air mixtures, methane-H2-air mixtures, and methane-plasmatron-air mixtures, for different temperatures and pressures are shown in figures 3-3 through 3-13.

3.2.1 Pure Methane Laminar Flame Speed Correlations

Figure 3-3 shows the effect of pressure on the laminar flame speed of methane for various temperatures and two different dilution levels. Figures 3-4 and 3-5 provide the same information as the previous chart but now the laminar flame speed is plotted as a function of the temperature for various pressures. The main observation from these sets of plots is the rapid detrimental effect of pressure on laminar flame speed, and the high sensitivity of laminar flame speed to changes in temperature. Looking again at figure 3-3, this large impact of pressure on S_L is clear. As pressure increases, the laminar flame speed decreases. The laminar flame speed is much higher at low pressure than at high pressures. At the lower pressure values (1- 15 atm), the laminar flame speed is much more sensitive to pressure changes, compared to the behavior at the higher pressure values (P>20 atm) where the laminar flame speed shows a small decrease with a large pressure increase. The behavior is very similar with higher dilution (lambda=1.6), but the absolute value of the laminar flame speed is lower.

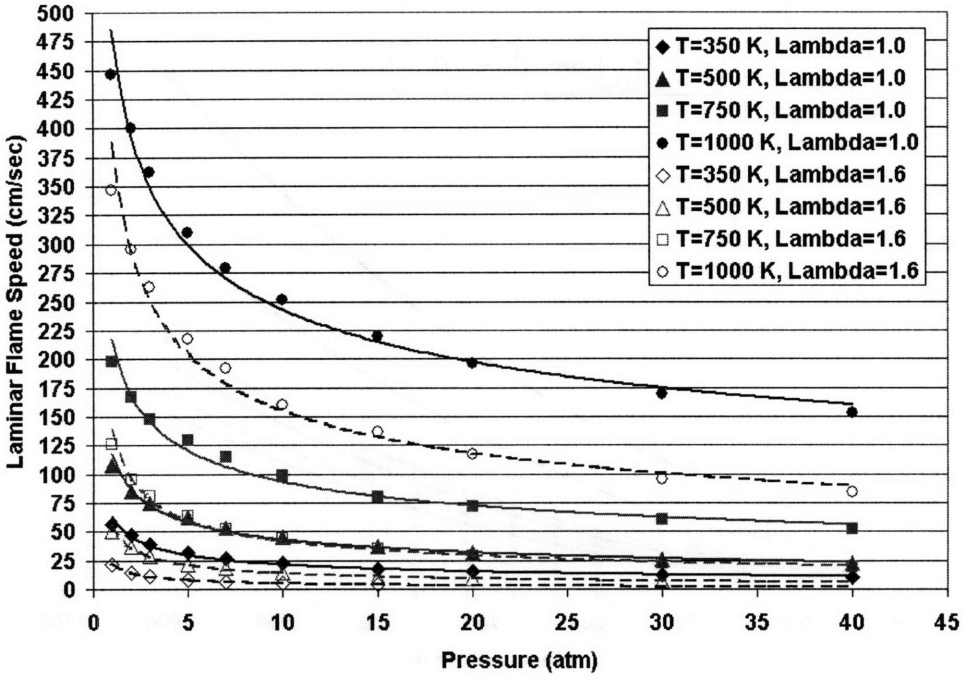

Figure 3-3 – Effect of pressure on methane's laminar flame speed for λ=1.0, and λ=1.6 for various temperatures (high range)

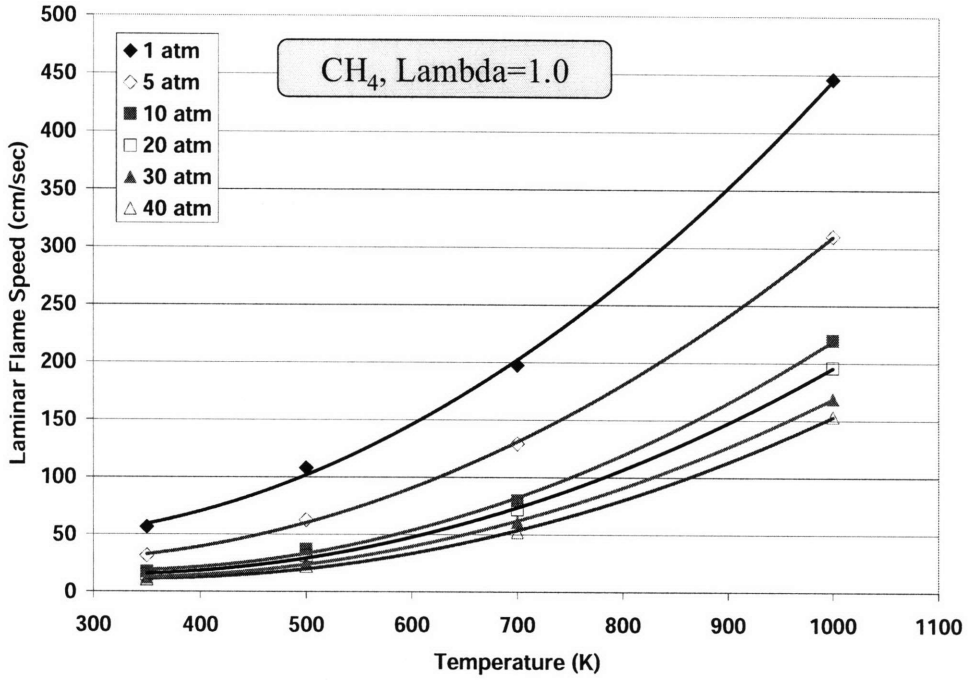

Figure 3-4 – Effect of Temperature on Laminar Flame Speed; Methane, λ=1.0, various pressures

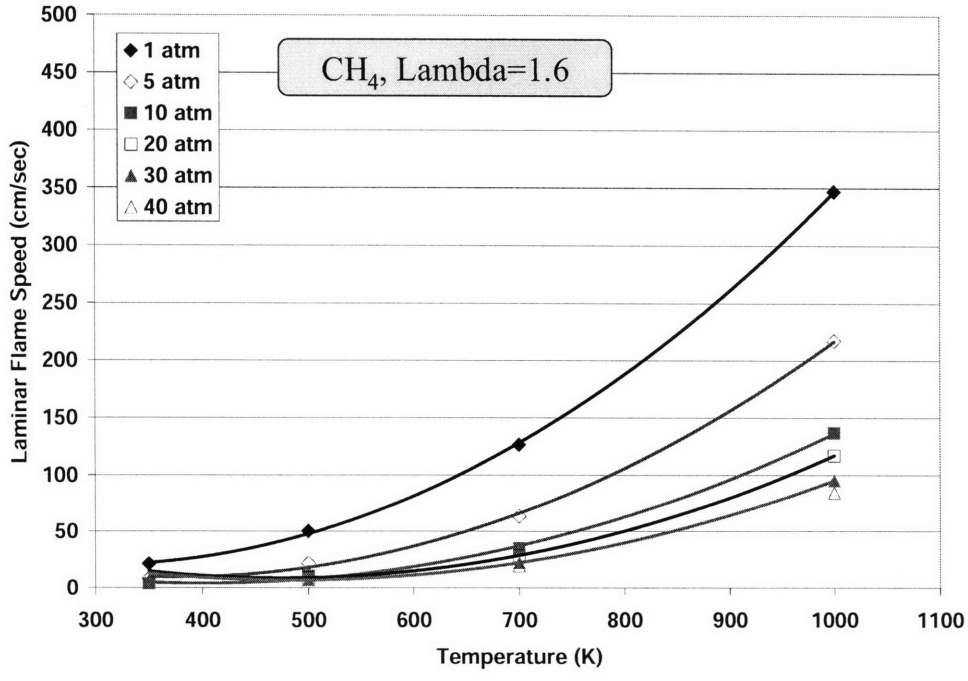

Figure 3-5 – Effect of Temperature on Laminar Flame Speed; Methane, λ=1.6, various pressures

3.2.2 H2-Methane correlations

The results of using pure hydrogen as a laminar flame speed enhancer for methane, are well behaved, as shown in the next figures, and can easily be expressed in terms of simple and consistent correlations. Figures 3-6 through 3-8 show the effect of hydrogen enhancement on the mixture laminar flame speed across three different temperatures, at stoichiometric conditions and holding the pressure constant for each case. Clearly hydrogen has a significant impact on the total mixture laminar flame speed. For example, adding 15% hydrogen by energy content, independent of the pressure will increase the mixture laminar flame speed by approximately 35% (relative to pure methane, no enhancement). The trends across these figures are very similar and do not vary much with pressure. Taking this into account, figures 3-9 and 3-10 are an attempt at constructing a universal correlation that describes the changes in laminar flame speed with hydrogen enhancement, independent of pressure, for various temperatures, and for two different dilution levels. The extracted correlations are well behaved, especially for the stoichiometric case. For leaner mixtures the correlations are not as clean, and for a few of these leaner individual cases, CHEMKIN would crash, without outputting a laminar flame speed value.

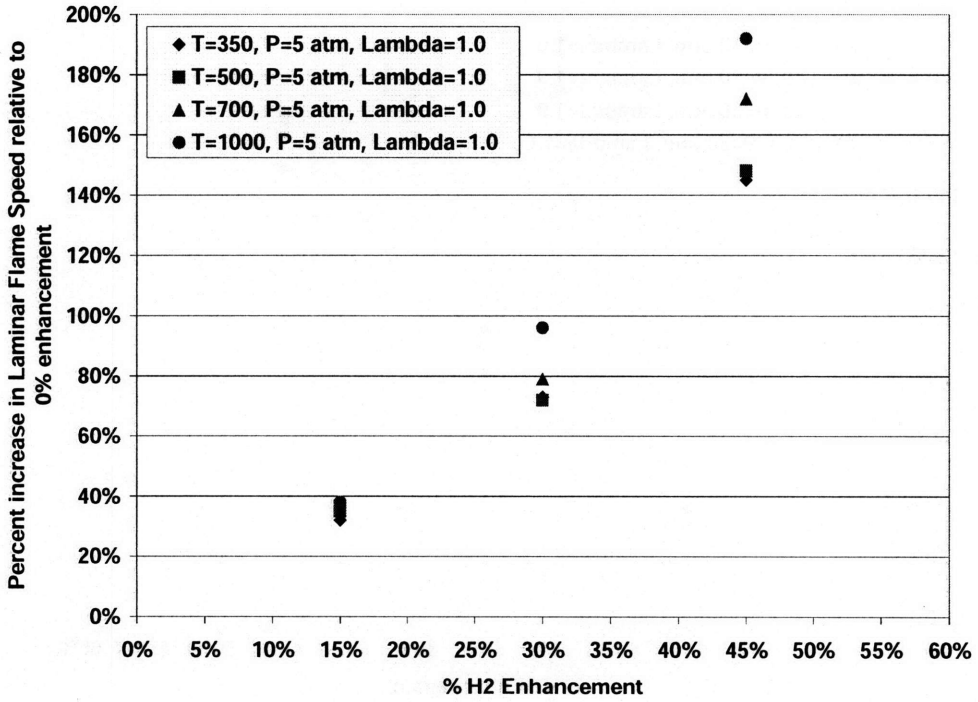

Figure 3-6 – Percent increase in laminar flame speed, relative to baseline conditions, with pure H2-enhancement; Methane, λ=1.0, P=5 atm, various temperatures

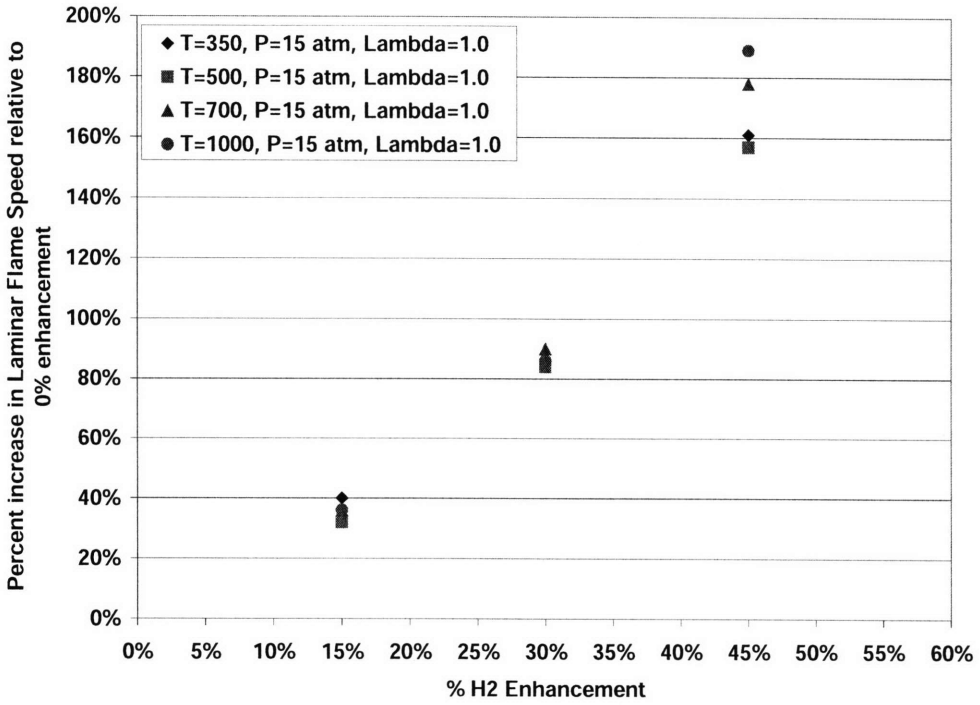

Figure 3-7 – Percent increase in laminar flame speed, relative to baseline conditions, with pure H2-enhancement; Methane, λ=1.0, P=15 atm, various temperatures

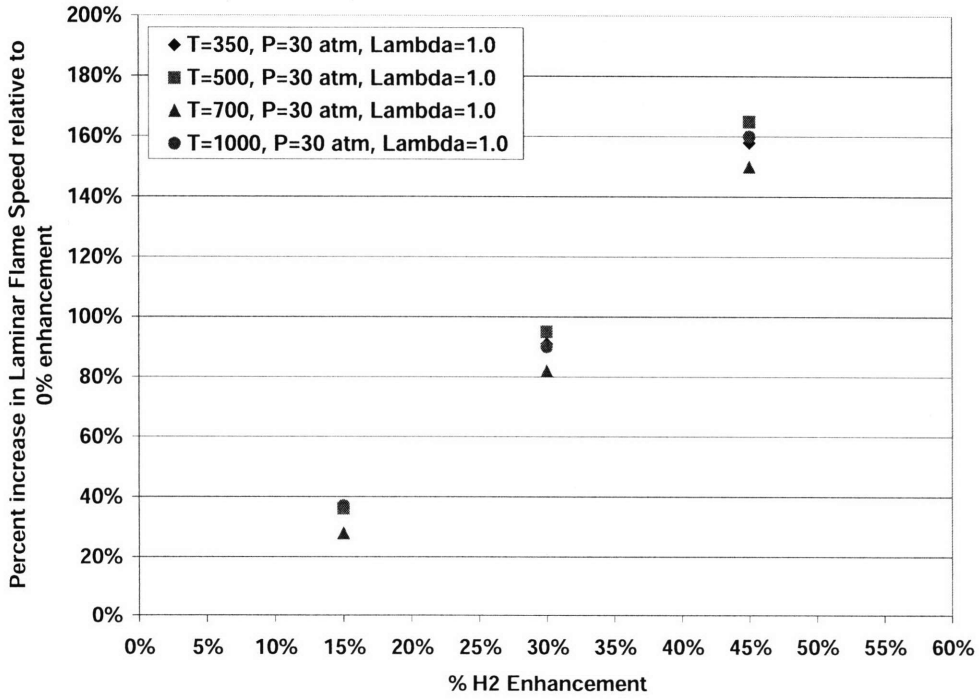

Figure 3-8 – Percent increase in laminar flame speed, relative to baseline conditions, with pure H2-enhancement; Methane, λ=1.0, P=30 atm, various temperatures

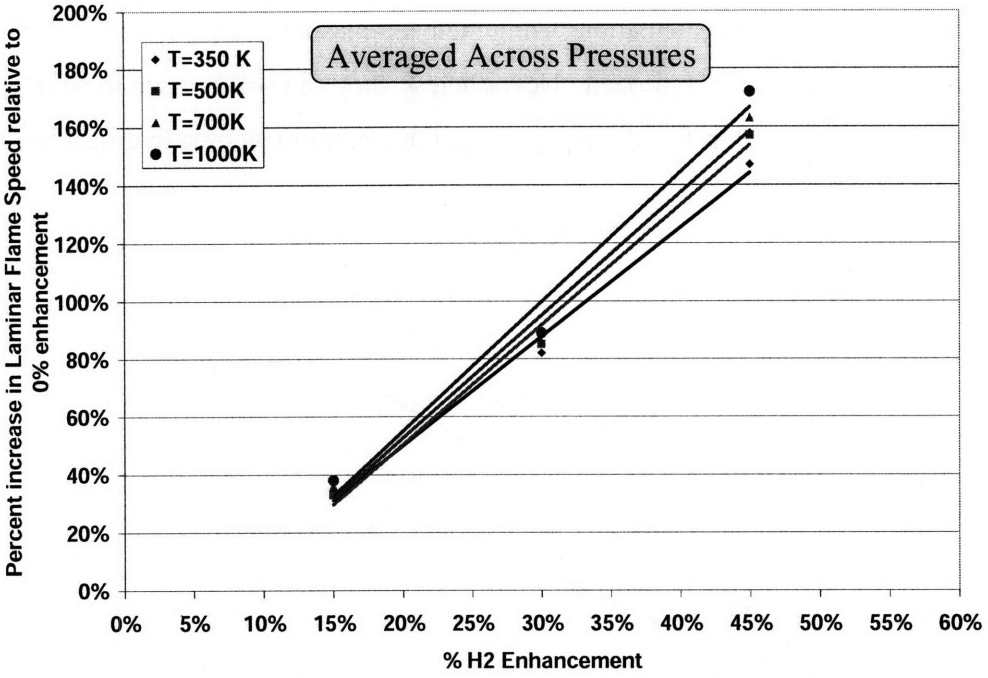

Figure 3-9 – Percent increase in laminar flame speed, relative to baseline conditions, with pure H2-enhancement; Methane, λ=1.0, various temperatures, averaged across six pressures

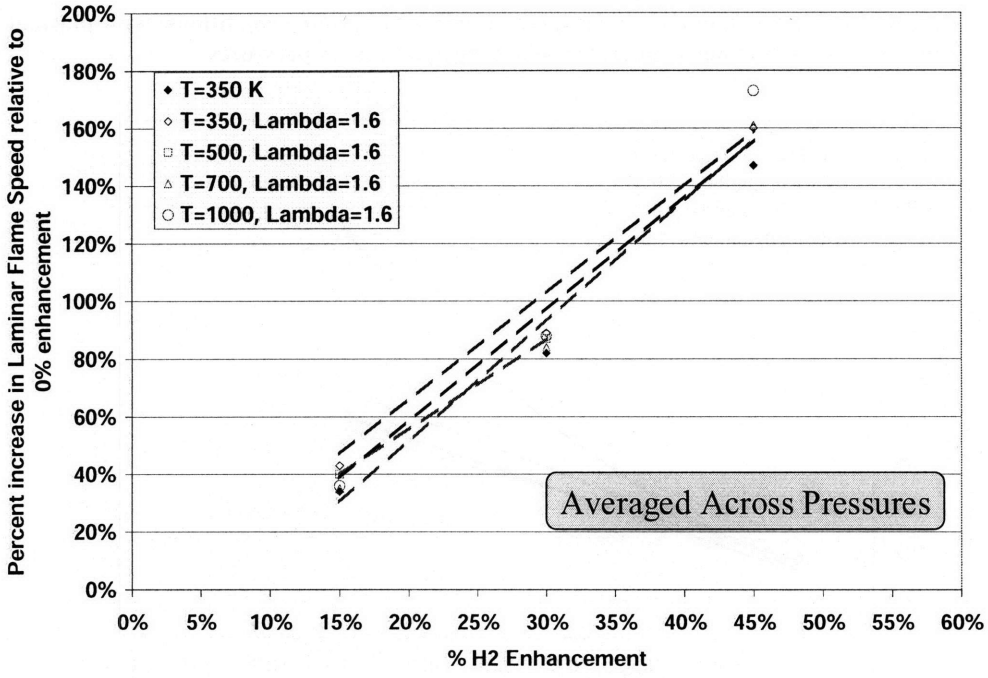

Figure 3-10 – Percent increase in laminar flame speed, relative to baseline conditions, with pure H2-enhancement; Methane, λ=1.6, various temperatures, averaged across six pressures

3.2.3 Plasmatron Results

The laminar flame speed calculations using methane-plasmatron-air mixtures, do not show trends as clean as those for Hydrogen. Nevertheless, they can still be used to develop an approximate correction factor for the effect of plasmatron enhancement on a hydrocarbon fuel.

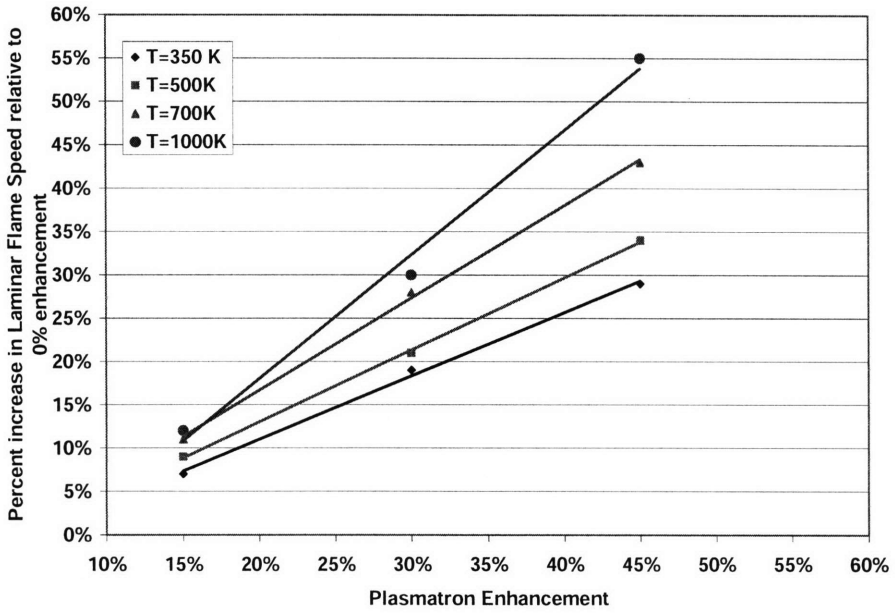

Figure 3-11 – Percent increase in laminar flame speed, relative to baseline conditions, with plasmatron H2-enhancement; Methane, λ=1.0, various temperatures, averaged across six pressures

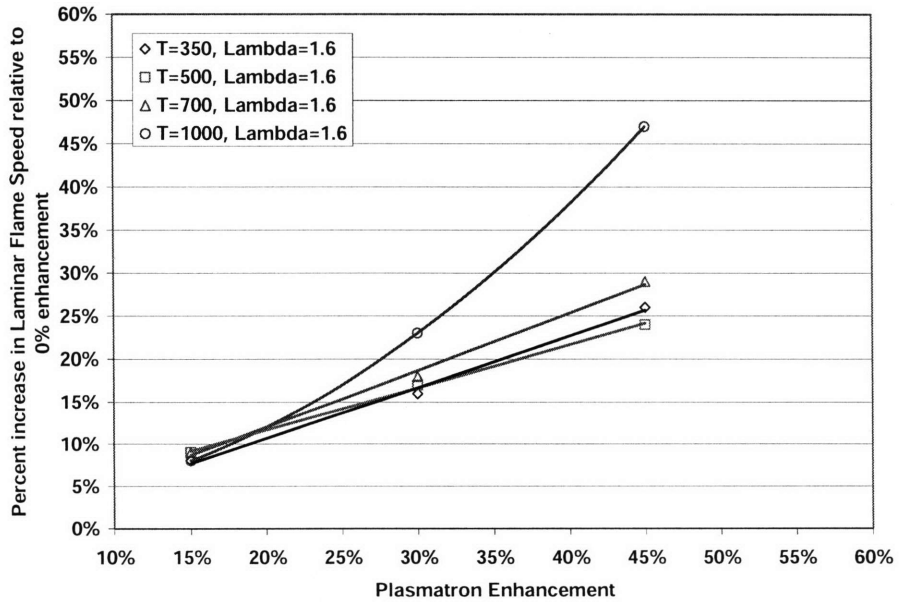

Figure 3-12 – Percent increase in laminar flame speed, relative to baseline conditions, with plasmatron H2-enhancement; Methane, λ=1.6, various temperatures, averaged across six pressures

Chapter 4 – AIR-FUEL RATIO EFFECTS ON EFFICIENCY: EXPERIMENTAL FINDINGS AND BASIC TRENDS

4.1 Introduction

As the relative air-fuel ratio in an engine is varied, two regimes become apparent in the efficiency vs. lambda curve as seen in Fig. 4-1, and in previous literature [4, 14]. The first regime which starts at stoichiometric conditions and ends at the location of peak efficiency is characterized by a steadily increasing engine efficiency and a low variability in NIMEP. Following the location of peak efficiency begins the second regime which is characterized by a falling efficiency and a rapid increase in NIMEP variability. The practical lean drivability limit, defined as 2% of COV in NIMEP is soon reached and is followed by a more erratic lean misfire limit. Figure 4-1 raises a few fundamental questions which have not yet been resolved: what determines the shape of the efficiency curve, what determines the location of both the peak efficiency and the drivability lean limit, and how can these be extended; what is the role of combustion variability; is there a direct link between the rapid fall in efficiency and the rapid rise in NIMEP variability? Answers to these questions are important to get a better understanding of engine efficiency in general and more specifically, to improve lean and hydrogen-enhanced engine concepts.

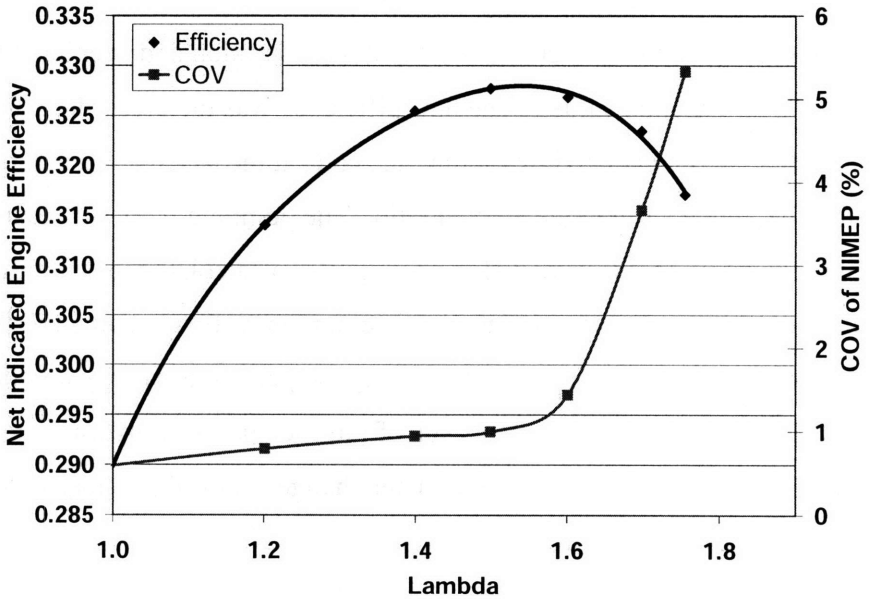

Figure 4-1 – Effect of air-fuel ratio on efficiency and coefficient of variation in NIMEP; MBT timing, 1500 rpm, r_c = 9.8:1, NIMEP = 3.5 bar, Indolene

4.2 Methodology

To better understand these questions, combustion modeling was performed. MIT's engine cycle model was used to simulate the experimental results obtained in the test engine; details of this code developed by Poulos can be found in [21, 29]. The code was initially run at MBT conditions and a constant load of 3.5 bar NIMEP. The experimental burn durations were used as an input; these were generated using an in-house burn rate code. Based on these inputs, the code would fit a Wiebe function to the burning profile. All other parameters such as engine geometry (e.g., compression ratio) and initial conditions were set to match the actual experimental setup.

Using the simulation, a framework was developed to analyze the effects of air-fuel ratio on efficiency. The framework consists of breaking down the changes in net indicated engine efficiency, relative to the baseline efficiency at stoichiometric conditions, into four different components: pumping losses, heat transfer losses, burn duration effects, and thermodynamic effects due to changes in the specific heats ratio, gamma. This method of analysis helps to understand the behavior of the efficiency curve, the location of the peak efficiency point, and the relative contribution of the variables affecting the efficiency.

Simulations were performed to isolate the effect of each variable, and thus determine the magnitude of its contribution to the overall efficiency. As a first step, a baseline efficiency was calculated for stoichiometric conditions. The burn duration effect at each lambda was then calculated by running the code using each experimental burn duration and keeping all other variables constant at their baseline values. The new efficiency was then recorded. Similarly, the gamma or dilution effect was calculated by running the code at the baseline burn duration and heat transfer multiplier, while varying the air-fuel ratio. The pumping work was easily separated from each one of the runs, since it is provided as an output. To calculate the heat transfer effect, both the burn duration and the gamma simulations were run twice, first keeping the Woschni heat transfer model multiplier constant, and then holding the percent of energy loss due to heat transfer constant. The difference between the results from each pair of runs was determined to be the relative change in efficiency due to heat transfer changes. For higher loads, the Woschni heat transfer multiplier was reduced based on data shown in [22].

4.3 Simulation Results

Figure 4-2 shows the magnitude of the different efficiency components predicted by the simulation, and the resulting change in net indicated efficiency. The results are plotted as absolute differences, in percentage points, relative to the baseline efficiency which is set as the reference point. Thus for example, as the mixture gets leaner, and the burn duration gets longer, everything else being the same, the efficiency would fall by 1 percentage point at lambda of 1.5. From the graph one can observe the behavior of the three components that enhance efficiency. As the relative air-fuel ratio increases, the ratio of specific heats increases due to thermodynamic effects, contributing to higher efficiency through higher expansion work; the pumping losses decrease because the amount of throttling decreases and the intake pressure increases as a larger mass of air is inducted; the total heat transfer losses decrease as well, due to lower combustion temperatures at higher dilution levels. However, these positive efficiency contributions are countered by a lengthening burn duration which increases the time over which the energy is released, increasing the deviation from ideal conditions.

The actual data is also shown in this chart. The agreement between the changes in the simulated total efficiency and the actual data is excellent. One discrepancy, not shown here, is that the absolute magnitude of the MIT model efficiency is 10% higher than the data. This difference can be accounted by the in-cylinder combustion inefficiency, which is not included in the model [23, 22]. Nevertheless the relative change between each point in the data is correctly predicted by the model.

It is important to note that the simulated peak efficiency location matches the actual location of peak efficiency, indicating that the detrimental impact due to lengthening burn duration has been well captured. From the graph it is clear that the eventual decrease in efficiency is due to the increasingly negative impact of the lengthening burn duration.

The agreement for different loads and different compression ratios was also quite good, as will be seen in later sections. This shows that the magnitude of each efficiency component has been adequately represented, and that this framework explains the shape of this efficiency curve.

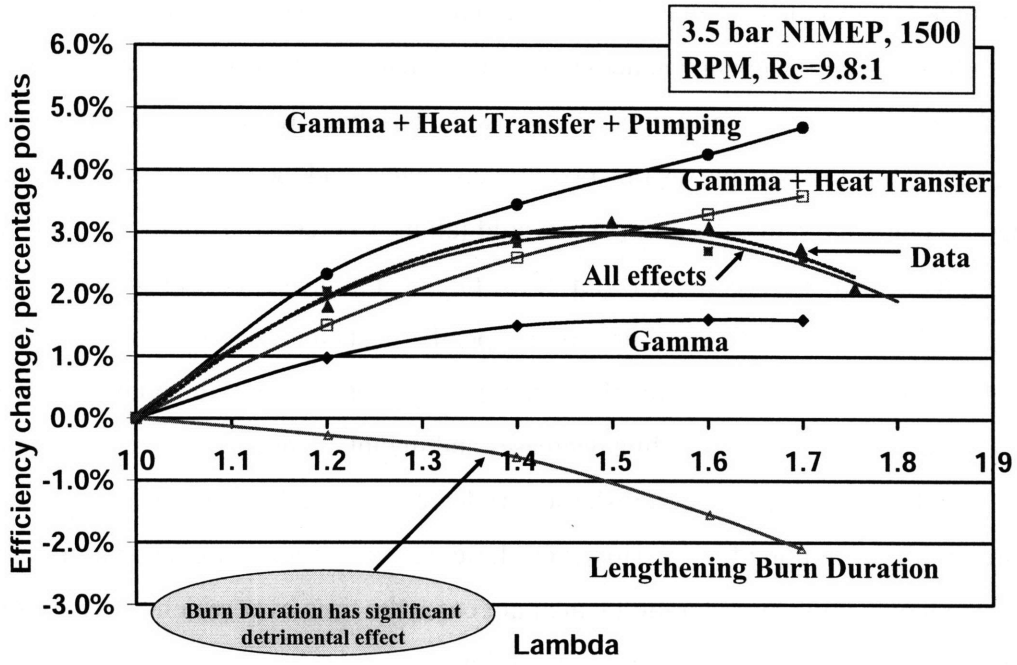

Figure 4-2 – Air-fuel ratio effect on efficiency, comparison of simulation results and actual data; MBT timing, 1500 rpm, r_c = 9.8:1, NIMEP = 3.5 bar, Indolene

4.4 Effect of 10-90% burn duration

As already seen, the time it takes to burn the mass in the cylinder has a major impact on the overall net indicated efficiency. In particular, the length of the time between burning 10% of the mass and 90% of the mass, also known as the 10-90% burn duration (main burning angle) and commonly associated with the flame propagation stage, is the most relevant for efficiency. References [24] agree with this statement, but this conclusion can be drawn from the data presented in this section.

In Fig. 4-3, combustion has been sped up using different levels of hydrogen enhancement (as a percent of total energy into the engine) at the same constant load of 3.5 bar NIMEP, for a compression ratio of 13.4:1. The result is a downward shift in the overall 10-90% burn duration curve (faster combustion), and an increase in net indicated efficiency with higher enhancement levels, relative to pure indolene. This graph shows that the burn duration at which the peak efficiency occurs, is constant, at approximately 30 CAD, irrespective of any shifting of the 10-90% burn duration curve. Connecting this observation to Fig. 4-2, two main implications

emerge. The effect of the entire burn duration process (0-100%) on efficiency is dominated by the 10-90% burn duration. Thus the burn duration effect shown in Fig. 4-2, can be thought of as the 10-90% burn duration effect. The second important implication is that there exists a critical 10-90% burn duration beyond which the detrimental effect on efficiency increases rapidly. Consequently, because of the balance of effects shown in Fig. 4-2, peak efficiency will occur right before this large increase in negative impact, or approximately at 30 CAD, for this specific engine. The deteriorating effect on efficiency caused by slower combustion can no longer be made up by the other positive factors such as pumping work reduction, heat transfer reduction, and thermodynamic effects.

The conclusion that the 10-90% is the dominating combustion component on the engine efficiency is not surprising because 80% of the total fuel is burned during this interval. However, what is surprising is that there is a limiting burn duration (30 CAD) beyond which the detrimental effect on efficiency increases substantially, causing the efficiency curve to bend downwards. This effect is not fortuitous, as it was observed across a variety of conditions. Figure 4-4 also shows the limiting 30 CAD while comparing different compression ratios at the same 3.5 bar NIMEP load. Similarly, Fig. 4-5 shows the same point using EGR dilution. At higher loads (Fig. 4-6), and different turbulence levels (Fig. 4-7), created using different turbulence plates [13, 14], the limiting burn duration was also 30 or 29 CAD, the difference of 1 CA degree being within experimental error.

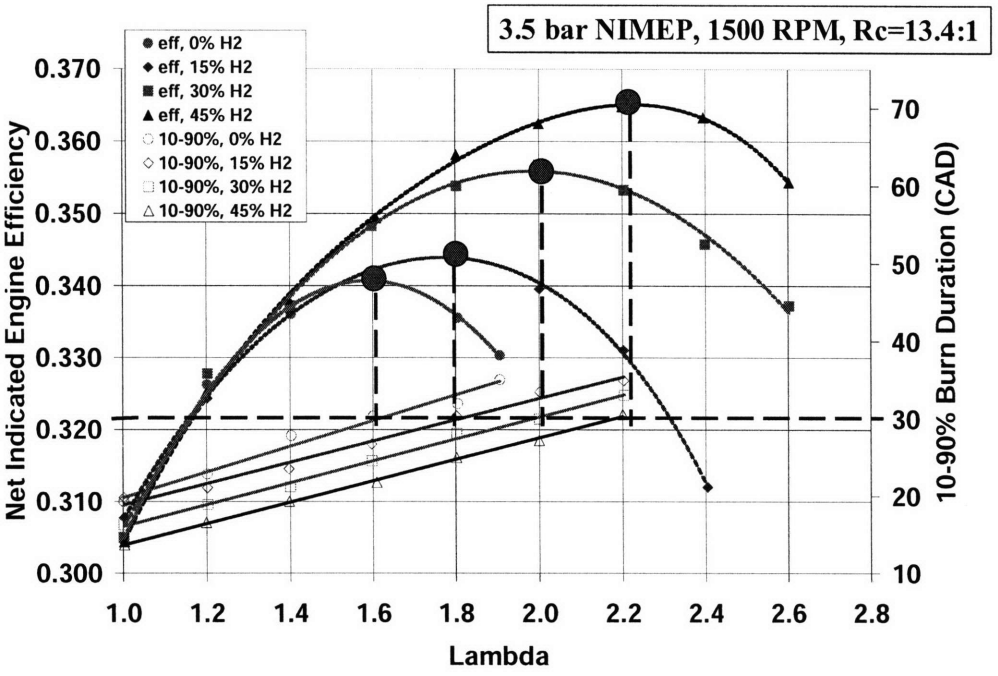

Figure 4-3 – Air-fuel ratio effect on efficiency and burn duration for different levels of hydrogen enhancement; MBT timing, 1500 RPM, r_c=13.4:1, NIMEP = 3.5 bar, Indolene

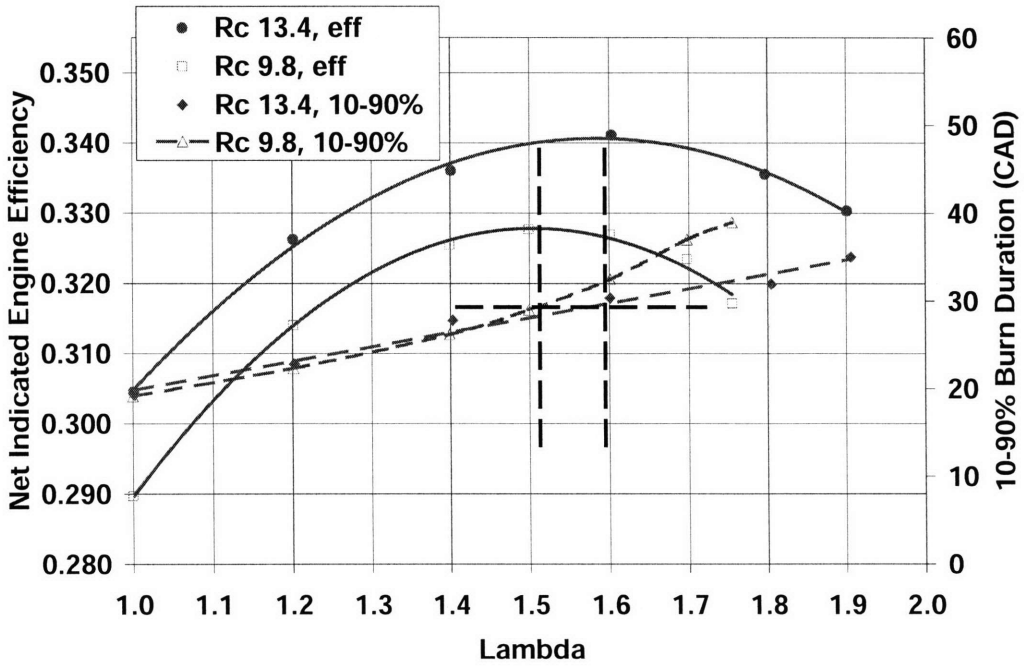

Figure 4-4 – Comparison of air-fuel ratio effect on efficiency and burn duration for two different compression ratios; MBT timing, 1500 RPM, NIMEP = 3.5 bar, Indolene

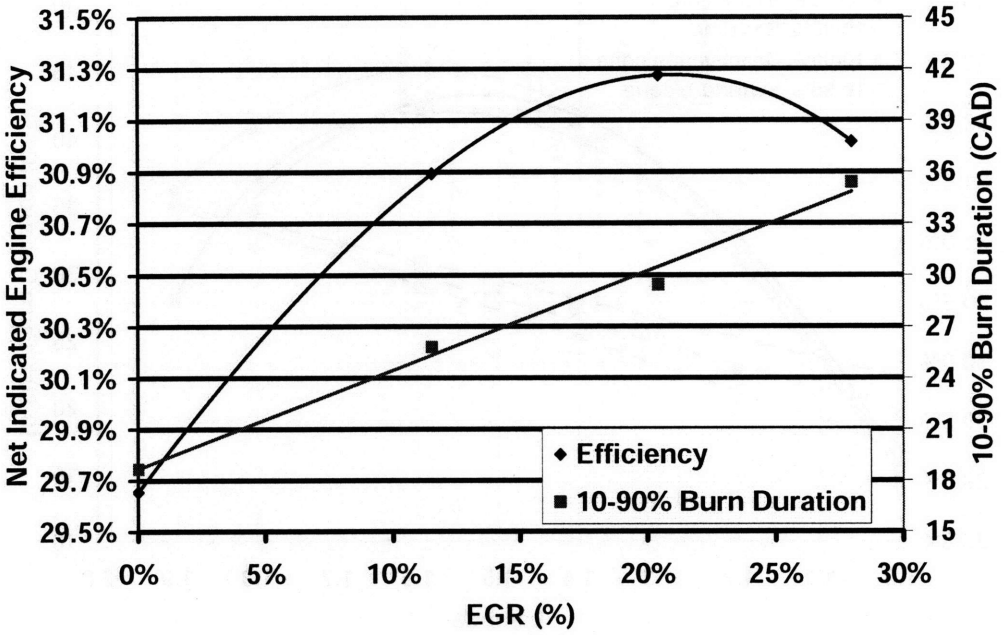

Figure 4-5 – EGR effect on efficiency and burn duration; MBT timing, 1500 RPM, r_c=9.8:1, NIMEP = 3.5 bar, Indolene

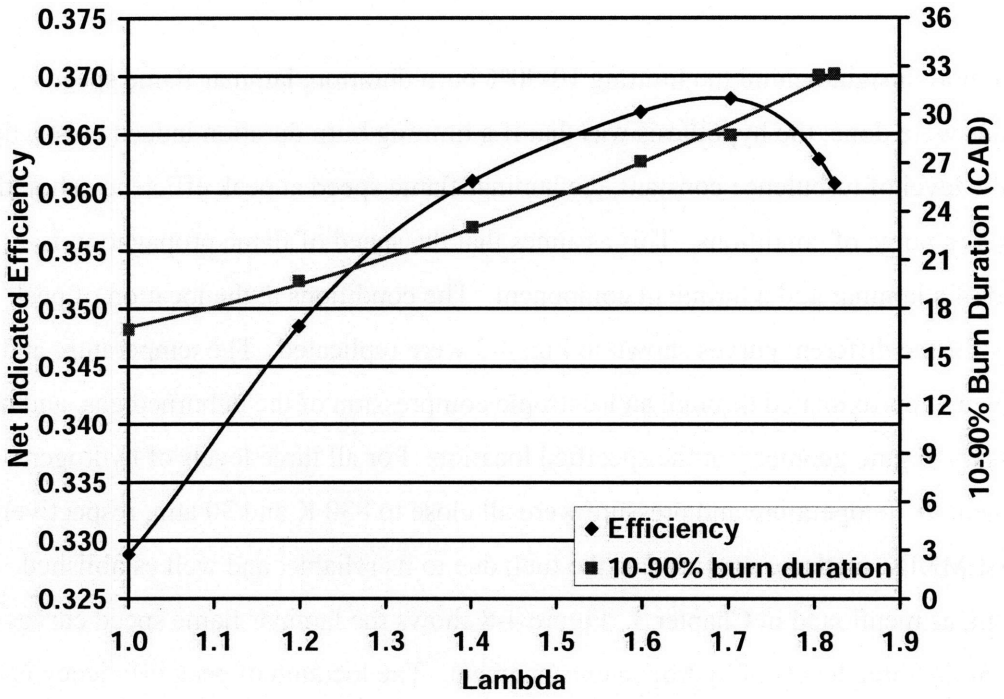

Figure 4-6 – Air-fuel ratio effect on efficiency and burn duration at high load; MBT timing, 1500 RPM, r_c=9.8:1, NIMEP = 6.0 bar, Indolene

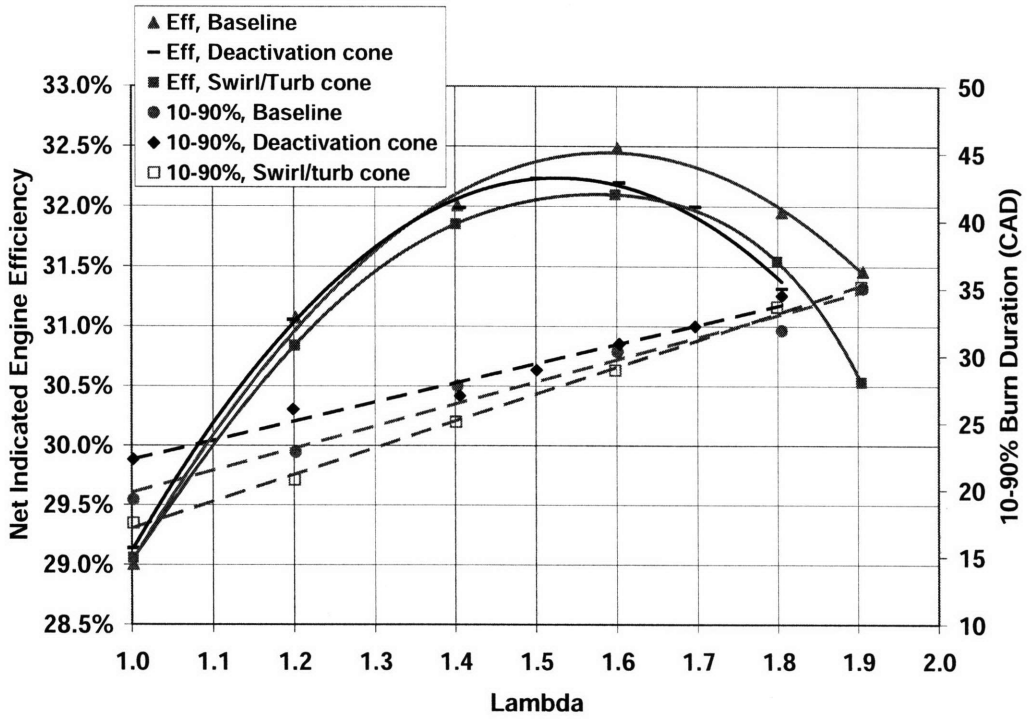

Figure 4-7 – Air-fuel ratio effect on efficiency and burn duration for different turbulence cones; MBT timing, 1500 RPM, r_c=9.8:1, NIMEP = 3.5 bar, Indolene

To obtain more insight behind the limiting 10-90% burn duration, laminar flame speed calculations were done; the hypothesis was that if a limiting burn duration indeed exists, then keeping the level of turbulence constant, the laminar flame speed at peak efficiency should be the same across a range of conditions. This assumes that the speed of flame propagation is composed of a laminar and a turbulent component. The conditions at the location of peak efficiency for the different curves shown in Fig. 4-3 were replicated. The temperature and pressure were approximated through an isentropic compression of the unburned gas, and using the necessary engine geometry at the specified location. For all three levels of hydrogen enhancement the temperature and pressure were all close to 830 K and 30 atm, respectively. Using CHEMKIN, methane was used as the fuel, due to its reliable, and well established, mechanism, as mentioned in Chapter 3. Figure 4-8 shows the laminar flame speed curves for methane, at the three levels of hydrogen enhancement. The location of peak efficiency is also noted. It stands out that the laminar flame speed at the location of peak efficiency for each level

of enhancement is constant, close to 50 cm/sec. This reinforces the conclusion that there is a limiting duration for burning the 10-90% mass fraction.

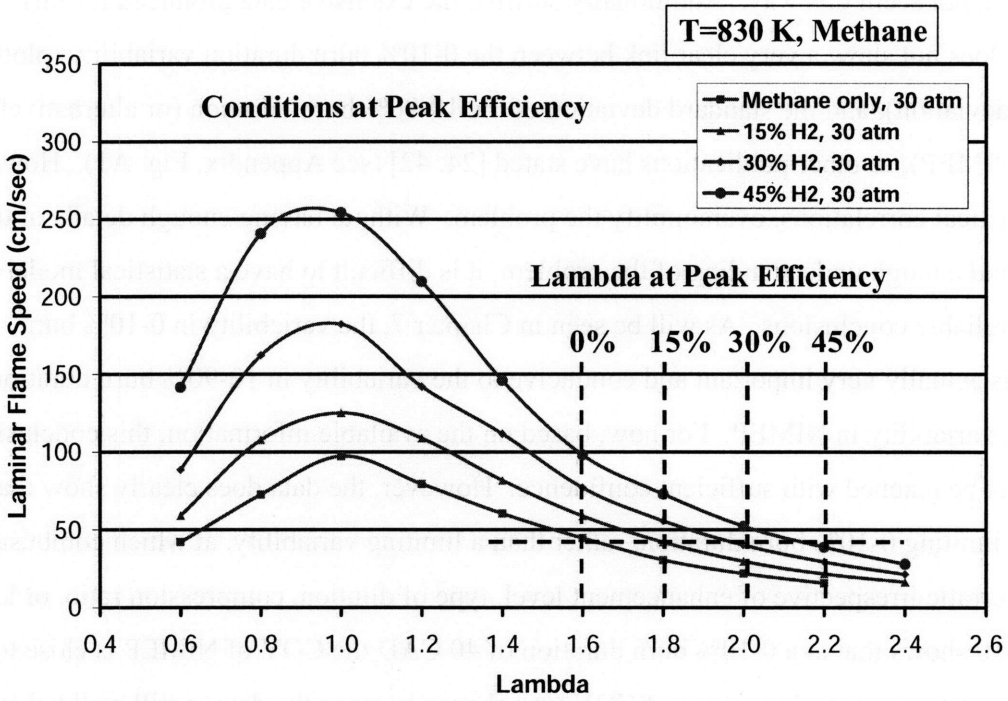

Figure 4-8 – Air-fuel ratio effect on laminar flame speed for different levels of hydrogen enhancement with CH_4 as the fuel; 830 K, 30 atm

4.5 Effect of 0-10% burn duration

Thus far, we have concluded that the 10-90% burn duration is the main variable controlling efficiency. Consequently, the variability in 10-90% burn duration will cause variability in NIMEP. Figure 4-9 shows the close link between the variability in these two variables. This chart shows the ratio of the actual standard deviation to the baseline stoichiometric standard deviation for NIMEP (C), 10-90% burn duration (B), and 0-10% burn duration (A). As the relative air-fuel ratio is varied, the variability in NIMEP follows the same trend as the variability in the 10-90% burn duration; the variability for both cases starts low, and quickly surpasses the initial stoichiometric variability by a factor greater than 2 beyond lambda of 1.4. The variability in the 0-10% burn duration however stays fairly low and remains well

behaved, closer to the baseline stoichiometric variability. It does also have a rapid increase after λ=1.6, similar to the other two curves, but the overall behavior of this curve does not quite coincide with the variability of the NIMEP or the variability of the 10-90% burn duration, at least it does not seem this way. Additionally, at first, the extensive data produced for this research, does not show a very clear link between the 0-10% burn duration variability (plotted as standard deviation), and the standard deviation of the 10-90% burn duration (or alternatively the COV of NIMEP), as other publications have stated [24, 42] (see Appendix, Fig. A1). However, these statistical correlations, oversimplify the problem. Without having enough details of the physics, and enough understanding of the problem, it is difficult to have a statistical model that provides reliable conclusions. As will be seen in Chapter 7, the variability in 0-10% burn duration is actually very important and conducive to the variability in 10-90% burn duration and therefore, variability in NIMEP. For now, based on the available information, this conclusion can not yet be reached with sufficient confidence. However, the data does clearly show that there is a limiting 0-10% burn duration, rather than a limiting variability, at which combustion becomes erratic irrespective of enhancement level, type of dilution, compression ratio, or load. Figure 4-10 shows that at a 0-10% burn duration of 40 CAD the COV of NIMEP is close to 2% for all conditions tested. This value of COV was chosen because the data is still well behaved, not having yet reached the lean misfire limit, and because it is typically used in industry as the practical COV drivability limit [3]. Figure 4-11 shows a similar limiting behavior when the COV in NIMEP is plotted against the 10-90% burn duration. It is believed that the first combustion event, 0-10% burn duration, is the cause for the similar behavior of the second combustion event, 10-90% burn duration. Figure 4-12 shows a specific comparison between different compression ratios, where the limiting flame initiation duration of 40 CAD is clear.

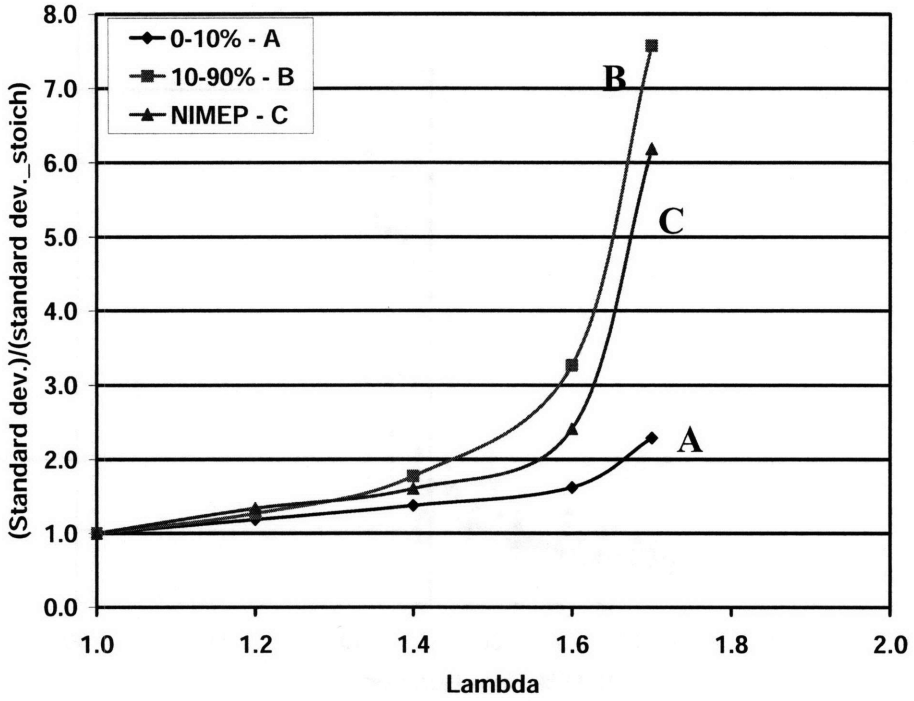

Figure 4-9 – Variability of NIMEP, 10-90% burn duration, and 0-10% burn duration with air-fuel ratio; MBT timing, 1500 RPM, r_c=9.8:1, NIMEP = 3.5 bar, Indolene

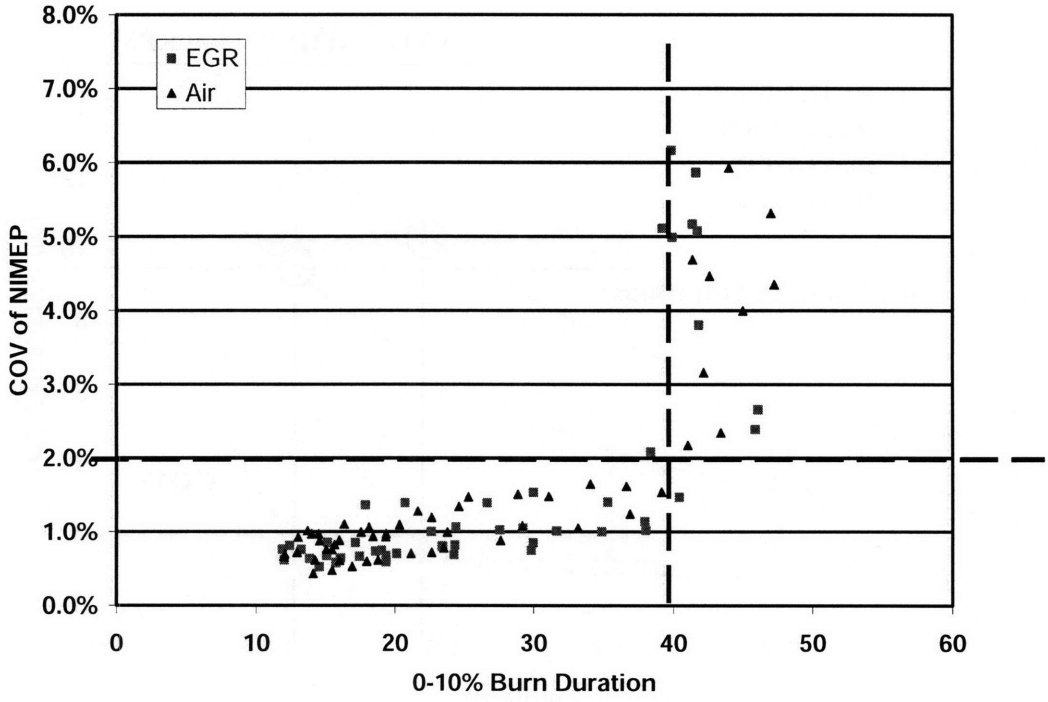

Figure 4-10 – Changes in COV of NIMEP with 0-10% burn duration; MBT timing, 1500 RPM, r_c=9.8:1, NIMEP = 3.5 bar, Indolene

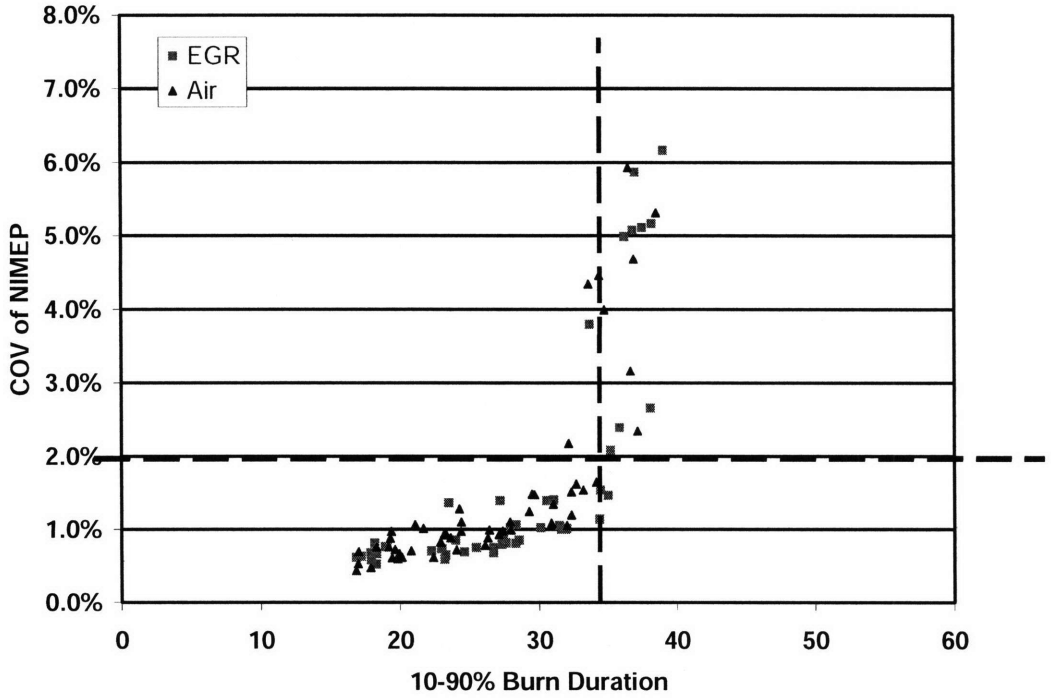

Figure 4-11 – Changes in COV of NIMEP with 10-90% burn duration; MBT timing, 1500 RPM, r_c=9.8:1, NIMEP = 3.5 bar, Indolene

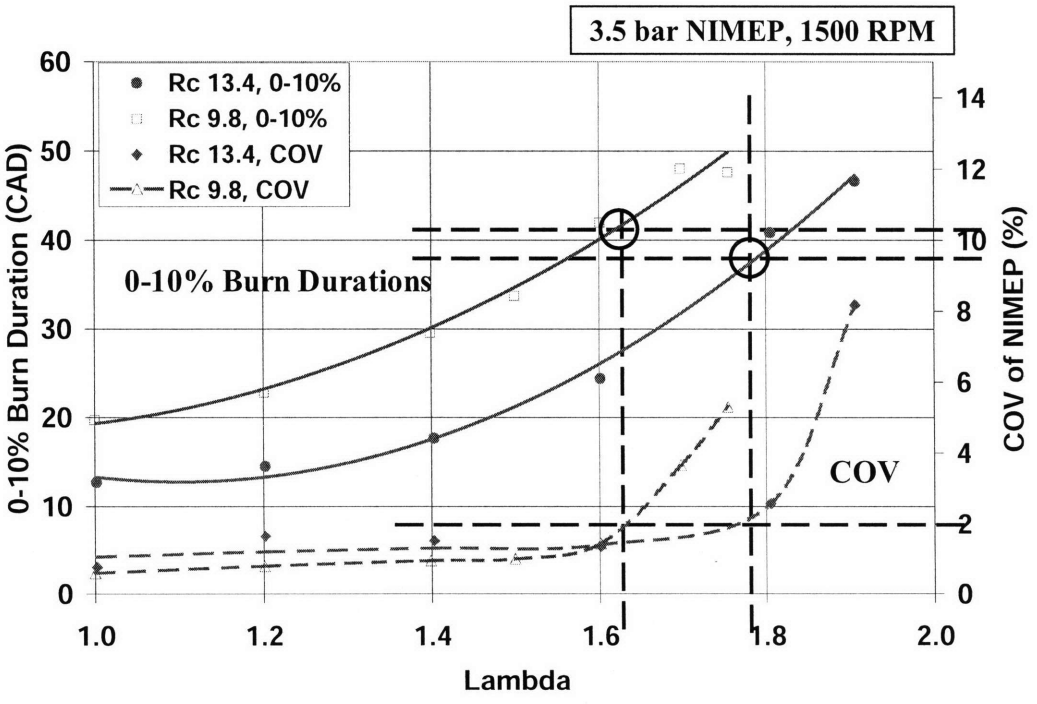

Figure 4-12 – Relationship between coefficient of variation and 0-10% burn duration as air-fuel ratio increases for two different compression ratios; MBT timing, 1500 RPM, r_c=9.8:1, NIMEP = 3.5 bar, Indolene

4.6 Location of Peak Efficiency Relative to Combustion Instability

In past publications, with experiments done at lower compression ratios [13, 14] it was thought that the peak in net indicated efficiency and the onset of combustion instability, as indicated by the rapid rise in COV of NIMEP, were directly linked. The curves typically lined up at peak efficiency and the onset of variability. However, this was not the case for the higher compression ratios used during this research. To examine this issue, one must again look at the burn durations for answers.

Figure 4-13 shows the non-linear relationship between the 10-90% burn duration and the 0-10% burn duration. Initially, the length of the 0-10% burn duration changes at a lower rate than the 10-90% burn duration (higher initial slope); but moving further along the x-axis, as the 0-10% burn durations get longer, the 10-90% burn duration increases at a lower rate, thus the slope at the longer burn duration end of the curve is lower than the slope at the beginning, or the faster burn duration part of the curve. This can be explained because at the higher burn durations, where the level of dilution is higher, the laminar flame speed, which strongly affects the 0-10% burn duration is lower, but the level of turbulence, which primarily dominates the 10-90% burn duration remains about the same. Thus, due to its weaker laminar flame speed dependence, the 10-90% burn duration will see less of a lengthening effect at higher dilution (higher burn durations), than the 0-10% burn duration.

The figure also shows the same trend for a higher compression ratio and for 30% plasmatron enhancement. The initial offset of the high compression ratio curve relative to the lower compression ratio curve can also be explained. For a given 10-90% burn duration, the flame initiation stage is faster for the higher compression ratio due to the higher laminar flame speeds caused by the higher pre-combustion temperatures, and due to a lower residual fraction. This faster laminar flame speed has the most impact on the 0-10% burn duration. Similarly, a faster laminar flame speed due to hydrogen addition explains the offset of the 30% enhancement curve.

Figure 4-14 shows the burn duration relationship for all data at various compression ratios, various plasmatron enhancement levels, air dilution, and EGR dilution, at MBT spark timing, and 3.5 bar NIMEP load. This figure shows that the 10-90% burn duration vs. 0-10% burn duration curve keeps the same shape irrespective of operating conditions. However, and as discussed previously, the exact relationship between the burn durations changes at different

operating conditions, as witnessed by the vertical spread in the data, due to the differences in laminar flame speeds.

Using the two previous conclusions, that is, the fixed relationship between 10-90% burn duration and efficiency, and the fixed relationship between 0-10% burn duration and 10-90% burn duration variability (or NIMEP variability), and knowing that the relationship between the 10-90% and 0-10% burn duration changes (at least until 2% COV of NIMEP is reached), as shown in Figs. 4-13 and 4-14, it follows that the location of peak efficiency and combustion instability will change relative to each other. Figure 4-15 shows this observation at two different compression ratios. For the high compression ratio, the onset of combustion instability occurs further away from the location of peak efficiency than in the lower compression ratio case. The implication of this is that the peak in net indicated engine efficiency and the rapid rise in combustion instability are not directly linked (at least not necessarily), and they happen at different locations depending on the operating conditions. Another implication, as will be examined more closely in the next section, is that variability only becomes important at or after the location of peak efficiency.

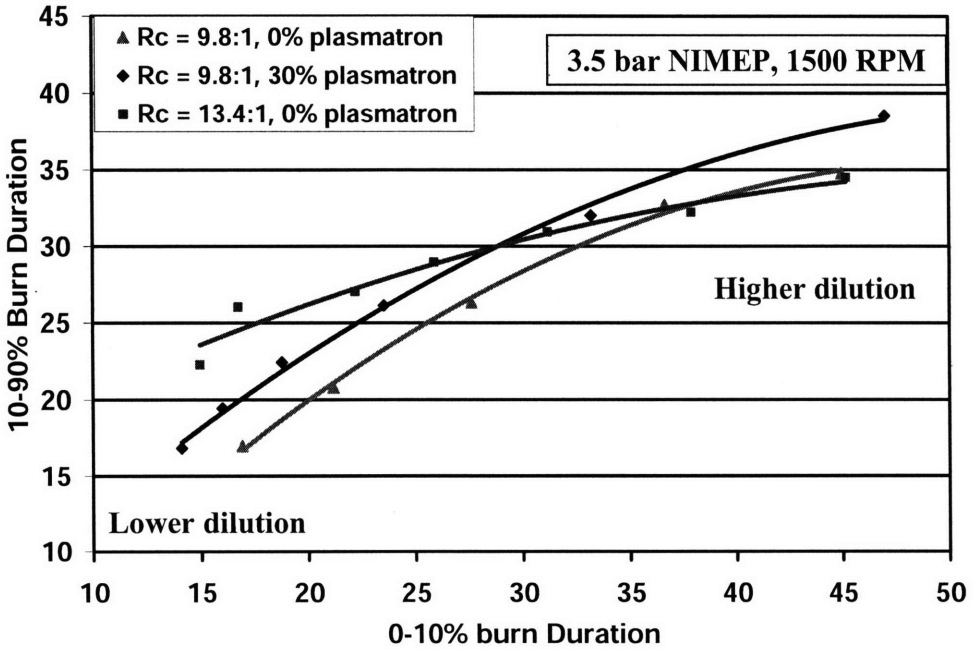

Figure 4-13 – Relationship between 10-90% burn duration and 0-10% burn duration for different levels of plasmatron enhancement; MBT timing, 1500 RPM, NIMEP = 3.5 bar, Indolene

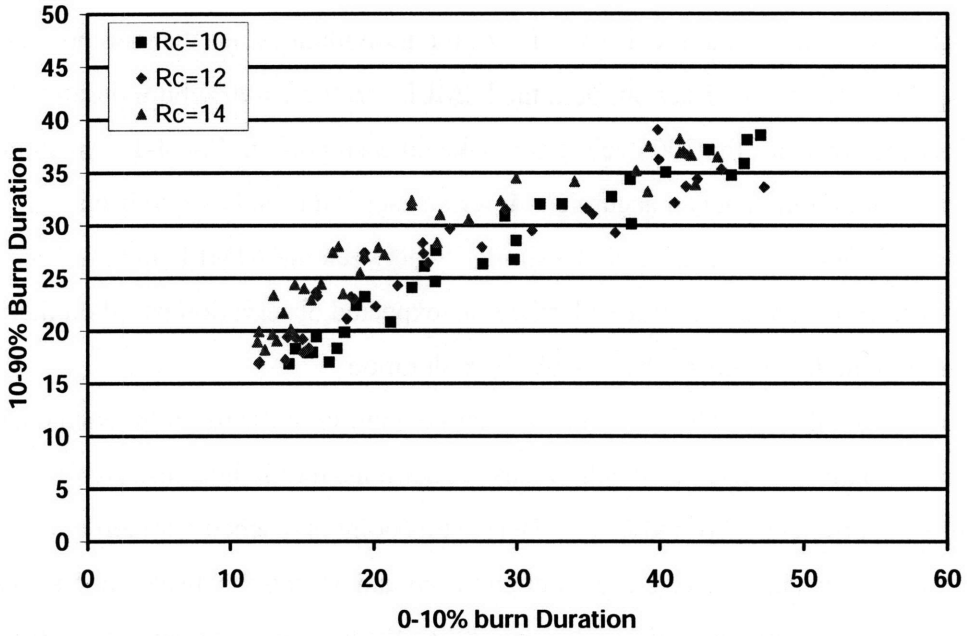

Figure 4-14 – Relationship between 10-90% burn duration and 0-10% burn duration for three different compression ratios using three levels of plasmatron enhancement, air and EGR dilution; MBT timing, 1500 RPM, NIMEP = 3.5 bar, Indolene

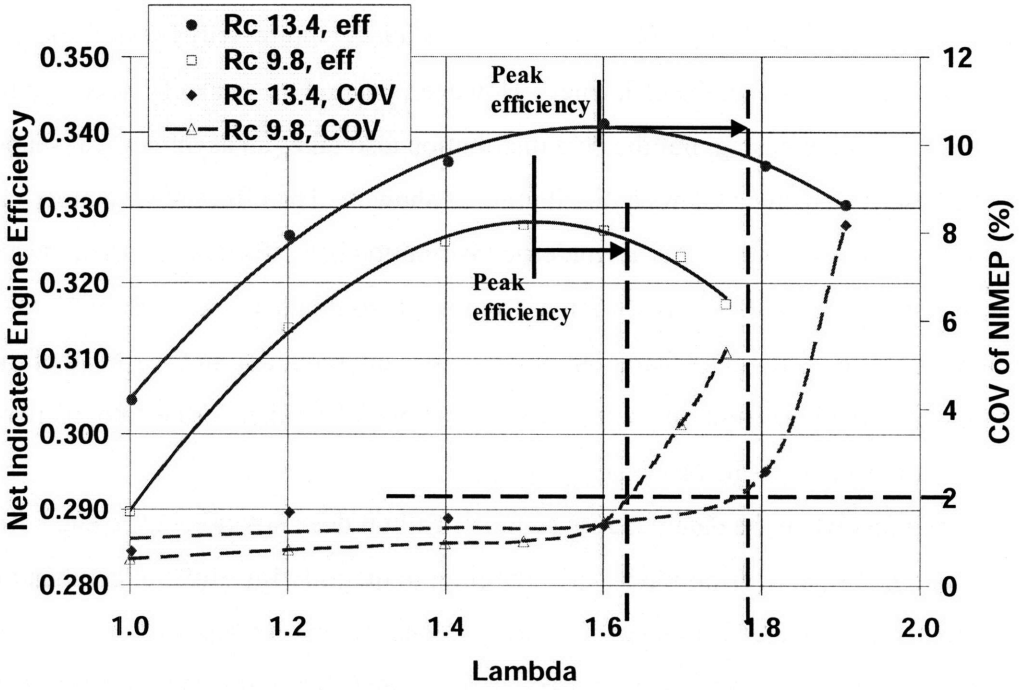

Figure 4-15 – Relationship between efficiency and coefficient of variation with increasing air-fuel ratio for two different compression ratios; MBT timing, 1500 RPM, NIMEP = 3.5 bar, Indolene

4.7 Effect of Combustion Variability on Efficiency

To understand the effect of combustion variability on efficiency, as the air-fuel ratio increases, it is necessary to look at the distribution of the individual cycles that compose each data point. Figures 4-16 and 4-17 lay out both the NIMEP and the 10-90% burn duration distributions, respectively, for the 300 cycles that make up each point in Fig. 4-1. An appropriate probability density function, that can accurately describe each data set, has also been superimposed to the data, as shown. Note the similarity between the NIMEP and the 10-90% burn duration distributions at each value of lambda, an expected observation based on the previous discussion on the effects of the 10-90% burn duration.

Although variability, as defined by the standard deviation of the mean for each data set, steadily increases relative to baseline stoichiometric conditions, it only becomes significant after the location of peak efficiency, around λ=1.6. Before this point is reached, variability does not affect efficiency. This occurs because even though the spread among the distribution keeps increasing, the data stays symmetrical and does not affect the average of either the NIMEP or the 10-90% burn duration. This can be verified by looking at the good agreement between the data and the superimposed Gaussian curves. Because of this symmetry, any cycles with low NIMEP are canceled out by cycles with high NIMEP. Consequently, any reduction in the spread, or variability, in the NIMEP distribution before the peak efficiency point, will not shift the average NIMEP, and thus will not affect the efficiency. However, beyond the peak efficiency point, the spread not only keeps increasing, but the data distribution also takes an asymmetrical shape which can be described using a Gamma distribution as shown[2]. The effect of variability on efficiency is now important since this asymmetric distribution has effectively shifted the average NIMEP and the average 10-90% burn duration, from what would have been obtained had the data kept a normal (i.e., Gaussian) shape. In other words, any reduction in the spread of the data with these asymmetrical distributions will now shift the overall average of the data, increasing the NIMEP average and thus the efficiency.

Knowing that when the data behaves symmetrically it does not affect efficiency, it is possible to use the normal distribution as an upper limit to quantify the effect of combustion variability on the net indicated efficiency. Figure 4-18 shows the resulting shift in the average NIMEP when a Gaussian distribution is superimposed on that part of the data that most closely

[2] See Chapter 7 for a more detailed discussion of the reason for this asymmetric variability

resembles a symmetric distribution. The result is a shift in the NIMEP average, increasing the net indicated efficiency. The average 10-90% burn duration distribution that results when only the NIMEP data enclosed by the superimposed Gaussian distribution from Fig. 4-18 is considered is also shown in Fig. 4-19. The average of the 10-90% burn duration has also shifted, becoming faster. This is consistent with the previous discussions of how the 10-90% burn duration and NIMEP go hand-in-hand, and how at MBT timing conditions a faster 10-90% burn duration is preferred and will have a lesser negative impact on the overall efficiency. Figure 4-20 shows the resulting efficiency and 10-90% burn duration curves assuming a normal distribution for all the data. In essence, variability does not play a role in these new curves, however, the efficiency still falls due to the lengthening burn duration. The original efficiency and burn duration curves are also shown in this graph. Comparing both efficiency curves, one can see that the efficiency loss due to variability is modest, around 2%.

A second method can be applied to quantify the effect of variability on the net indicated engine efficiency. Figure 4-21 shows three efficiency curves used in figure 4-3, along with their corresponding COV of NIMEP. Due to the magnitude of the 10-90% burn duration relative to the 0-10% burn duration, the rapid rise in COV for the H2-enhanced curves occurs much later in the relative air-fuel ratio scale, compared to the location of peak efficiency. For example, for 30% H2 enhancement, efficiency peaks at lambda of close to 2.0, but the COV is fairly flat until lambda of around 2.8. This implies, that efficiency is not affected by variability until lambda of 2.8. Efficiency still falls, however, due to a lengthening burn duration, as has been previously explained. The implication of this observation is that the H2-enhanced curves provide an upper limit for net indicated efficiency in the absence of variability. That is, the effect of variability and burn duration on efficiency can be effectively separated. This can be done by taking the fall in efficiency from the baseline indolene curve, which is affected by both variability and lengthening burn duration, and comparing this efficiency drop to the corresponding efficiency drop that occurs in the presence of a lengthening burn duration only (as occurs with the H2-enhanced curves). The result of this analysis is shown in figure 4-22, where the percent change in the efficiency relative to peak efficiency, for each of the three curves from figure 4-21 has been lined up at the lambda for peak efficiency. Moving away from this peak efficiency point, the H2-curves show an almost identical fall in efficiency, as should be expected with fairly symmetrical burn duration

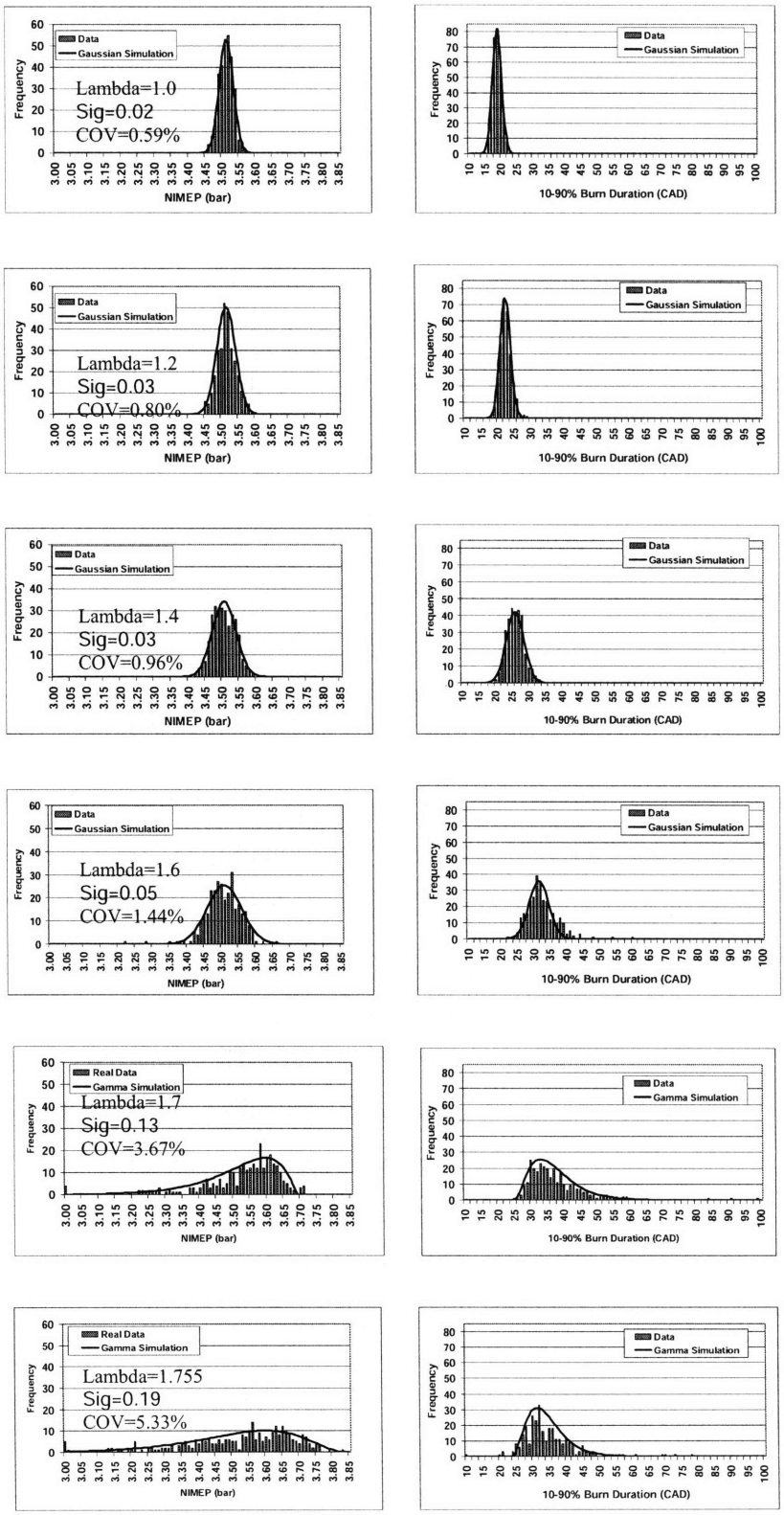

Figure 4-16 and Figure 4-17; NIMEP and 10-90% burn duration distributions respectively for different air-fuel ratios; MBT timing, 1500 RPM, r_c=9.8:1, NIMEP = 3.5 bar, Indolene

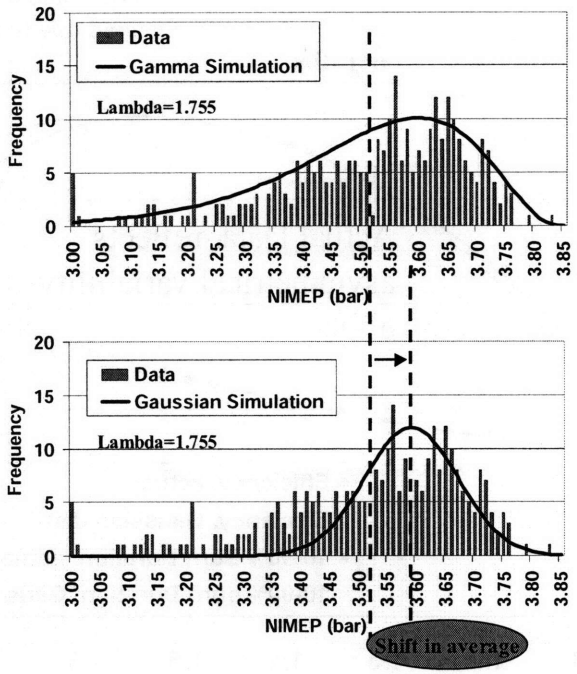

Figure 4-18 – Comparison between symmetric and asymmetric NIMEP distributions, and their effect on the overall average; MBT timing, 1500 RPM, r_c=9.8:1, NIMEP = 3.5 bar, Indolene

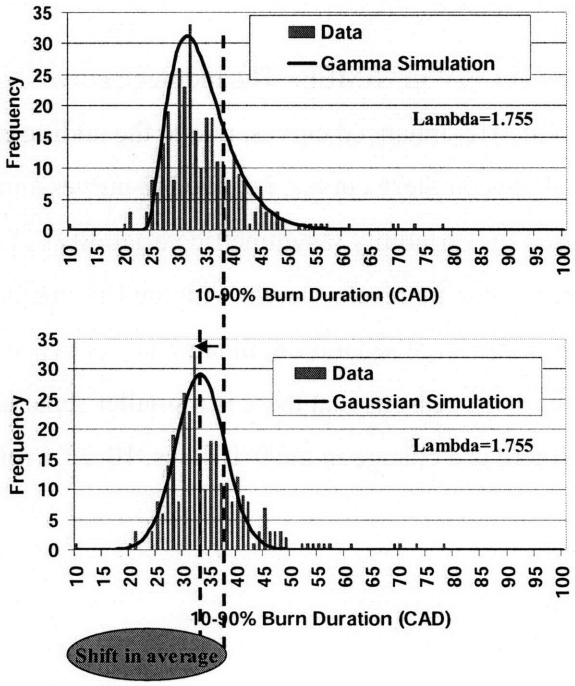

Figure 4-19 – Comparison between symmetric and asymmetric 10-90% burn duration distributions, and their effect on the overall average; MBT timing, 1500 RPM, r_c=9.8:1, NIMEP = 3.5 bar, Indolene

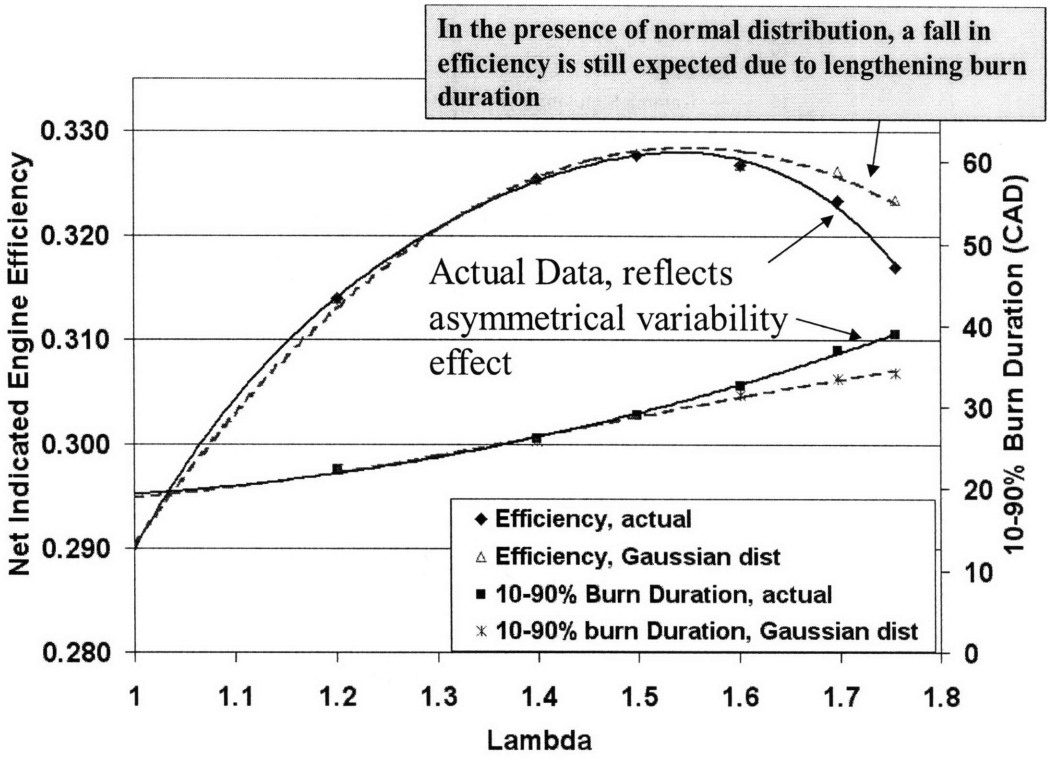

Figure 4-20 – Effect of asymmetric NIMEP and burn duration distributions on efficiency; MBT timing, 1500 RPM, r_c=9.8:1, NIMEP = 3.5 bar, Indolene

variability, and a relatively flat COV in NIMEP. The indolene curve, however, shows a sharper fall in efficiency relative to the H2-enhanced curves, due to the additional effect of asymmetrical variability. The difference between these curves, i.e., the H2-curves and the pure indolene curve, is the efficiency effect caused by variability (asymmetric variability). This loss in efficiency is approximately 2%, consistent with the results shown with the first method.

It should be noted that the large separation, in lambdas, between the peak efficiency and the COV limit occurs for the same reasons that there is a smaller separation in figure 4-15, as was previously explained; there is a change in the 0-10% vs. 10-90% relationship

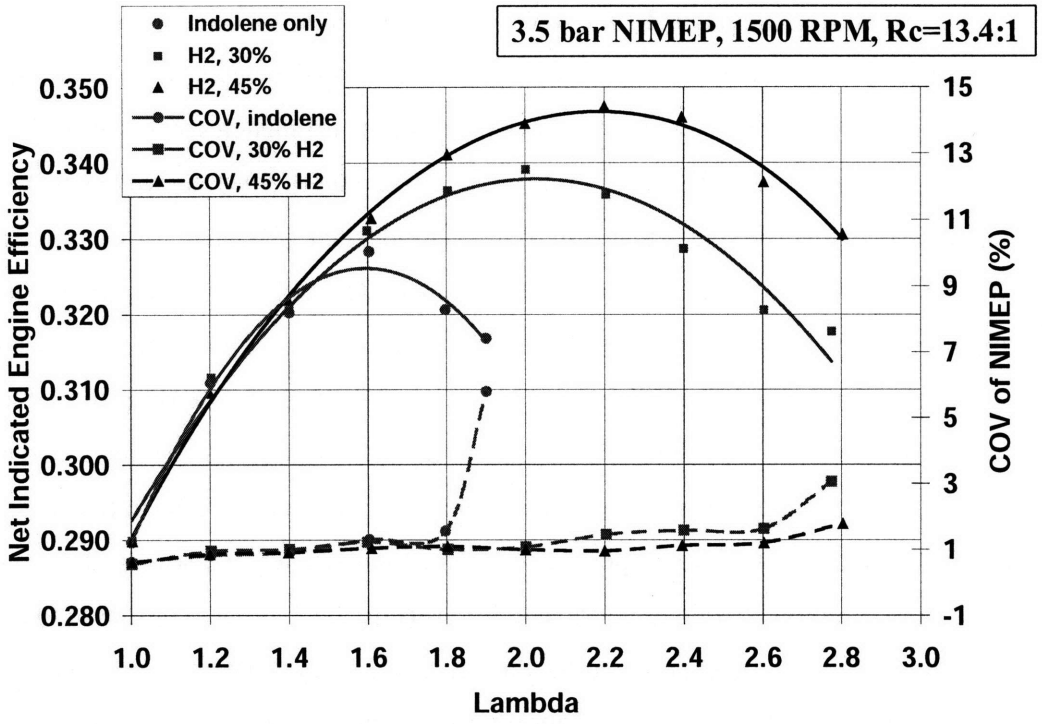

Figure 4-21 – Comparison of fall efficiency and COV of NIMEP vs. dilution for baseline indolene curve, and two H2-enhanced curves; MBT timing, 1500 RPM, r_c=13.4:1, NIMEP = 3.5 bar, Indolene

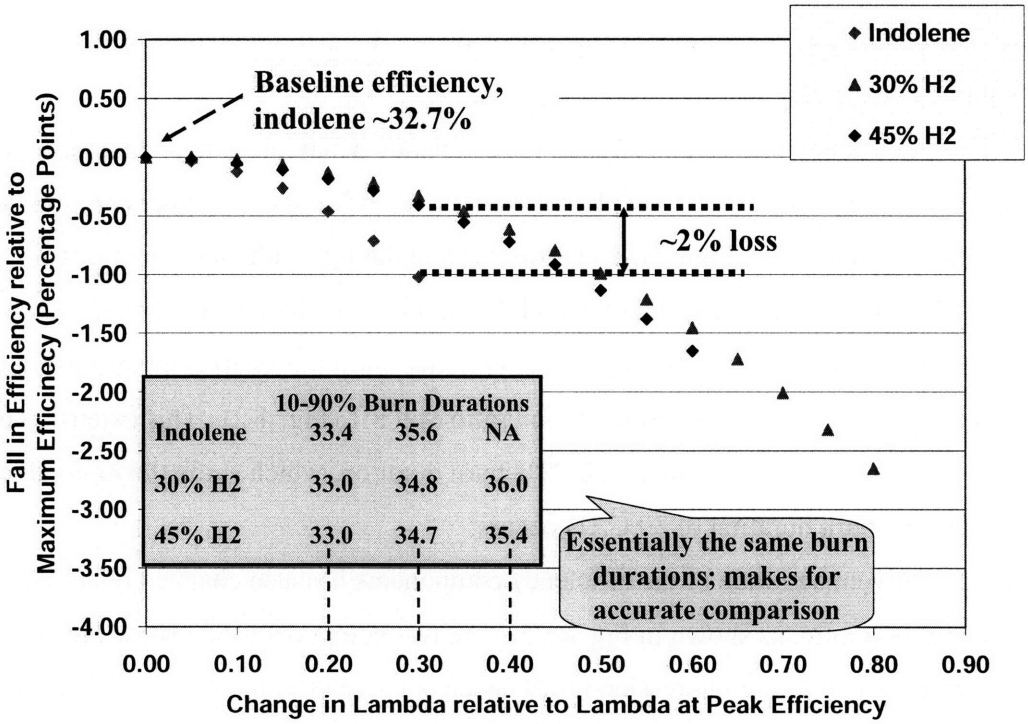

Figure 4-22 – Peak efficiency decrease with dilution; baseline indolene curve with high COV of NIMEP and two hydrogen-enhanced curves with flat COV of NIMEP; MBT timing, 1500 RPM, r_c=13.4:1, NIMEP = 3.5 bar

4.8. Compression Ratio Effects on Efficiency With Changes in Air-fuel Ratio

The impact of higher compression ratio on the baseline efficiency at stoichiometric conditions is seen in Fig. 4-23. This figure shows the absolute efficiencies, starting from the estimated ideal gross indicated efficiency for a compression ratio of 9.8:1, as well as the breakdown of the efficiency changes that lead to the net indicated efficiency for a compression ratio of 13.4:1. The changes in efficiency have been separated into heat transfer effect, pumping losses, expansion work, and burn duration effect. The absolute pumping loss has increased at the higher compression ratio. Higher efficiency has required a higher throttling (less air and less fuel), to maintain a load of 3.5 bar NIMEP. The absolute heat transfer has also increased at the higher compression ratio due primarily to higher temperatures and an increase in the surface area to volume ratio [22, 25] but the overall percentage of the total efficiency is lower. The small differences in burn duration at stoichiometric conditions (Fig. 4-27) do not contribute to any differences in the baseline efficiencies, and so, this effect has been neglected. However, as the air-fuel ratio increases, the 10-90% burn duration for the higher compression ratio becomes shorter than the burn duration for the 9.8:1 compression ratio, as shown in Fig. 4-27, and consequently, the detrimental effect due to burn duration also becomes smaller for a given lambda. The majority of the efficiency increase is due to the thermodynamic effect of having a larger volume expansion ratio.

The same framework used to explain the efficiency behavior with air-fuel ratio in the previous section can also be used to explain the efficiency behavior for higher compression ratios as the air-fuel ratio changes. Figure 4-24 shows the simulation results for a compression ratio of 13.4:1. The match between the simulation and the data is good, and the predicted location of peak efficiency is also accurate. The first thing to notice from this chart is the extension of the peak efficiency point, relative to a compression ratio of 9.8:1 (Fig. 4-2). This extension of almost 0.1 lambda results from a faster 10-90% burn duration, which shifts the $\lambda_{A/F}$-value at which the critical burn duration of 30 CAD occurs.

The relative magnitude of the efficiency components has also changed relative to the lower compression ratio, as shown in Fig. 4-25. The two components that show the largest relative difference between compression ratios, as the air-fuel ratio increases, are burn duration and gamma. As expected, the relative effect of burn duration at the higher compression ratio is lower with higher lambda than at the lower compression ratio, due to the faster 10-90% burn

duration at the high compression ratio, and due to the higher efficiency impact from other components. For high compression ratio, the effect of gamma on efficiency, relative to stoichiometric conditions, has decreased compared to the lower compression ratio.

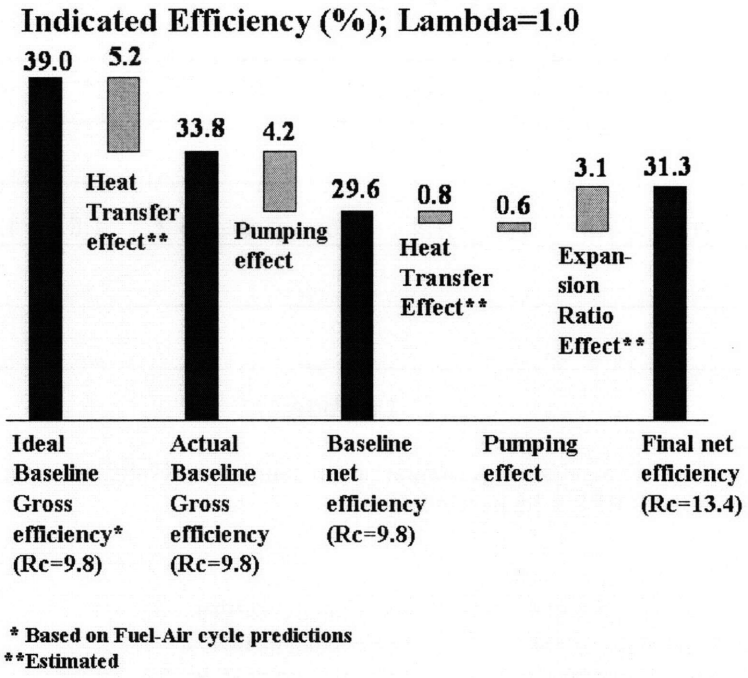

Figure 4-23 – Comparison of efficiency change between two different compression ratios; MBT timing, 1500 RPM, NIMEP = 3.5 bar, Indolene

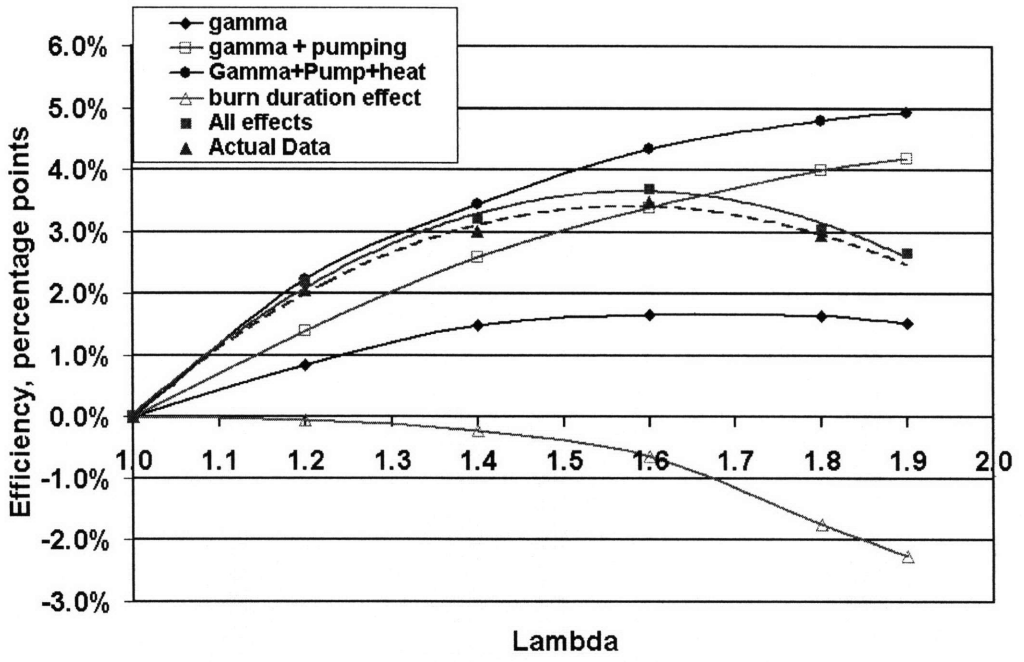

Figure 4-24 – Air-fuel ratio effect on efficiency, comparison of simulation results and actual data; MBT timing, 1500 rpm, r_c = 13.4:1, NIMEP = 3.5 bar, indolene

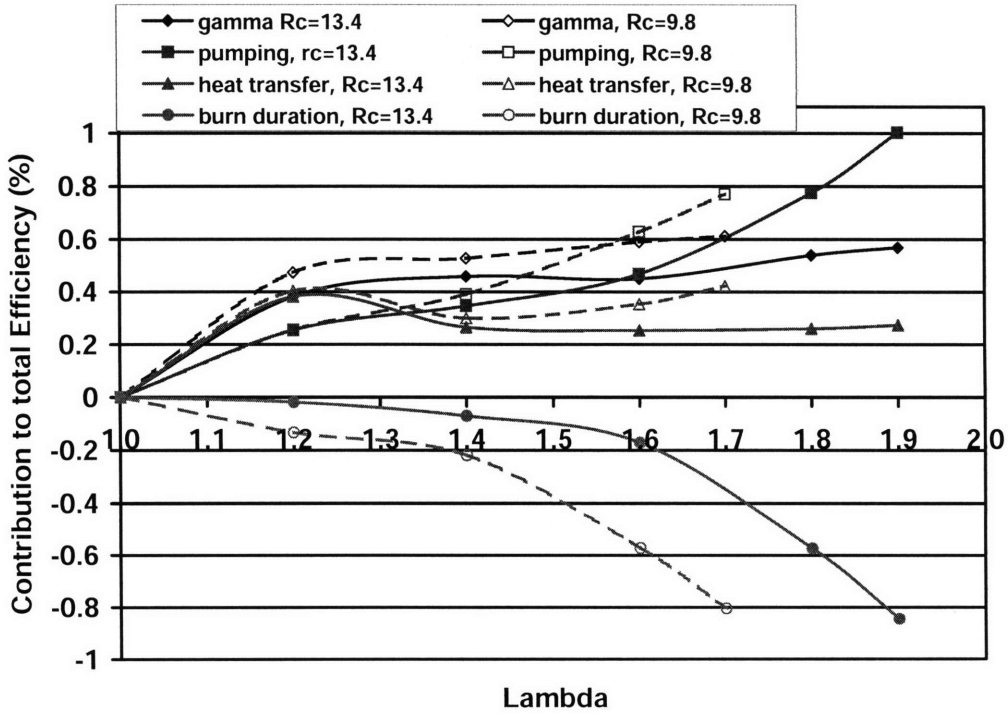

Figure 4-25 – Comparison of relative efficiency contributions between two different compression ratios; MBT timing, 1500 RPM, NIMEP = 3.5 bar, Indolene

4.9 Load Effects on Efficiency with Change in Air-fuel Ratio

As the load increases, the efficiency also increases due primarily to reduced pumping losses, as more air is inducted into the combustion chamber, and due to reduced heat transfer as a percent of the total fuel consumed. Figure 4-26 shows the source and approximate magnitude of the total efficiency increase at 6.0 bar NIMEP and stoichiometric conditions, relative to a baseline load of 3.5 bar NIMEP at the same air-fuel ratio. A reduction in pumping loss dominates the change in efficiency, accounting for approximately 80% of the net indicated efficiency increase. The remaining 20% of the efficiency increase is associated with reduced heat transfer. Although the 10-90% burn duration at the high load is overall faster, as shown in Fig. 4-27, due to reduced residual and higher combustion temperatures, previous experiments at the Sloan lab have shown that under stoichioimetric conditions a reduction in 4 CAD on the 10-90% burn duration has a small effect on efficiency. This is verified in Fig. 4-3, where faster burn durations caused by hydrogen enhancement at stoichiometric conditions show small changes in efficiency (less than 0.3%). Thus, the effect of burn duration on efficiency for this stoichiometric case, has been assumed to be negligible (i.e., zero). Nevertheless, when the air-fuel ratio is increased, burn duration once again is critical in determining the overall efficiency, as shown in Fig. 4-28. This chart shows the behavior of the actual efficiency and the simulated efficiency with changes in air-fuel ratio at the higher load. The agreement between the simulation and the data is good. The simulation does not predict the initial efficiency slope very accurately, but does an excellent job at predicting the relative efficiency changes between the rest of the points, as well as the location of the peak efficiency. This last one is located at lambda of 1.7, representing an extension of 0.2 lambdas relative to the baseline load (3.5 bar NIMEP).

Figure 4-29 shows the relative effects of each simulated efficiency component with increasing air-fuel ratio, for both 3.5 bar NIMEP and 6.0 bar NIMEP. One can notice the reduced effects from burn duration, and heat transfer at the higher load. Pumping work also shows a lower effect at the high load, since the reference point of comparison is the stoichiometric efficiency, where pumping losses are already much lower than at the lower load. Gamma is not affected significantly with load but because the relative effect of the other efficiency components has decreased, the relative impact of gamma is now slightly higher at the higher load, than at the lower load.

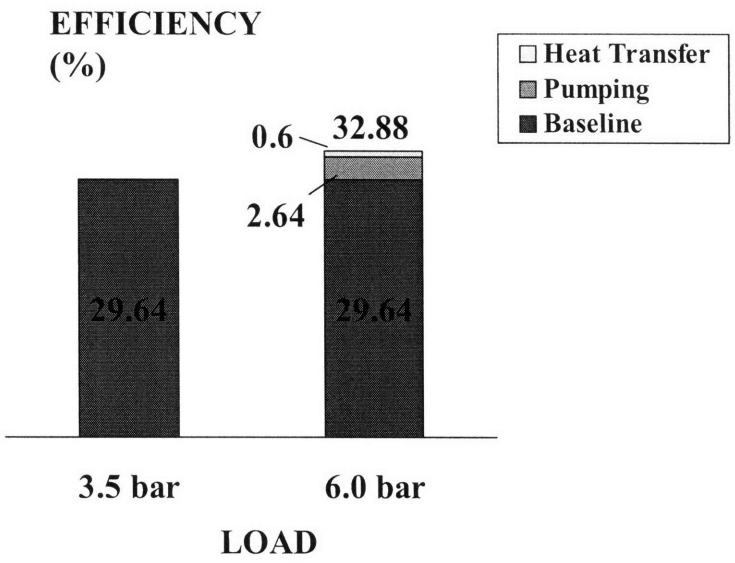

Figure 4-26 – Comparison of changes in net indicated efficiency between two different loads; MBT timing, 1500 RPM, r_c=9.8:1, Indolene

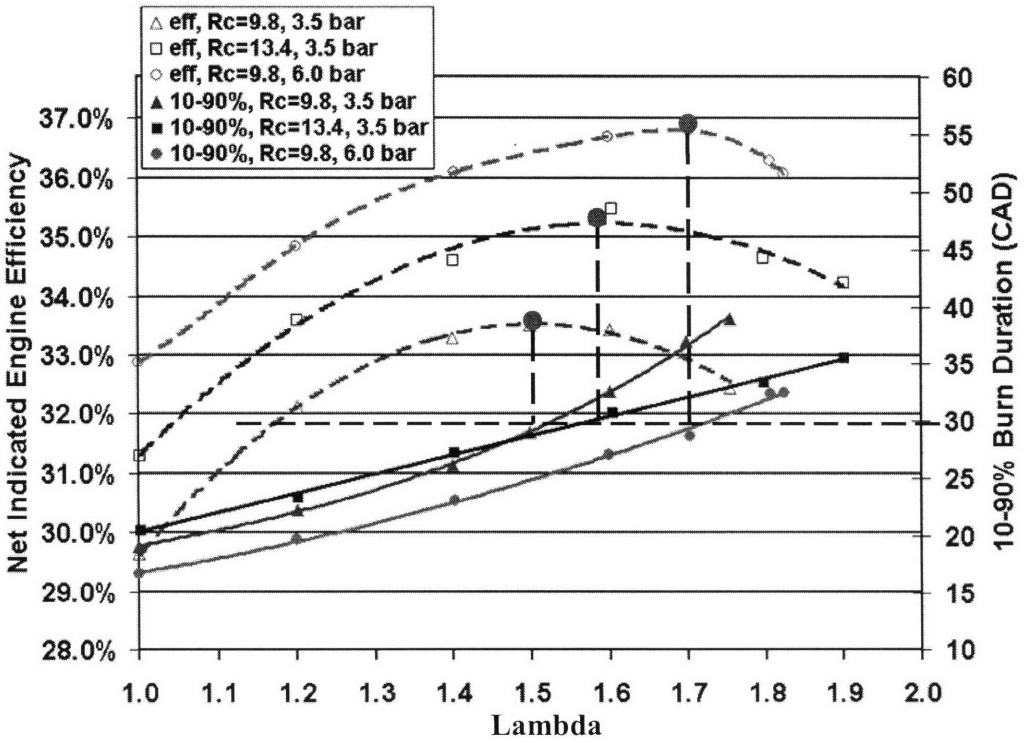

Figure 4-27 – Comparison of changes in burn duration and efficiency with increasing air-fuel ratio for different loads and compression ratios; MBT timing, 1500 RPM

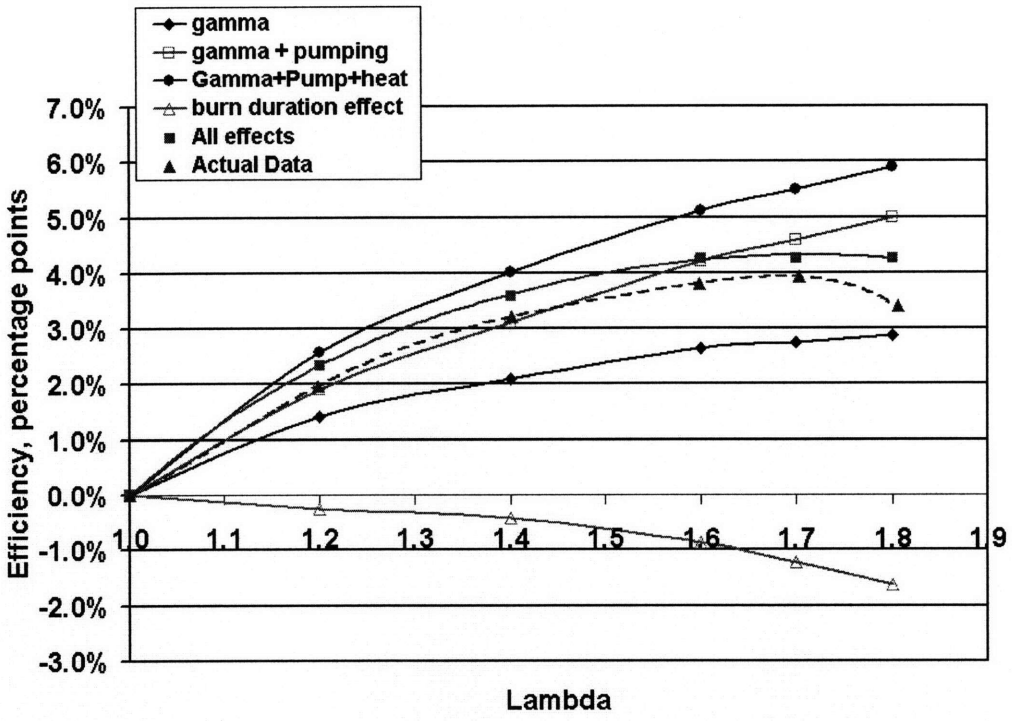

Figure 4-28 – Air-fuel ratio effect on efficiency, comparison of simulation results and actual data; MBT timing, 1500 RPM, r_c = 9.8:1, NIMEP = 6.0 bar, Indolene

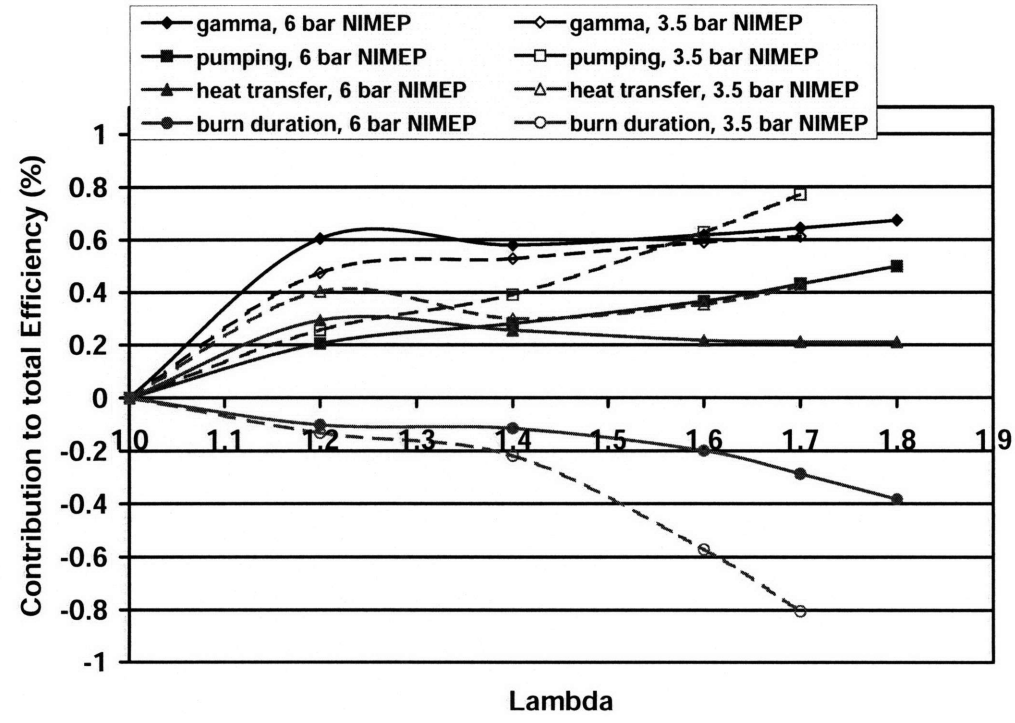

Figure 4-29– Comparison of relative efficiency contributions between two different loads; MBT timing, 1500 RPM, r_c = 9.8:1, NIMEP = 3.5 bar, Indolene

(this page was intentionally left blank)

Chapter 5 – HYDROGEN ENHANCEMENT EXPERIMENTAL RESULTS

Having established a basic understanding and framework for analyzing and explaining the trends and behavior of lean combustion, it is now important to apply this knowledge to the concept of hydrogen-enhanced combustion in more detail. As seen in figure 4-3, hydrogen addition will speed up combustion and lower the burn duration curve. With enhancement, the detrimental burn duration effect on efficiency with increasing dilution (figure 4-2), decreases, causing a rebalancing of the factors affecting efficiency; this shifts the location of peak efficiency, as well as the location of the lean limit to higher levels of dilution, getting higher efficiency and lower NOx emissions. As explained in Chapter 1, hydrogen enhancement is not free and it comes at a cost, in terms of an efficiency penalty. Therefore, when developing a hydrogen-enhanced engine, it is important to first asses the characteristics and potential of hydrogen enhancement under a wide range of operating conditions. Will enhancement have the same impact for air dilution and EGR dilution? What will be the effect of enhancement with higher compression ratio and load? How does plasmatron enhancement compare with pure hydrogen enhancement? These are just some of the important questions to answer when assessing the effectiveness of H2-enhancement.

5.1 Plasmatron enhancement: Air and EGR Dilution

The effect of plasmatron enhancement on air dilution was briefly seen in Chapter 1, where figure 1-2 compared the efficiency and COV of NIMEP for baseline conditions (pure indolene), 15% plasmatron enhancement, and 30% plasmatron enhancement for MBT spark, compression ratio 9.8:1, and 3.5 bar NIMEP. This efficiency comparison is shown again in figure 5-1, but now the 10-90% burn durations are also included, since in Chapter 4, this burning interval was shown to play a significant role in determining the location of peak efficiency. Consistent with the findings from Chapter 4, figure 5-2 shows how the 10-90% burn duration at peak efficiency stays fairly constant, ~30 CAD, for all three cases. Similarly, when the 0-10% burn duration and the COV of NIMEP are plotted together on the same chart, the limiting 0-10% burn duration of 40 CAD right at the onset of combustion instability is evident. The 10-90% and 0-10% burn durations are well behaved, and their extensions are fairly proportional with the percentage of plasmatron enhancement. Similar conclusions can be drawn from using EGR

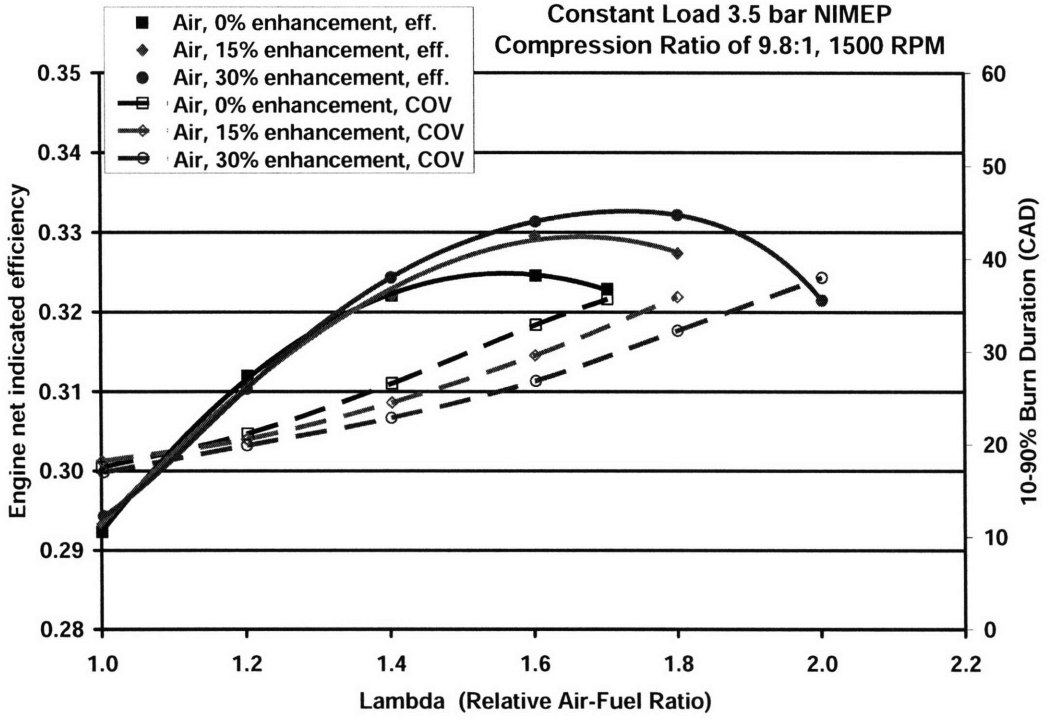

Figure 5-1 – Effect of relative air-fuel ratio on engine net indicated efficiency and on 10-90% burn duration for different levels of plasmatron enhancement; MBT timing, 1500 RPM, r_c=9.8:1, NIMEP = 3.5 bar

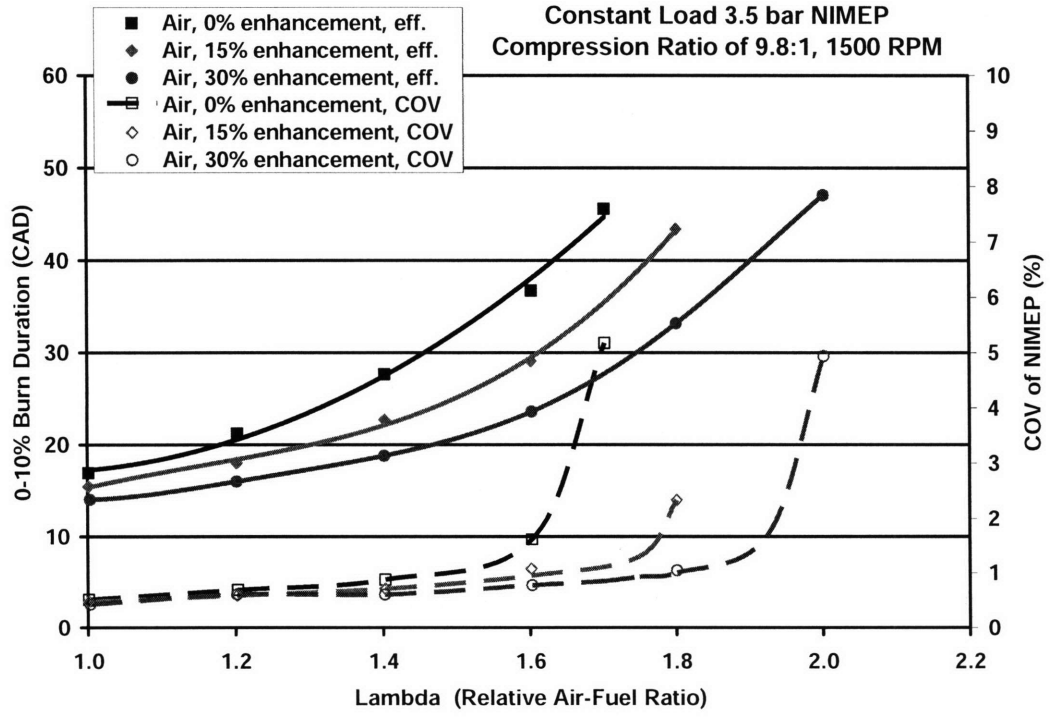

Figure 5-2 – Effect of relative air-fuel ratio on 0-10% burn duration and on COV of NIMEP for different levels of plasmatron enhancement; MBT timing, 1500 RPM, r_c=9.8:1, NIMEP = 3.5 bar

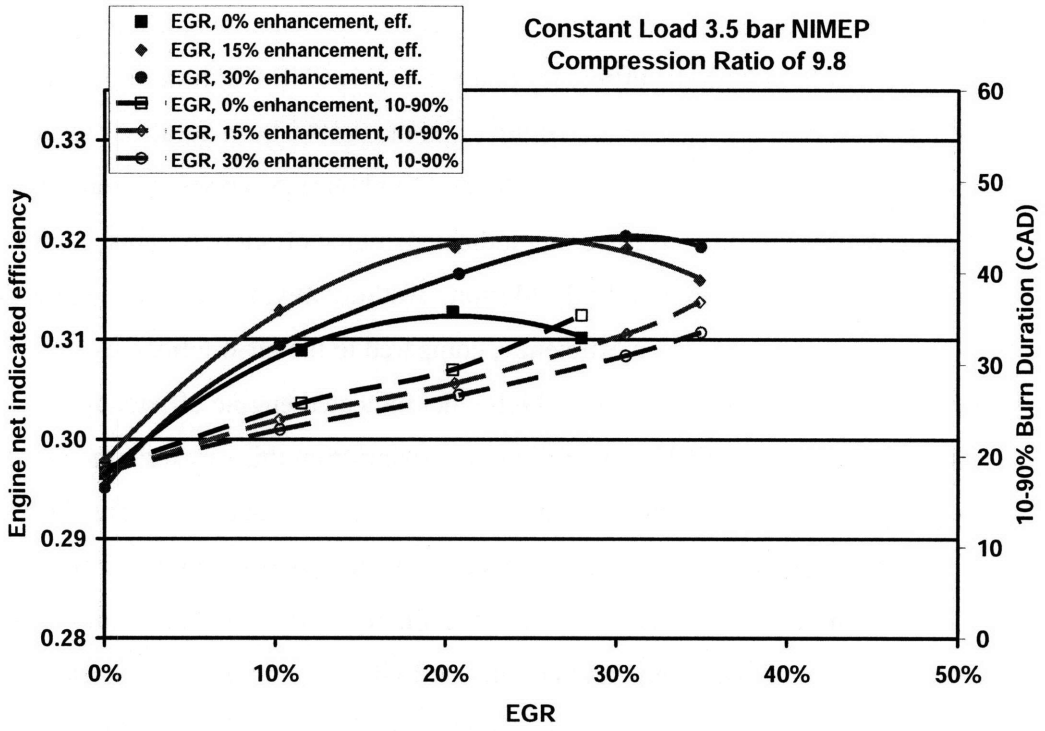

Figure 5-3 – Effect of EGR dilution on engine net indicated efficiency and on 10-90% burn duration for different levels of plasmatron enhancement; MBT timing, 1500 RPM, r_c=9.8:1, NIMEP = 3.5 bar

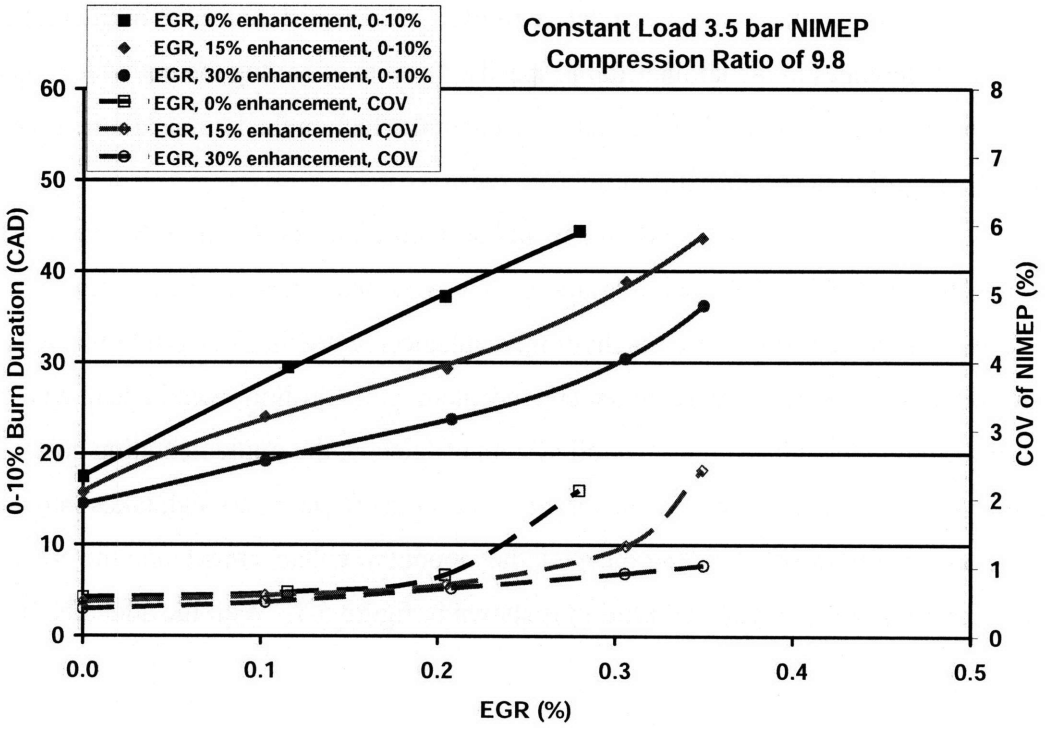

Figure 5-4 – Effect of EGR dilution on 0-10% burn duration and on COV of NIMEP for different levels of plasmatron enhancement; MBT timing, 1500 RPM, r_c=9.8:1, NIMEP = 3.5 bar

dilution with plasmatron enhancement, as shown in figure 5-3. Again, there is a proportional extension with plasmatron of both the efficiency and the COV of NIMEP limit; this behavior is consistent with the observed decrease in the 10-90% and the 0-10% burn durations respectively.

Although the enhanced behavior of the efficiency and burn durations is similar for both air and EGR dilution, this last one has lower net indicated engine efficiency. This is due primarily to the slower combustion with EGR dilution. Additionally, these burned gases do not contribute to increasing the combustion efficiency, compared to the air-dilution case where combustion will be more complete, yielding a higher net indicated engine efficiency.

Detailed comparisons of EGR and air dilution, arising from this research, in conjunction with Ivanic's research, have already been published [4]. Figures 5-5 and 5-6, derived from the mentioned joint work, summarize the results of this dilution comparison, for a compression ratio of 11.6:1 and a constant load of 3.5 bar NIMEP. Normalizing by the Thermal Dilution Parameter[3] [4] allows for a direct comparison of air and EGR. In light of the new understanding of the effect of the burn durations on peak efficiency and the COV of NIMEP limit, the observed differences between air dilution and EGR dilution can now be better explained. Consistent with the differences in the locations of peak efficiencies, figure 5-6 shows faster burn durations for the same amount of thermal dilution for air relative to EGR. These differences in burn duration are rooted in the differences in the laminar flame speeds. In spite of having the equivalent thermal dilution in both cases, EGR will have a more detrimental effect on the laminar flame speed, compared to the equivalent thermal dilution using air.

The observed differences in efficiency and burn durations between EGR and air dilution as shown in figures 5-5 and 5-6 are important especially as one considers the practical implications and the possibility of using hydrogen enhancement with EGR dilution and normal catalytic converters versus using hydrogen enhancement with air dilution and a lean NOx trap. While the second method has higher overall system efficiency, the implementation cost will also be higher. A more practical comparison among the system efficiency (which takes into account the efficiency penalty from reforming the gas), the amount of enhancement, and the NOx emissions for both of these types of dilution is shown in figure 5-7. With the added NOx

[3] TDP is a parameter used to normalize data with different diluents, and compare them on a common basis. It accounts for heat capacities of all diluents present in the charge mixture. See appendix for definition.

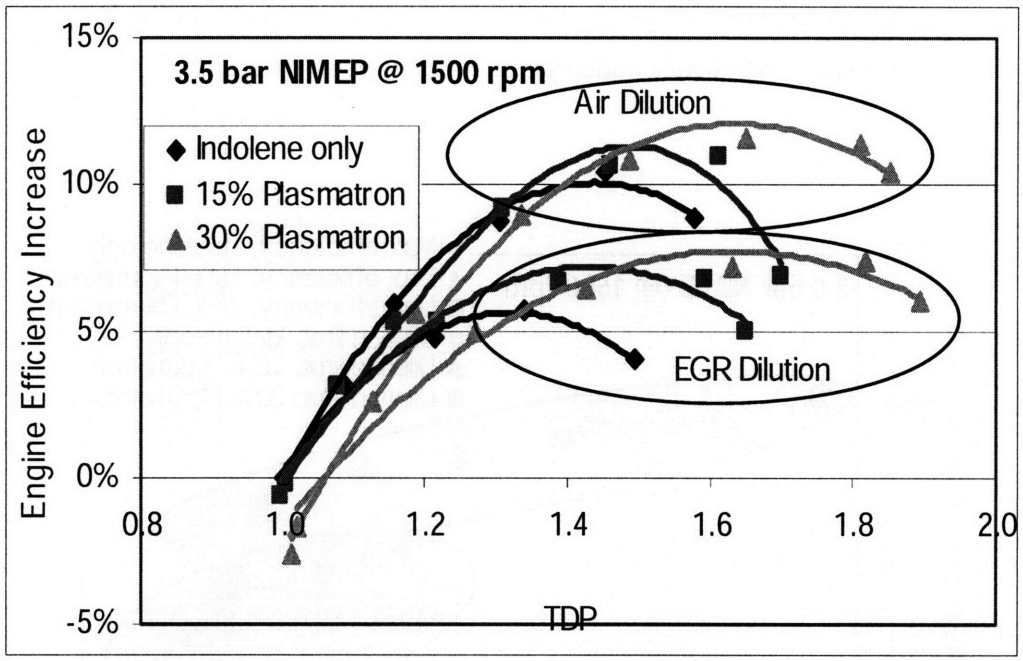

Figure 5-5 – Comparison of net indicated engine efficiency increase for air and EGR diluted mixtures; MBT timing, 1500 RPM, r_c=11.6:1, NIMEP=3.5 bar

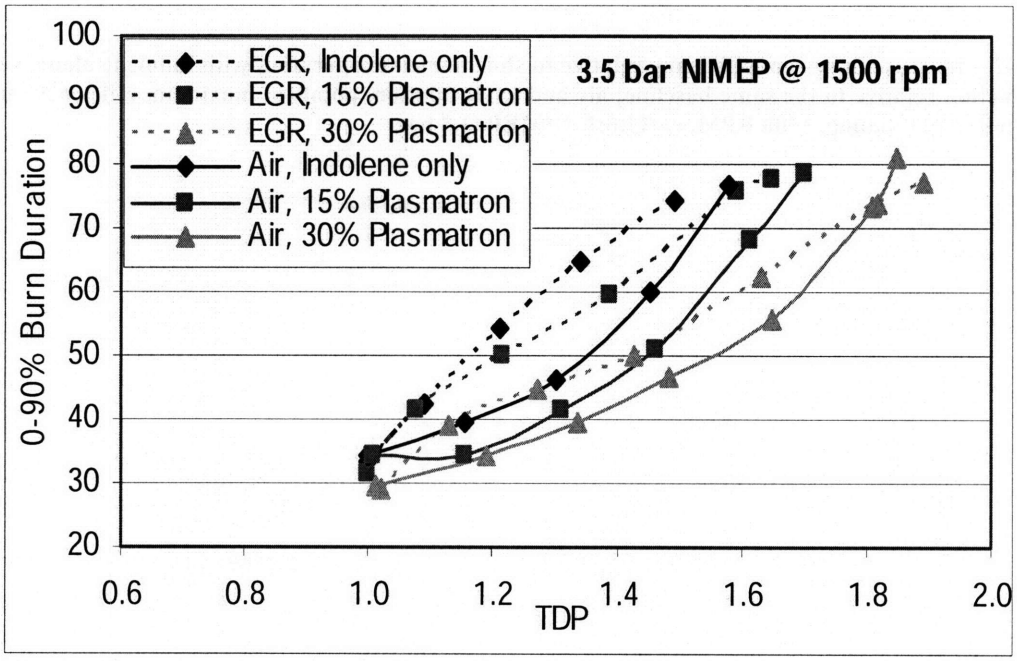

Figure 5-6 – Comparison of 0-90% burn duration for Air and EGR diluted mixtures MBT timing, 1500 RPM, r_c=11.6:1, NIMEP=3.5 bar

dimension, it is clear that choosing between both types of dilution involves efficiency, emissions, and economic and system complexity tradeoffs.

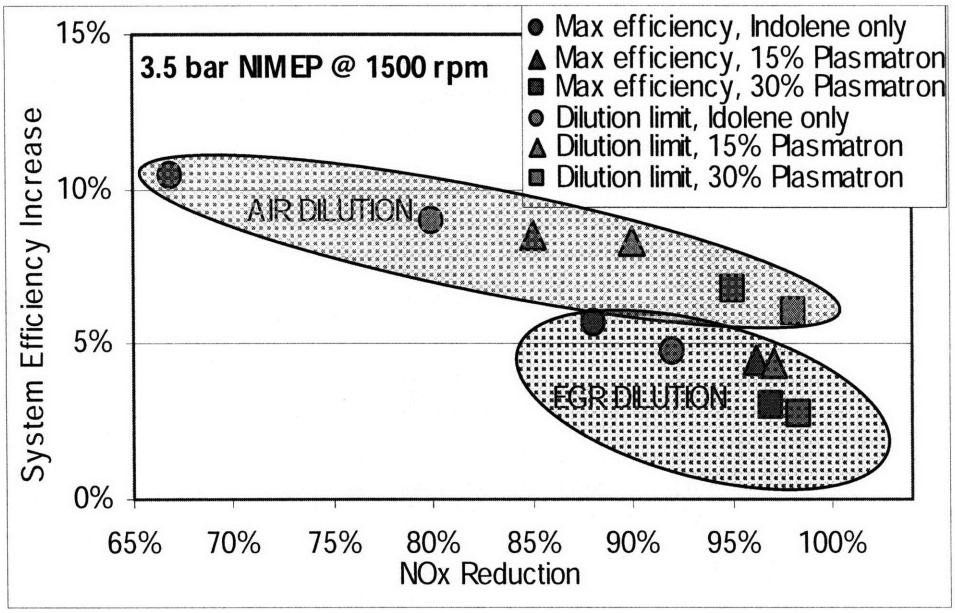

Figure 5-7 – Increase in system efficiency relative to stoichiometric operation with indolene alone, versus the NOx reduction relative to the same baseline; air and EGR dilution, points of maximum efficiency and points of lean limit; MBT timing, 1500 RPM, r_c=11.6:1, NIMEP=3.5 bar

5.2 Plasmatron enhancement: Increasing Compression Ratio

The higher compression ratio (11.6:1) air-dilution data from figures 5-5 and 5-6 are plotted as a function of relative air-fuel ratio in figure 5-8. Comparing directly with the lower compression ratio (9.8:1) data from figure 5-1, the spread in the 10-90% burn durations for the difference levels of enhancement seems to have been reduced for the higher compression ratio cases. That is, the advantage of plasmatron, in terms of speeding up combustion, seems less. Decent extension of the location of peak efficiency still exists at the higher compression ratio, because the 10-90% burn durations for the different enhanced cases show some differentiation right before peak efficiency. However, the overall difference in the 10-90% burn durations has decreased compared to the lower compression ratio case. There is no noticeable decrease in the plasmatron effectiveness on the 0-10% burn duration, as shown in figure 5-9; the plasmatron-enhanced curves show clear differentiation due to faster combustion. The effect of plasmatron on EGR dilution for this same compression ratio is similar.

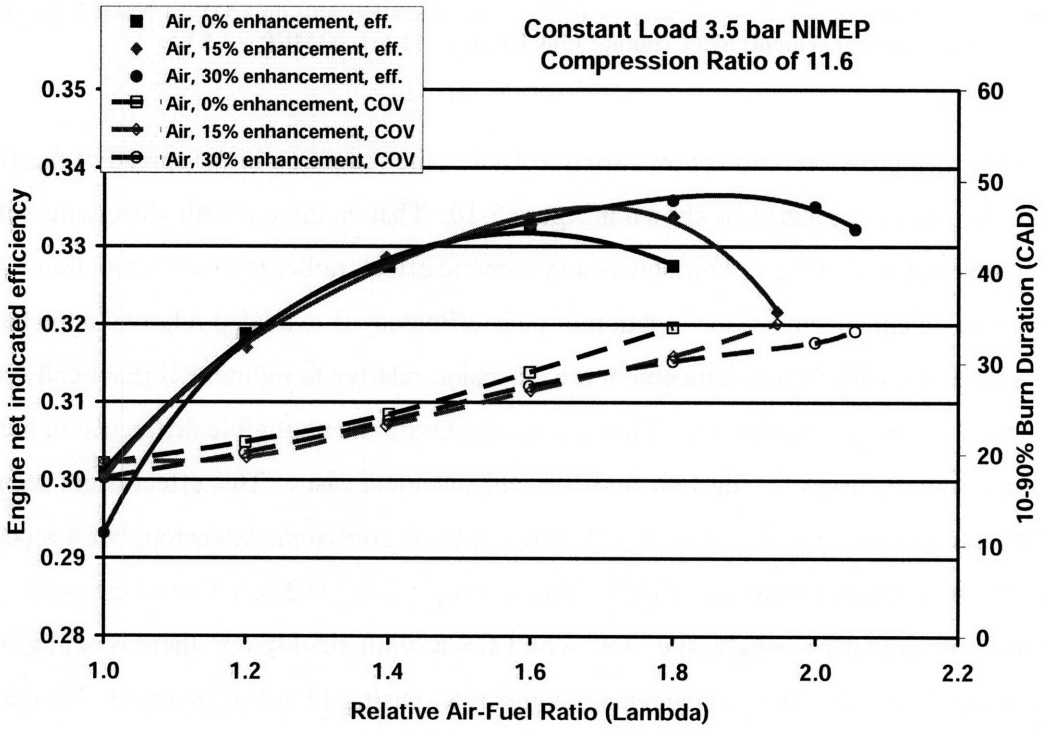

Figure 5-8 – Effect of relative air-fuel ratio on engine net indicated efficiency and on 10-90% burn duration for different levels of plasmatron enhancement; MBT timing, 1500 RPM, r_c=11.6:1, NIMEP = 3.5 bar

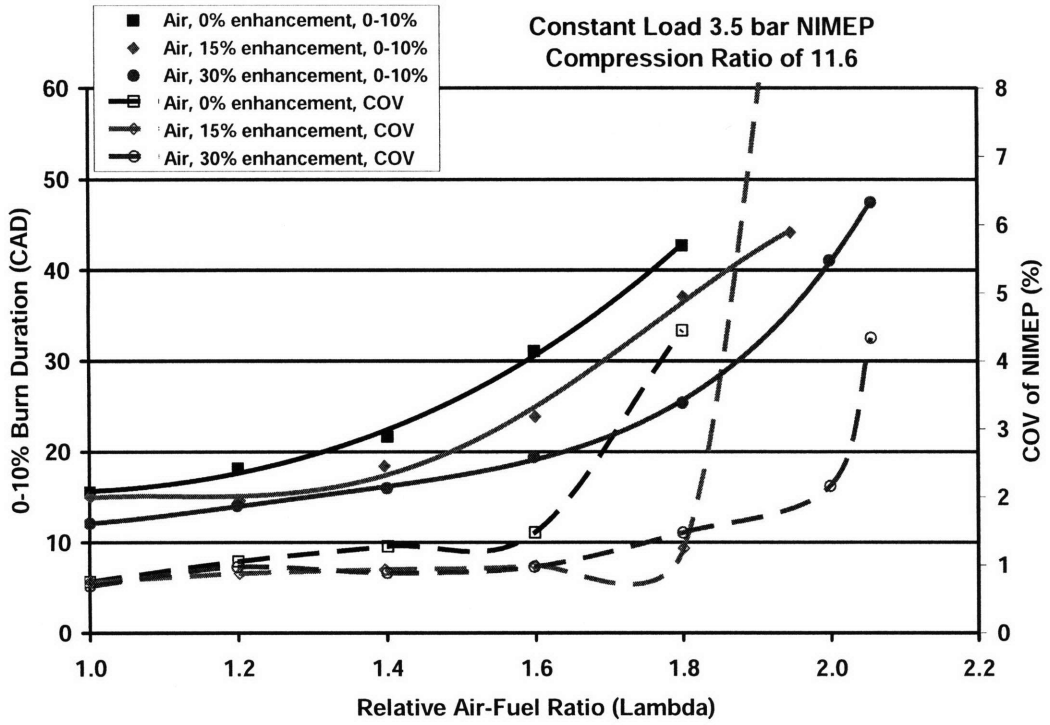

Figure 5-9 – Effect of relative air-fuel ratio on 0-10% burn duration and on COV of NIMEP for different levels of plasmatron enhancement; MBT timing, 1500 RPM, r_c=11.6:1, NIMEP = 3.5 bar

If the compression ratio is now raised to 13.4:1, the reduction in the spread of the 10-90% burn durations is even greater, as shown in figure 5-10. That is, there is little differentiation between the enhanced curves. This shows a systematic effect, rather than a random trend. With 15% plasmatron enhancement, the location of peak efficiency is extended relative to the baseline indolene case, but with 30% enhancement the extension relative to indolene is practically the same as the 15% enhancement case. This is consistent with the negligible difference in the 10-90% burn duration curves for the 15% and 30% enhancement cases. This effect is not seen with the 0-10% burn duration curves (Fig. 5-11), where there is consistent extension, but it reoccurs in the 10-90% burn duration curves for EGR dilution (Fig. 5-12). The behavior of the peak efficiency extension is essentially the same with EGR as with air-dilution; there is negligible improvement from using 30% enhancement compared to using 15% enhancement. With higher compression ratio there is a diminishing returns effect from adding plasmatron. The next section looks at this effect in more detail.

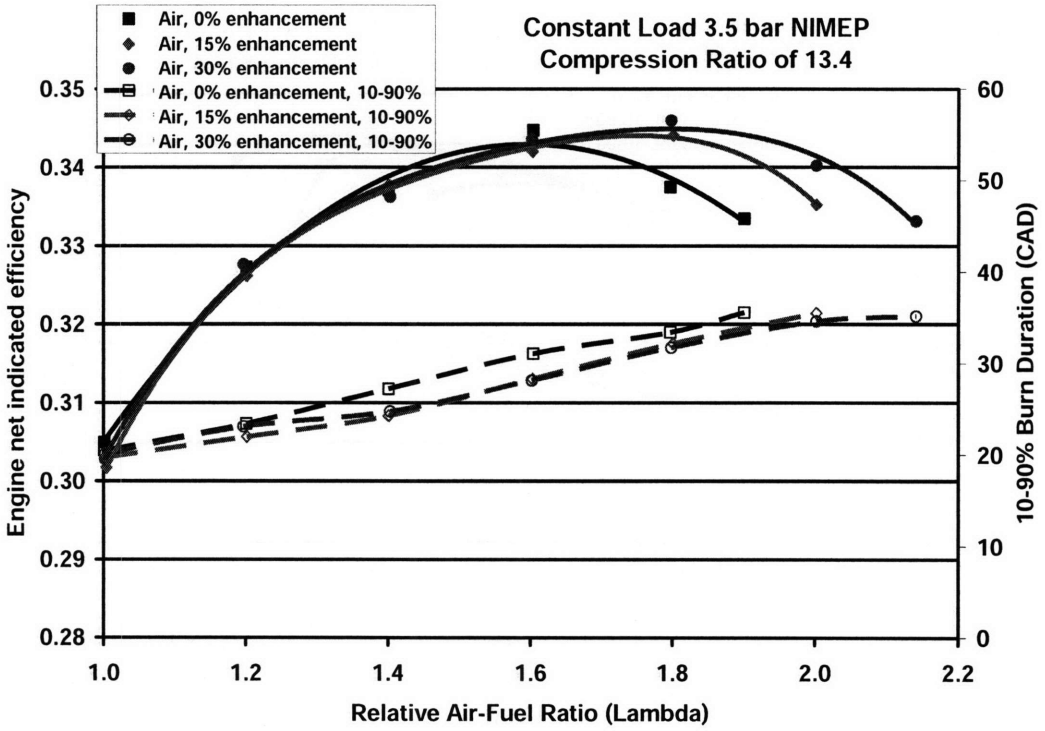

Figure 5-10 – Effect of relative air-fuel ratio on engine net indicated efficiency and on 10-90% burn duration for different levels of plasmatron enhancement; MBT timing, 1500 RPM, r_c=13.4:1, NIMEP = 3.5 bar

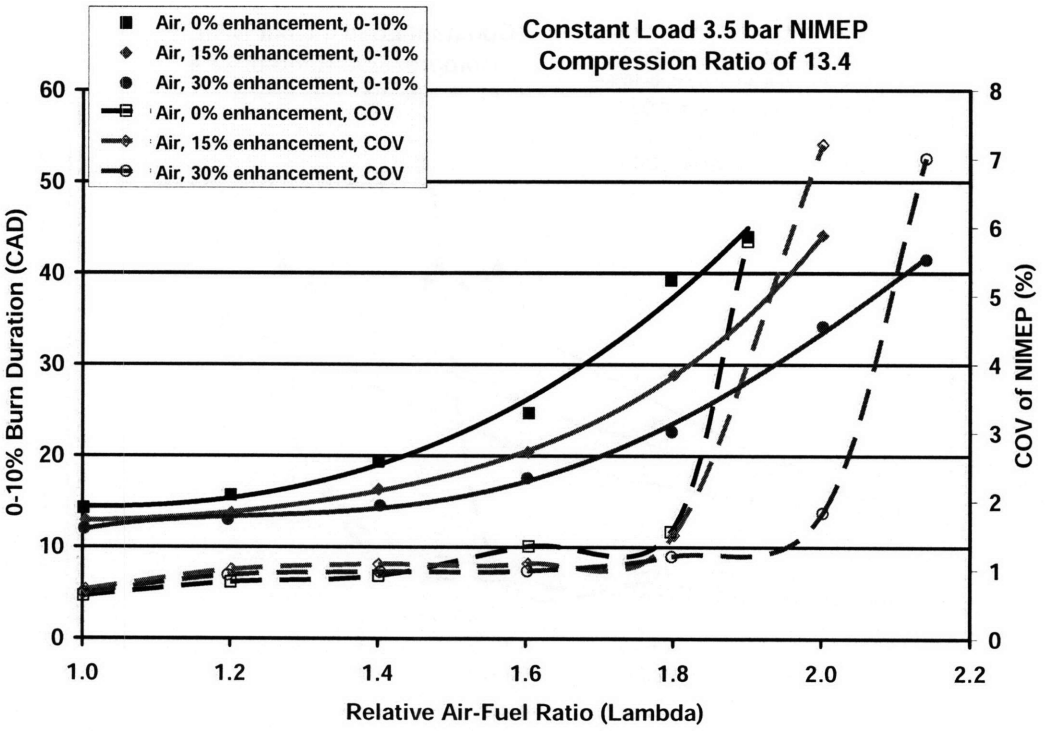

Figure 5-11 – Effect of relative air-fuel ratio on 0-10% burn duration and on COV of NIMEP for different levels of plasmatron enhancement; MBT timing, 1500 RPM, r_c=13.4:1, NIMEP = 3.5 bar

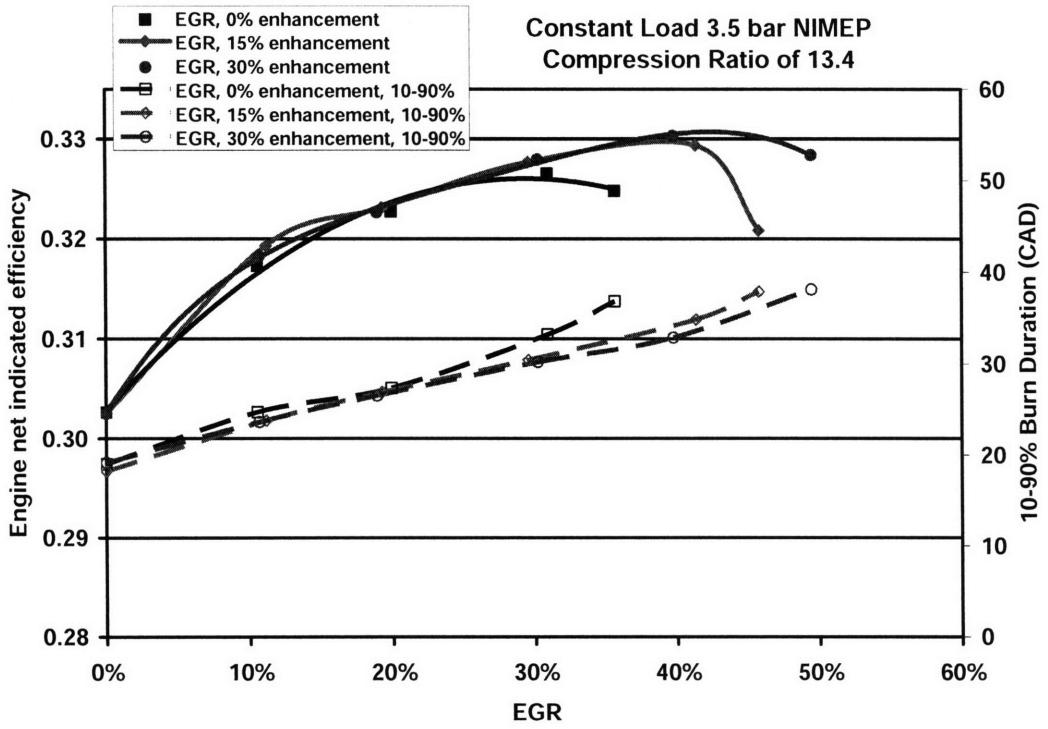

Figure 5-12 – Effect of EGR dilution on engine net indicated efficiency and on 10-90% burn duration for different levels of plasmatron enhancement; MBT timing, 1500 RPM, r_c=13.4:1, NIMEP = 3.5 bar

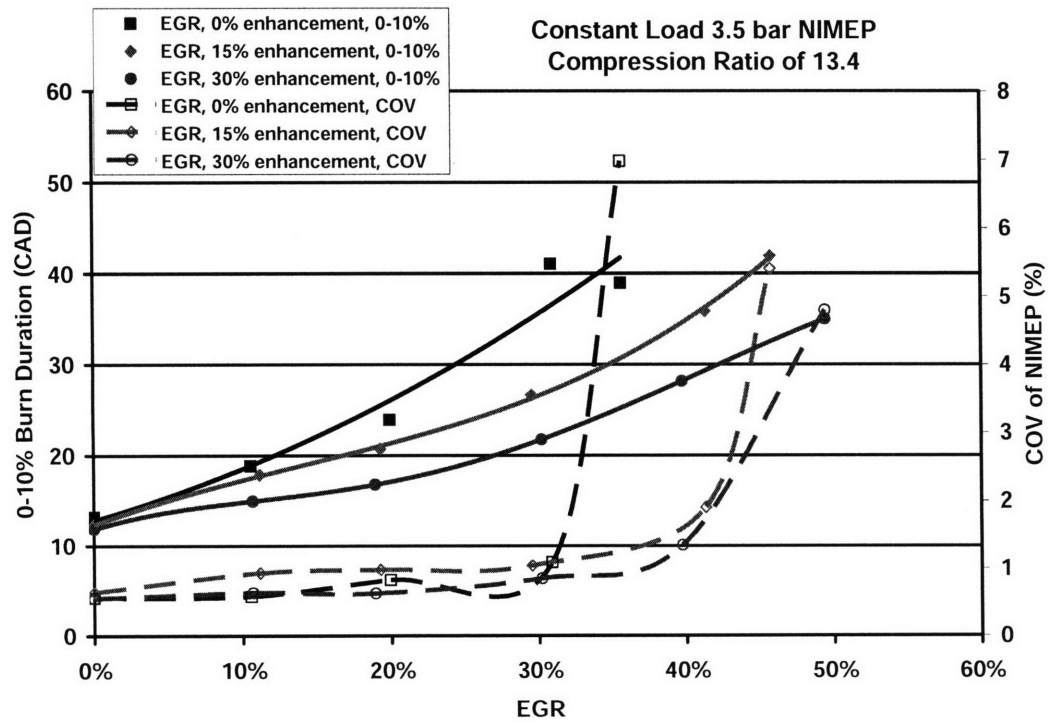

Figure 5-13 – Effect of EGR dilution on 0-10% burn duration and on COV of NIMEP for different levels of plasmatron enhancement; MBT timing, 1500 RPM, r_c=13.4:1, NIMEP = 3.5 bar

5.3 Pure Hydrogen vs. Plasmatron Enhancement and Diminishing Returns

The previous sections showed a modest but almost linear extension of the peak efficiency with increasing hydrogen enhancement for lower compression ratios (9.8:1). A similar effect occurred with the extension of the lean limit. However, at high compression ratios, (13.4:1), the improvement from plasmatron addition seemed to diminish. This was clear for air dilution and EGR dilution, where marginal peak efficiency extensions were seen when going from 15% enhancement to 30% enhancement. The proportional improvement in the extension of the lean limit with plasmatron enhancement was still present at the high compression ratio. To further investigate this diminishing effect, the experiments were repeated on a different day, and one additional curve, for 45% plasmatron enhancement, was produced. The results were the same, and this confirmed that the observed "diminishing returns" effect is real, and not just due to experimental error. Additionally, similar curves using pure hydrogen enhancement were produced. This allowed a direct comparison against an extra set of data points to try to better frame the problem and understand this diminishing effects trend. It should be noted, that the percent energy contributed by hydrogen for both the pure hydrogen enhancement experiments, and the plasmatron enhancement experiments, is different. Regardless, in both cases, hydrogen is increased in proportional amounts, allowing for a direct comparison (see section 5.5)

A comparison between the two sets of hydrogen-enhanced curves (pure hydrogen and plasmatron) is shown in figure 5-14. The hydrogen curves show a clear, proportional, extension of peak efficiency; as discussed in Chapter 4, this is the result of a proportional extension of the location of the critical 10-90% burn duration of 30 CAD. On the other hand, the plasmatron curves are almost indistinguishable, that is, they all provide about the same amount of peak efficiency extension, regardless of whether 15%, 30%, or 45% enhancement is added. The lean limit, however, seems to be proportionally extended for all cases; the extension for pure hydrogen enhancement is much larger, but the extension with plasmatron is still fairly proportional nevertheless. Looking at the burn duration curves should help understand this effect/observation. Figure 5-15 compares the 10-90% burn durations for each set of curves from Fig. 5-14. There is a shift in the burn duration curve when going from the baseline indolene case to the 15% plasmatron enhancement case. However, beyond this 15% enhancement case, the curves using plasmatron are again indistinguishable, regardless of an increasing percent of plasmatron enhancement. The burn durations are almost the same, and more important, the

limiting 30 CAD 10-90% burn duration occurs at around the same relative air-fuel ratio of 1.7 for all three cases. Thus, the negligible extension in the location of peak efficiency is consistent with having a negligible extension in the 10-90% burn duration curves, specifically a negligible extension in the critical 30 CAD 10-90% burn duration point. The behavior of the hydrogen 10-90% burn duration curves is much different, and their proportional extension is also consistent with the observed peak efficiency extension, as seen from the alignment between peak efficiency and the critical 30 CAD 10-90% burn duration point, as discussed in Chapter 4 (Fig. 4-3).

A similar comparison is shown in Figure 5-16 where the 0-10% burn durations are plotted. Contrary to the previous 10-90% burn durations figure (Fig. 5-15), the extension in the 0-10% burn duration for the plasmatron-enhanced curves, is proportional to the amount of enhancement. This behavior is expected because figure 5-14 shows a proportional extension of the COV limit, and recalling from Chapter 4, the rapid rise in COV is connected to the critical 0-10% burn duration of 40 CAD. Therefore, an extension in the COV drivability limit will go hand-in-hand with an extension of the location of the critical 40 CAD 0-10% burn duration point. While the 10-90% burn durations are almost unchanged beyond 15% enhancement, the 0-10% burn durations continue to decrease with added reformate, and consequently the COV limit is extended. The hydrogen curves again show similar trends, although their extension in the 0-10% burn duration is much greater than it is for plasmatron.

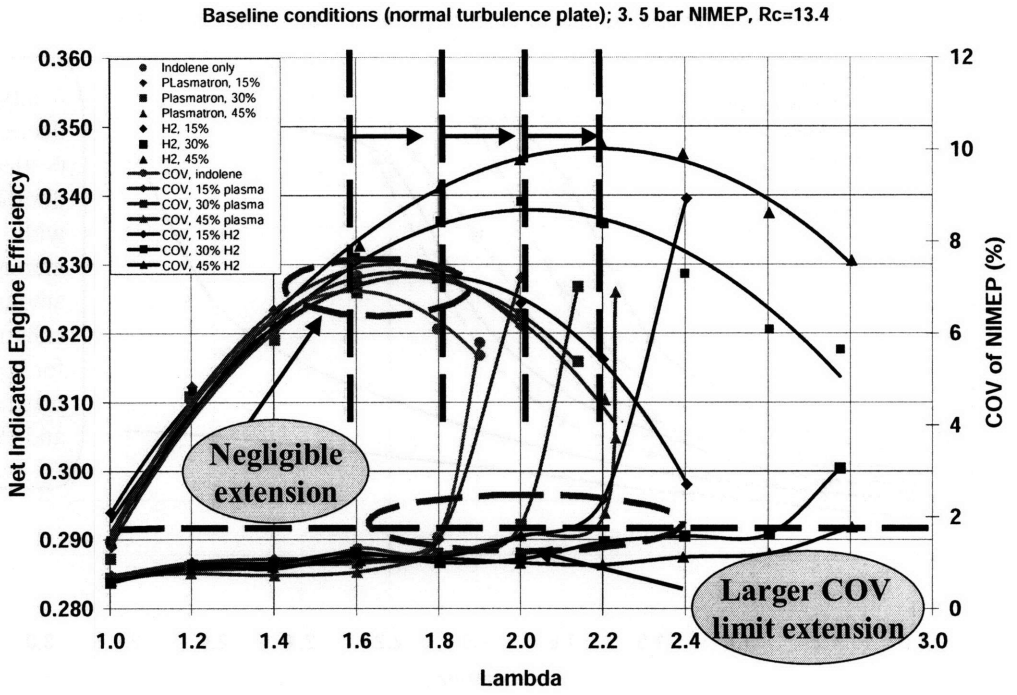

Figure 5-14 – Effect of air dilution on net indicated engine efficiency and on COV of NIMEP for different amounts of both plasmatron enhancement and pure H2-enhancement; MBT timing, 1500 RPM, r_c=13.4:1, NIMEP = 3.5 bar, indolene

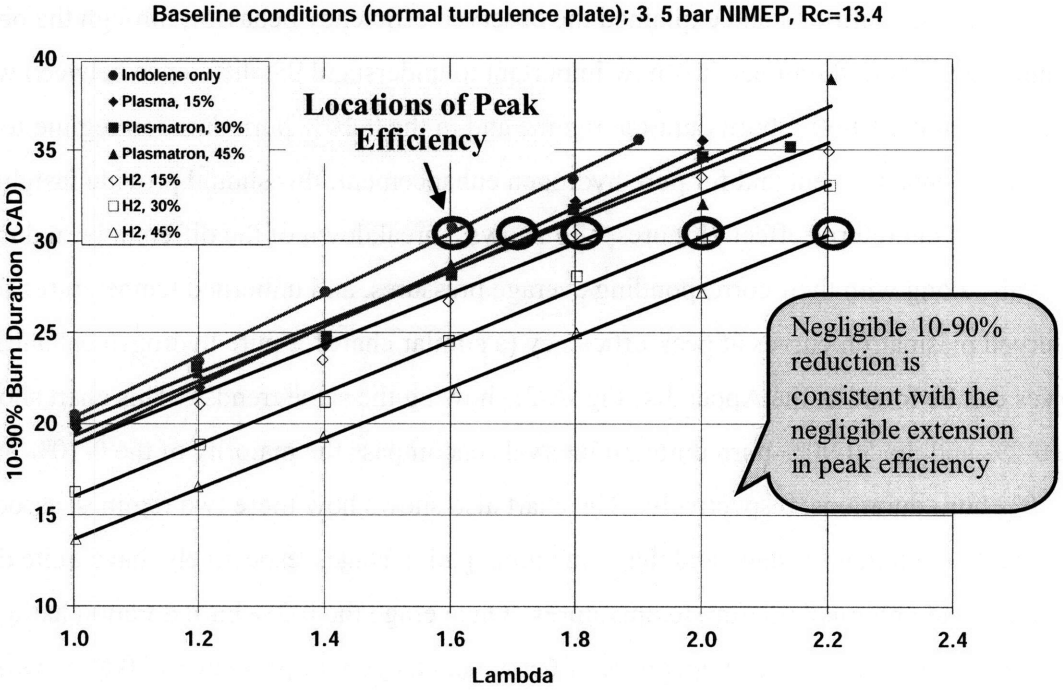

Figure 5-15 – Effect of air dilution on 10-90% burn duration for different amounts of both plasmatron enhancement, and pure H2-enhancement; MBT timing, 1500 RPM, r_c=13.4:1, NIMEP = 3.5 bar, indolene

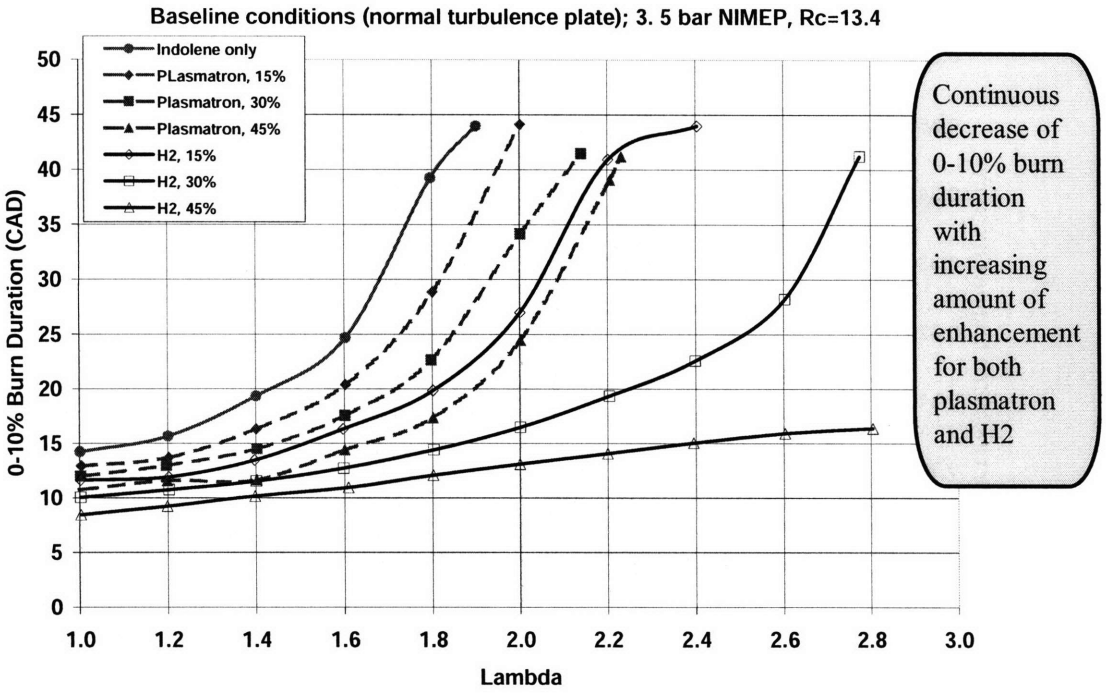

Figure 5-16 – Effect of air dilution on 0-10% burn duration for different amounts of both plasmatron enhancement, and pure H2-enhancement; MBT timing, 1500 RPM, r_c=13.4:1, NIMEP = 3.5 bar, indolene

Having confirmed and explained the observed efficiency behavior, through the observed changes in the burn durations, it is now important to understand the difference between what is happening in the 10-90% burn duration regime and in the 0-10% burn duration regime for plasmatron enhancement and for pure hydrogen enhancement; this should provide insight into the diminishing returns effect. Figures 5-17 shows a breakdown of the different burn duration intervals, along with their corresponding average pressures, and unburned temperatures for the observed plasmatron curves at peak efficiency (a similar chart for pure hydrogen enhancement curves can be found in the Appendix, Fig. A-3, showing the same trends). This chart shows how the 0-2% and the 50-90% burn duration intervals encompass the majority of the 0-10% and the 10-90% burn durations, respectively. The chart also shows how these two regimes, associated with the flame initiation stage and the flame propagation stage, respectively, have quite different pressures and unburned mixture temperatures. On average the 0-2% burn duration has an adiabatic unburned mixture temperature of 650K, and a cylinder pressure of 10 atm, while the 50-90% burn duration has an adiabatic unburned mixture temperature of 830K and a cylinder pressure of 30 atm. Thus, there is a factor of 3 difference in pressures between these two

intervals. With this new information, a possible explanation for the "diminishing returns" effect in peak efficiency is the fact that the higher pressure will have a higher detrimental effect on the laminar flame speed, as was studied in Chapter 3. The given combination of differences in pressure and temperature between the two burn duration regimes could affect the laminar flame speed in such a way that would account for the observed changes. To confirm this hypothesis, it is necessary to look closer at the laminar flame speeds for these conditions.

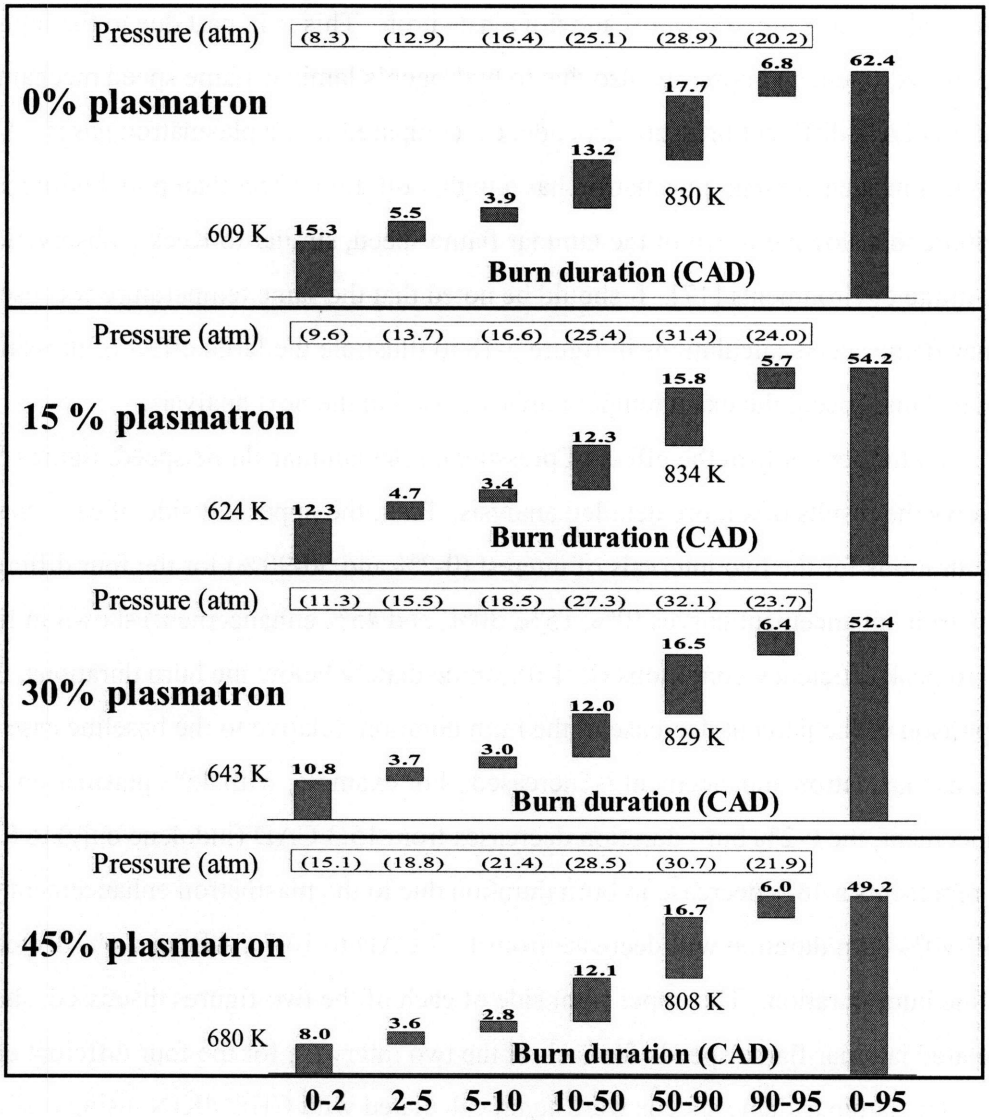

Figure 5-17 – Comparison of pressure, temperature, and duration of mass burning intervals, for baseline conditions and 3 levels of plasmatron enhancement, near peak efficiency (λ=1.6); MBT timing, 1500 RPM, r_c=13.4:1, NIMEP = 3.5 bar

Figure 5-18 provides a comparison of laminar flame speeds as a function of air dilution for the same temperature but two different pressures and for various levels of plasmatron enhancement. The selected pressures are close to the pressures observed for the 0-2% burn duration interval (10 atm) and the 50-90% burn duration interval (30 atm) from figure 5-17. Raising the pressure by a factor of 3 has a significant impact on the laminar flame speeds, which show a negligible improvement with enhancement for highly lean conditions (λ>1.6), relative to the lower pressure curves. Although this same pressure change also has a detrimental effect on the laminar flame speeds of pure hydrogen-enhanced mixtures (figure 5-19), the absolute detrimental effect is much lower than with plasmatron. This is in part due to the high baseline speed of hydrogen, and possibly also due to hydrogen's laminar flame speed mechanism, which might involve a different pressure dependence, compared to the plasmatron gases. Additionally, due to its nitrogen content, plasmatron has a higher dilution effect than pure hydrogen. This will contribute to a slowing down of the laminar flame speed, similar to Keck's observations with EGR-dilute environments [17]. It should be noted that the same temperature was used in the laminar flame speed calculations in figure 5-18 to illustrate the large effect of pressure on the laminar flame speed; the exact temperatures are used in the next analysis.

To further confirm the effect of pressure on the laminar flame speed, figures 5-20 and 5-21 shows the results of a more detailed analysis. First, the upper left side of each chart shows the burn durations for the two intervals of interest (0-2% and 50-90%) for the four different plasmatron enhancement curves (0%, 15%, 30%, and 45% enhancement) shown in figure 5-14, close to peak efficiency conditions (λ=1.6). Immediately below the burn durations, is a comparison of the percent decrease in the burn duration, relative to the baseline case (indolene only), as plasmatron enhancement is increased. For example, with 45% plasmatron enhancement, the 0-2% burn duration decreases from 15.3 CAD (indolene only) to 8.0 CAD. This represents a 48% decrease in burn duration due to the plasmatron enhancement. Similarly, the 50-90% burn duration will decrease from 17.7 CAD to 16.7 CAD, or a 6% decrease in the baseline burn duration. The upper right side of each of the two figures discussed, shows the calculated laminar flame speeds for each of the two intervals, for the four different enhancement cases. The laminar flame speeds were again calculated with CHEMKIN, using methane as the fuel, and they incorporate the average of the measured pressure across each interval, as well as the average calculated adiabatic unburned mixture temperature. These values are shown at the

bottom of each chart. The bottom right side of these two figures show the percent change in the calculated laminar flame speed, relative to the baseline case (methane only, 0% enhancement). For example, with 45% plasmatron enhancement, the laminar flame speed near peak efficiency (λ~1.6) for the 0-2% burn duration interval will be ~44 cm/sec compared to 29 cm/sec for the baseline 0% enhancement case (methane only). This represents an increase of 51%. In the same way, the laminar flame speed for the 50-90% burn duration interval of this 45% plasmatron enhancement case will increase from 47 cm/sec to ~52 cm/sec, or 10% increase. The main point to notice from these figures is how the relative changes in laminar flame speed with enhancement are consistent with the observed changes in the burn durations. This is sensible, if to a first order approximation the change in burn duration is taken as proportional to $1/S_L$. For the 50-90% burn duration interval, where pressures are higher, the laminar flame speed with 15% enhancement increases by 8%, but beyond this enhancement, the change is approximately the same, consistent with the observed decreases in burn duration. For the 0-2% burn duration interval, on the other hand, there is a steady increase in the laminar flame speed, consistent with a steady, and noticeable, decrease in the burn duration time. This confirms that the diminishing returns effect of plasmatron is due primarily to the relatively high pressures during the main burning angle.

To conclude this section, figures 5-22 and 5-23 show a more systematic analysis to study the diminishing returns effect. These charts display laminar flame speeds, calculated with CHEMKIN, as a function of pressure for 4 levels of plasmatron-enhanced methane (0%, 15%, 30%, 45%), at two different temperatures (850 K and 860 K). As plasmatron is added, all else equal, the effect will be a proportional increase in the laminar flame speed, irrespective of the magnitude of the pressure. However, higher pressures will cause smaller proportional changes than will lower pressures. Under very high pressures the observed changes could easily get lost in the presence of small variability in temperature (e.g., due to experimental error from one enhancement level to another, error in the measured level of dilution, etc.) For example, figures 5-22 and 5-23 demonstrate how going from a pressure of 10 atm to 32 atm will decrease the benefit in laminar flame speed from plasmatron enhancement from 10 cm/sec down to 3 cm/sec. Figure 5-23 also shows how a small change in temperature, of less than 10 K would easily erode this flame speed improvement of 3 cm/sec. Thus, for all practical purposes, the effect of

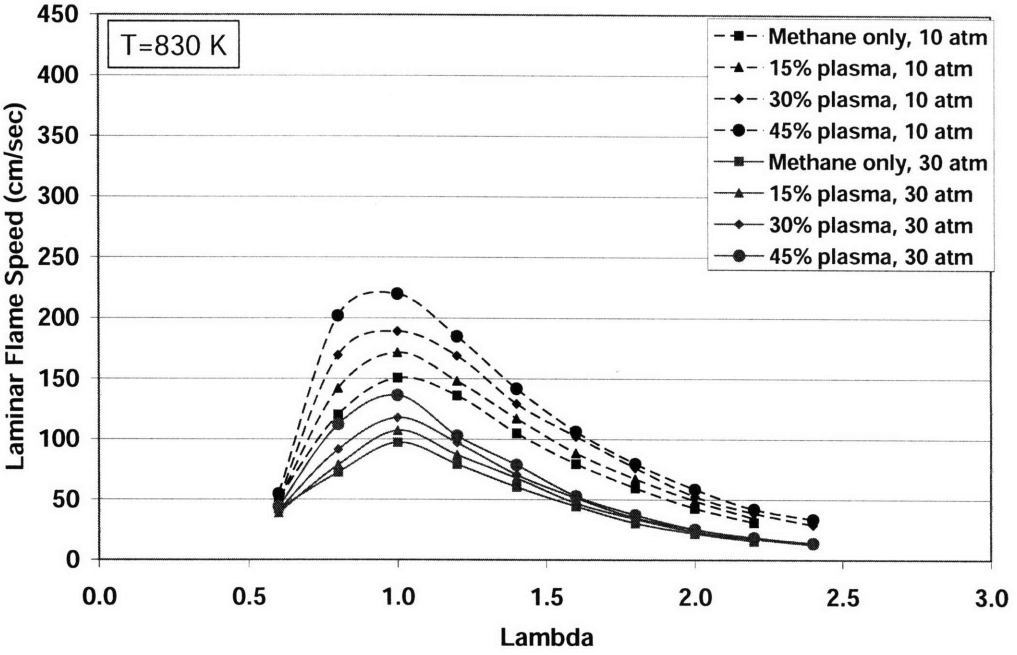

Figure 5-18 – Air-fuel ratio and pressure effect on laminar flame speed for different levels of plasmatron enhancement with CH_4 as the fuel; 830 K

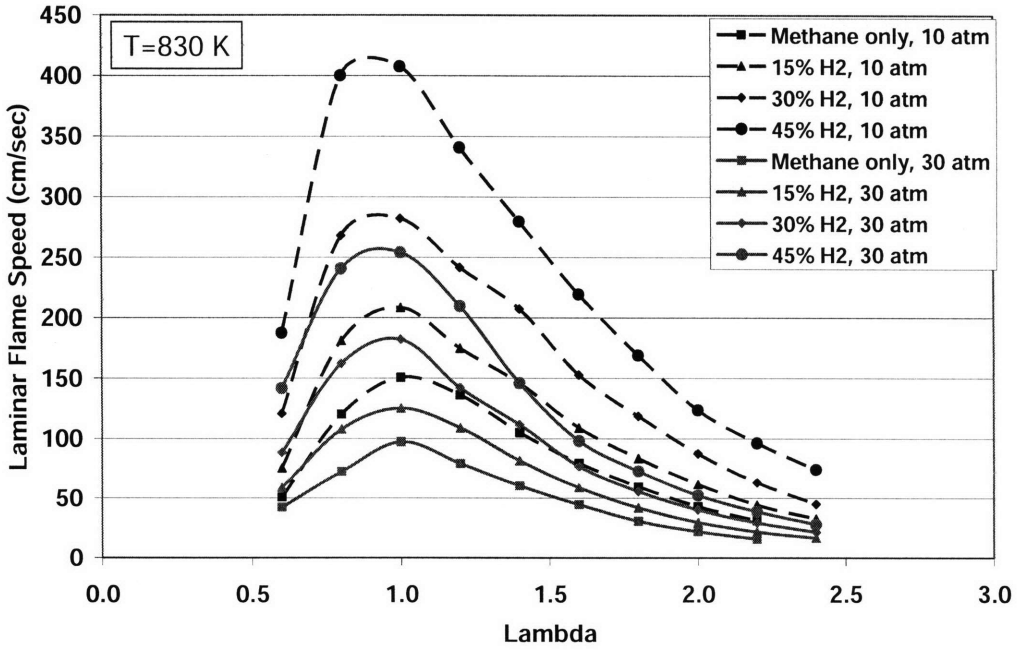

Figure 5-19 Air-fuel ratio and pressure effect on laminar flame speed for different levels of pure hydrogen enhancement with CH_4 as the fuel; 830 K

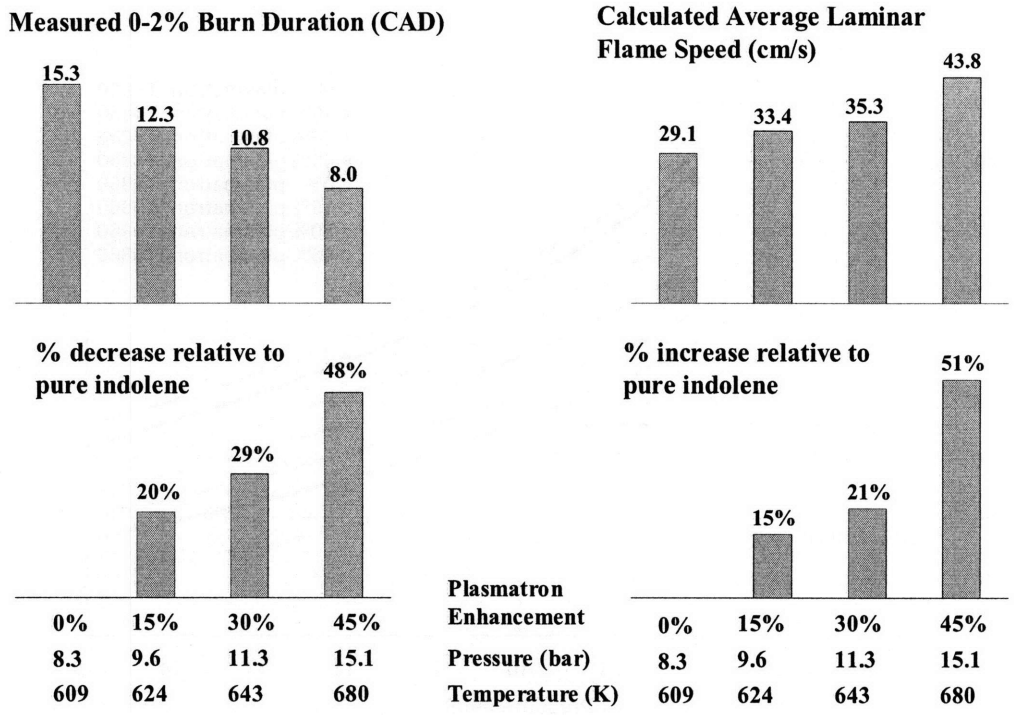

Figure 5-20 – Comparison of 0-2% burn duration intervals and their corresponding calculated average laminar flame speeds (CHEMKIN, CH_4), for different levels of plasmatron enhancement; MBT timing, Rc=13.4, 1500 RPM, λ=1.6, 3.5 bar NIMEP

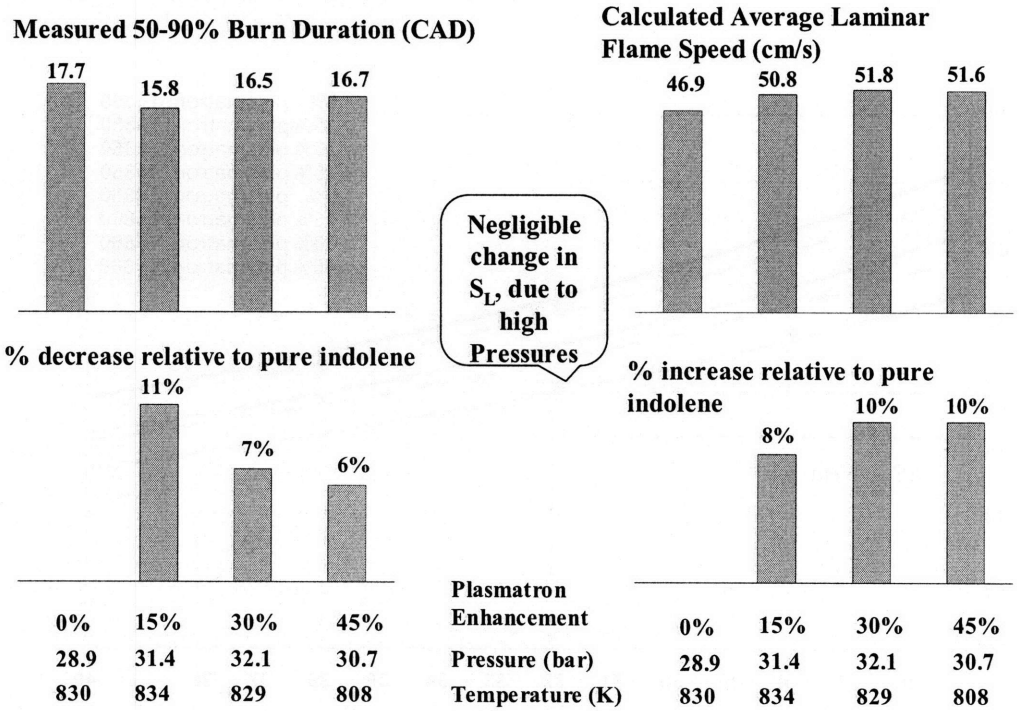

Figure 5-21 – Comparison of 50-90% burn duration intervals and their corresponding calculated average laminar flame speeds (CHEMKIN, CH_4), for different levels of plasmatron enhancement; MBT timing, Rc=13.4, 1500 RPM, λ=1.6, 3.5 bar NIMEP

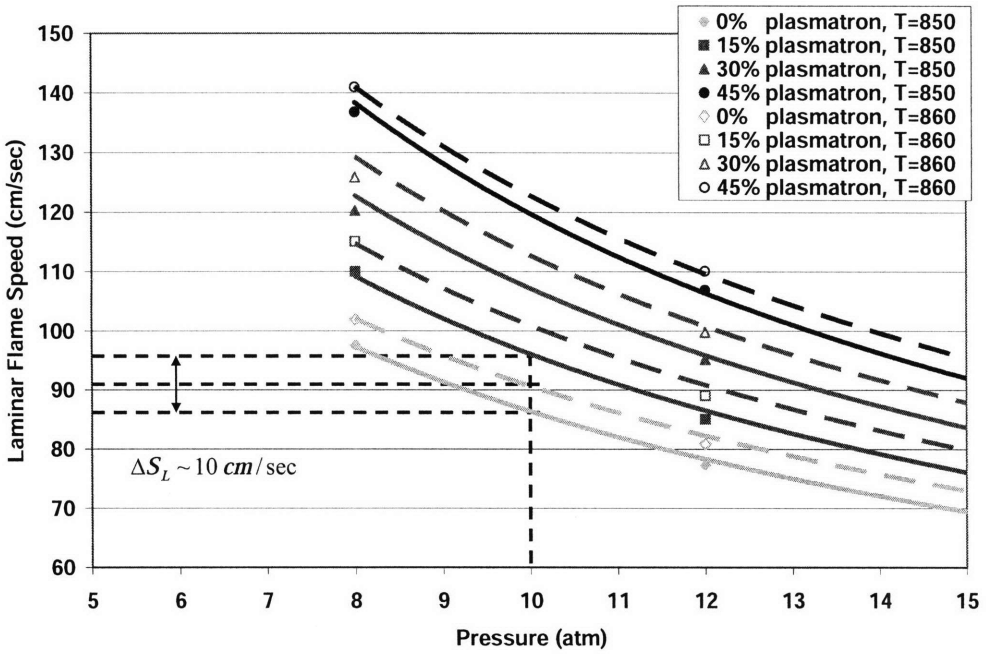

Figure 5-22 – Low pressure effect on laminar flame speed for different levels of plasmatron enhancement and two different temperatures with CH_4 as the fuel, λ=1.6

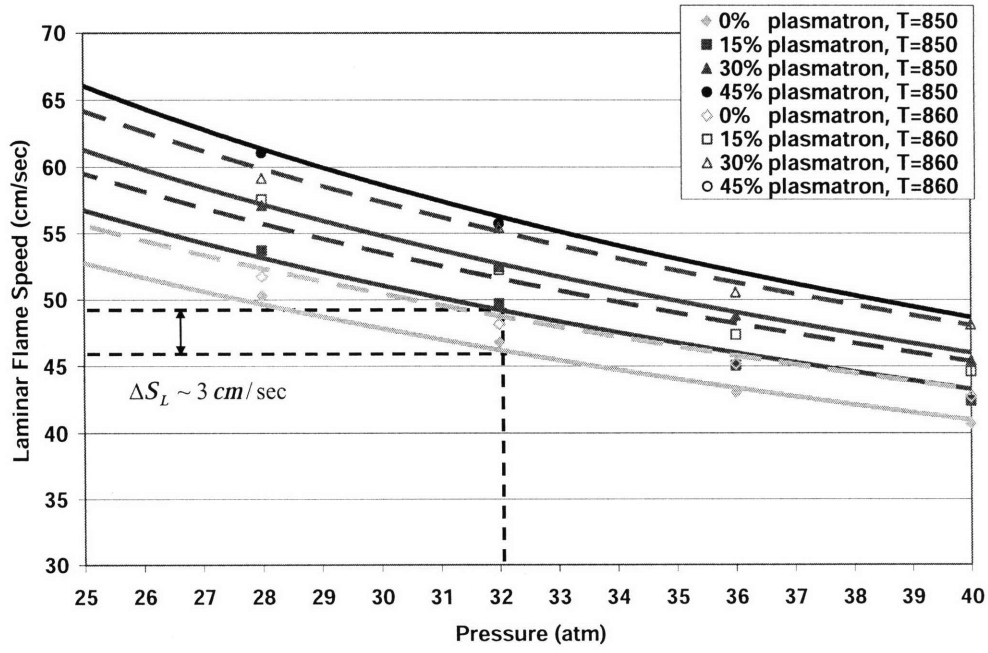

Figure 5-23 High pressure effect on laminar flame speed for different levels of plasmatron enhancement and two different temperatures with CH_4 as the fuel, λ=1.6

plasmatron enhancement is almost negligible under these high-pressure conditions. This is an important consideration when developing a hydrogen-enhanced engine, which is intended to run boosted and at high compression ratios [26]. The expected engine efficiencies of such concepts, should be carefully studied. Under relatively high operating pressures, hydrogen enhancement through reformate addition should not be seen as a way to increase efficiency only, since this improvement will be minor; the other advantages from Hydrogen enhancement, such as suppression of knock, will be much more important, especially in conjunction with other engine modifications [26].

5.4 Higher Load, Diminishing Returns

The conclusions from section 5.3 imply that for operating conditions where peak pressures are high (e.g., greater than 30 atm), plasmatron enhancement will show diminishing returns. As already mentioned, this is an important practical consideration, and worth further confirmation. Figure 5-24 shows the results of plasmatron enhancement at the lower compression ratio, 9.8:1, but at a load of 7 bar NIMEP. Peak pressures for these conditions are

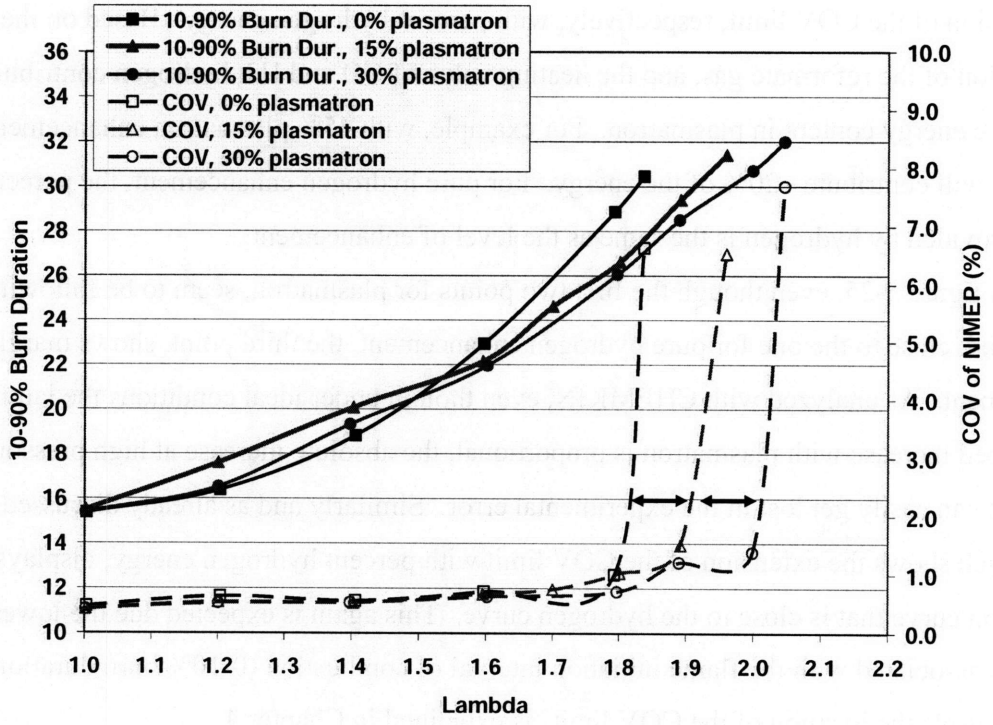

Figure 5-24 Effect of relative air-fuel ratio on 10-90% burn duration and COV of NIMEP for different levels of plasmatron enhancement; MBT timing, 1500 RPM, r_c=9.8:1, NIMEP = 7.0 bar, indolene

greater than 40 atm, and consequently a "diminishing returns" effect similar to what was observed for the higher compression ratio, 13.4:1, should also be evident for this data, according to the previous analyses and conclusions. This is exactly the case. Although there is not much spread in the 10-90% burn duration curves, it is clear that the shift in the burn duration, going from the baseline indolene-only curve to 15% enhancement is much greater than the shift from the 15% enhancement curve to the 30% enhancement curve.

5.5 Note on H2 vs. Plasmatron Comparison

The amount of hydrogen content in the H2 vs. plasmatron comparison is clearly different. The hydrogen experiments are similar to the plasmatron experiments because the amount of hydrogen enhancement was proportionally increased, from 0% to 15%, to 30 and 45%, just like the amount of plasmatron was proportionally increased by the same percentage. Therefore, these experiments allow a comparison of the effect of proportional change of enhancement on the laminar flame speed. The diminishing returns trend is clear. However, for the sake of a more direct comparison, Figs. 5-25 and 5-26 analyze the results from figure 5-14 as a function of the energy content provided by hydrogen only. The figures plot the extension of peak efficiency and the extension of the COV limit, respectively, with percent hydrogen energy. Based on the molar composition of the reformate gas, and the heating value of CO and H2, hydrogen contributes 45% of the energy content in plasmatron. For example, with 45% plasmatron enhancement, hydrogen will contribute ~20% of the energy. For pure hydrogen enhancement, the percent energy provided by hydrogen is the same as the level of enhancement.

In figure 5-25, even though the first two points for plasmatron, seem to be following a linear trend, close to the one for pure hydrogen enhancement, the third point, shows marginal improvement. As analyzed with CHEMKIN, even though under ideal conditions the laminar flame speed increase with plasmatron is proportional, the absolute increase at high pressures is small and can easily get lost in the experimental error. Similarly and as already discussed, figure 5-26, which shows the extension of the COV limit with percent hydrogen energy, displays a plasmatron curve that is close to the hydrogen curve. This again is expected due the lower pressures associated with the flame initiation interval of combustion (0-10% burn duration), which controls the location of the COV limit, as explained in Chapter 4.

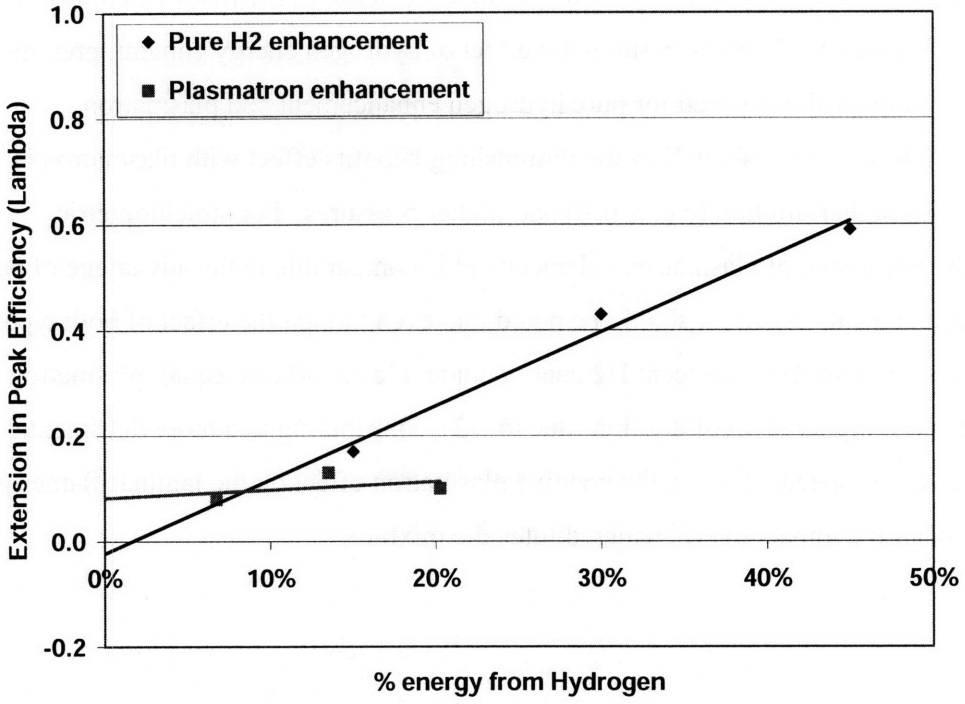

Figure 5-25 Peak efficiency extension as a function of the percent energy content provided by hydrogen, for pure hydrogen enhancement and plasmatron enhancement; MBT timing, 1500 RPM, r_c=13.4:1, NIMEP = 3.5 bar

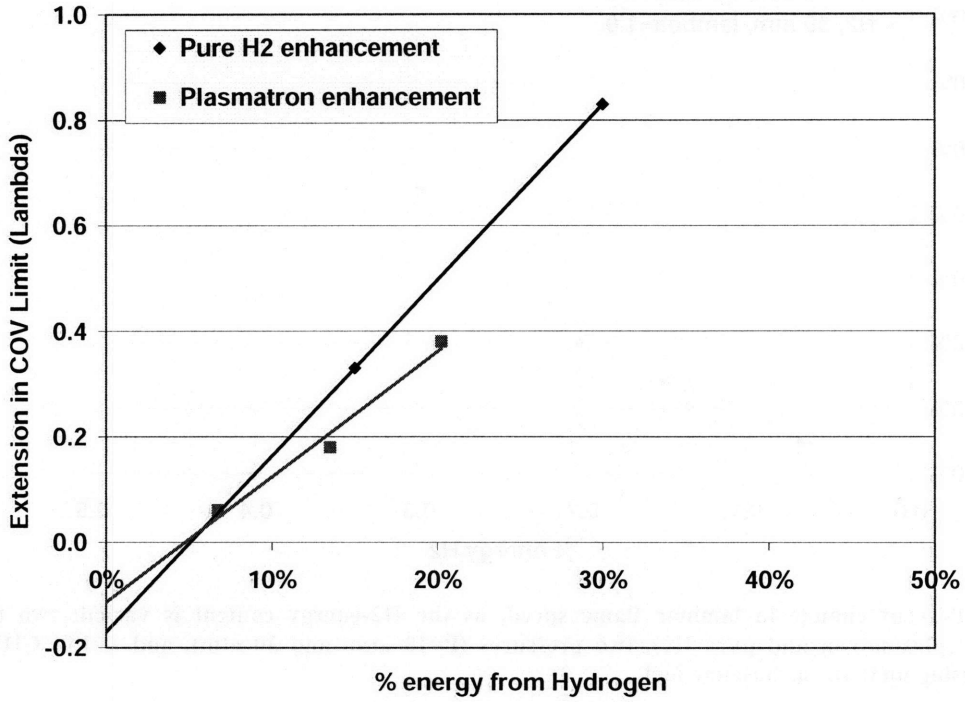

Figure 5-26 COV limit extension as a function of the percent energy content provided by hydrogen, for pure hydrogen enhancement and plasmatron enhancement; MBT timing, 1500 RPM, r_c=13.4:1, NIMEP = 3.5 bar

Similar trends are displayed, when looking at the increase in the CHEMKIN-calculated laminar flame speeds. Figures 5-27 and 5-28 study the effect of hydrogen energy content, pressure, and dilution on the laminar flame speed for pure hydrogen enhancement and plasmatron enhancement. These figures show how the diminishing benefits effect with plasmatron is exacerbated with higher dilution (e.g. λ=1.6) and higher pressures. For stoichiometric conditions, the advantage of plasmatron enhancement is comparable to the advantage of pure hydrogen enhancement. Again, it should be noted that even though the effect of both types of enhancement is compared on a percent H2 energy content level, all else equal, plasmatron enhancement has a higher level of dilution (due to N2), contributing to a more detrimental effect on the laminar flame speed. That is, the positive plasmatron effect on the laminar flame speed is offset by the negative impact of N2, which dilutes the mixture.

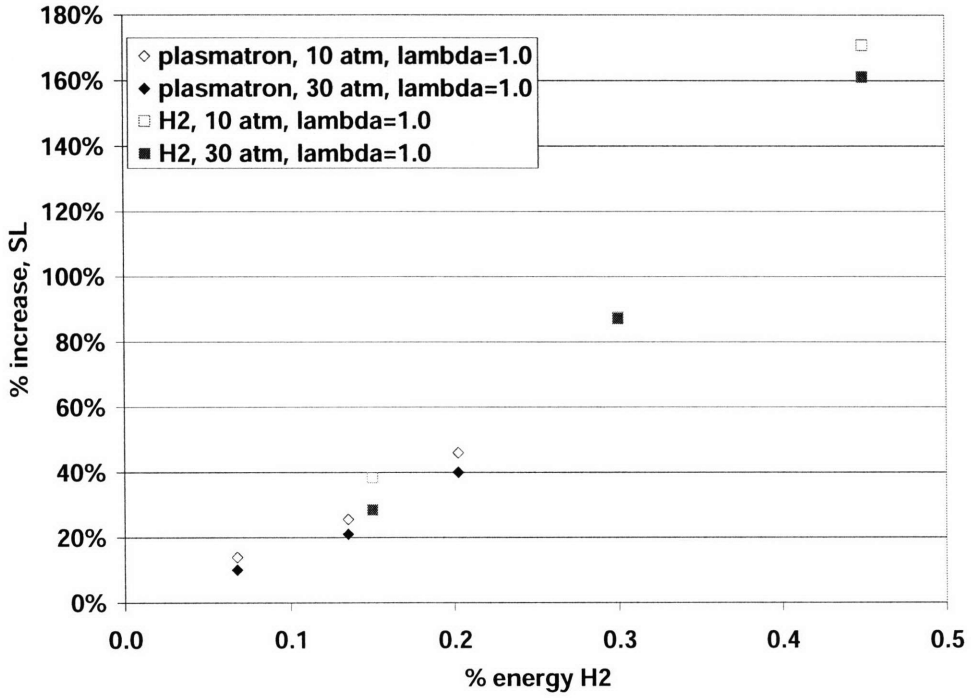

Figure 5-27 Percent change in laminar flame speed, as the H2-energy content is varied; two types of enhancement (plasmatron and pure H2), two pressures (P=10 atm, and 30 atm), and λ=1.0; CHEMKIN calculations using methane as baseline fuel

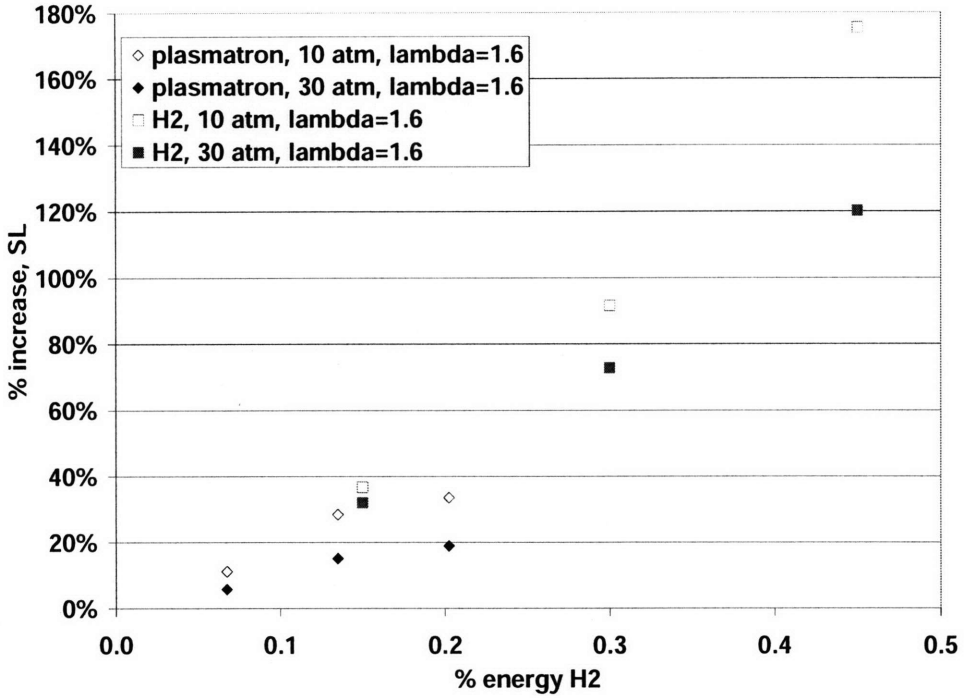

Figure 5-28 Percent change in laminar flame speed, as the H2-energy content is varied; two types of enhancement (plasmatron and pure H2), two pressures (P=10 atm, and 30 atm), and λ=1.6; CHEMKIN calculations using methane as baseline fuel

(this page was intentionally left blank)

Chapter 6 – FUNDAMENTAL COMBUSTION MODEL

6.1 The Combustion Process

As described by Heywood [22], combustion in a spark ignition engine is initiated with the electrical discharge of the spark plug, creating a flame kernel that develops into a self-sustaining flame front that burns and propagates through the unburned mixture. Initially the flame is laminar, and becomes affected by scales of turbulence that have the same or smaller length scale magnitude. Thus, as the radius of the flame grows, it will be increasingly affected by turbulence, steadily encompassing a wider range of turbulence length scales that can wrinkle its area, affecting the rate of burning. Eventually the flame evolves into a fully developed turbulent flame and is affected by the majority of the turbulence scales. The wrinkled flame keeps propagating, entraining the unburned mixture ahead of the flame front, until the wrinkles begin to reach the chamber walls. As the unburned mixture becomes entrained by the flame, it burns locally at the rate of the laminar flame speed. Eventually all the pockets of unburned mixture entrained in the flame will burn, and the flame will extinguish on the walls, reaching the end of combustion. Even under the most stable conditions, cycle-to-cycle variability in the combustion process will exist, arising from random initial fluctuations in the variables that determine the mass entrainment and the mass burning processes. To understand the fundamental physics of combustion and its variability under a wide range of conditions, it becomes necessary to build a well-grounded physical model.

6.2 Combustion Model Description

A turbulent flame entrainment model of the type originally proposed by Keck and Blizard [27], and later modified by Tabaczynski [28] has been developed to help understand the fundamentals of lean combustion. The model consists of equations 6-1 and 6-2, responsible for entraining and burning the mass, respectively. The first expression, responsible for the rate of mass entrainment consists of a laminar flame speed component and a turbulent flame speed component. This last component is multiplied by an exponential factor that determines the rate at which turbulence develops. Per the form of this factor, as the length scale of the flame, taken as the burned radius (r_b), grows relative to a characteristic length (λ_1), the turbulence increases as a percent of its fully developed value. When the burned radius has achieved a sufficiently large

size, the term in parenthesis, containing the exponent becomes close to one and turbulence assumes its fully developed value. This is consistent with a growing flame kernel that is being affected by increasingly larger turbulence length scales.

$$\frac{dm_e}{dt} = \dot{m}_e = \rho_u A_b \left(S_L + u' \left(1 - e^{\frac{-r_b}{\lambda_1}} \right) \right) \tag{6-1}$$

$$\frac{dm_b}{dt} = \dot{m}_b = \rho_u A_b S_L + \frac{m_e - m_b}{\tau_b} \tag{6-2}$$

$$\tau_b = \frac{\lambda_{micrsc}}{S_L} \tag{6-3}$$

It is not well defined whether the exponential term should be based on a length scale as shown in equation 6-1, or based on a time scale as shown in equation 6-4. Both expressions were tested, and the length-scale approach gave a better match with the data. However, for the best model calibration, the exponential term ended up having a negligible role, being very close to a value of one early in the combustion process.

$$\frac{dm_e}{dt} = \dot{m}_e = \rho_u A_b \left(S_L + u' \left(1 - e^{\frac{-t}{\tau_b}} \right) \right) \tag{6-4}$$

The second expression (eq. 6-2) determines the rate at which the mixture is burned. This rate has the same laminar-burning component as the previous equation. This is the rate at which both the flame is entrained and the flame is burned at time equal to zero. That is, at the beginning of combustion, when turbulence is fairly small due to the small size of the kernel, the rate of mass entrainment is equal to the rate of mass burning. As time progresses, and larger turbulence scales wrinkle the flame, the entrainment equation is primarily governed by the turbulent component. Similarly, as time evolves, the mass burning equation becomes dominated by the rate at which the pockets of entrained unburned mass burn. This is represented by the second term in equation 6-2, indicated as the difference between the entrained mass and the entrained mass that has burned, divided by a characteristic burning time. The characteristic burning time

equation (6-3) is the time to burn the unburned turbulent eddies in the entrained mass. It is defined as the ratio of the characteristic length scale of the turbulent eddies to a burning speed; for this length scale, diffusion occurs at the laminar flames speed as discussed next.

Three length scales represent the turbulence spectrum. The macroscale represents the size of the large coherent eddies that make up the turbulent flow. The smallest eddies are the size of the kolmogorov scale, and for this model they represent the size of the vortex tubes; the spacing between the vortex tubes is defined by the turbulence microscale [29]. These length scales (with the exception of the macroscale) are shown in figure 6-1, along with a diagram depicting the flame entrainment and burn-up process. Burning of the kolmogorov scale is assumed instantaneous, while burning of the microscale is assumed to occur at the laminar flame speed. The Taylor microscale is commonly used to characterize the spacing of the vortex tubes. After calibrating the model, the microscale that provides better agreement with the data, has a magnitude consistent with the Taylor microscale.

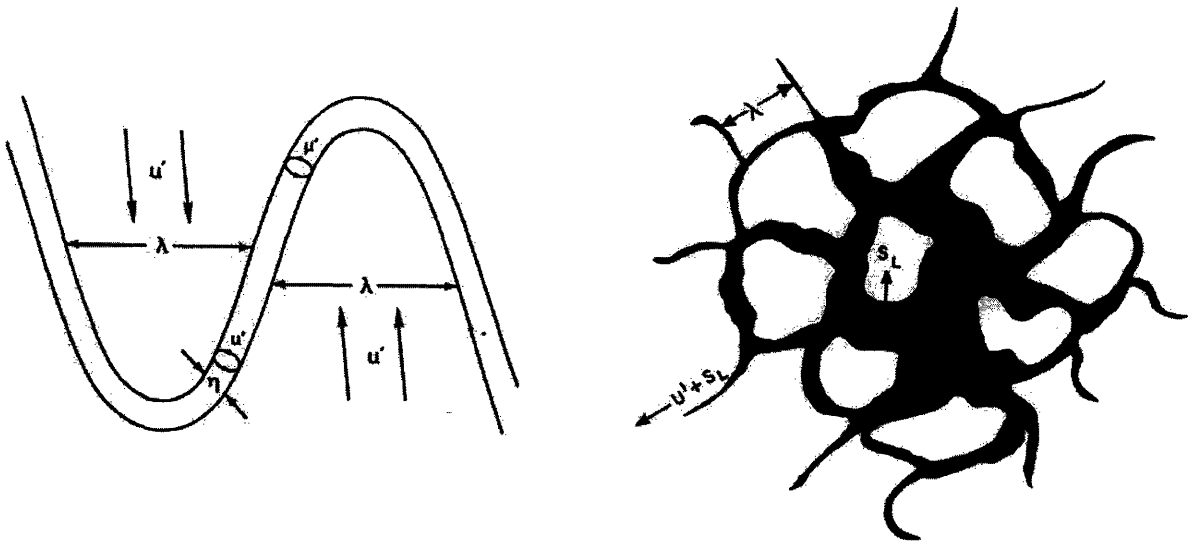

Figure 6-1 characteristic turbulence length scales, and flame entrainment process [28]

The model expressed by equations 6-1 through 6-3 essentially has three unknown variables that must be determined. These are the turbulence intensity (u'), the laminar flame speed (S_L), and the turbulence microscale (λ_{micrsc}). Treatment of these variables is discussed in section 6.4. All other variables in the model (e.g. density) can be determined based on the thermodynamic properties of the mixture in the combustion chamber. A flame-area relationship

is also required, but can be approximated knowing the physical dimensions of the combustion chamber, as discussed in the next section.

This quasi-dimensional combustion model calculates a burned and an unburned region, each of which is assumed to be thermodynamically uniform. The model runs as a sub-model of the previously described MIT engine cycle simulation, which calculates the intake and exhaust processes. A heat transfer submodel works together with the combustion model to determine the losses affecting the thermodynamic state of the burned and unburned mixture [29].

6.3 Flame Geometry and Wall Interactions

To calculate the burned and entrained areas at any given radius, the flame geometry must be specified. The original model was designed to generate a flame geometry for a generic engine based on the basic engine dimensions: compression ratio, bore, and stroke. A series of triangles would then be used to define the chambers walls of a central spark engine, as well as the developing flame. For the specific engine used during the current research, it was found that this approach yields inconsistent results, overestimating the area for a given flame radius, and thus calculating faster burn durations than expected. Therefore, it was necessary to use a more accurate flame and combustion chamber geometry, within the constraints of the modest software tools available at the Sloan Lab. Using previously generated Autocad drawings [30] of the Volvo engine used to produce the real data, the flame growth and wall interactions were simulated for a given piston position (crank angle). The flame was assumed spherical at all times and the radius of the sphere was varied at a constant crank angle. At each radius, the flame area was calculated and recorded. Using arithmetic together with Autocad tools, the sphere representing the flame was truncated upon touching a chamber surface; the remaining flame area would again be calculated and recorded. The remaining spherical area would continue to grow until the entire sphere had been truncated by the chamber walls. This flame growth exercise was repeated for a series of crank angles, until a well defined discrete map of flame area as a function of radius and crank angle had been produced. Matlab was then used to refine the area map, increasing the number of points available through interpolation. In the absence of more advanced, and usually more expensive, 3-D modeling packages, this provided a very robust and accurate flame representation, using the real cylinder chamber geometry.

To simulate offset centers of the flame, due to "random walk" [31] of the flame kernel, a new flame geometry can be generated, following the exact same procedure described above. The only difference will be that the center of spark will be offset by a specified distance.

6.4 Turbulence Model

The MIT cycle simulation uses two different turbulence models, one for the intake and exhaust processes, and one for the combustion process. The first turbulence model finds the necessary turbulence length scales and velocity scales to correctly simulate the intake and exhaust processes, and to ensure a smooth transition between these processes and combustion. The details for this turbulence model can be found in [29]. Some of the components calculated in the non-combustion turbulence model continue to be used during combustion in order to calculate the kinetic energy and velocity needed for the heat transfer correlations in the heat transfer submodel. However, aside from the heat transfer interactions, the turbulence variables required to run the combustion model and propagate the flame are the turbulent intensity and the turbulence microscale, as shown in equations 6-1, 6-2, and 6-3. Turbulence throughout the combustion phase is assumed isotropic. Using the rapid distortion theory [32], conservation of Momentum yields the following expression for the turbulent intensity:

$$u' = const(u'_o)\left(\frac{\rho_u}{\rho_{u_{sp}}}\right)^{\frac{1}{3}} \tag{6-5}$$

For the initial value of the turbulent intensity a correlation developed by Keck [33] is used. Through experiments, Keck found that the initial turbulent intensity is proportional to the piston speed and the ratio of the gas density to the inlet density raised to the power of a half:

$$u'_o = const(\bar{u}_p)\left(\frac{\rho_u}{\rho_{inlet}}\right)^{\frac{1}{2}} \tag{6-6}$$

Various approaches have been used to model the Taylor microscale. In his original definition, Tennekes [34] defined the ratio of the taylor microscale to the turbulence macroscale as being

proportional to the inverse square root of the Reynolds number based on the turbulence intensity and the macroscale as shown in eq. 6-7:

$$\frac{\lambda_{micrsc}}{L} = CONST * (\mathrm{Re}_t)^{-0.5} = CONST * \left(\frac{\rho_u u' L}{\mu} \right)^{-0.5} \tag{6-7}$$

Using conservation of angular momentum, to express the turbulence intensity and the macroscale (eqs 6-8 and 6-9), some authors have simplified the original Tennekes expression into equation 6-10, where the dependence on the density has changed from a power of –1/2 to a power of –5/6.

$$u' = u'_o \left(\frac{\rho_u}{\rho_{uo}} \right)^{1/3} \tag{6-8}$$

$$L = L_0 \left(\frac{\rho_u}{\rho_{uo}} \right)^{-1/3} \tag{6-9}$$

$$\lambda_{micrsc} = (CONST)(\mathrm{Re}_t)^{0.5} = CONST * \left(\mu \frac{L_o}{u_o} \right)^{1/2} \left(\frac{1}{\rho_{uo}} \right)^{-1/3} \rho_u^{-5/6} \tag{6-10}$$

In his research, Keck [33] assumed a different dependence of the microscale on the unburned density:

$$\lambda_{micrsc} = CONST * \left(\frac{\rho_{uo}}{\rho_u} \right)^{3/4} \tag{6-11}$$

Tabaczynsky [35] also used a different expression for the microscale, embedded in the time to burn an eddy, previously defined as the microscale over the laminar flame speed

$$\tau_b = \frac{1}{2} \left(\frac{\rho_b}{\rho_u} \right)^{-2/3} \left(\frac{L}{u' + S_L} \right) \tag{6-12}$$

Other authors have used still other expressions relating the microscale to the unburned density [36]. Clearly there is not a very tight definition on the exact form of the microscale expression. Staying within the range of expressions used by different researchers, two approaches were tested for this model, one where the microscale depends on the inverse of the unburned density raised to the power of 1/2, and one where the inverse of the unburned density is raised to the power of 5/6, as shown in Eqs. 6-13 and 6-14.

$$\lambda_{micrsc} \propto \left(\frac{\rho_{uo}}{\rho_u} \right)^{\frac{1}{2}} \tag{6-13}$$

$$\lambda_{micrsc} \propto \left(\frac{\rho_{uo}}{\rho_u} \right)^{\frac{5}{6}} \tag{6-14}$$

6.5 Laminar Flame Speed and Residual Fraction Correlations

As previously discussed in Chapter 3, the laminar flame speed during the combustion process was calculated using the Rhodes-Keck correlations. The Fox correlation [37] was used to predict the residual mass fraction, a parameter that will affect the laminar flame speed, and must therefore be included.

6.6 Model Behavior

Figures 6-2 and 6-3 show a descriptive view of how the model works, and the relative magnitude of the components that make up equations 6-2 and 6-3. The rates of mass fraction entrained and mass fraction burned for stoichiometric conditions, compression ratio of 9.8:1, and 1500 rpm are shown in figure 6-2. Initially, the laminar component has a major role in starting the combustion process. As time progresses turbulence grows, increasing the rate of mass entrained, and consequently the rate of mass burned. After the flame has entrained all the mass, and reached the cylinder walls, the unburned entrained mixture continues to burn, but at a decreasing rate as figure 6-2 shows. The end of combustion is then reached at around 390 CAD. A comparison between the mass fraction entrained and the mass fraction burned as a function of crank angle is shown in figure 6-3. It is clear how the inflection point of the mass burning curve lines up with the end of entrainment, a process that marks a deceleration of combustion. It is

also clear how there is a delay in mass burning, relative to mass entrainment. Entrained mass does not burn instantaneously, bur rather at the rate of the laminar flame speed; thus although a higher rate of mass entrainment will raise the rate of mass burning, since more mass is available to burn, there will still be a delay determined by the size of the microscale and the laminar flame speed. Physically, this delay can be thought of as the time that it takes to burn the mass that has just been entrained, or the mass in the flame thickness area. A faster laminar flame speed will reduce the time to burn this mass, reducing the flame thickness, and increasing the rate of mass burning.

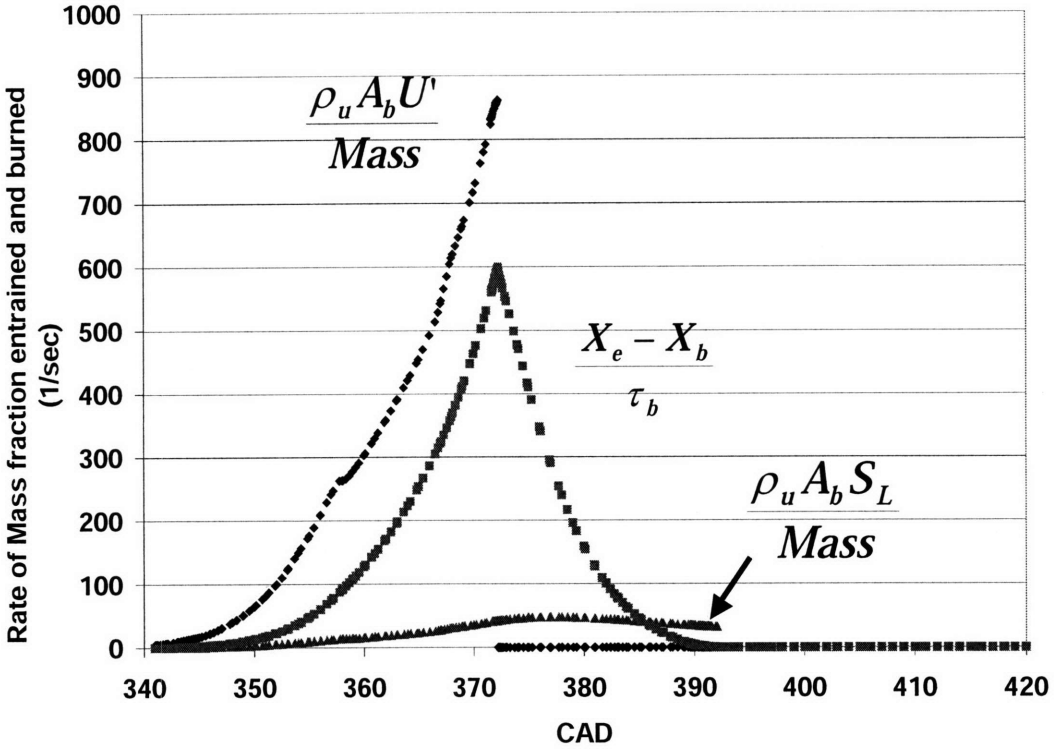

Figure 6-2 – Time history of components of flame entrainment combustion model; MBT timing, 1500 RPM, r_c=9.8:1, NIMEP = 3.5 bar, indolene, λ=1.0

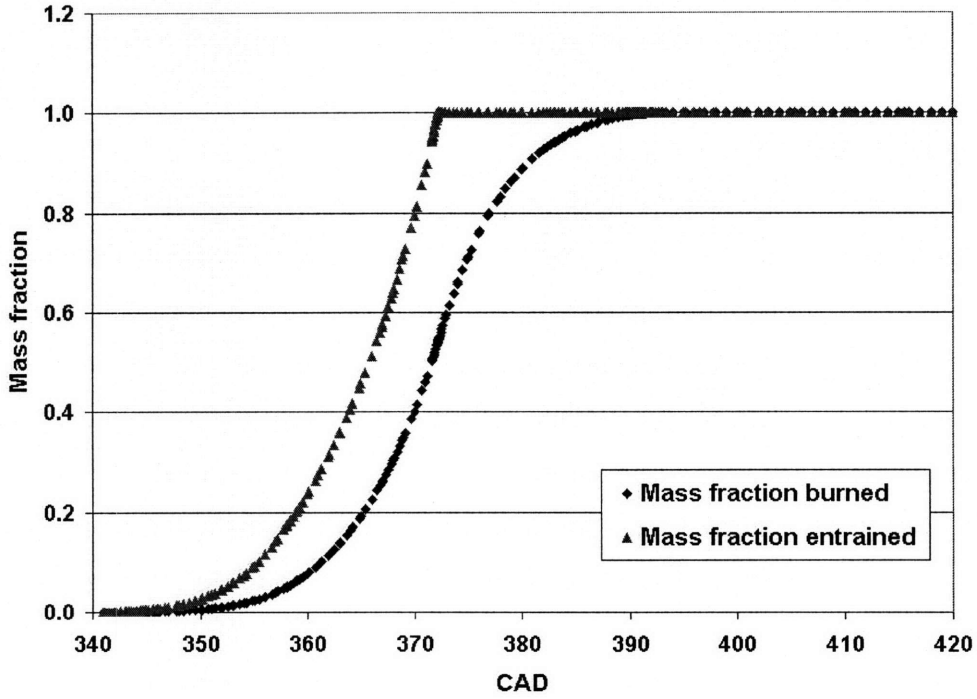

Figure 6-3 – Time history of mass the mass fraction burned and the mass fraction entrained, predicted by the model; MBT timing, 1500 RPM, r_c=9.8:1, NIMEP = 3.5 bar, indolene, λ=1.0

6.7 Combustion Parameters and Characteristic Times

Traditionally, the primary combustion variables that the engineering community studies and compares when analyzing data are the burn durations. The duration of the combustion process is typically broken down into terms like the 10-90% burn duration, indicating the time elapsed between burning 10% of the mass and burning 90% of the mass. The intervals associated with the flame initiation stage range from the 0-2% to the 0-10% burn duration, while the 10-90% burn duration is associated with the flame propagation stage. Most of the data and model results in this thesis have been compared using this terminology for the different combustion regimes.

Other researchers have suggested using different parameters to compare the data. Keck et. al. [38] suggested that the burning profiles all exhibit clear characteristics that are the results of physical events occurring during combustion. Keck explains how using these characteristics as a basis for comparing burn duration profiles, is a more consistent approach, and reduces the arbitrary nature of choosing for example the 10-90% vs. the 10-85% burn duration as a combustion interval. Additionally, other useful parameters can be obtained through his suggested approach. Because it is difficult to replace the traditional standards, but yet there is value in using other approaches to analyze combustion, the traditional approach is used throughout this thesis, while the second approach is included in this modeling chapter.

6.8 Inflection Point Method

Figure 6-4 shows the relevant time characteristics that can be extracted from the burn profile, as suggested by Keck. The characteristic burning time is determined by the inflection point of the mass fraction burned curve. This is the point of peak energy released and occurs approximately when the flame area has begun to reach the chamber walls, decelerating the rate of combustion. The characteristic burning time (tau burn) is defined by drawing a line tangent to the inflection point and subtracting the resulting x-intercept from the CA where the tangent line and the 100% mass fraction burned (mfb) line intersect. The characteristics delay time (tau delay) is defined as the difference between this same x-intercept and the location of spark. A third characteristic time is the final burning time, encompassed by Tau burn, and defined as the difference between the CA for the intersection of the 100% mfb line and the tangent line, and the CA for the location of the inflection point.

Comparing the characteristic eddy-burning time produced by the model as defined by equation 6-3, at the mass burning inflection point, with the geometrically extracted tau burn (see Fig. 6-4), shows that there is a consistent and well-behaved proportionality between these two terms defined as follows:

$$\tau_{b\_geometric} \approx (2.1)(\tau_{b\_eddy\_burning}) \tag{6-15}$$

Thus, in essence knowing the laminar flame speed at the inflection point (which can be calculated through the Rhodes-Keck correlations), the extracted characteristic time can be used to back-calculate a microscale for the real data:

$$\lambda_{micrsc} = (S_L)(\tau_b) \tag{6-16}$$

The validity of equation 6.15 should be further explored; for the moment, and to keep all analyses independent of the calculated burn durations, the microscale used is extracted from the model predictions, as defined by eq. 6-3.

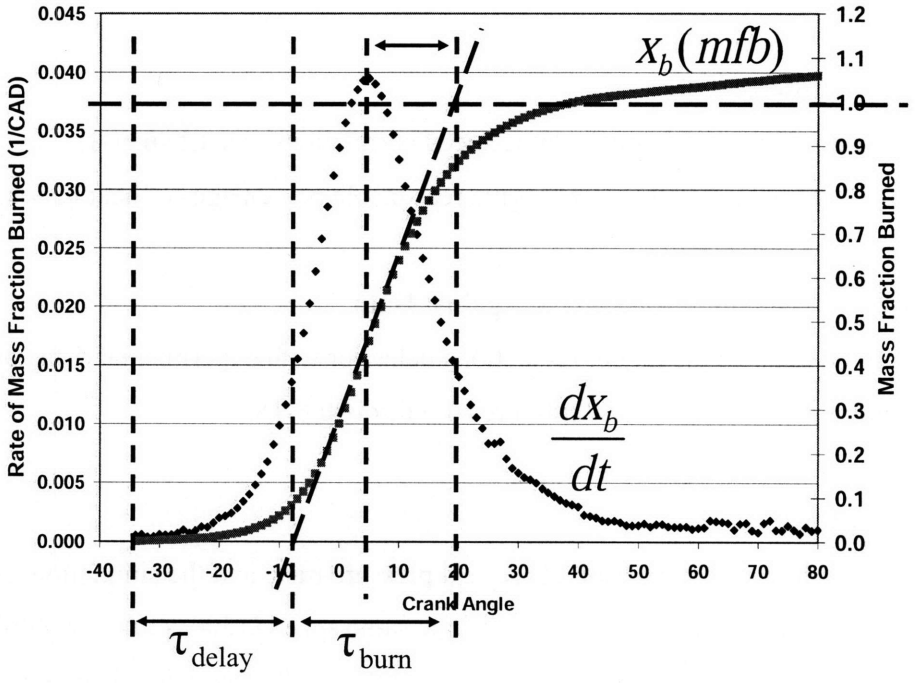

Figure 6-4 – Inflection point analysis for calculating characteristic burning times; MBT timing, 1500 RPM, r_c=9.8:1, NIMEP = 3.5 bar, indolene, λ=1.6

6.9 Model Limitations

The current combustion model, along with MIT's engine simulation, has some limitations. A detailed ignition model is missing, consequently discrepancies between the model and the data during the flame initiation interval become evident for different operating conditions. As was previously mentioned, the model assumes complete combustion of the air-fuel mixture. There is also room for improvement in the exact representation of the flame geometry and the flame/wall interactions.

6.10 Model Calibration

To calibrate the model, the following procedure was followed:

- The load of the real experiments was matched (3.5 bar NIMEP) at MBT conditions, and the same speed (1500 rpm). Due to the higher combustion efficiency, the air flow of the model is lower by 8.5% compared to the experiments. Spark timing is also different by 3-6 CAD
- The calibration is performed by varying the following variables, within realistic constraints, until the model has good agreement with the 0-10% and the 10-90% burn durations for stoichiometric conditions:
    - Turbulence intensity
    - Microscale
    - n-coefficient in laminar flame speed correlations (see Chapter 3)
    - Heat transfer coefficient, to give reasonable percentages of heat losses

6.11 Model Assessment: Comparison Against Data

This next section compares the model predictions/behavior with experimental data across a wide range of operating conditions, as shown figures 6-5 through 6-18.

6.11.1 Baseline Case

Figure 6-5 shows a comparison of the real pressure trace and the simulation's pressure trace for the same compression ratio (9.8:1) and the same speed (1500 rpm). Two different relative air-fuel ratios are shown, lambda=1.6, and lambda=1.0. There is decent agreement between the model and the data, indicating that the real physics is adequately modeled in the

simulation. Figure 6-6, shows the mass fraction burned profiles for the same conditions shown in figures 6-1 and 6-2. For comparison purposes, the curves were lined up near the inflection point of the mass burning profiles. Differences in spark timing and flame initiation for the leaner mixtures can be seen between the model and the real data, but the overall agreement is fairly good. Tables 6.1 and 6.2 compare a breakdown of various burn duration intervals for the data and model, for the conditions shown in the discussed figures, using the microscale expression from eq. 6-13, i.e., with a dependance on the unburned density raised to the power of –1/2. Table 6.1 shows the good agreement across all the burn durations, for stoichiometric conditions. Looking closer at the initial burn duration intervals, 0-2% and 2-5%, for lean conditions in table 6.2 shows considerable differences. The discrepancy is reduced if both of these intervals are combined (e.g., 0-5%); this difference is most likely due to the lack of a flame ignition model. The later combustion intervals show good agreement.

Burn Duration (CAD); Lambda=1.0

Interval	Data	Model
0-2%	13.5	13.1
2-5%	3.3	3.5
5-10%	2.8	3.2
10-50%	9.7	10.4
50-90%	9.2	9.3

Table 6.1 – Comparison of burn duration intervals for model and data; MBT timing, 1500 RPM, r_c=9.8:1, NIMEP = 3.5 bar, indolene, λ=1.0

Burn Duration (CAD) Lambda=1.6

Interval	Data	Model
0-2%	23.6	27.4
2-5%	12.4	5.8
5-10%	6.1	4.9
10-50%	14.9	15.2
50-90%	17.5	17.4

Table 6.2 – Comparison of burn duration intervals for model and data; MBT timing, 1500 RPM, r_c=9.8:1, NIMEP = 3.5 bar, indolene, λ=1.6

The next two figures (Figs. 6-7 and 6-8) show the 0-10% and 10-90% burn duration comparisons between the model and the data as a function of the relative air-fuel ratio. In general the agreement is fairly good for both burn durations, but the discrepancy is larger for the 0-10%, which includes the flame initiation interval. Figures 6-9 and 6-10 make the same comparison for the model that uses the microscale expression that depends on the unburned density to the power of -5/6. The agreement for the 0-10% burn duration is better than the previous simulation. Although the 10-90% agreement is apparently not as good, this result is actually more accurate than the previous case with the -1/2 density dependence; this is the case because the model does not include the effect of variability, which will lengthen the burn duration affecting the NIMEP of the cycle, as discussed in section Chapter 4. If the model prediction was corrected for high variability, then the resulting curve would have a closer match to the data, as shown by the dotted line. Overall, the results of this section give confidence that the model has an acceptable behavior, doing a proper job at modeling the physics behind combustion. As the operating conditions change, there are larger discrepancies between the data and the model, particularly in the flame initiation stage, however the trends are still good, as will be seen in the next sections. These sets of comparisons provide confidence that the model is a good tool to try to help understand the fundamentals of lean combustion. The comparisons done in the next sections were done with the (-5/6) density dependence of microscale, which showed the better agreement across various operating conditions.

Having selected a relationship for the microscale structure, an important point to notice, is that eq. 6-14 can be rearranged, using equation 6-8, and expressed in terms of the turbulence intensity:

$$\lambda_{micrsc} \propto \left(\frac{u'_o}{u'}\right)^{\frac{5}{2}} \tag{6-17}$$

After calibrating the model, there is a better fit with the data, if a dependence on the dynamic viscosity, as shown in the original Tennekes formulation (eq. 6-7), is also included:

$$\lambda_{micrsc} = CONST * \left(\frac{u'_o}{u'}\right)^{\frac{5}{2}} (\mu)^{\frac{1}{2}} \quad \Rightarrow \quad \lambda_{micrsc} = \frac{(232.6)\left(\frac{u'_o}{u'}\right)^{\frac{5}{2}} (\mu)^{0.5}}{[(Vp_{mean})(cmult)]^{0.5}} \tag{6-18}$$

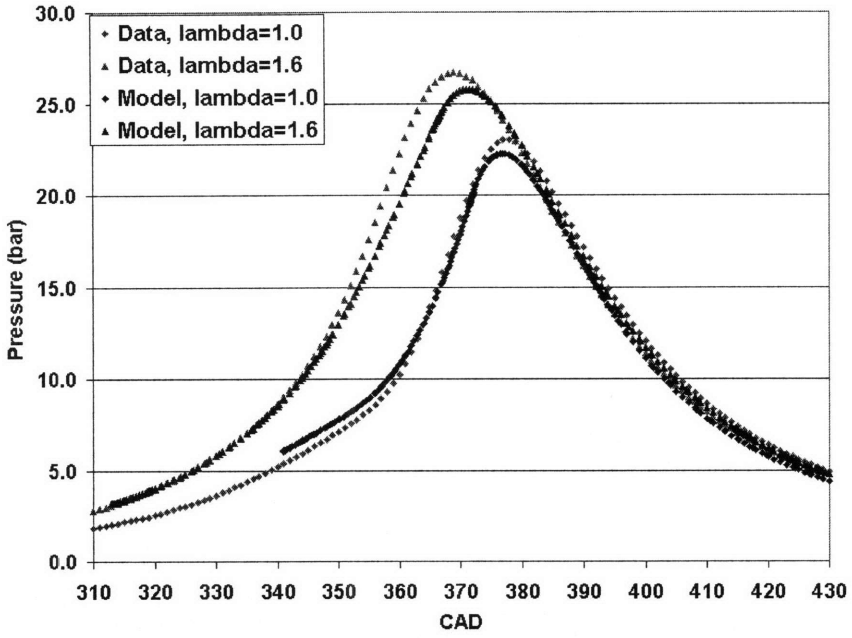

Figure 6-5 – Comparison of pressure time histories for model and data; MBT timing, 1500 RPM, r_c=9.8:1, NIMEP = 3.5 bar, indolene, λ=1.0 and λ=1.6, 1/2 model micrsc dependence on density ratio

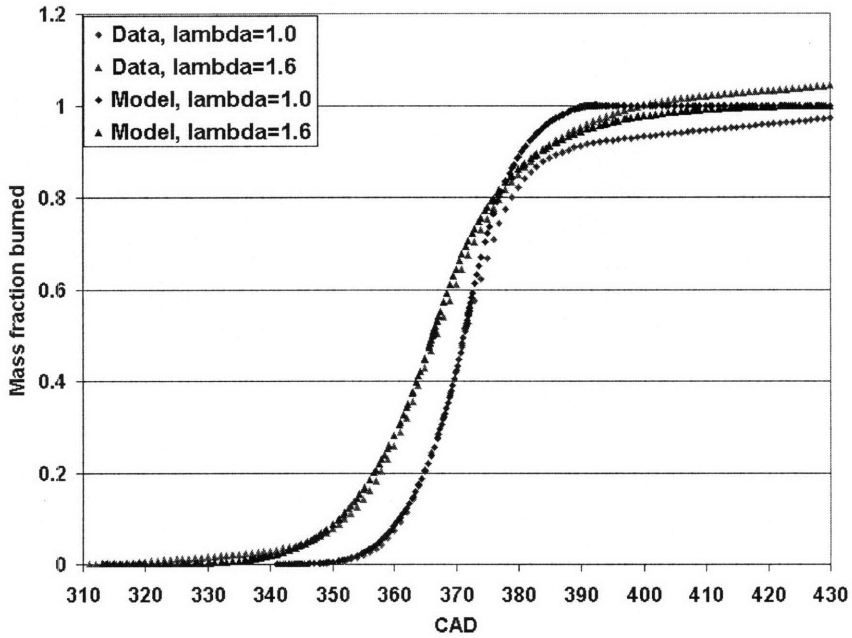

Figure 6-6 – Comparison of mass fraction burned (mfb) time histories for model and data; MBT timing, 1500 RPM, r_c=9.8:1, NIMEP = 3.5 bar, indolene, λ=1.0 and λ=1.6, 1/2 model micrsc dependence on density ratio

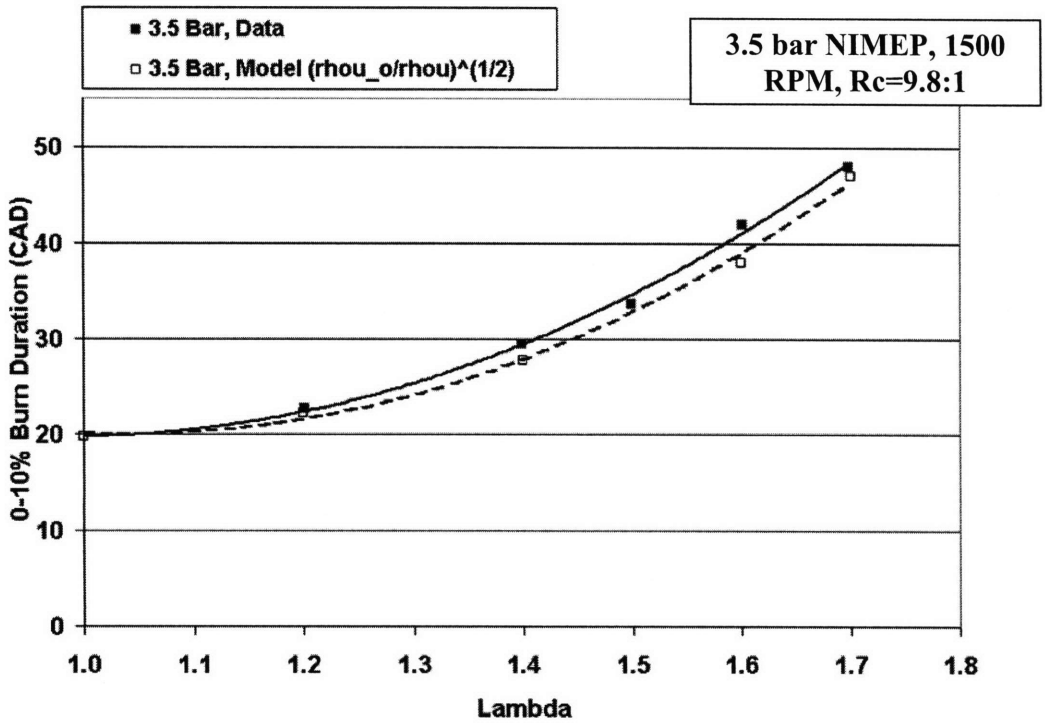

Figure 6-7 – Comparison of 0-10% burn durations with air dilution for model and data; MBT timing, 1500 RPM, r_c=9.8:1, NIMEP = 3.5 bar, indolene, 1/2 model microscale dependence on density ratio

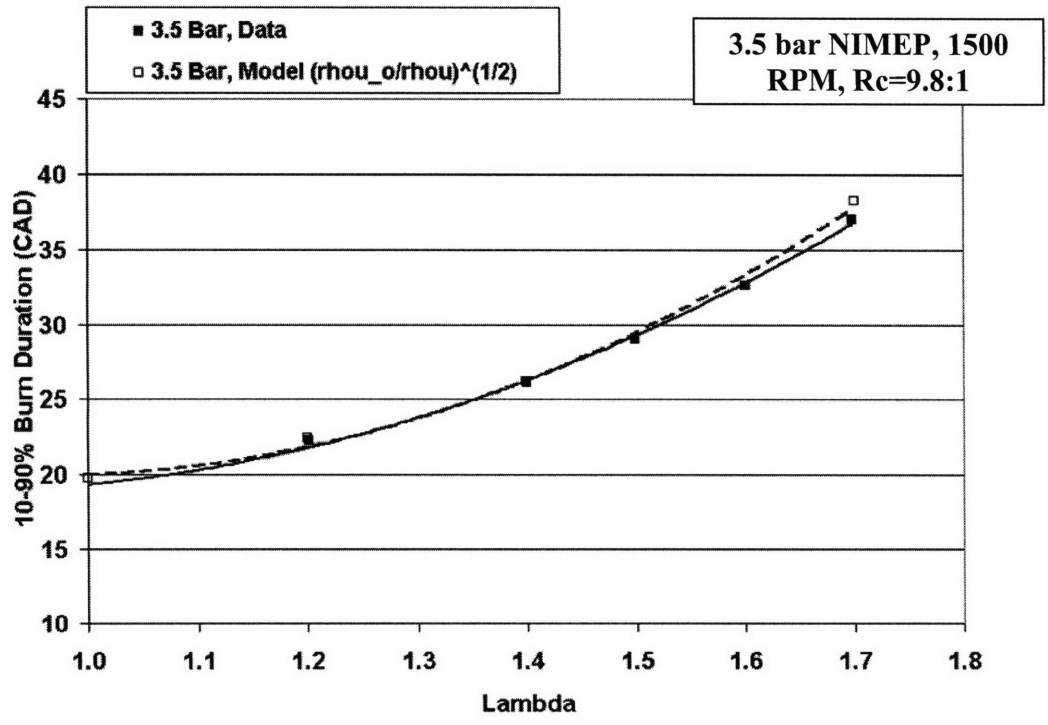

Figure 6-8 – Comparison of 10-90% burn durations with air dilution for model and data; MBT timing, 1500 RPM, r_c=9.8:1, NIMEP = 3.5 bar, indolene, 1/2 model microscale dependence on density ratio

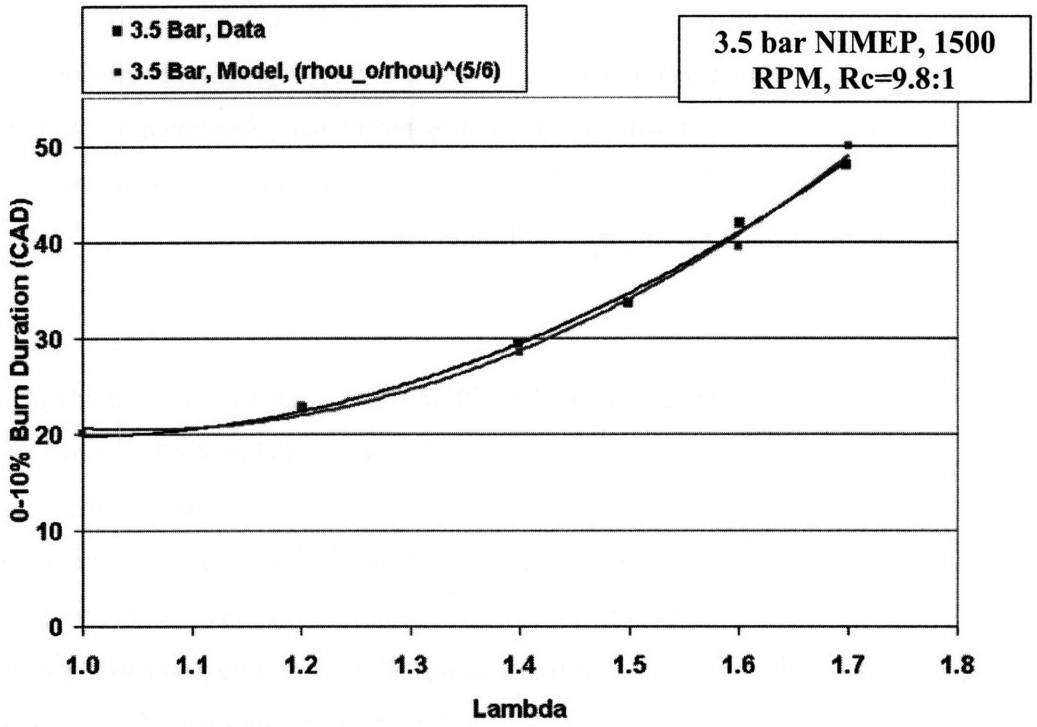

Figure 6-9 – Comparison of 0-10% burn durations with air dilution for model and data; MBT timing, 1500 RPM, r_c=9.8:1, NIMEP = 3.5 bar, indolene, 5/6 model microscale dependence on density ratio

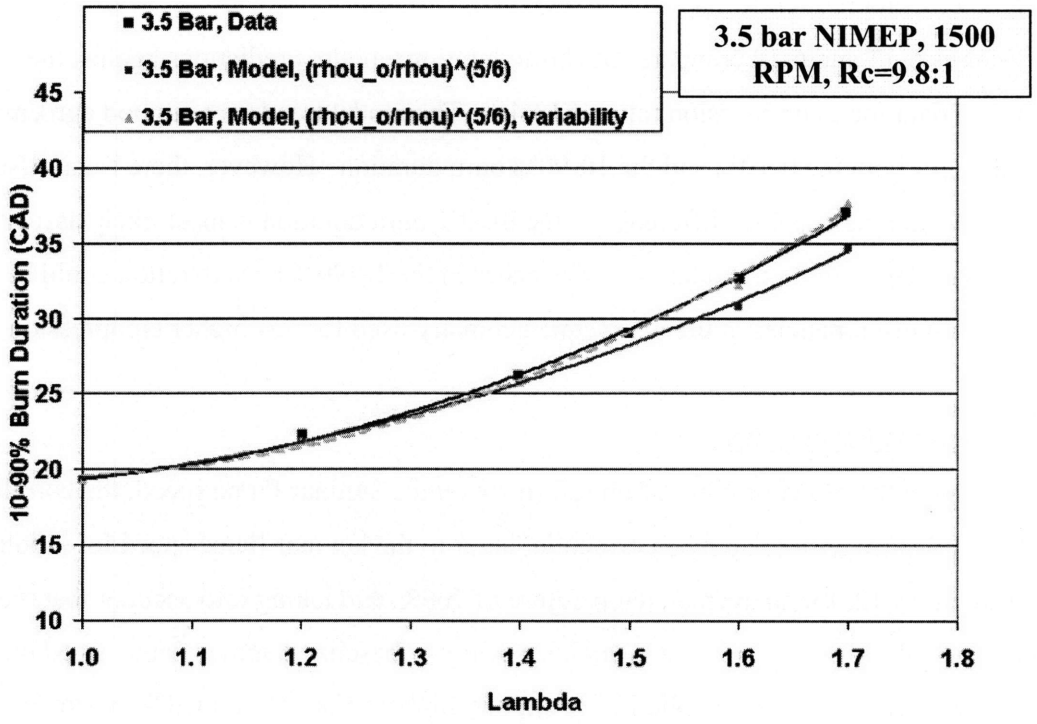

Figure 6-10 – Comparison of 10-90% burn durations with air dilution for model and data; MBT timing, 1500 RPM, r_c=9.8:1, NIMEP = 3.5 bar, indolene, 5/6 model microscale dependence on density ratio

The implication of expression 6-17, is that as the turbulence intensity increases, the size of the microscale decreases. As will be seen in Chapter 7, this is a very important conclusion; essentially, combustion variability is directly affected by turbulence. As shown by more detail in equation 6-18, the dependance of turbulence is brought through the inverse dependance on both the piston speed, and the turbulence intensity multiplier (cmult).

6.11.2 Higher Load

Figures 6-11 and 6-12 compare the model with the data at a load of 6.0 bar NIMEP, compression of 9.8:1, and 1500 rpm. The 0-10% burn duration model prediction shows an initial offset relative to the data, most likely due to the lack of a flame ignition model, as previously explained. However, the relative change with lambda follows the same trend as the real data. At high dilutions ($\lambda_{A/F}$>1.6), this trend begins to deviate. In contrast, the agreement model/data agreement for the 10-90% burn duration, with increasing dilution is quite good, as shown in figure 6-12. Small deviations begin to appear at $\lambda_{A/F}$>1.7, where S_L approaches zero (see section 6.12)

6.11.3 Higher Compression Ratio

Figures 6-13 and 6-14 compares the burn durations model predictions against the experimental data for a compression ratio of 13.4:1. The model trends are in good agreement with the data for both the 0-10% and the 10-90% burn duration. However, there is an offset for both cases. While the absolute difference in the 0-10% burn duration is most likely associated with a missing flame ignition model, the differences in the 10-90% burn duration could be associated with discrepancies in the new flame geometry used for this higher compression ratio.

6.11.4 Plasmatron Enhancement

To model the effect of plasmatron reformate on the laminar flame speed, the correlations from Chapter 3 were used to apply a correction factor to the laminar flame speed for indolene. Based on figure 3-12, for an average temperature of 700K, and taking into account that the fuel used for these calculations is methane which has a higher baseline laminar flame speed than indolene, the correction factors applied were slightly higher. For 15% and 30% plasmatron enhancement, the flame speed was increased by 15% and 30% respectively. The comparison of

the simulations results, for the baseline compression ratio of 9.8:1, engine speed of 1500 rpm, and load of 3.5 bar NIMEP are shown in figures 6-15 and 6-16. The model-predicted trends are good, but the absolute improvement in the 0-10% burn duration is not accurately captured. Once again, this is attributed to the missing flame ignition model, where hydrogen enhancement and higher laminar flame speed will play a significant effect. The discrepancy shown in figure 6-15 is due to the very early stage of combustion (0-2% and 0-5%), as was previously indicated in table 6.2. Other effects such as flame curvature and flame stretch are not ruled out, although they are unlikely based on the conclusions from research done at Northeastern University [7], where laminar flame speed measurements in combustion bombs, under engine like conditions, have not shown flame stretch effects. On the other hand, the flame propagation portion, as depicted by the 10-90% burn duration comparison in figure 6-16 is excellent, showing that the physics of the model, with the exception of the very early stages of combustion, is well captured. The improvement from hydrogen enhancement is simply the consequence of a higher laminar flame speed.

6.11.5 Tau burn & Tau delay Comparison of Characteristic Times (Rashidi-Keck Method)

The Figure 6-17 and 6-18 compare the model predictions using the inflection point method from Rashidi and Keck, as discussed in section 6.8. Similar to figures 6-9 and 6-10, where the exact same model conditions were used, the agreement with the data is very good. As previously explained, this method could be a better way to compare the model against the data, but due to the standard conventions for analyzing combustion intervals, the burn duration approach is used.

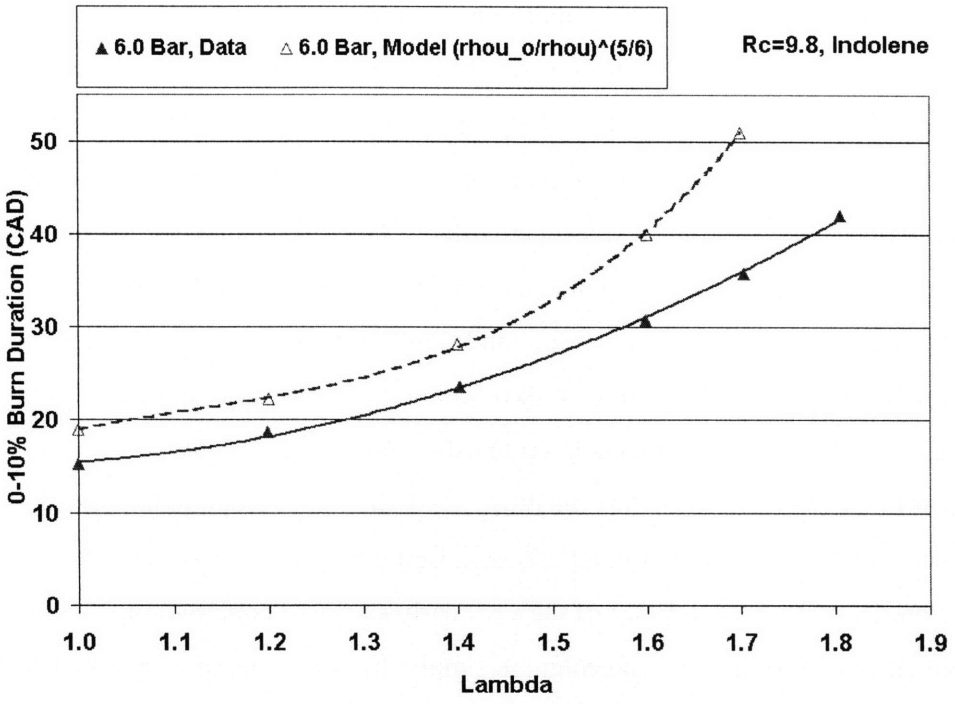

Figure 6-11 – Comparison of 0-10% burn durations with air dilution for model and data; MBT timing, 1500 RPM, r_c=9.8:1, NIMEP = 6.0 bar, indolene, 5/6 model microscale dependence on density ratio

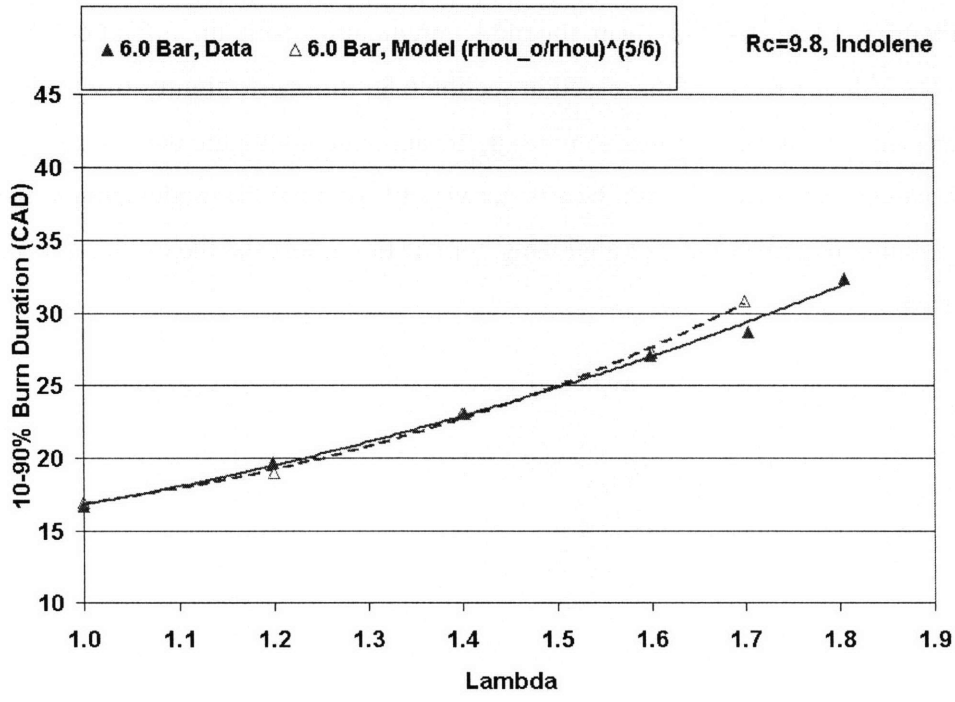

Figure 6-12 – Comparison of 10-90% burn durations with air dilution for model and data; MBT timing, 1500 RPM, r_c=9.8:1, NIMEP = 6.0 bar, indolene, 5/6 model microscale dependence on density ratio

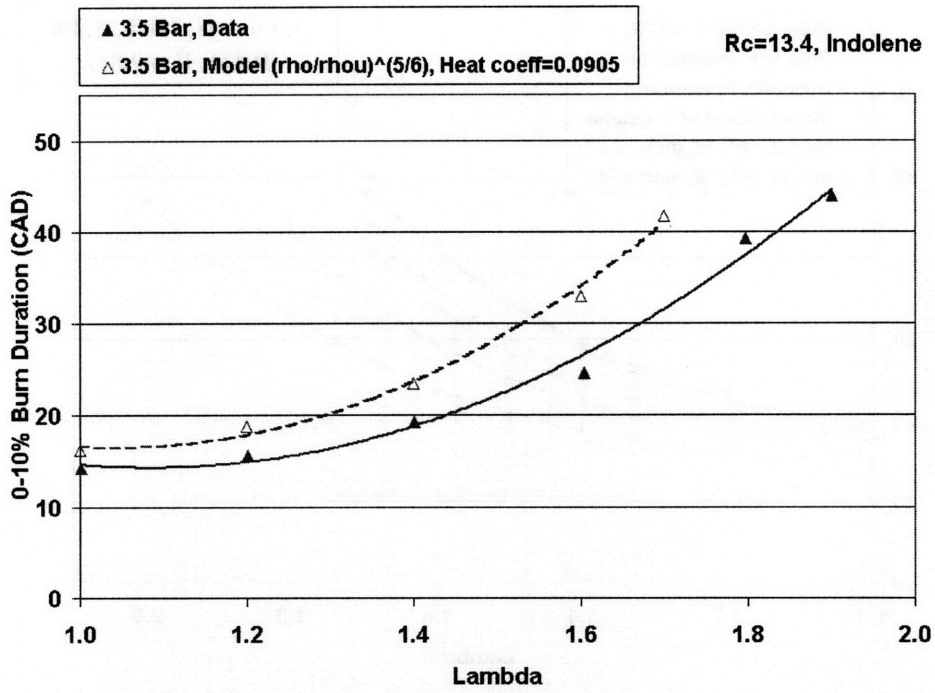

Figure 6-13 – Comparison of 0-10% burn durations with air dilution for model and data; MBT timing, 1500 RPM, r_c=13.4:1, NIMEP = 3.5 bar, indolene, 5/6 model microscale dependence on density ratio

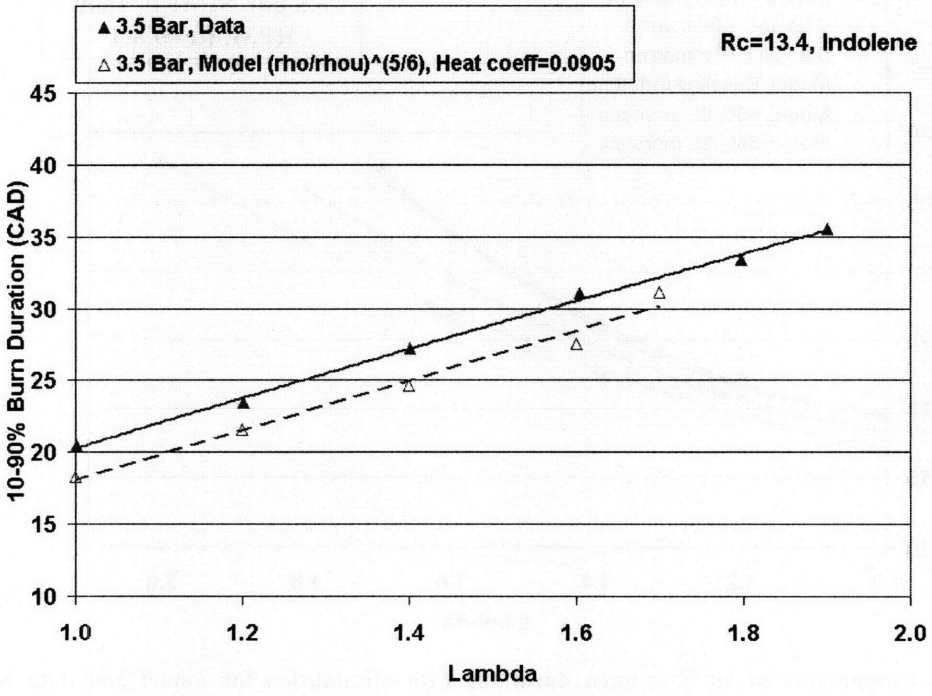

Figure 6-14 – Comparison of 10-90% burn durations with air dilution for model and data; MBT timing, 1500 RPM, r_c=13.4:1, NIMEP = 3.5 bar, indolene, 5/6 model microscale dependence on density ratio

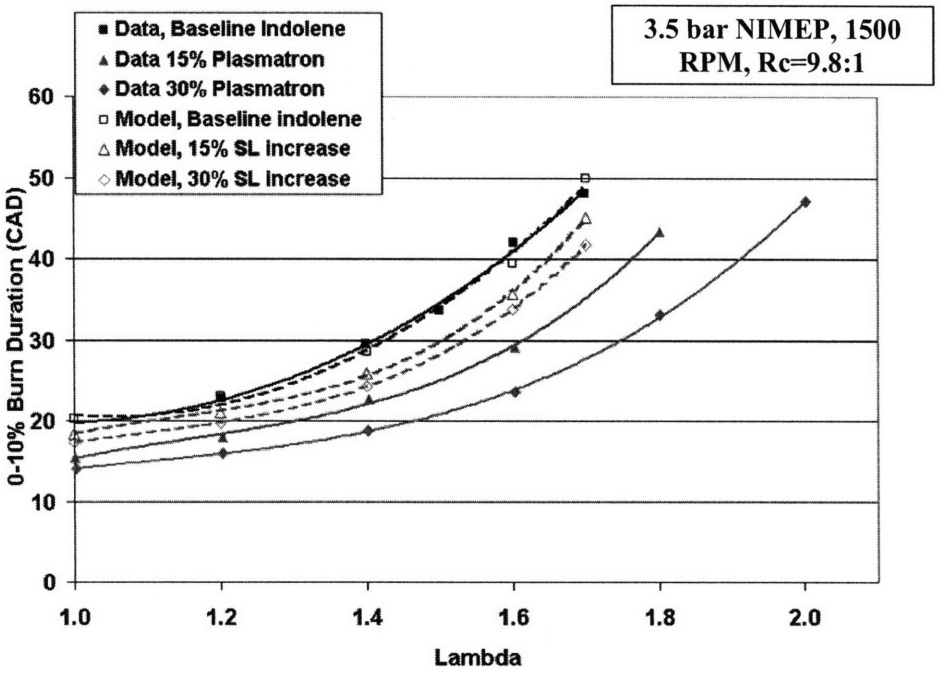

Figure 6-15 – Comparison of 0-10% burn durations with air dilution for model and data for various amounts of plasmatron enhancement; MBT timing, 1500 RPM, r_c=9.8:1, NIMEP = 3.5 bar, indolene, 5/6 model microscale dependence on density ratio

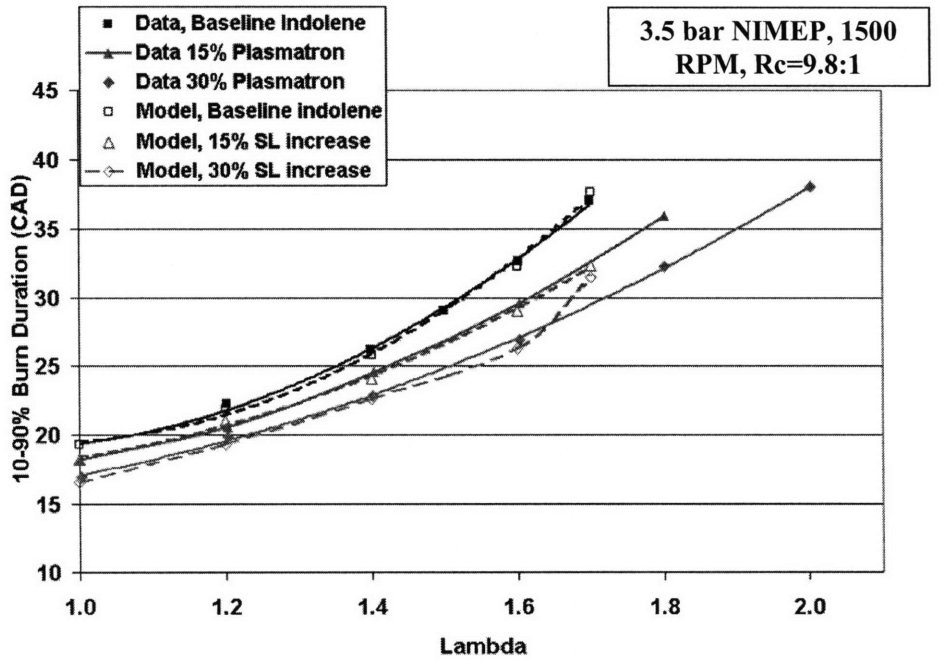

Figure 6-16 – Comparison of 10-90% burn durations with air dilution for model and data for various amounts of plasmatron enhancement; MBT timing, 1500 RPM, r_c=9.8:1, NIMEP = 3.5 bar, indolene, 5/6 model microscale dependence on density ratio

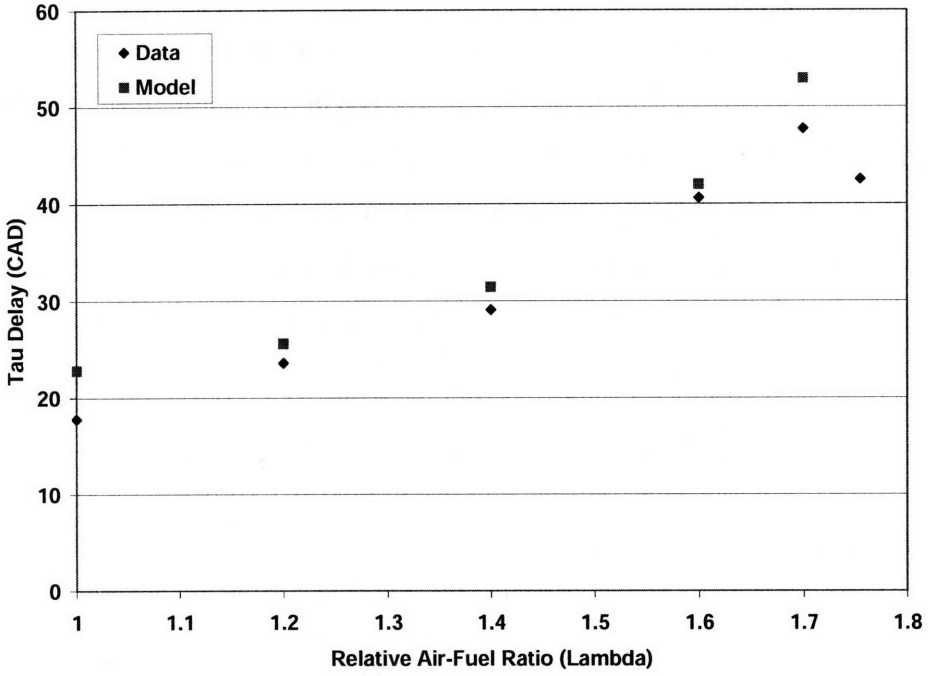

Figure 6-17 – Comparison of Tau delay with air dilution for model and; MBT timing, 1500 RPM, r_c=9.8:1, NIMEP = 3.5 bar, indolene, 5/6 model microscale dependence on density ratio

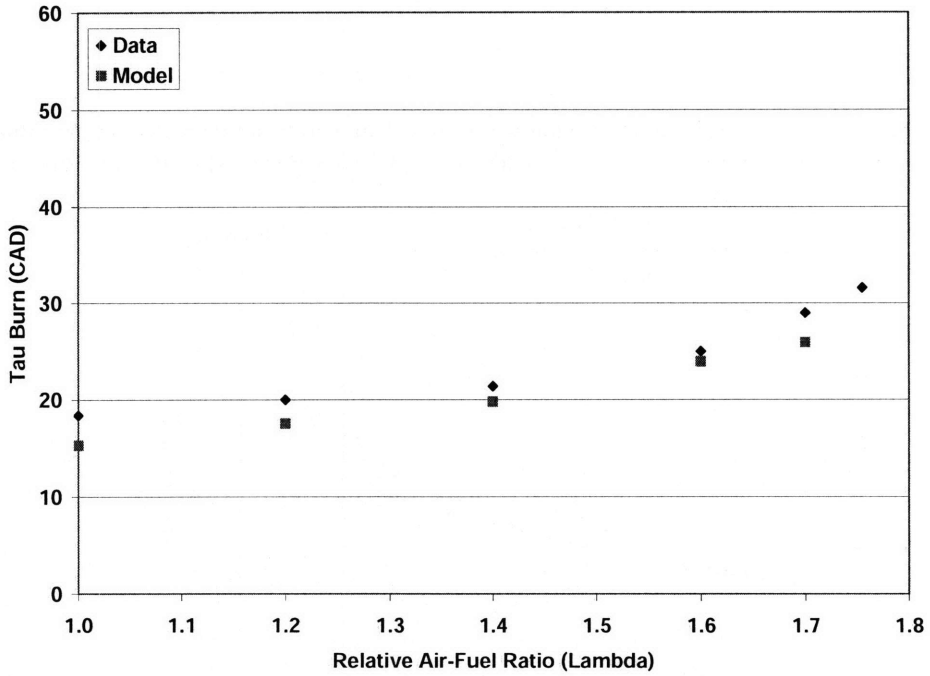

Figure 6-18 – Comparison of Tau delay with air dilution for model and; MBT timing, 1500 RPM, r_c=9.8:1, NIMEP = 3.5 bar, indolene, 5/6 model microscale dependence on density ratio

6.12 Model Criticality: SL becomes zero

As shown in the next two charts, the model will "break down" when the laminar flame speed becomes zero. As shown in Chapter 3 (Fig. 3-2), this will occur around λ=1.95. Before this occurs, the burn durations will rapidly increase because the laminar flame speed is decreasing and the model eddy-burning time is dependent on the inverse of the laminar flame speed. Figures 6-19 and 6-20 show a comparison of the model and the data at these extreme conditions. Data was only taken until λ~1.76; beyond this point, the engine began to misfire.

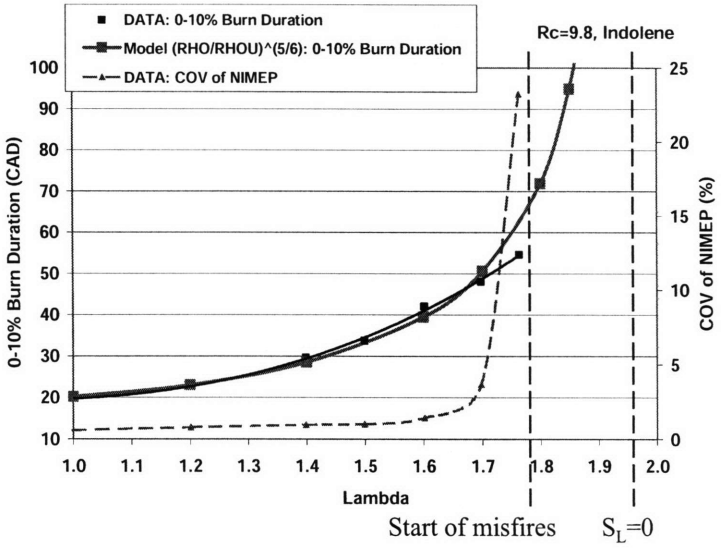

Figure 6-19 – Comparison of 0-10% burn duration for model and data under extreme conditions; MBT timing, 1500 RPM, r_c=9.8:1, NIMEP = 3.5 bar, indolene, 5/6 model microscale dependence on density ratio

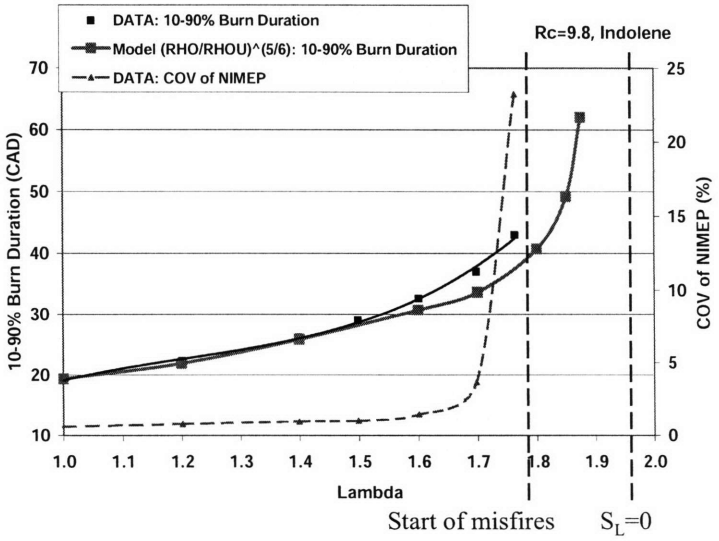

Figure 6-20 – Comparison of 0-10% burn duration for model and data under extreme conditions; MBT timing, 1500 RPM, r_c=9.8:1, NIMEP = 3.5 bar, indolene, 5/6 model microscale dependence on density

Chapter 7 – FUNDAMENTAL ASPECTS OF VARIABILITY IN LEAN COMBUSTION

7.1 Introduction: Variability During Flame Initiation

In chapter 4, the topic of combustion variability was explored. The rapid rise in combustion variability at a critical 0-10% burn duration was identified, as well as the transition to an asymmetrical change of the 10-90% burn duration, and the NIMEP distributions. The various pieces of variability were then connected based on the experimental observations, but the fundamental questions behind the behavior of variability remained unanswered. This chapter addresses these more fundamental questions through combustion modeling and analyses.

The rate at which mass burns in the combustion chamber is primarily determined by the rate of mixture entrainment into the turbulent propagating flame front, and by the rate of local burning as defined by the time to burn the turbulent eddies. Variability in the rate of entrainment, and the time to burn eddies, will therefore cause variability in the rate at which mass is burned. Going one step further, this means that variability in the phenomena that govern and affect both the rate of mass entrainment and the rate of eddy burn-up will lead to combustion variability. Thus, the main sources of combustion variability include variability in the turbulence intensity, variability in the laminar flame speed, variability in the turbulence microscale, variability in flame area and wall interactions, and variability in the location of the flame center. Variability in the turbulence intensity, microscale, and laminar flame speed will play a role throughout the entire combustion process, while variability in the flame/wall interactions becomes important as the flame is more developed. Variability in the flame center location will be the highest early in the combustion process, when the flame is small, affecting the initial laminar flame speed [40, 41]. The effect from this offset center becomes important again when the flame is near the walls, as explained in section 7-8.

As the turbulent flame develops, variability in the eddy-burning time[4] is the main source of combustion variability. During the early stages of combustion, the developing turbulent flame already exhibits a microscale structure of the same magnitude as the Taylor microscale. Smith took schlieren photographs (Fig. 7-1) at various time intervals during flame initiation, and showed that at 0.07 mseconds (0.25 CAD @ 600 rpm), a microscale structure was already present, with a spectrum of sizes varying with time [39]. Additionally, changes in laminar flame

[4] Eddy-burning time was defined in Chapter 4 as the ratio of the turbulence microscale to the laminar flame speed.

speed during early flame development can be significant, as shown by Psichinger and Heywood [40, 41]. Other sources of variability during this stage of combustion, such as variations in the flame center location (aside from its effect on laminar flame speed), or flame/wall interactions, will not yet affect the combustion process; Consequently, early combustion variability will be mostly affected by changes in the turbulence microscale and in the laminar flame speed, which determine the eddy-burning time.

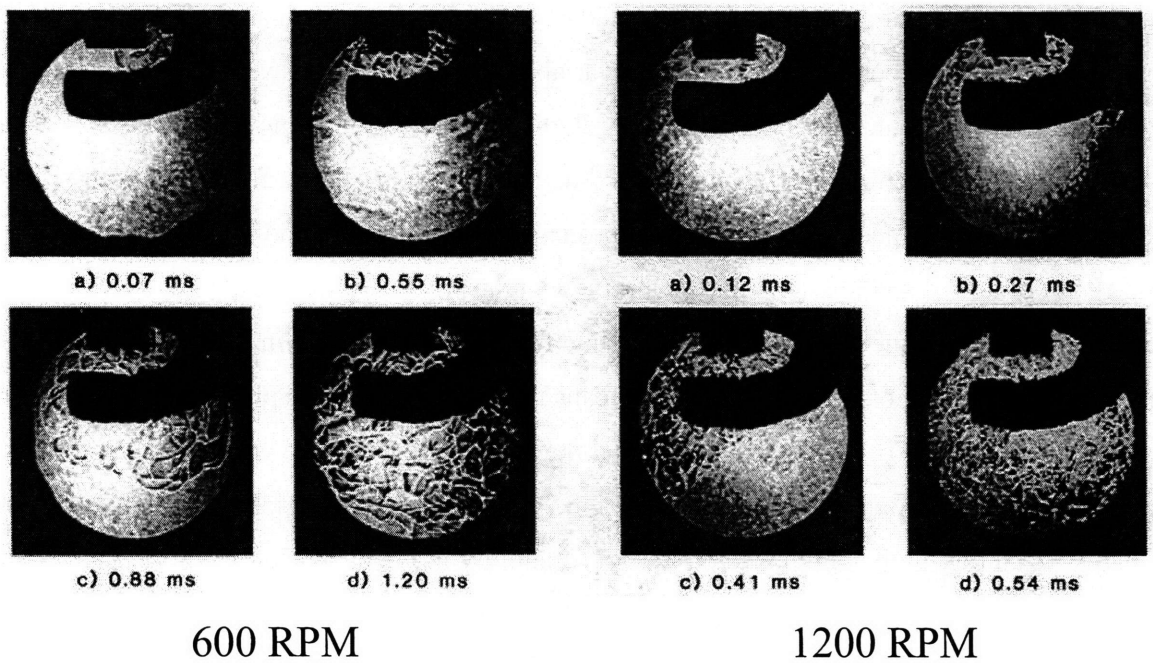

Figure 7-1 – Turbulence structure shortly after ignition for two different engine speeds [39]

7.2 Previous Work on Initial Variability

The problem of initial combustion variability has been studied in the past. In his work, Hill concluded [42, 43] that the initial variability in the combustion process is proportional to the size of the ratio of the microscale to the laminar flame speed, as shown below:

$$\sigma_{\text{early burn duration}} = \frac{\lambda}{4S_L} \tag{7-1}$$

In this equation, $\sigma_{\text{early burn duration}}$ is the variability in the early/initial mass burning time, or burn duration (i.e., the cyclic variation in the earliest burning times). This expression has the same form as the eddy-burning time defined in MIT's flame entrainment model. Using this model, a similar variability expression has been derived as shown later in this chapter. Hill also plotted the standard deviation in the combustion process, starting around 10% mfb, where he could

safely assume that he had an accurate calculation of the mass burned. His data is shown in figure 7-2 below. Hill then extrapolated the y-intercept of this curve, and assumed this to be the variability during the early burning stage. He found a good correlation between this extrapolated variability, and that calculated using equation 7-1. Hill then explained how the variability increased linearly with burn duration due to "random heat transfer interactions between the chamber wall and the growing flame kernel." This last conclusion is not correct. While his results did agree with the existence of initial combustion variability, Hill did not develop an appropriate explanation to connect this initial variability with the variability in the rest of the combustion process. This explanation is important to understand why variability in the main part of the combustion process (i.e., the 10-90% mfb) becomes fairly asymmetrical for highly diluted conditions, as shown in Chapter 4 (Figs. 4-16 and 4-17). Additionally, beyond the 50% mfb point, variability, as defined by figure 7-2, is not linear anymore, particularly for lean conditions. This data was left out of figure 7-2 perhaps due to a lack of a plausible explanation. The work presented in this chapter provides an explanation for how initial combustion variability affects the variability for the entire combustion process, why variability in the main combustion stage becomes so asymmetrical, and why variability in general increases with leaner mixtures.

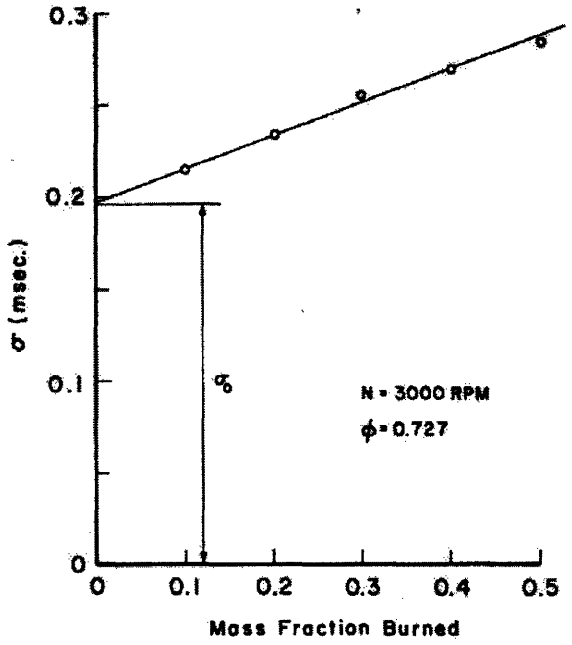

Figure 7-2 – Standard deviation in burn duration as the mass fraction burned increases; from Hill [42]

7.3 Initial Variability and Combustion Phasing

Simulations using MIT's flame entrainment model in conjunction with detailed analyses of engine data under various conditions, show that the initial variability in the eddy-burning time (due to variability in microscale and laminar flame speed) is the leading factor that causes variability throughout the entire combustion process.

7.3.1 Analysis using experimental data

Using MIT's data at stoichiometric conditions, figure 7-3 shows a similar curve to the one Hill showed (Fig. 7-2). The trend in both cases agrees. Variability increases linearly due to differences in combustion phasing, particularly, differences in the 50-90% burn duration, as will be later explained. To better understand why this occurs, it is important to study figure 7-4. This figure shows a comparison between three cycles taken out of the set of 300 cycles that make up figure 7-3. The three different burning profiles were selected to show the differences caused by changes in combustion phasing. Out of the three cycles, the center curve is representative of an optimum-burning cycle, as indicated by a higher NIMEP. Each of the outer curves has the same, but opposite, difference in 0-10% burn duration relative to the center curve (3 CAD). The curve to the right has a longer 0-10% burn duration, and the one to the left has a shorter 0-10% burn duration. Variability in the eddy-burning time is largely responsible for this variability in the 0-10% burn duration. All else equal, cycles with longer microscales and/or slower laminar flame speeds, will take a longer time to burn the initial eddies, than cycles with shorter microscales and/or faster laminar flame speeds. This results in a longer flame initiation for some cycles, and a shorter initiation for others; that is, it will take longer or shorter to burn the first few percentages of the mass, depending on the relative magnitude of the eddy-burning time. This difference in flame initiation (0-10% for simplicity) causes differences in the initial burning conditions for the remaining 90% of the mass, for each of the three curves shown. Aside from the differences in microscale and laminar flame speed, each of the curves begins the burn up of the remaining 90% of the mass at a different initial pressure, temperature, and crank angle; these initial differences will exacerbate the differences in the laminar flame speed and turbulence characteristics with time. Additionally, differences in density, flame geometry, and flame area will also grow. Consequently, as more mass is burned, the outside curves will develop differently relative to the center curve. Because the subsequent pressure and temperature

depends on the previous conditions, both curves will continue to follow a different path, or different burning profile. As more mass is burned, the difference relative to the center curve increases, since the previous time history of the thermodynamic properties will affect the present and future states; for example, a mixture burning at a slower laminar flame speed, relative to the other cycles, due to a given combination of pressure and temperature, will continue to burn more slowly, increasing the spread in burn duration relative to the faster-burning curves. This is reflected in figure 7-4 where the spread of the "retarded" outer curve relative to the center curve, increases from 3 CAD at 10% mfb, to 5 CAD at 85% mfb. This is the reason for why figures 7-2 and 7-3 show an increase in variability with mass fraction burned. In particular, combustion differences across the different cycles will grow at a larger rate after the 50% mass fraction burned point during the early part of the expansion stroke, where pressure and density changes are large. This deviation is not obvious for fast-burning stoichiometric mixtures, where the initial spread in 0-10% burn durations is small, but becomes more important for slower burning lean mixtures as will be seen later in this chapter. In fact the spread in the 50-90% mfb accounts for close to 90% of the observed spread in the 10-90% mfb.

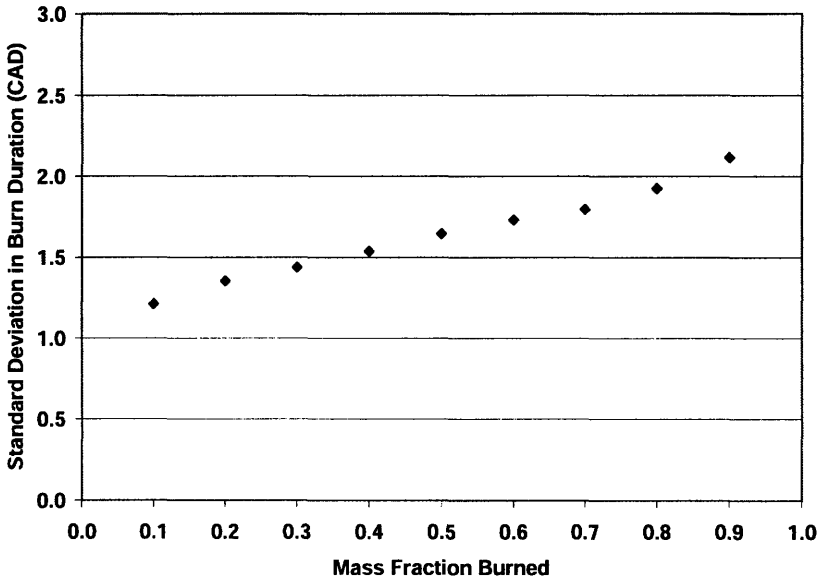

Figure 7-3 – Standard deviation of burn duration as the mass fraction burned increases; MBT timing, 1500 RPM, r_c=9.8:1, NIMEP = 3.5 bar, λ=1.0

Figure 7-5 shows the average of sets of curves with the same 0-10% burn duration for the same 300 cycles at stoichiometric conditions. Essentially, all the individual burning profiles with the same 0-10% burn duration have been grouped and averaged, to produce one representative

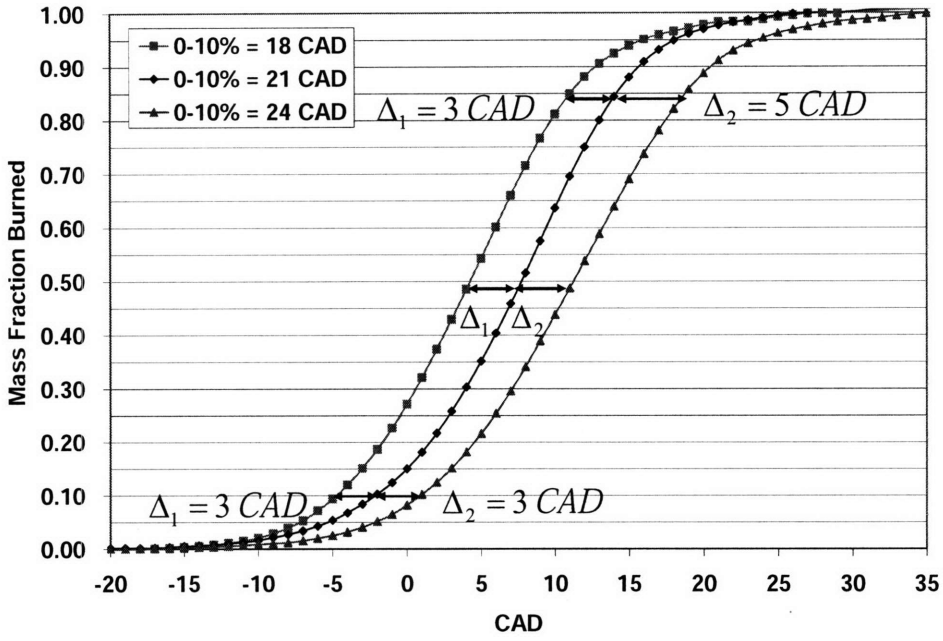

Figure 7-4 – Time history of spread in burn duration among three curves, optimum, retarded, advanced; outer curves differ by +/- 3 CAD in 0-10% burn duration relative to center curve; 1500 RPM, r_c=9.8:1, NIMEP = 3.5 bar, λ=1.0

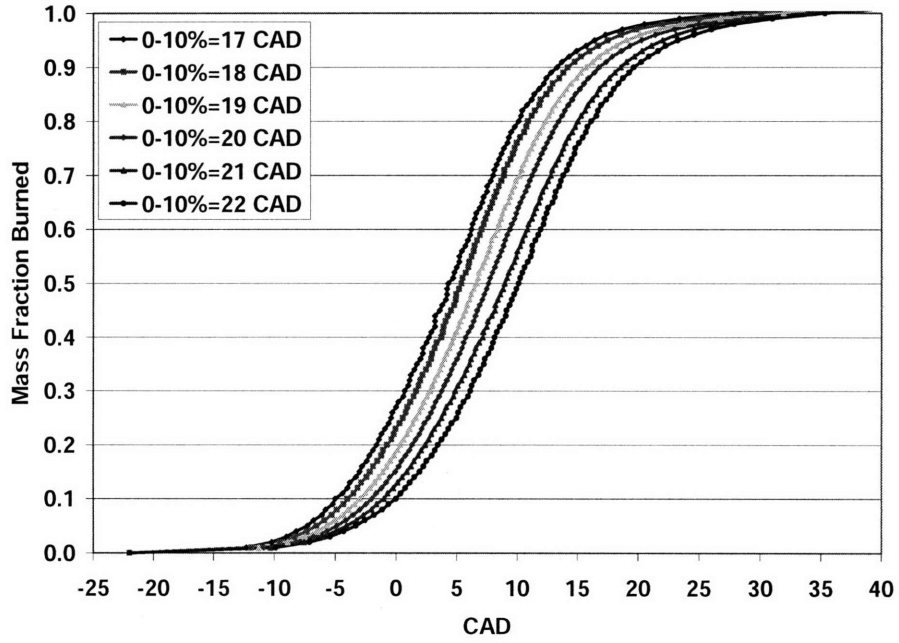

Figure 7-5 – Comparison of average burning profiles with different 0-10% burn duration; MBT timing, 1500 RPM, r_c=9.8:1, NIMEP = 3.5 bar, λ=1.0

burning profile. The data is well behaved and shows a distribution of curves about an optimum center curve which has a 0-10% burn duration between 19 and 20 CAD. This is consistent with the 0-10% burn duration distribution of all 300 cycles making up each point, for the stoichiometric case, shown in figures 7-13 and 7-14.

The following four tables (7.1 through 7.4) show how the three data curves shown in figure 7-4 compare in terms of their burn durations and NIMEP, as well as the chamber conditions at three different mass fraction burned points. The pressures were experimentally measured, the unburned temperature was calculated by assuming isentropic compression of the unburned gas, and the laminar flames speeds were calculated with the Rhodes-Keck correlations.

Curve	0-10% (CAD)	10-90% (CAD)	NIMEP (bar)
Advanced Curve	18	24	3.50
Optimum Phasing	21	22	3.56
Retarded Curve	24	25	3.52

Table 7.1 – Comparison of the 0-10% and 10-90% burn durations and the NIMEP for the individual cycles shown in figure 7-4; 1500 RPM, r_c=9.8:1, NIMEP = 3.5 bar, λ=1.0

Mass fraction burned = 0.10

Curve	CA	Pressure (bar)	Temperature (K)	SL (cm/sec)
Advanced Curve	-5	11.3	799.4	67.5
Optimum Phasing	-2	11.5	802.4	67.8
Retarded Curve	1	11.4	801.7	66.3

Table 7.2 – Comparison of the characteristics among the three curves from figure 7-4 for mass fraction burned (mfb) of 10%; 1500 RPM, r_c=9.8:1, NIMEP = 3.5 bar, λ=1.0

Mass Fraction burned = 0.50

Curve	CA	Pressure (bar)	Temperature (K)	SL (cm/sec)
Advanced Curve	4	20.8	913.5	78.5
Optimum Phasing	8	20.3	908.9	78.1
Retarded Curve	11	18.4	890.0	76.3

Table 7.3 – Comparison of the characteristics among the three curves from figure 7-4 for mass fraction burned (mfb) of 50%; 1500 RPM, r_c=9.8:1, NIMEP = 3.5 bar, λ=1.0

Mass fraction burned = 0.80

Curve	CA	Pressure (bar)	Temperature (K)	SL (cm/sec)
Advanced Curve	10	24.8	947.8	91.8
Optimum Phasing	13	23.2	934.8	80.6
Retarded Curve	17	18.1	911.2	78.3

Table 7.4 – Comparison of the characteristics among the three curves from figure 7-4 for mass fraction burned (mfb) of 50%; 1500 RPM, r_c=9.8:1, NIMEP = 3.5 bar, λ=1.0

7.3.2 Analysis using flame entrainment model, and comparison to data

To further verify this "initial phasing" explanation as the source of the observed variability in the later stages of combustion, MIT's flame entrainment model is now used. The effects of differences in combustion phasing, caused by variability during flame initiation, have been simulated by producing three different curves. The first curve is the result of running the code at MBT conditions for 1500 rpm, 3.5 bar NIMEP, relative air-fuel ratio of 1.0, and compression ratio of 9.8:1. To model the effect of longer and shorter 0-10% burn duration, all else equal, the spark timing was retarded and advanced, respectively, until the desired spread in 0-10% was produced. Although in reality when spark is retarded, the resulting curve will have a shorter 0-10% burn duration relative to an MBT curve, this curve will be offset to the right of the MBT curve, or "retarded", burning the same 0-10% charge at a later time. This essentially simulates a longer flame initiation, taking of course, the spark at MBT as the starting point for both curves. The opposite can be said of an "advanced" curve. The results are shown in figure 7-6 which shows a pair of curves with a symmetric initial spread in the 0-10% burn duration of +/- 2 CAD, about MBT. The trend is the same as shown in the real data (figures 7-4 and 7-5). As shown before, and similar to an initial value problem, the different initial conditions in the combustion process will lead to different burn profiles. These differences will continue to grow as more mass is burned, and the changes in pressure and temperature and laminar flame speed inside the chamber become greater.

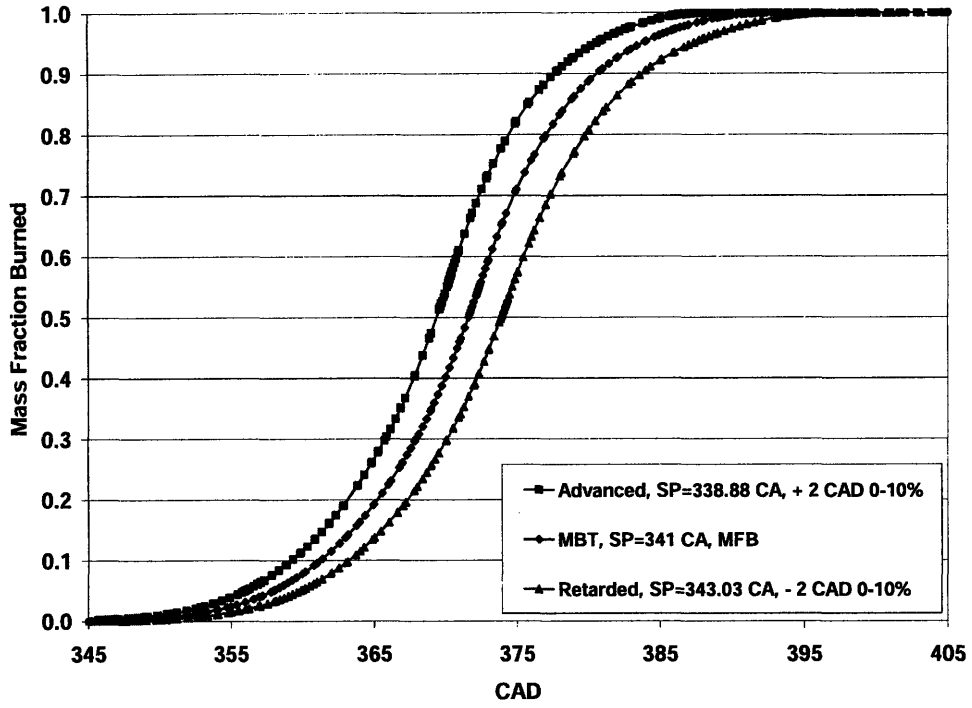

Figure 7-6 – Comparison of optimum, advanced, and retarded burning profiles (+/- 2 CAD 0-10% burn duration) produced with model; 1500 RPM, r_c=9.8:1, NIMEP = 3.5 bar, λ=1.0

Similar again to Hill's analysis, figure 7-7 plots the spread of the data for various cases. The middle curve (A) shows the standard deviation in the burn duration with increasing mass fraction burned, for all 300 cycles, as previously shown. The outer pairs of curves (top - B, and bottom - C) compare the spread across a set of three "average cycles" similar to the comparison done in figure 7-4. The term "average cycles" is used because, as previously explained, each of the three cycles compared (advanced, optimum, retarded) is an average of all the cycles with the same 0-10% burn duration. As already mentioned Figure 7-5 shows these well-behaved "average cycles." The spread is defined as follows:

$$\delta_{spread} = \frac{\Delta_1 + \Delta_2}{2} \tag{7-2}$$

In eq. 7-2, Δ_1 and Δ_2 indicate the absolute difference between the advanced cycle and the MBT cycle at a given burn duration, and the difference between the retarded cycle and the MBT cycle at the same burn duration, respectively, as shown in figure 7-4. This definition of spread allows for a direct comparison with the standard deviation of the 300 cycles, since by dividing by 2,

each cycle (advanced and retarded) is given the same weight, as occurs in the definition of standard deviation, where the data (in this case the cycles) are weighted by their frequency.

In figure 7-7, both model and data are compared for two different cases, sets of cycles with an initial 0-10% burn duration spread of 1 CAD on each side (bottom pair of curves - C), and sets of cycles with an initial 0-10% burn duration spread of 2 CAD (top pair of curves - B). Similar to the middle curve (A), encompassing all 300 cycles, and as pointed out by Hill, the outer curves (C and B) rise up fairly linearly, becoming slightly non-linear towards the later part of combustion. This shows that the increasing spread in the data is systematic, not random, and is due to phasing differences, as has already been explained. The phasing differences are in fact caused by random but symmetric variability in flame initiation, shown in the distributions of figures 7-13 and 7-14. But the differences beyond the 10% mfb point clearly have an explanation; they are caused by a specific and well-behaved mechanism, rather than a random process.

Another point to notice is the fact that the full 300 cycle curve lies between the +/-2 CAD in 0-10% burn duration curves and the +/-1 CAD in 0-10% burn duration curves. This is expected considering that the standard deviation of the 300 cycles will weight all cycles equally. Therefore, this curve could not start at a standard deviation of 1 CAD for 10% mass fraction burned, since there will be a distribution of cycles about the optimum phased curve, ranging in spread of 0-10% burn duration from 0 to 3 CAD. If the model is run 300 times, simulating each cycle and producing the actual 0-10% burn duration distribution from the data, the resulting standard deviation curve will be very close to curve A shown in figure 7-7.

Having shown that the model does a good job at explaining the data, and simulating the actual physics, it can further be used to understand in more detail the effect of phasing on increasing the spread/variability in the curves. Looking in more detail at the physics of the combustion process, figure 7-8 shows the time history of the eddy-burning time and of the mass burning profile for the three simulation cycles shown in figure 7-6 with an initial 0-10% burn duration spread of +/-2 CAD. The chart shows how the advanced curve has the lowest initial eddy-burning time out of the three cycles, while the retarded curve has the highest eddy-burning time. The details behind these eddy-burning times are shown in figures 7-9 and 7-10 which plot the turbulence microscale and the laminar flame speed, respectively. The retarded cycle shows a

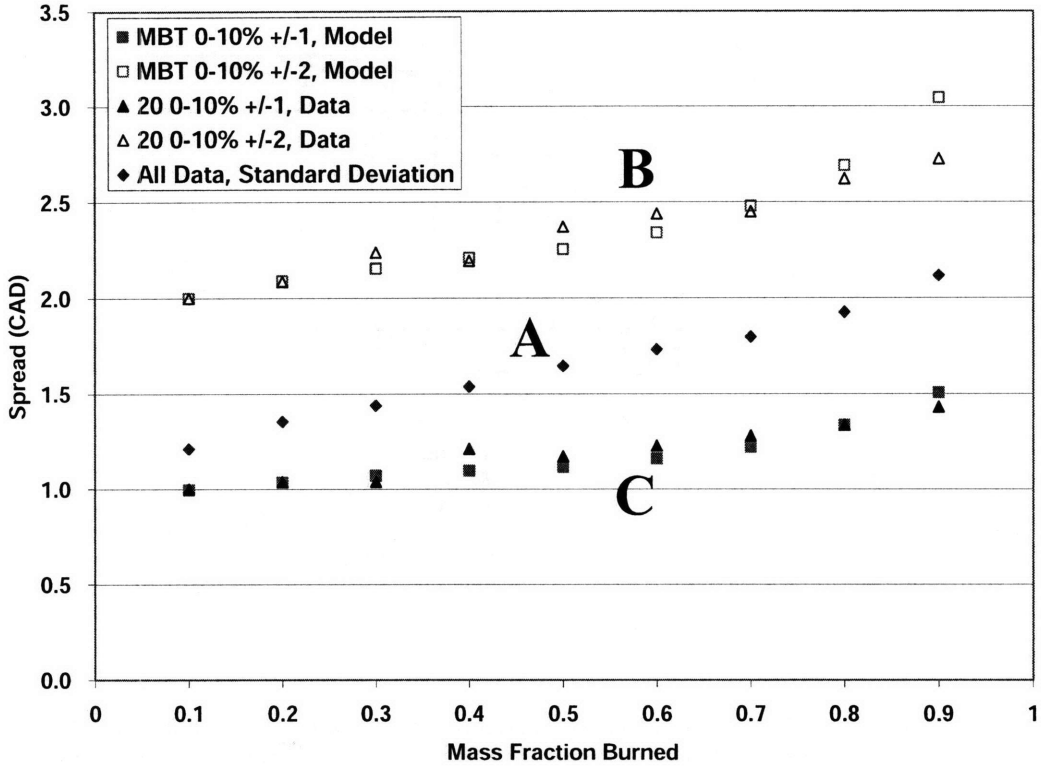

Figure 7-7 – Comparison of spread in burn duration with increasing mass fraction burned for two model and data comparisons (+/- 1 and +/- 2 CAD 0-10% burn duration) and for all 300 cycles; 1500 RPM, r_c=9.8:1, NIMEP = 3.5 bar, λ=1.0

larger microscale. This forces a slower burning, which causes a slower rise in cylinder pressure and temperature. Consequently, the laminar flame speed will also be lower for the retarded cycle. This creates a reinforcing effect. The retarded cycle will continue to have a longer eddy-burning time, and the pressure and temperature will continue to increase at a slower rate, causing a slower laminar flame speed. The opposite can also be said of the advanced cycle. This is essentially an "integration" effect, where the history of each previous element of mass burned will affect the final state. The result is that the burning profiles will continue to diverge with time. For each cycle, the same percentage of mass will be burned at a different time, based on the eddy-burning time of each cycle. As will be seen in later sections, these effects become greater with higher initial burn duration spread, and slower-burning mixtures.

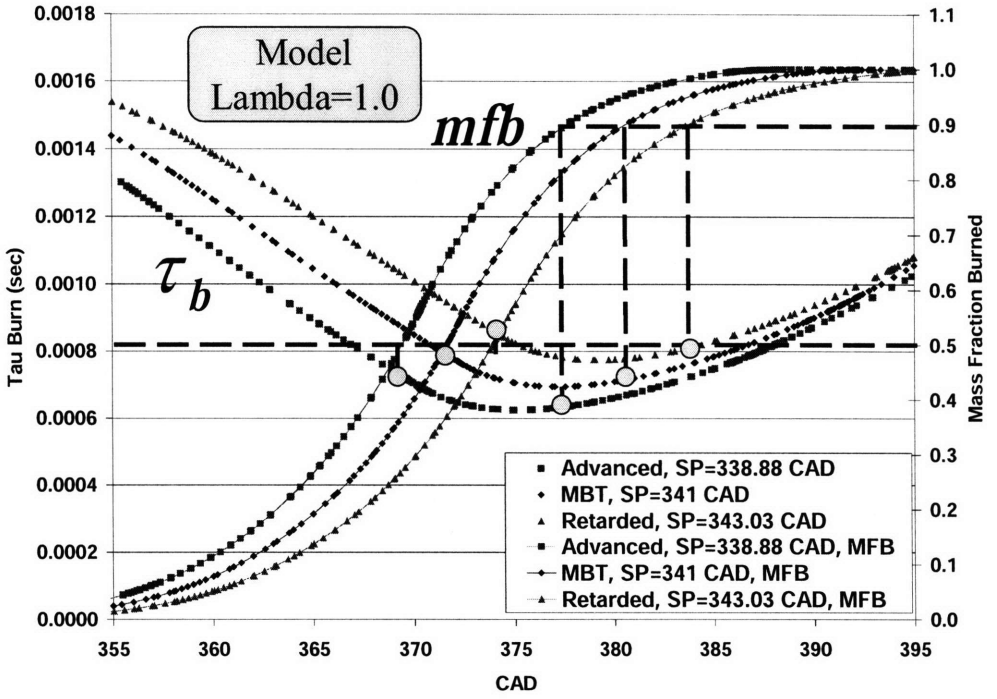

Figure 7-8 – Model Time history of eddy-burning time and mass fraction burned for optimum, retarded, and advanced curves (+/- 2 CAD in 0-10% burn duration); 1500 RPM, r_c=9.8:1, NIMEP = 3.5 bar, λ=1.0

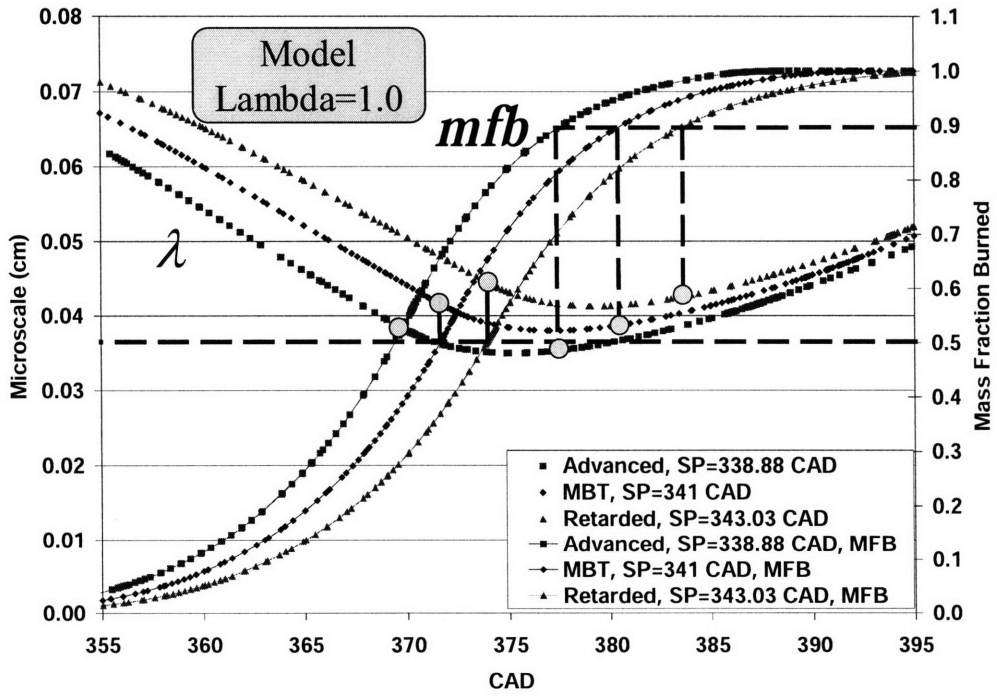

Figure 7-9 – Model Time history of microscale and mass fraction burned for optimum, retarded, and advanced curves (+/- 2 CAD in 0-10% burn duration); 1500 RPM, r_c=9.8:1, NIMEP = 3.5 bar, λ=1.0

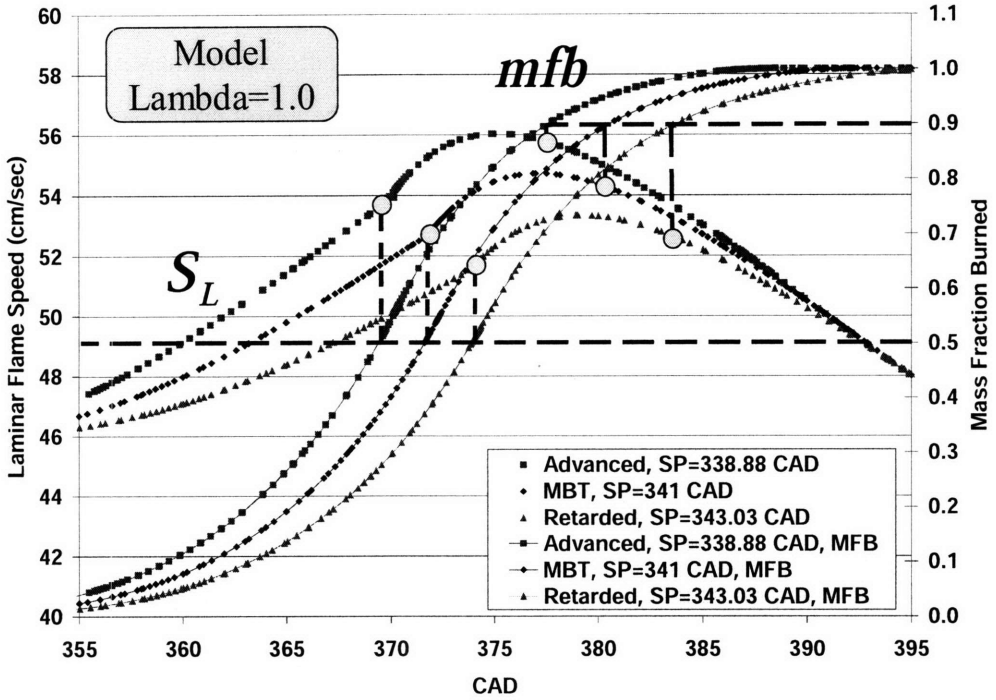

Figure 7-10 – Model Time history of laminar flame speed and mass fraction burned for optimum, retarded, and advanced curves (+/- 2 CAD in 0-10% burn duration); 1500 RPM, r_c=9.8:1, NIMEP = 3.5 bar, λ=1.0

7.4 Variability in Lean Combustion

Engine experiments show how combustion variability increases as the mixture becomes leaner. Figure 4-9 showed how variability occurs throughout the entire combustion process (0-10% and 10-90% burn durations), causing variability in NIMEP. Variability steadily increases with increasing relative air-fuel ratio, in a stable manner. Beyond the lambda for peak efficiency, when the 0-10% burn duration is close to a value of 40 CAD, variability rises very rapidly. The data also shows (figures 7-13 and 7-14) that even though variability during flame initiation (0-10% burn duration) increases with dilution, its distribution remains fairly symmetrical; on the other hand, the variability of the 10-90% burn duration, and the variability in NIMEP, not only increases but also becomes asymmetrical for highly lean mixtures (relative air-fuel ratio ~1.7).

Combustion modeling is again useful to try to understand the source of these two effects, an increasing variability with dilution and what seems to be a critical point where variability of 10-90% burn duration and NIMEP increases rapidly and becomes asymmetrical. As previously discussed, MIT's flame entrainment model does a fairly good job at predicting the real data for various different conditions, indicating that the physics of the process is properly modeled. Thus, a starting point to understand combustion variability and how it changes with air dilution is to understand the variability in the physics behind the model. Based on the relative magnitude of the terms in the entrainment model equations, there are two components that if perturbed can cause significant changes to the burn rate equations. These are the time to burn an eddy (τ_b), and the turbulence intensity (u'). While the turbulence intensity will depend on the cylinder conditions through the rapid distortion theory, its dependence on laminar flame speed, which is the main variable that changes as the mixture becomes dilute and combustion variability increases, will be weak. The time to burn an eddy encompasses the other two variables of the model, the microscale and the laminar flame speed, and thus, is directly affected by their variability. Its dependence on the laminar flame speed makes τ_b a more likely source for the observed combustion variability. Taking the differential of τ_b as defined in the entrainment model (eq. 6-3) we have:

$$\Delta\tau_b = \frac{\partial\tau_b}{\partial\lambda_{micrsc}}\Delta\lambda_{micrsc} + \frac{\partial\tau_b}{\partial S_L}\Delta S_L \qquad (7\text{-}3)$$

which simplifies to:

$$\Delta\tau_b = \left(\frac{1}{S_L}\Delta\lambda_{micrsc}\right) - \left(\frac{\lambda_{micrsc}}{(S_L)^2}\Delta S_L\right) \tag{7-4}$$

Variability due to microscale — Variability due to laminar flame speed

Assuming the microscale and laminar flame speed distributions are statistically independent, expression 7-4 is reduced to:

$$\Delta\tau_b = \sqrt{\left(\frac{1}{S_L}\Delta\lambda_{micrsc}\right)^2 + \left(\frac{\lambda_{micrsc}}{(S_L)^2}\Delta S_L\right)^2} \tag{7-5}$$

As noted above, the first half of the right side of eq. 7-4 is due to variability in the microscale, while the second half is associated with variability in the laminar flame speed. Through its dependence on the inverse of the laminar flame speed, this expression is similar to the initial variability expression derived by Hill (eq. 7-1). In fact, if the ratio of microscale to laminar flame speed is factored out of the equation, and if it is assumed that the variability of the microscale and laminar flame speed relative to their respective mean ($\Delta\lambda$, ΔS_L) is approximately constant, the resulting variability expression is almost identical to Hill's expression, differing only by a proportionality constant:

$$\Delta\tau_b = \frac{\lambda_{micrsc}}{S_L}\sqrt{\left(\frac{\Delta\lambda_{micrsc}}{\lambda_{micrsc}}\right)^2 + \left(\frac{\Delta S_L}{S_L}\right)^2} \approx \frac{\lambda_{micrsc}}{S_L}C \tag{7-6}$$

As previously discussed in chapter 6 (Figs. 6-19 and 6-20), the inverse dependence on laminar flame speed indicates that there will be a criticality, or point/region of rapid increase, in the time to burn eddies, as the laminar flame speed becomes sufficiently low. As seen above (eq. 7-5 and 7-6), this dependence on the laminar flame speed also means that the variability in the eddy-burning time will also have a criticality, or rapid change in behavior, determined primarily from

the magnitude of the laminar flame speed, as well as the magnitude of the microscale and laminar flame speed variations.

Figure 7-11 helps confirm the dependence of variability on the laminar flame speed, as defined by equations 7-1 and 7-6. The chart shows the percent change in the standard deviation of both the 0-10% burn duration and NIMEP, as a function of the laminar flame speed for a lean sweep at constant load of 3.5 bar, compression ratio of 9.8:1, 1500 rpm, and MBT conditions. The percent change in the ratio of the microscale to the laminar flame speed is also shown, which represents, to a first order, the behavior of the eddy-burning time variability, as already explained. Both the 0-10% burn duration variability and the NIMEP variability behave similar to the eddy-burning time variability. The curves rise slowly but steadily, and beyond a critical laminar flame speed of approximately 15 cm/sec, their variability increases rapidly. Again, this behavior is rooted in the inverse dependence of the eddy-burning time on the laminar flame speed. Figure 7-11 simplifies the dependence of the NIMEP and the 0-10% burn duration on the eddy-burning time. The variability in microscale and laminar flame speed as defined by eq. 7-5 has not been included; variability in the turbulence intensity, as well as other random fluctuations (e.g., flame center location and flame/wall interactions) has also been omitted. These other factors would tend to shift the exact location of the rapid increase in variability. Nevertheless, the reason for this rapid increase is clear. Section 7.10 studies a more integrated perturbation model.

Using the information from figure 7-11, it is now possible to explain the reason for the critical 0-10% burn duration of approximately 40 CAD, at the onset of rapid combustion instability as shown in Chapter 4. Figure 7-12 plots the 0-10% burn duration as a function of laminar flame speed at spark, for the same data conditions from figure 7-11. The graph shows that the critical laminar flame speed, of approximately 15 cm/sec, occurs within the observed critical 0-10% burn duration indicating that this burn duration is a consequence of the critical laminar flame speed. For the given turbulence characteristics and laminar flame speed during flame initiation, at the specified dilution level where the critical S_L occurs, the resulting 0-10% burn duration will be close to 40 CAD. Figure 7-12 shows some spread in the data for the different compression ratios. The spread seems systematic, suggesting that there could be differences in turbulence characteristics for the different compression ratios, yielding slightly different burn durations for a given laminar flame speed, or there could also be small

discrepancies with the Rhodes-Keck correlations, or how they were used here to calculate the laminar flame speeds. Either way, the trends are clear.

Reiterating the above findings, the average value of the 0-10% burn duration by itself, does not impact the variability of the 10-90% or the NIMEP. However, it is the changes (i.e. the spread) in the 0-10% burn duration, relative to the average, that cause the large and asymmetric variability in the 10-90% burn duration and in NIMEP for ultra lean conditions. At a 0-10% burn duration of around 40 CAD, the eddy-burning time variability is quite high, due to the low value of the laminar flame speed. As a result, the variability in the 0-10% burn duration is also large, but symmetric. This was confirmed by figures 7-13 and 7-14, which show well-behaved normal 0-10% burn duration distributions with an increasing spread (i.e. variability). As will be explained next, these symmetric, but large fluctuations in 0-10% burn duration, relative to the mean, cause the asymmetric variability in the 10-90% burn duration, and thus in NIMEP.

In essence, any source of combustion variability in the microscale or the laminar flame speed, even if small and constant across different relative air-fuel ratios, will be amplified as the relative air-fuel ratio increases, due to a decreasing laminar flame speed. Slow combustion amplifies the system variability.

A better approach to understanding the integrated effect of changes in any of the three variables, λ_{micrsc}, u', S_L, on the combustion process, is to perform complete simulations using MIT's entrainment model. This is shown in a later section. The important point that has been established in this section, is that early variability will show a rapid increase due to the inverse dependence of the eddy-burning time on laminar flame speed. From what was learned in the previous sections, this rapid increase in the flame initiation (0-10% burn duration) variability will cause variability in the 10-90% burn duration and thus variability in NIMEP. The next question to address is why the 10-90% and NIMEP distributions become so asymmetric.

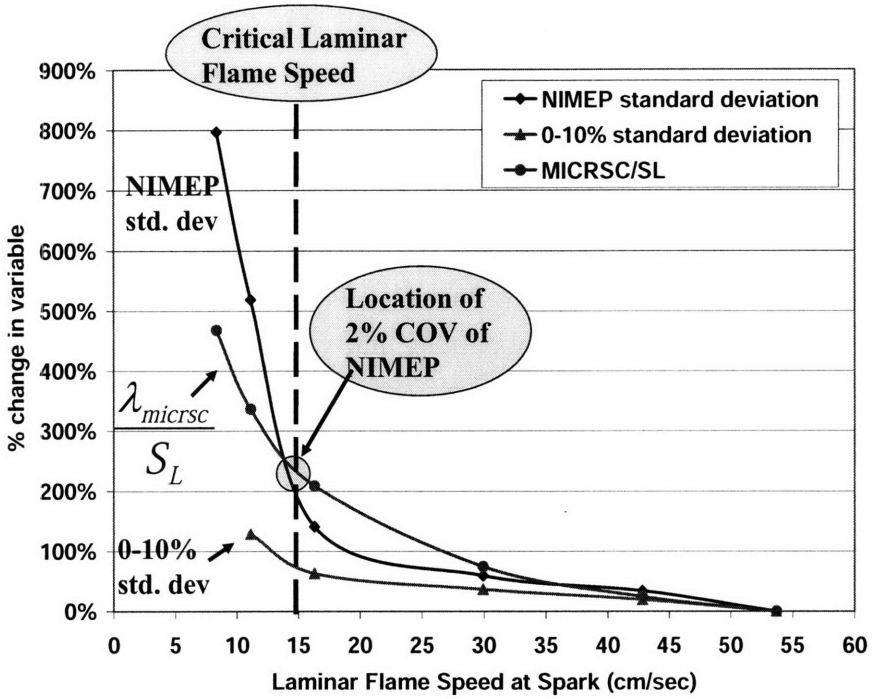

Figure 7-11 – Percent change in the standard deviation of 0-10% burn duration, in the standard deviation of NIMEP, and in the eddy-burning time with changes in the laminar flame speed; MBT timing, 1500 RPM, r_c=9.8:1, NIMEP = 3.5 bar

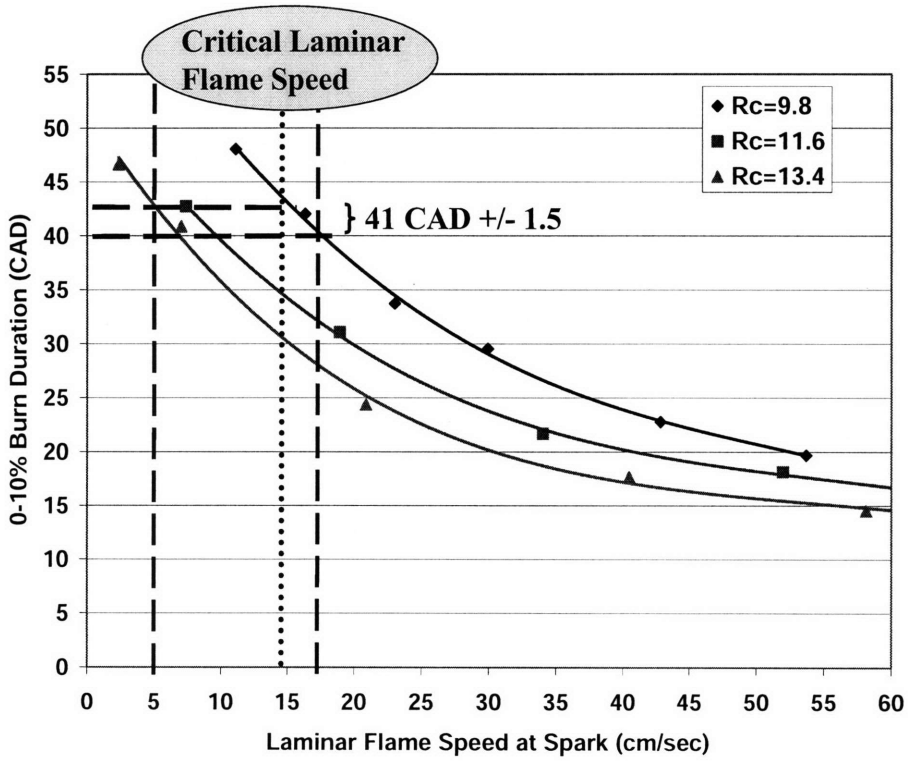

Figure 7-12 – Effect of laminar flame speed on the 0-10% burn duration for different compression ratios; MBT timing, 1500 RPM, NIMEP = 3.5 bar

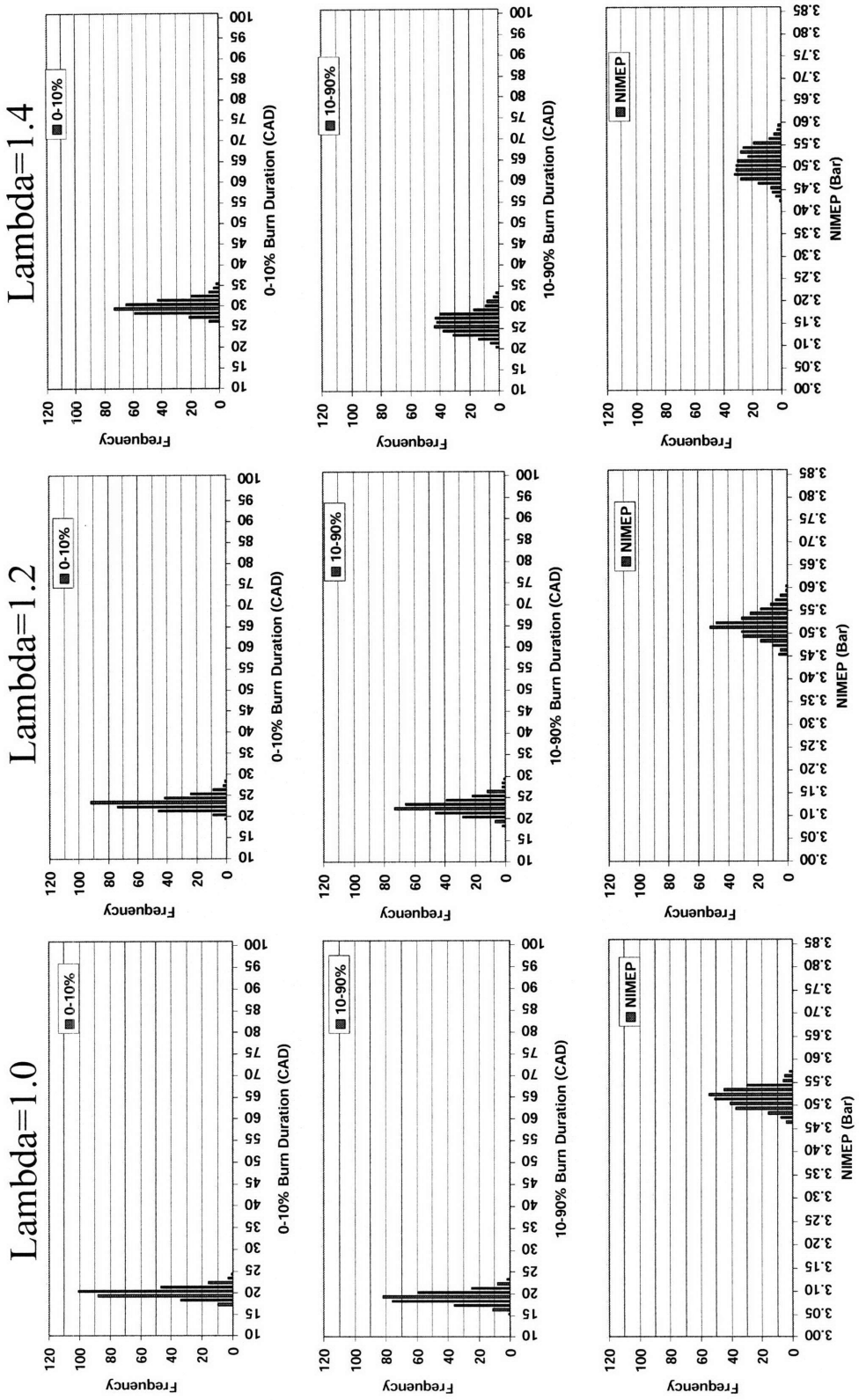

Figure 7-13 – Distribution of 0-10% and 10-90% burn durations, and NIMEP; λ=1.0, 1.2, 1.4; MBT timing, 1500 RPM, r_c=9.8:1, NIMEP = 3.5 bar

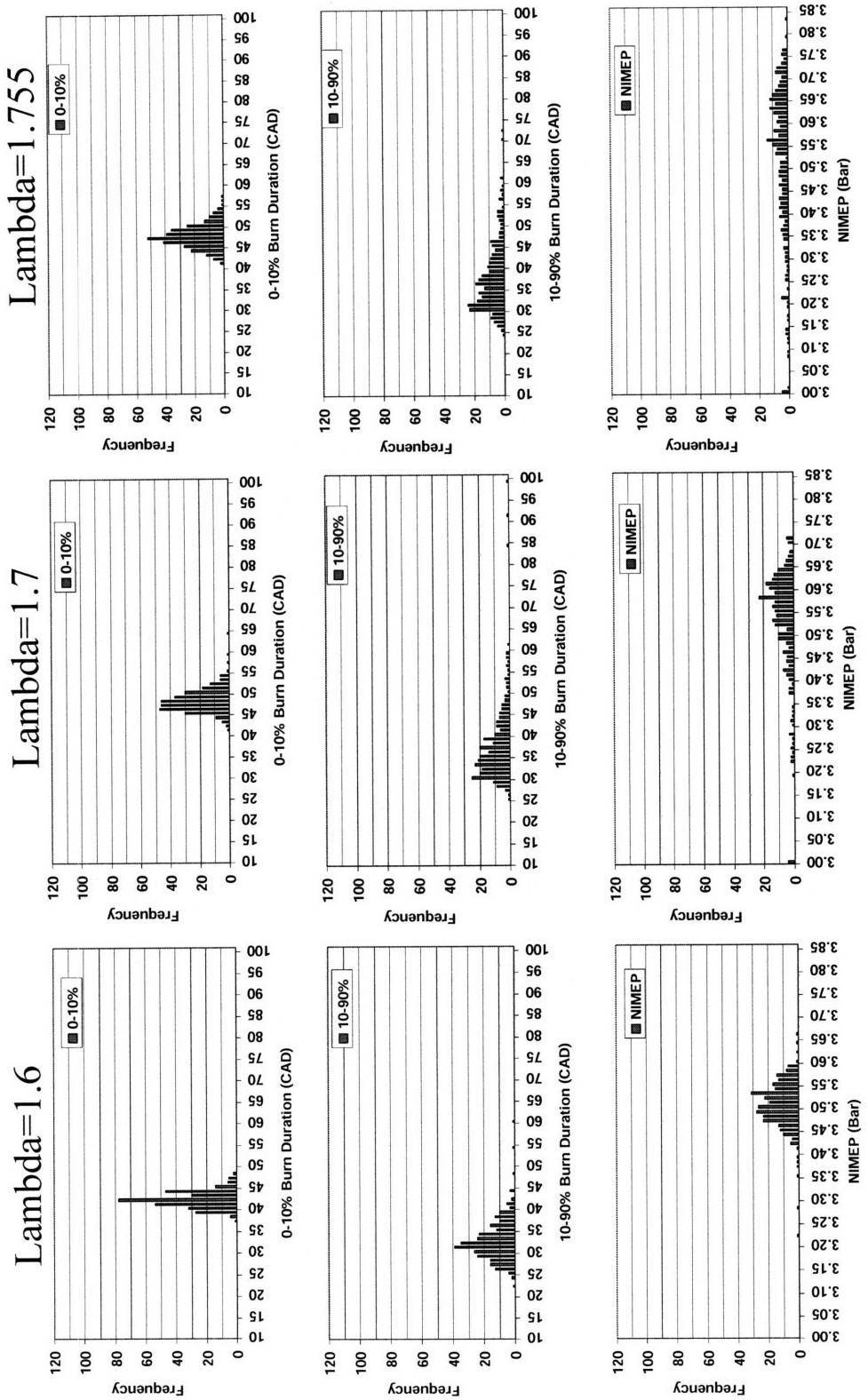

Figure 7-14 – Distribution of 0-10% and 10-90% burn durations, and NIMEP; λ=1.6, 1.7, 1.75; MBT timing, 1500 RPM, r_c=9.8:1, NIMEP = 3.5 bar

7.5 **Combustion Phasing and Asymmetry**

As was explained in section 7.3, for stoichiometric conditions, early variability in the microscale and laminar flame speed will lead to variability in the eddy-burning time and consequently variability in the time duration of the 0-10% mass fraction burned; this in turn will lead to variability in combustion phasing, causing variability in the 10-90% burn duration, and in NIMEP. Figure 7-15 shows the variability in the burning process for various relative air-fuel ratios. The trends are similar to those shown in Hill's data (Figure 7-16), and consistent with the analysis from section 7.3. As the mixture becomes leaner, the initial variability steadily increases. Based on the explanation from the previous section, a rapid increase in the initial variability occurs when the laminar flame speed reaches a critically low value; for this case, this value is reached when the relative air fuel ratio lies between 1.6 and 1.7. Figure 7-15 shows how the variability increases fairly linearly from 10% mass fraction burned up the 50% mass fraction burned point.

Figure 7-17 shows the complete variability curves. As previously mentioned, and as seen in figure 7-16, Hill did not show this entire range, most likely due to a lack of explanation for the rapid rise in variability beyond 50% mass fraction burned for very lean mixtures. Once again, this behavior is caused by phasing differences which are rooted in the cycle-to-cycle differences in initial eddy-burning time. There are two reasons for why this non-linear behavior only shows up under highly lean conditions (lambda>1.4). As shown in figure 7-6, the spread in the burn duration between the "optimum" cycle and the advanced cycle is roughly equal to but opposite to the spread between the retarded cycle and the "optimum" cycle, as time progresses. This apparent symmetry in spread for curves that have a symmetrical flame initiation about the optimum curve, occurs for small initial differences in the flame initiation (0-10% burn duration ~ +/-2 CAD) and for fast burning curves (e.g. stoichiometric or moderately lean curves). Even fast burning curves with small spread in flame initiation, are not exactly symmetrical. Due to the "integration" of the physics involved in the process, the retarded curve will have a larger spread towards the end of combustion; this effect is fairly small, and can not be noticed in figure 7-6. However, as the spread in flame initiation increases beyond 2-3 CAD, the differences in spread between the optimum cycles and the advanced and retarded ones, becomes more asymmetrical as the mass fraction burned increases. This effect, although small for stoichiometric conditions, is shown in figure 7-18, where the same model MBT curve from figure 7-6 is shown along with

two modeled cycles with an equal but opposite initial 0-10% burn duration spread of +/- 5 CAD. The asymmetric effect is small, but the spread of the retarded curve, relative to the MBT curve at the 90% mfb point is 1 CAD greater than the spread of the advanced curve relative to the MBT curve. If the curves are slow burning, as happens under highly lean conditions, then this non-symmetric effect will be exacerbated. To understand this effect, the same modeling analysis used in section 7.3 is used in this section.

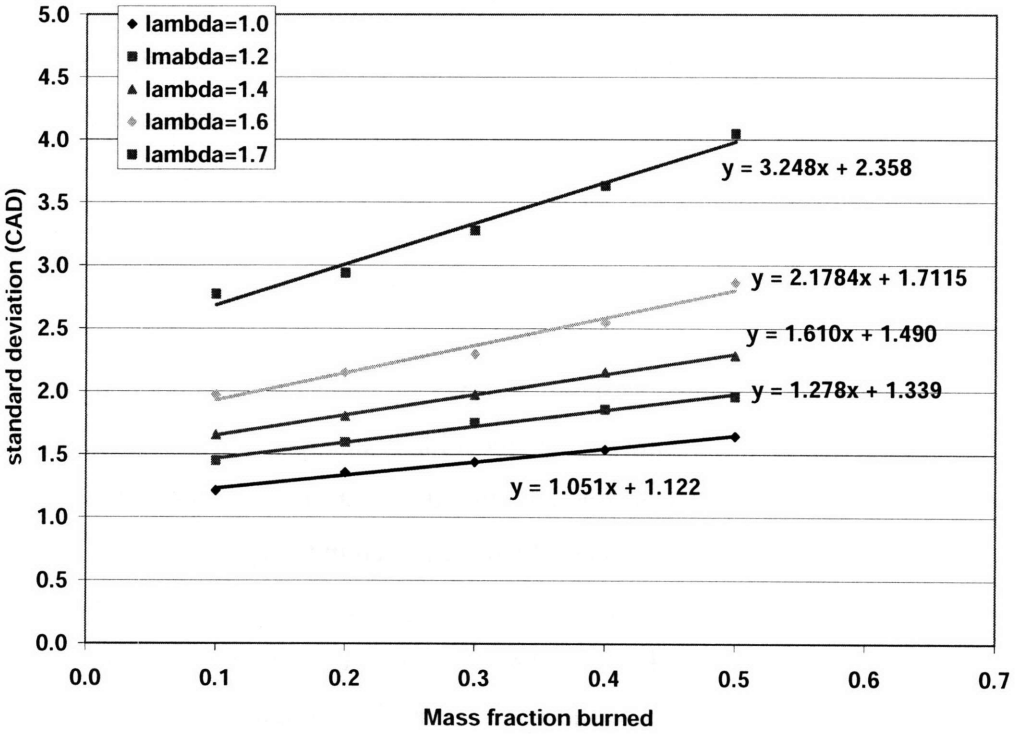

Figure 7-15 – Standard deviation of burn duration as the mass fraction burned increases; MBT timing, 1500 RPM, r_c=9.8:1, NIMEP = 3.5 bar, λ=1.0, 1.2, 1.4, 1.6, 1.7, 1.75; incomplete range

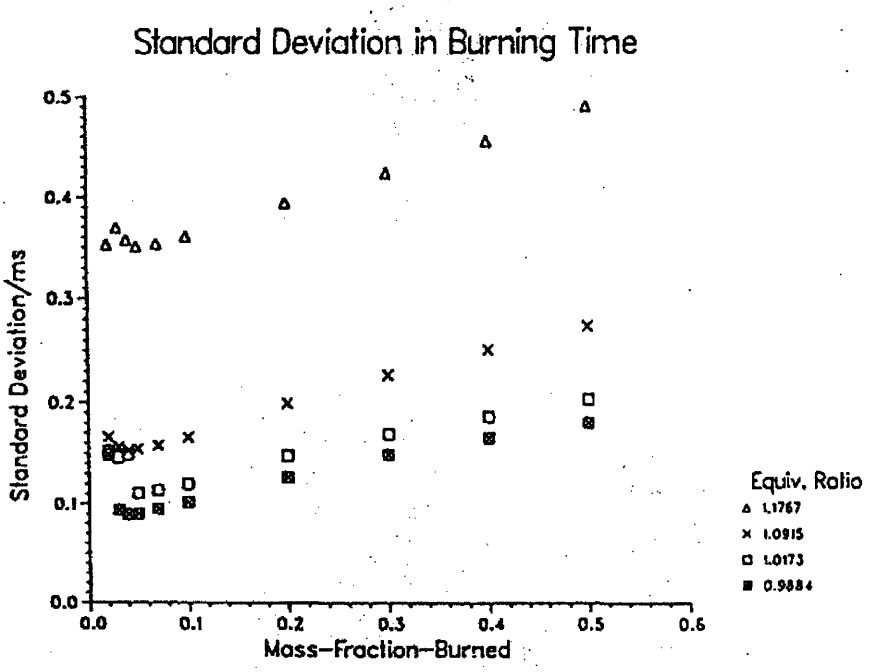

Figure 7-16 – Standard deviation of burn duration as the mass fraction burned increases; various relative air-fuel ratios; data from Hill

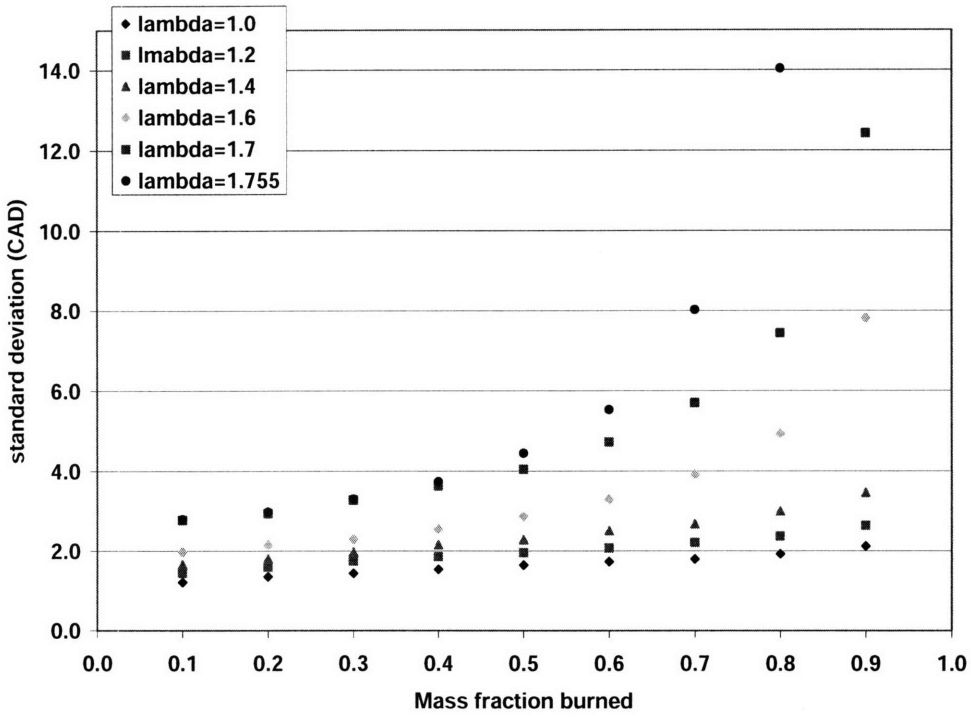

Figure 7-17 – Standard deviation of burn duration as the mass fraction burned increases; MBT timing, 1500 RPM, r_c=9.8:1, NIMEP = 3.5 bar, λ=1.0, 1.2, 1.4, 1.6, 1.7, 1.75; complete range

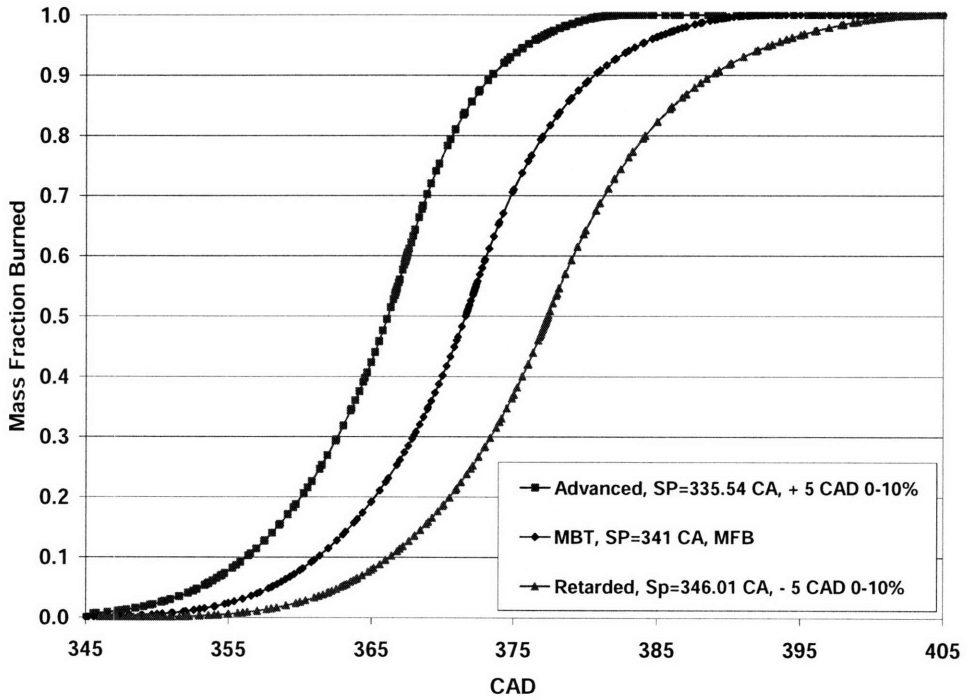

Figure 7-18 – Comparison of model burning profiles: optimum, retarded, and advanced curves (+/- 5 CAD in 0-10% burn duration); 1500 RPM, r_c=9.8:1, NIMEP = 3.5 bar, λ=1.0

Figure 7-19 shows an example of three representative average data cycles with different combustion phasing each, for relative air-fuel ratio of 1.7 and the same speed and load as the previous data. The center curve is the optimum curve out of the three average cycles, with 0-10% burn duration of 47 CAD. As previously explained, this curve averages all the individual curves that have a 0-10% burn duration of 47 CAD; the remaining two average curves have the same but opposite spread in the 0-10% burn duration, +/- 5 CAD; that is, the left outer curve has a 0-10% burn duration of 42 CAD, and right outer curve has a 0-10% burn duration of 52 CAD. This spread is much larger than the maximum spread in 0-10% burn duration shown for the stoichiometric case, of approximately +/- 2 CAD (figure 7-5), and can be found in the cycles making up the tails of the 0-10% distribution, shown in Figs. 7-13 and 7-14. Curves with even larger spread can still be found among the 300 cycles that make up this lambda=1.7 data point. The most striking point from this chart is the large differences in the development of the curves. The average cycle that started later (far-right curve) ends up with a much larger difference in 10-90% burn duration relative to the center curve, compared to the average cycle that started earlier (far-left curve). As previously explained, the differences in the initial conditions are causing differences in the combustion phasing, affecting the burn durations and NIMEP.

Using the combustion model, a closer look can be taken at the physics of the process. But first the behavior of the combustion model for these highly lean conditions must be validated. Figure 7-20 shows a set of curves produced by the model, similar to the ones shown in figure 7-19. The center curve is the MBT curve, and the retarded and advanced curves, have the same +/- 5 CAD spread in 0-10% burn duration, respectively, relative to MBT. The model and data have a similar behavior, confirming the validity of the model.

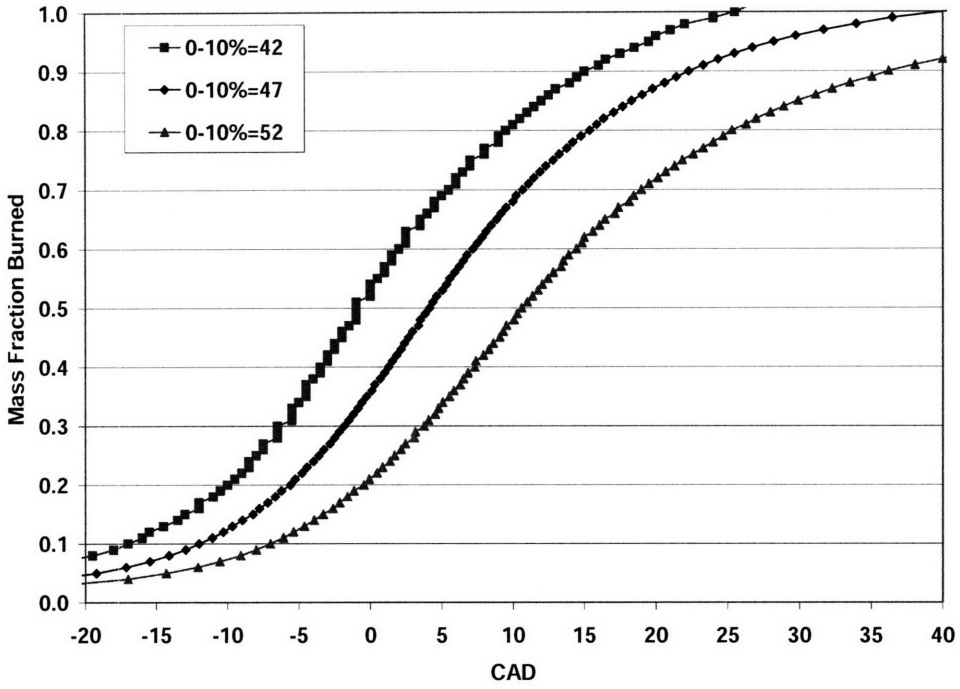

Figure 7-19 – Comparison of data average burning profiles: optimum, retarded, and advanced curves (+/- 5 CAD in 0-10% burn duration); 1500 RPM, r_c=9.8:1, NIMEP = 3.5 bar, λ=1.7

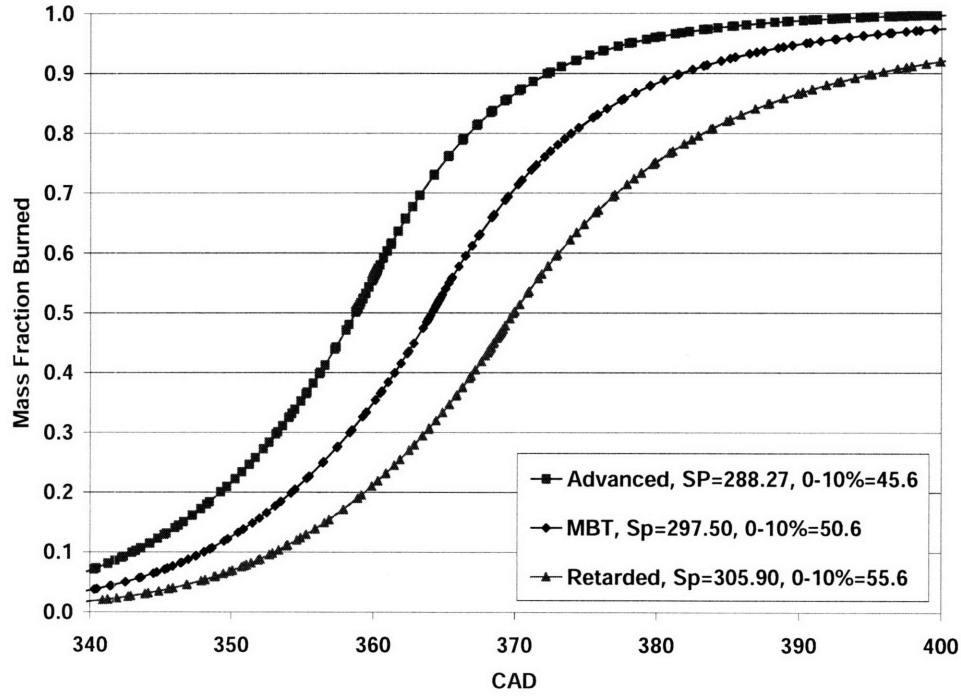

Figure 7-20 – Comparison of model burning profiles: optimum, retarded, and advanced curves (+/- 5 CAD in 0-10% burn duration); 1500 RPM, r_c=9.8:1, NIMEP = 3.5 bar, λ=1.7

Figure 7-21 shows the spread in burn profiles, as previously defined (eq. 7-2), for various sets of curves, including the curves shown in figures 7-19 and 7-20 (label C), as well as a similar set of curves with a +/- 1 CAD difference in 0-10% burn duration (label A). The standard deviation in burn duration for all 300 cycles (label B) is also plotted. There are a few important points to notice from this graph. First, there is good agreement between the model and the data, for both the small initial spread (+/-1 CAD in 0-10% burn duration – label A), and the large initial spread (+/- 5 CAD in 0-10% burn duration – label C). Second, the rapid non-linear rise in spread, in particular beyond the 50% mfb point, seen in figure 7-17, where all 300 cycles, were included, also shows up for the pair of curves from figures 7-19 and 7-20 (label C). This confirms that this non-linear behavior is due to phasing differences. Both sets of curves, with small and large initial 0-10% burn duration spread, exhibit this non-linear behavior. However, for the +/- 1 CAD 0-10% burn duration curves (label A), the magnitude of the spread beyond the 50% mfb point (e.g. spread at 90% mfb) is quite small, especially when compared to the magnitude produced by the +/- 5 CAD curves (label C). Also, for the +/- 1 CAD curves, the non-linear behavior occurs later in the combustion process (mfb>0.8) compared to the non-linear behavior in the +/- 5 CAD curves (mfb>0.5).

Another point to notice from figure 7-21 is that, as expected, the standard deviation in burn duration curve for all 300 cycles (label B) lies between the +/- 1 CAD curve (label A), and the +/-5 CAD curve (label C). For comparison purposes, and to establish a definite upper limit on the spread, a data curve with initial 0-10% burn duration spread of +/- 6 CAD (label D) is also plotted, representing one of the most extreme spreads in the data 0-10% burn duration distribution of the real data. Because the standard deviation curve contains the weight of all 300 cycles, its initial variability starts at around the middle of the upper and lower limits. As the mass fraction burned increases, the cycles with larger spread in initial combustion phasing will have a higher spread, and consequently a larger effect on the standard deviation, causing this curve to increase rapidly and non-linearly.

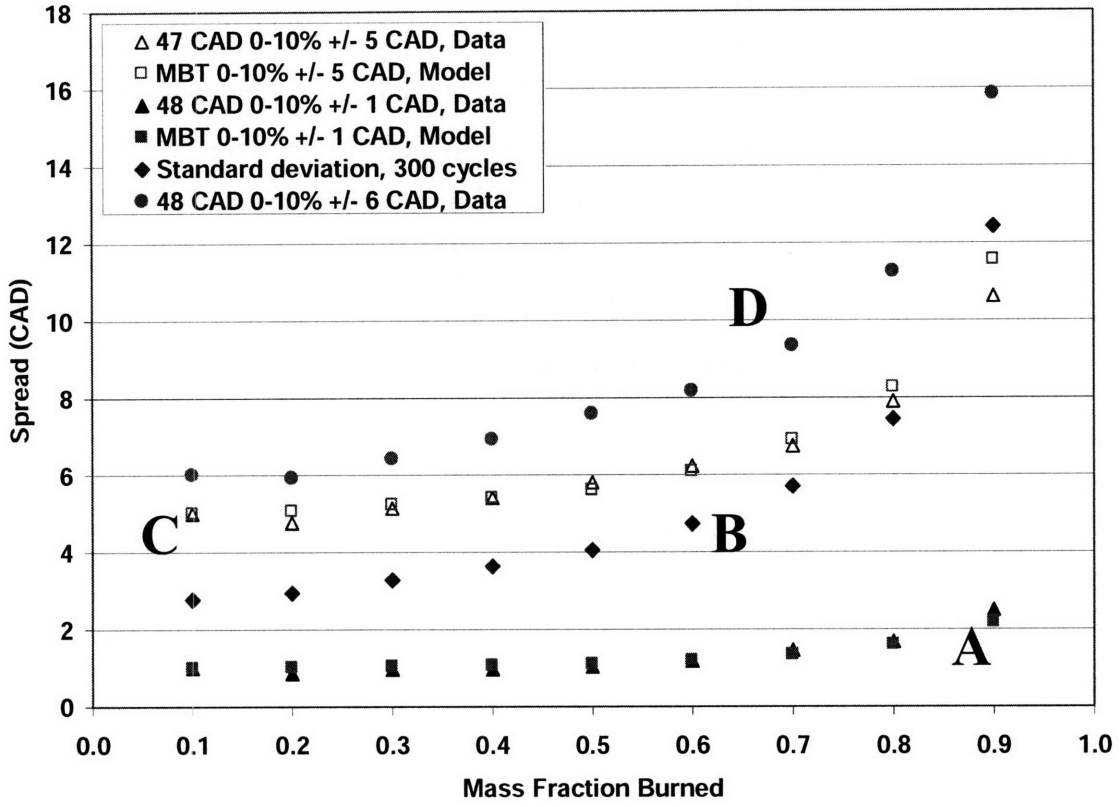

Figure 7-21 – Comparison of spread in burn duration with increasing mass fraction burned for two model and data comparisons (+/- 1 and +/- 5 CAD 0-10% burn duration) and for all 300 cycles; 1500 RPM, r_c=9.8:1, NIMEP = 3.5 bar, λ=1.7

7.6 **Eddy-burning Time Analysis For Lean Cases**

The model again, can be used to understand in more detail, why curves that are symmetrically phased about an optimum curve will develop differently, with the burn duration spread between them increasing the greater the phasing difference, and the leaner the mixture. Figures 7-22 and 7-23 show the development of the eddy-burning time for lambda=1.4, and for a symmetric spread in 0-10% burn duration of +-/ 3 and +/- 5 CAD, respectively. For the advanced curves, the eddy-burning time has decreased when going from the smaller initial spread (- 3 CAD), to the larger initial spread (- 5 CAD). On the other hand, this eddy-burning time has increased for the retarded curves, when going from the smaller to the larger initial 0-10% burn duration spread. The differences in these eddy-burning times between the smaller and the larger 0-10% phasing differences are mainly caused by the differences in the microscales for both of these conditions. Figures 7-24 and 7-25 show the microscale and laminar flame speed development for these sets of curves. Although the laminar flame speed at spark has increased

for the advanced curve, going from an initial spread of -3 CAD to - 5CAD, the increase is fairly small, about 1.5%; likewise for the retarded curves, the decrease in laminar flame speed going from an initial spread of +3 CAD to +5 CAD, relative to the optimum curve, is fairly small. The corresponding changes in the microscale are larger, on the order of 7-8%. This combination of changes causes the observed behavior in the eddy-burning time. For both cases (+/- 3 and +/-5), the initial conditions will affect the later combustion events, as previously explained. Therefore, the slower burning curve (retarded) will continue to burn at a slower rate, increasing the difference relative to the optimum curve. This is clear by looking at the difference across the eddy-burning times for the three curves at the 50% mass fraction burned point, and at the 90% mass fraction burned point for both cases (+/-3 and +/-5); the difference between the curves has increased. This is due to the "integration" effect of the burning process, whereby slow combustion continues to burn slow, and fast combustion continues to burn fast.

Because the eddy-burning times, are longer for the curve with +/- 5 CAD spread in 0-10%, compared to the +/- 3 CAD spread curves, then, as expected, the spread between the curves will be larger for the +/- 5 CAD curves. This increase in combustion spread is not proportional to the increase in the 0-10% spread. Looking at the 90% mass fraction burned point, for the advanced curve, the spread has increased by close to 50% going from the advanced curve with -3 CAD spread, to the advance curve with -5 CAD spread. But for the retarded curve the respective increase in spread is approximately 70%. This is due again to the effect of the initial burning conditions, on the remainder of the combustion process

By the same arguments presented in this section, it is expected that all else equal, the spread in combustion will increase and become asymmetrical as the mixture becomes leaner. This is clear by looking at figure 7-28, which shows an initial spread of +/- 5 CAD in 0-10% burn duration for a relative air-fuel ratio of 1.7. Compared to the same 0-10% phasing spread, for a relative air-fuel ratio of 1.4, the difference in burn durations across the three curves for lambda of 1.7 is much larger. This is expected considering that with leaner combustion, the laminar flame speed will be lower, and thus the eddy-burning time will be longer. Thus, with a slower initial combustion process for lambda=1.7 compared to lambda=1.4, the differences due to phasing will be much larger (especially after the 50% mfb point).

The main conclusions from this section can be summarized as follows: the spread between symmetrically phased burn profiles will increase asymmetrically. This asymmetry will

be exacerbated with larger initial 0-10% spread, and with leaner conditions. These conclusions explain why the 10-90% burn duration and NIMEP distributions shown in figures 7-13 and 7-14 become very asymmetrical for lean conditions, in spite of having a symmetrical 0-10% burn duration distribution. It should be noted that although the distribution in the 0-10% burn duration stays close to normal, its standard deviation (spread) is increasing. Therefore, both drivers of asymmetry mentioned in this section are clearly playing a role: a growing spread in the 0-10% burn duration distribution, and a lengthening 0-10% burn duration (as measured by the average) as combustion progresses, due to leaner conditions.

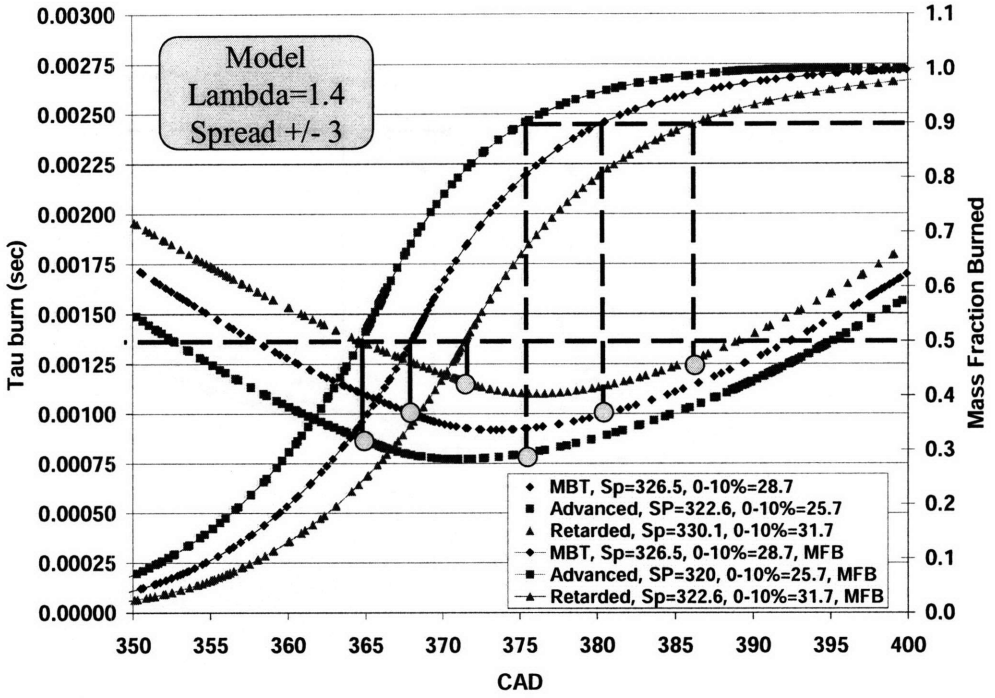

Figure 7-22 – Model time history of eddy-burning time and mass fraction burned for optimum, retarded, and advanced curves (+/- 3 CAD in 0-10% burn duration); 1500 RPM, r_c=9.8:1, NIMEP = 3.5 bar, λ=1.4

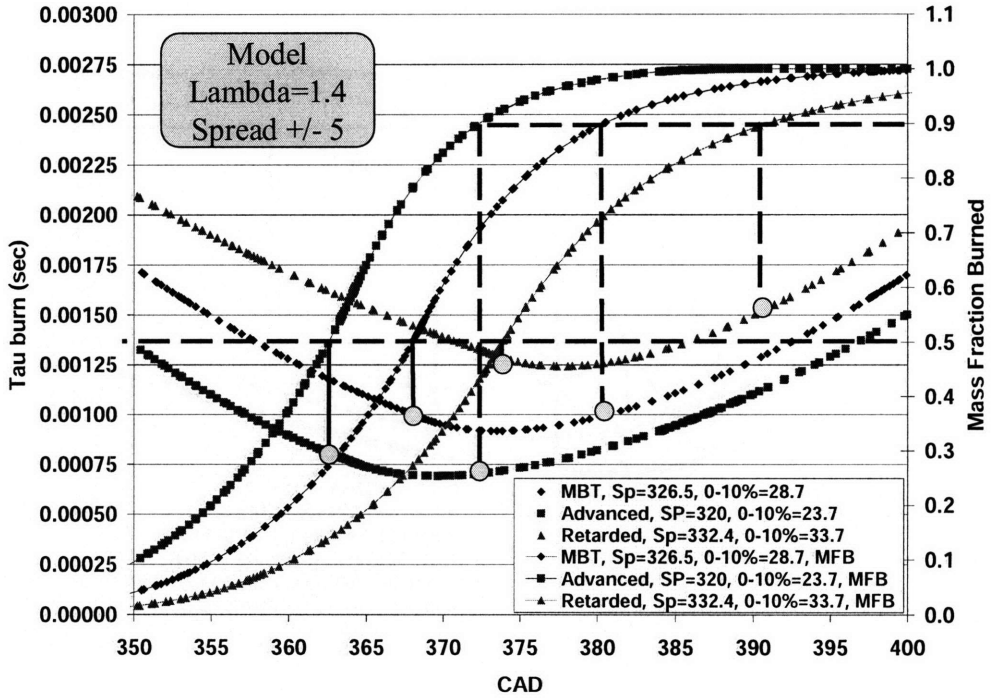

Figure 7-23 – Model time history of eddy-burning time and mass fraction burned for optimum, retarded, and advanced curves (+/- 5 CAD in 0-10% burn duration); 1500 RPM, r_c=9.8:1, NIMEP = 3.5 bar, λ=1.4

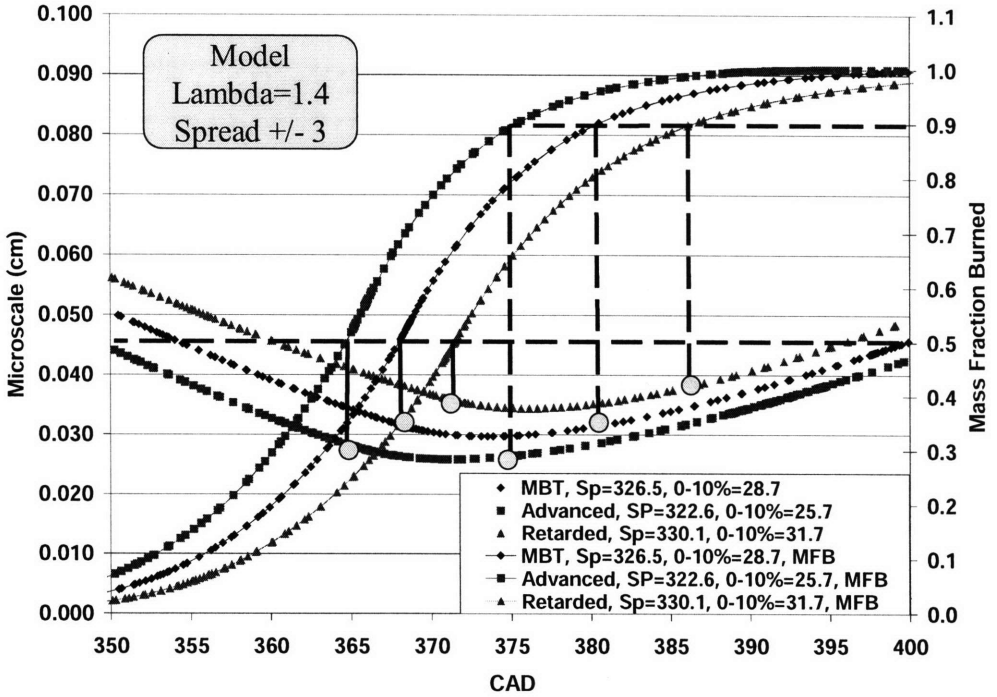

Figure 7-24 – Model time history of microscale and mass fraction burned for optimum, retarded, and advanced curves (+/- 3 CAD in 0-10% burn duration); 1500 RPM, r_c=9.8:1, NIMEP = 3.5 bar, λ=1.4

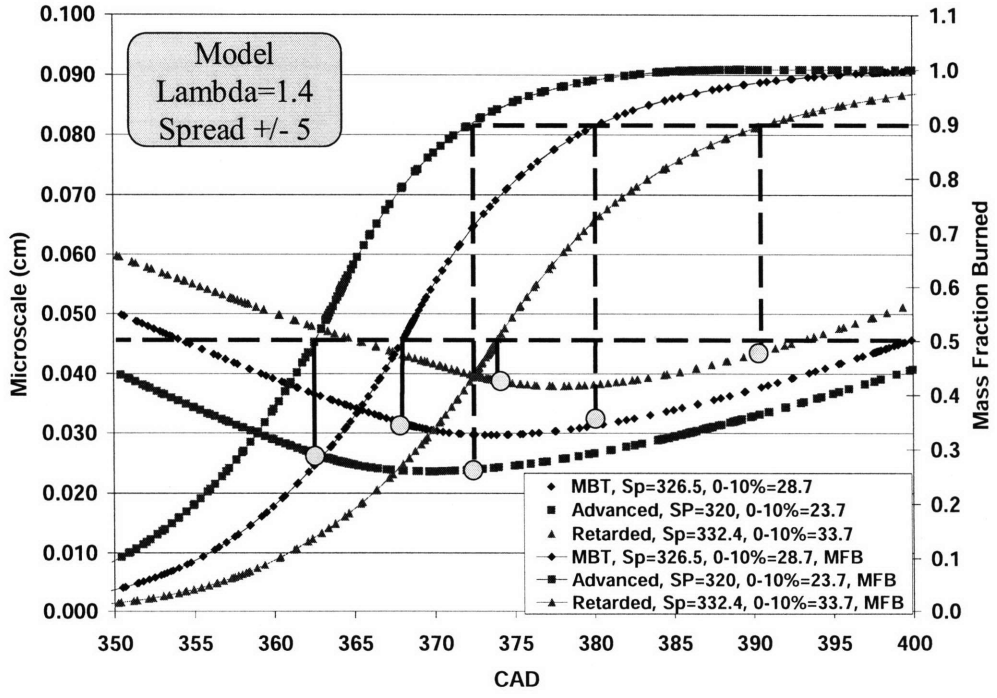

Figure 7-25 – Model time history of microscale and mass fraction burned for optimum, retarded, and advanced curves (+/- 5 CAD in 0-10% burn duration); 1500 RPM, r_c=9.8:1, NIMEP = 3.5 bar, λ=1.4

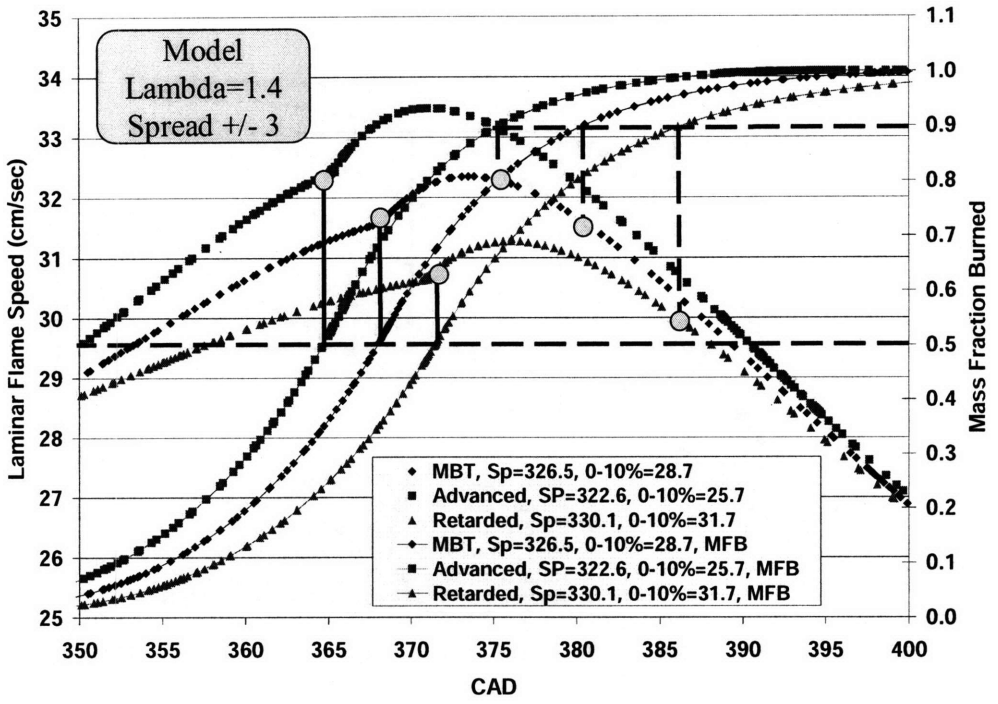

Figure 7-26 – Model time history of laminar flame speed and mass fraction burned for optimum, retarded, and advanced curves (+/- 3 CAD in 0-10% burn duration); 1500 RPM, r_c=9.8:1, NIMEP = 3.5 bar, λ=1.4

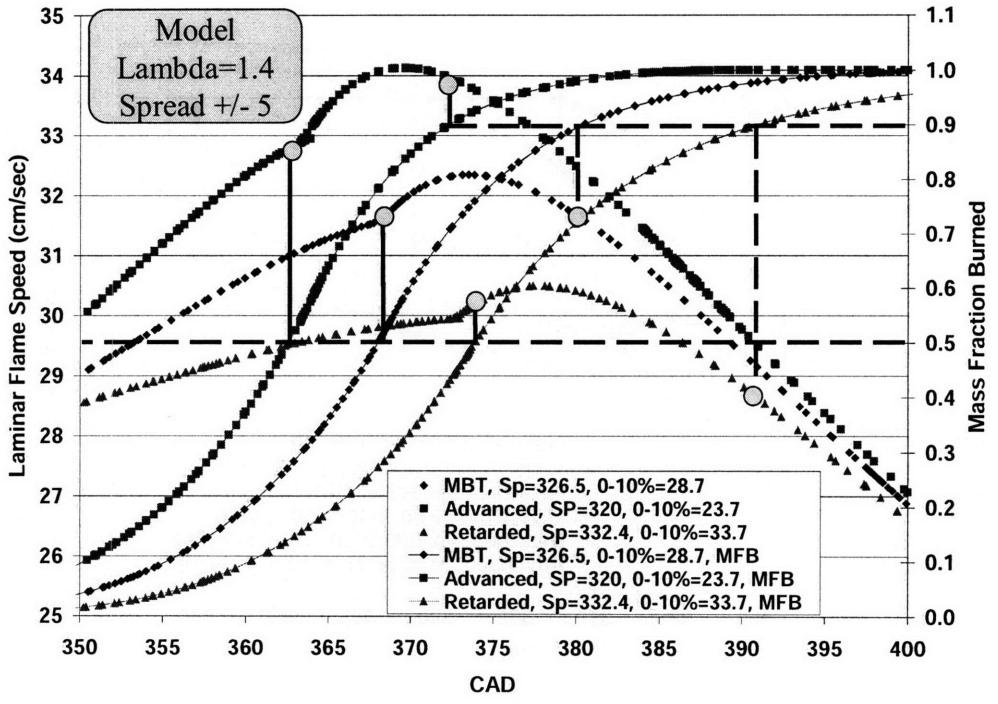

Figure 7-27 – Model time history of laminar flame speed and mass fraction burned for optimum, retarded, and advanced curves (+/- 5 CAD in 0-10% burn duration); 1500 RPM, r_c=9.8:1, NIMEP = 3.5 bar, λ=1.4

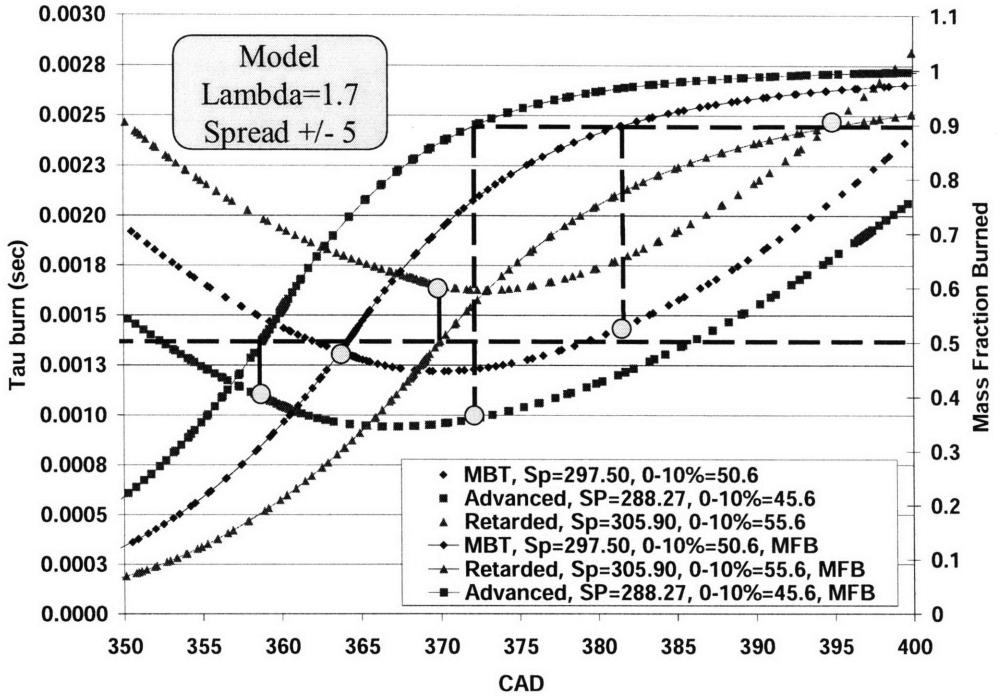

Figure 7-28 – Model time history of eddy-burning time and mass fraction burned for optimum, retarded, and advanced curves (+/- 5 CAD in 0-10% burn duration); 1500 RPM, r_c=9.8:1, NIMEP = 3.5 bar, λ=1.7

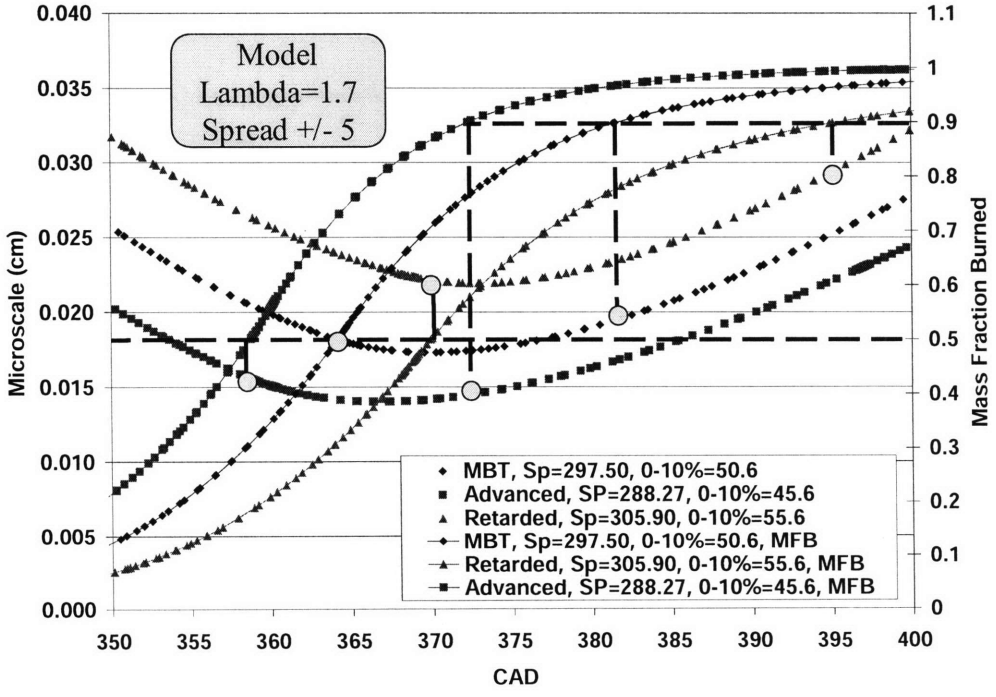

Figure 7-29 – Model time history of microscale and mass fraction burned for optimum, retarded, and advanced curves (+/- 5 CAD in 0-10% burn duration); 1500 RPM, r_c=9.8:1, NIMEP = 3.5 bar, λ=1.7

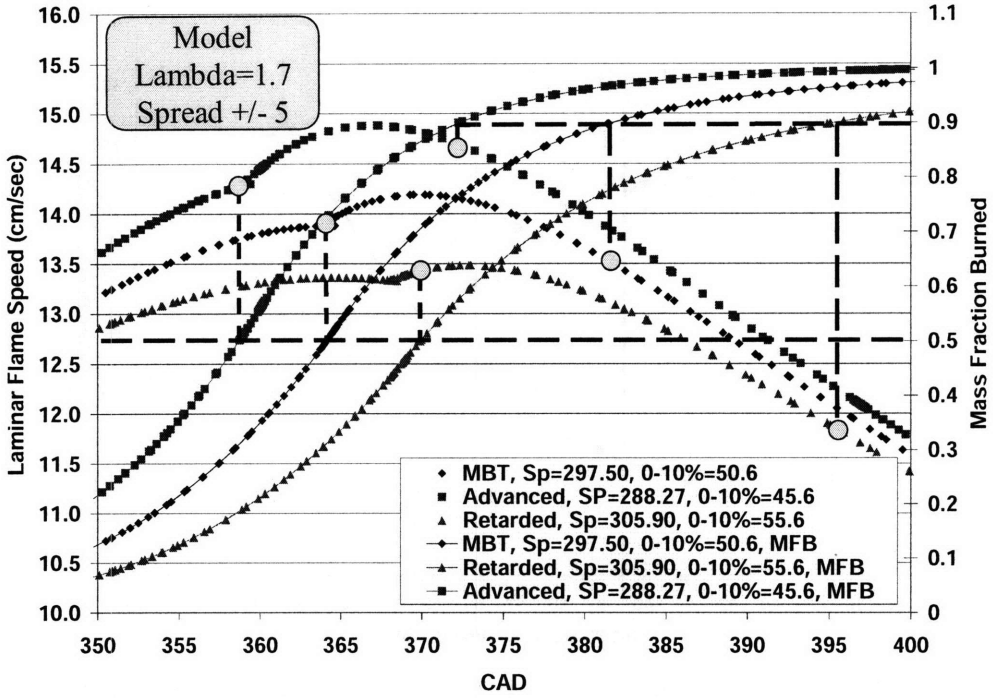

Figure 7-30 – Model time history of laminar flame speed and mass fraction burned for optimum, retarded, and advanced curves (+/- 5 CAD in 0-10% burn duration); 1500 RPM, r_c=9.8:1, NIMEP = 3.5 bar, λ=1.7

7.7 Additional Evidence of Phasing Effect

To reinforce the previous phasing explanation, one more piece of evidence is presented. Figure 7-31 shows how large variations in 0-10% burn duration cause large and non-linear variations in both the 50-90% burn duration and in NIMEP. Each point represents the average result of all cycles that have the specified 0-10% burn duration, out of the set of 300 individual cycles that make up the data point for lambda=1.7, 3.5 bar NIMEP, MBT conditions, 1500 rpm and Rc=9.8. This effect is expected based on this chapter's discussion. Also, it should be added that this asymmetric effect had already been observed in previously published data from the Sloan Lab [15] as shown in figure 7-32. This provides additional confidence in the presented mechanism that connects the variability during flame initiation (0-10% burn duration) with the variability in the later stages of combustion (10-90% burn duration), and consequently, variability in NIMEP.

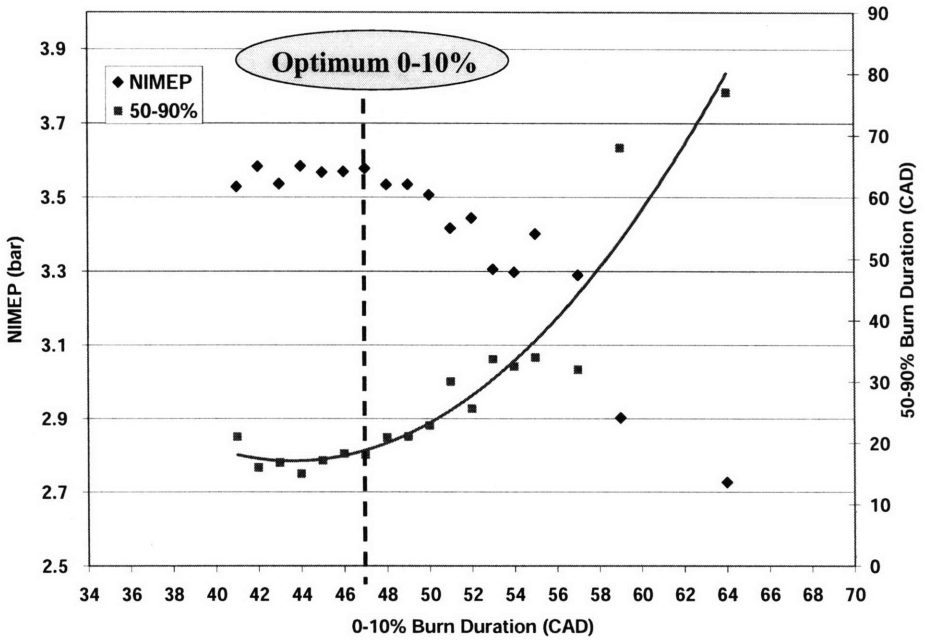

Figure 7-31 – Effect of 0-10% burn duration on NIMEP and 50-90% burn duration; 1500 RPM, r_c=9.8:1, NIMEP = 3.5 bar, λ=1.7

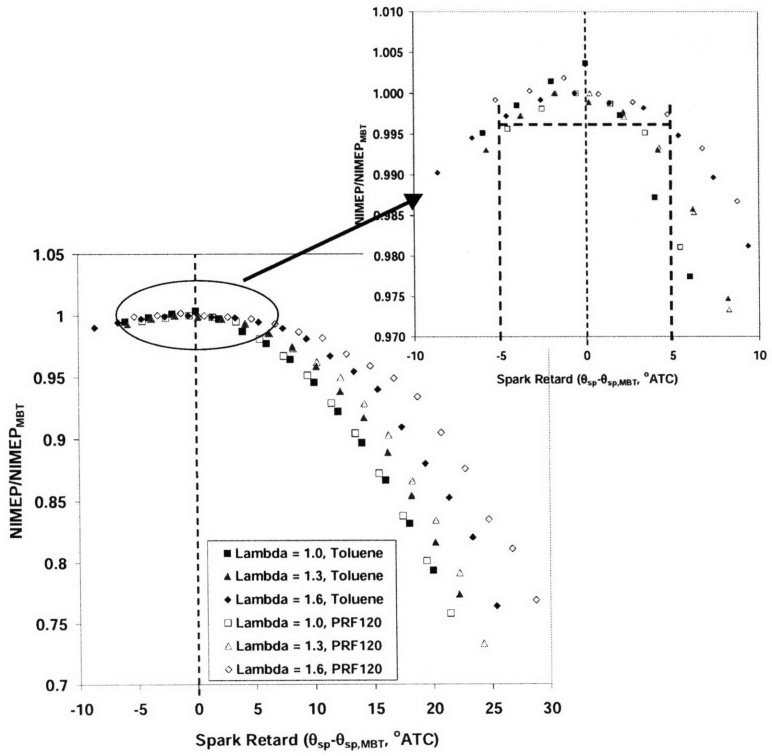

Figure 7-32 – Effect of spark retard on normalized torque; 1500 RPM, r_c=9.8:1, various $\lambda_{A/F}$, Toluene and PRF

7.8 **Random Variability in 50-90%**

Having explained how variability in the laminar flame speed and in the turbulence microscale will produce variability in the early eddy-burning time, and consequently variability in combustion phasing, leading to the asymmetrical behavior observed, it should be noted that there are other sources of variability. Figures 7-33, 7-34, and 7-35 show the variability in NIMEP caused by variability in the 50-90% burn duration for λ=1.0, 1.4, and 1.7. The 0-10% burn duration for each figure is constant, and the data has been grouped by location of the 50% mass fraction burned point (i.e., constant 0-50% burn duration). These figures show that cycles that have closely comparable burning profiles up to the location of 50% mass fraction burned, can still differ in the 50-90% burn duration. As expected, this variability in the 50-90% burn duration will bring corresponding variability in the NIMEP. Potential sources for this variability include one or a combination of the following:

- Variability in the microscale: Affects combustion at all times, primarily during flame initiation. Size and variability in the microscale depends on the fluid motion, in particular the turbulence intensity. Valve lift also affects the microscale [33].
- Variability in the laminar flame speed: Affects combustion at all times, primarily during flame initiation. Many factors affect the variability in the laminar flame speed, including the early flame motion, as discussed below, changes in dilution, residual, temperature, pressure, and spark energy discharge.
- Variability in the flame/wall interactions: These interactions will be most significant after the mixture has been mostly entrained. As shown in figure 7-36, this occurs approximately after 50% of the mass has been burned
- Offset of the combustion center, due to the flame kernel "random walk" effect. This motion has two main effects on combustion variability. As shown by Pischinger and Heywood [40, 41], the motion of this flame is largest when the flame is small. The location of the flame center, relative to the spark plug electrodes, affects the amount of heat transfer that is lost from the kernel to the spark plug. This heat loss in turn, affects the initial laminar flame speed, and consequently the eddy-burning time. Beyond a flame radius of approximately 1.5 mm (0.2-0.4 ms), these heat losses peak, and become less important. The effect of this offset center becomes important again when the flame is close to reaching the walls, close to the 50% mfb point, per figure 7-36. All else equal,

for a centered kernel, combustion will be optimum in terms of maximizing the flame area before reaching the walls. For an offset kernel center, however, part of the flame will touch the cylinder walls faster, losing this burning front and ending up with a slower combustion process, as shown in figure 7-37.

Because of the increasing nature of the variability with leaner mixtures, the variability shown in Figs. 7-33 through 7-35 is most likely dominated by the variability in the eddy-burning time, through variability in the microscale and in the laminar flame speed. As already noted, these two variables are affected by other variables, (e.g., turbulence intensity, dilution, flame center, etc.) whose fluctuations can be random. Figure 7-33 shows how for baseline stoichiometric conditions, the variability is not very high; in fact, if this baseline variability, is taken as the intrinsic variability of the system, associated with random variations in the micrsocale and/or S_L at later parts of combustion, the behavior from figures 7-34 and 7-35 would be expected. The variability of the microscale and/or S_L would still be constant, but due to the inverse dependence of the eddy-burning time on laminar flame speed, this variability will grow rapidly under very lean conditions, as was previously discussed. Thus, in essence, a decreasing laminar flame speed will amplify any variability in the system, in particular the one associated with the eddy-burning time. Although random variability in the 50-90% burn duration interval is relevant, the majority of the variability can still be explained by phasing differences, as can be confirmed by figure 7-38, 7-39, and 7-40, which show the average burning profiles for all the data points, for λ=1.0, 1.4, and 1.7, respectively.

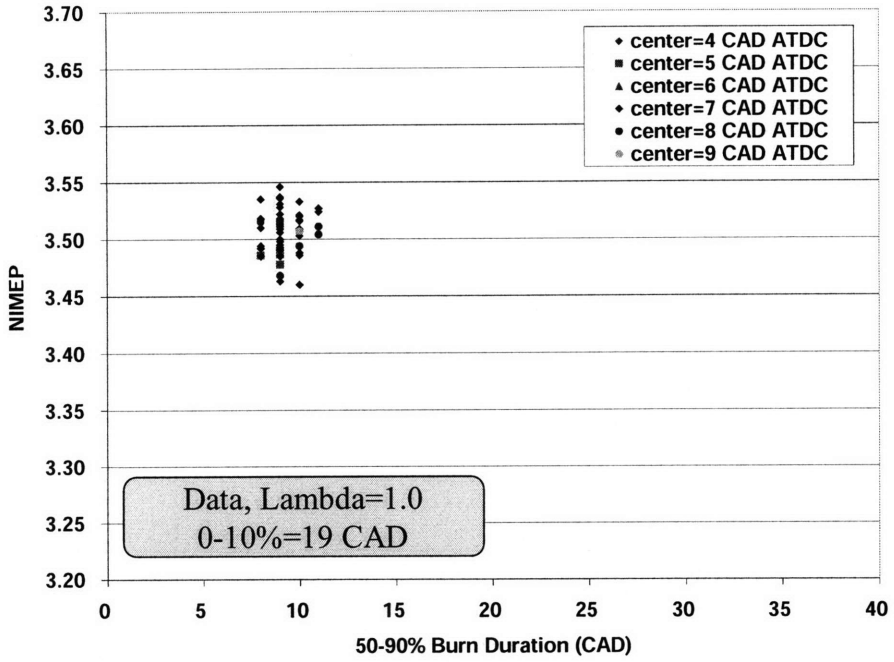

Figure 7-33 – Variability in 50-90% burn duration, and its effect on NIMEP. All points have the same 0-10% burn duration (19 CAD); points are also grouped by common location of 50% mfb point; MBT, 1500 RPM, r_c=9.8:1, NIMEP = 3.5 bar, λ=1.0

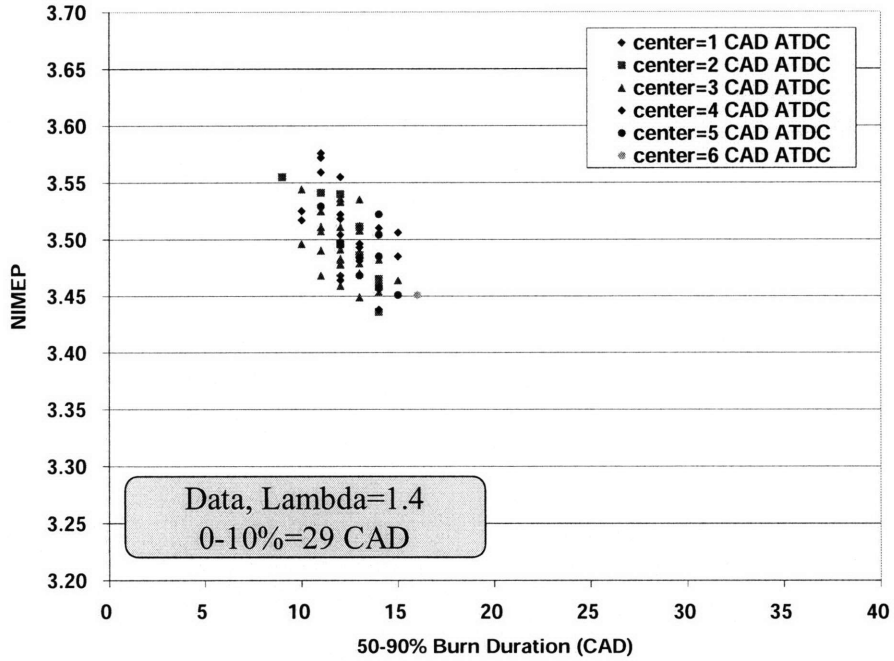

Figure 7-34 – Variability in 50-90% burn duration, and its effect on NIMEP. All points have the same 0-10% burn duration (29 CAD); points are also grouped by common location of 50% mfb point; MBT, 1500 RPM, r_c=9.8:1, NIMEP = 3.5 bar, λ=1.4

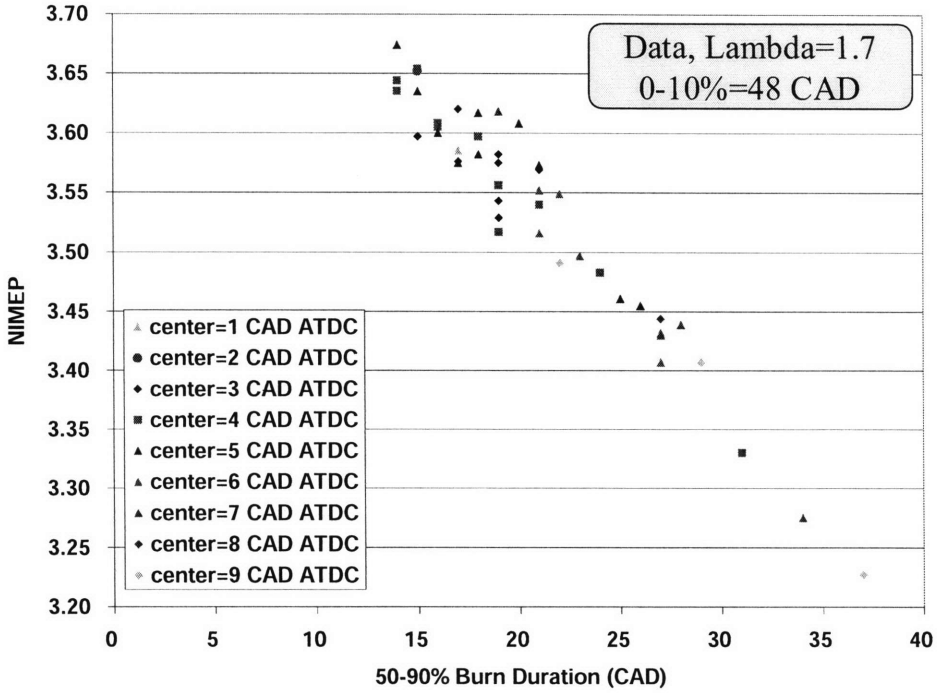

Figure 7-35 – Variability in 50-90% burn duration, and its effect on NIMEP. All points have the same 0-10% burn duration (48 CAD); points are also grouped by common location of 50% mfb point; MBT, 1500 RPM, r_c=9.8:1, NIMEP = 3.5 bar, λ=1.7

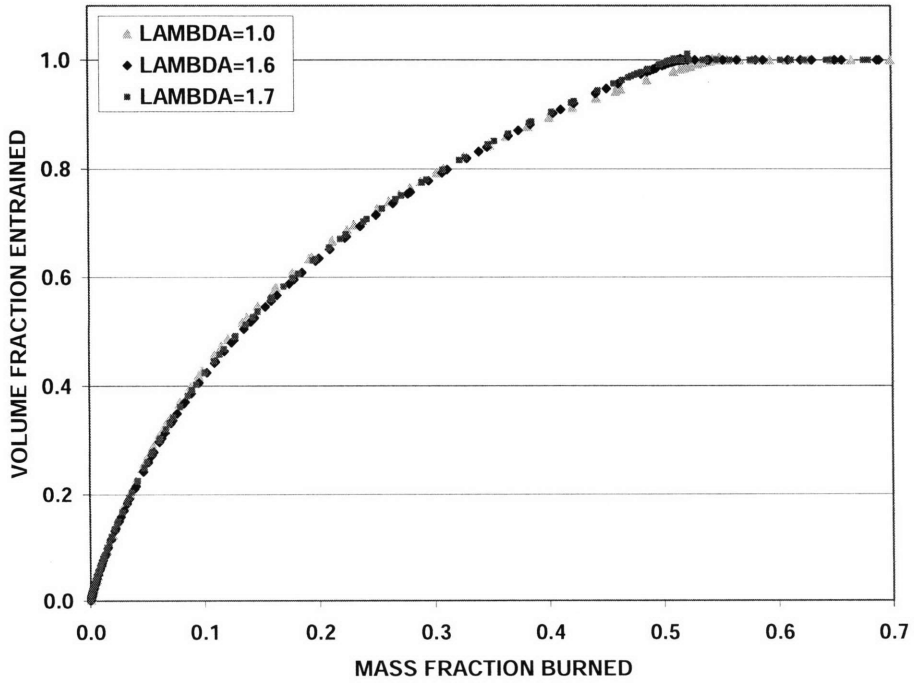

Figure 7-36 – Volume fraction entrained with mass fraction burned; model simulations for λ=1.0, 1.6, 1.7; MBT, 1500 RPM, r_c=9.8:1, NIMEP = 3.5 bar

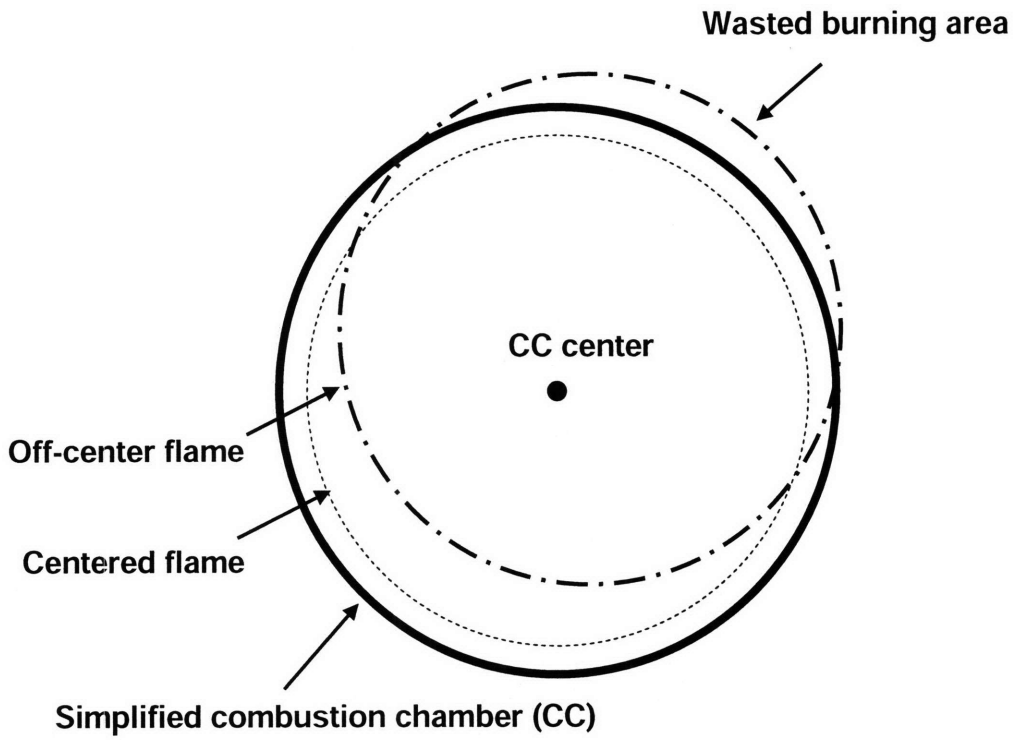

Figure 7-37, schematic showing centered and off-centered flame in a combustion chamber. Off-centered flame burns slower, due to loss of burning area

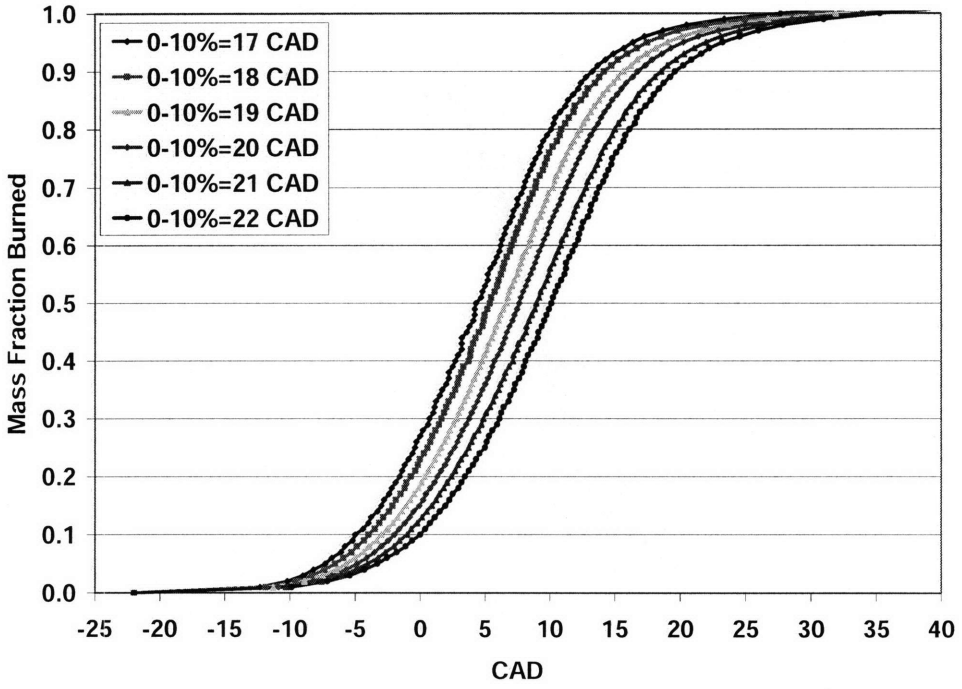

Figure 7-38 – Comparison of average burning profiles with different 0-10% burn duration; MBT timing, 1500 RPM, r_c=9.8:1, NIMEP = 3.5 bar, λ=1.0

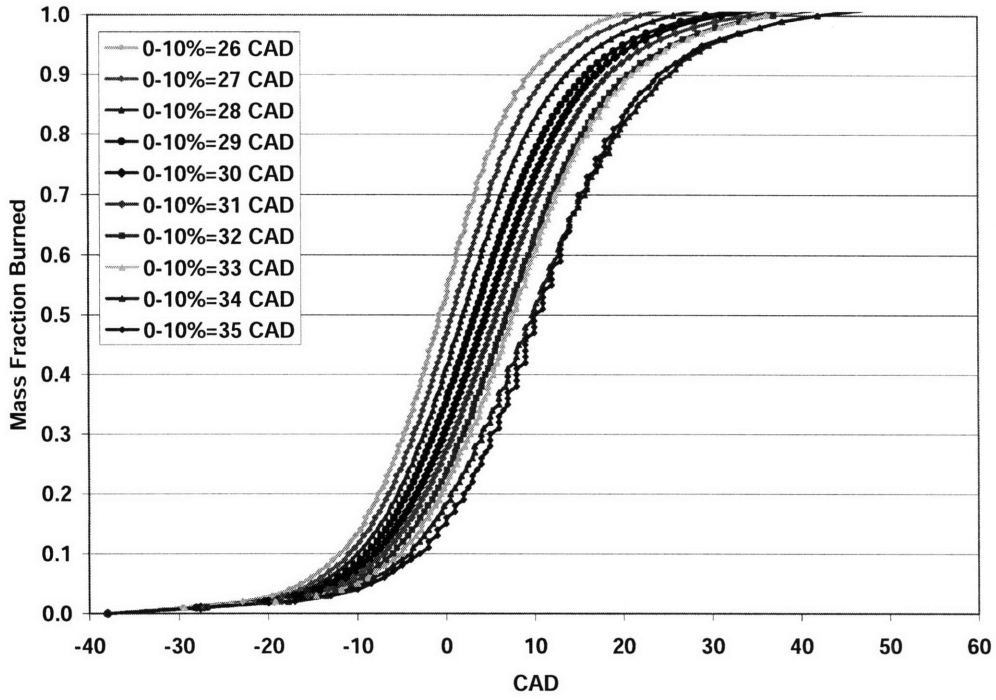

Figure 7-39 – Comparison of average burning profiles with different 0-10% burn duration; MBT timing, 1500 RPM, r_c=9.8:1, NIMEP = 3.5 bar, λ=1.4

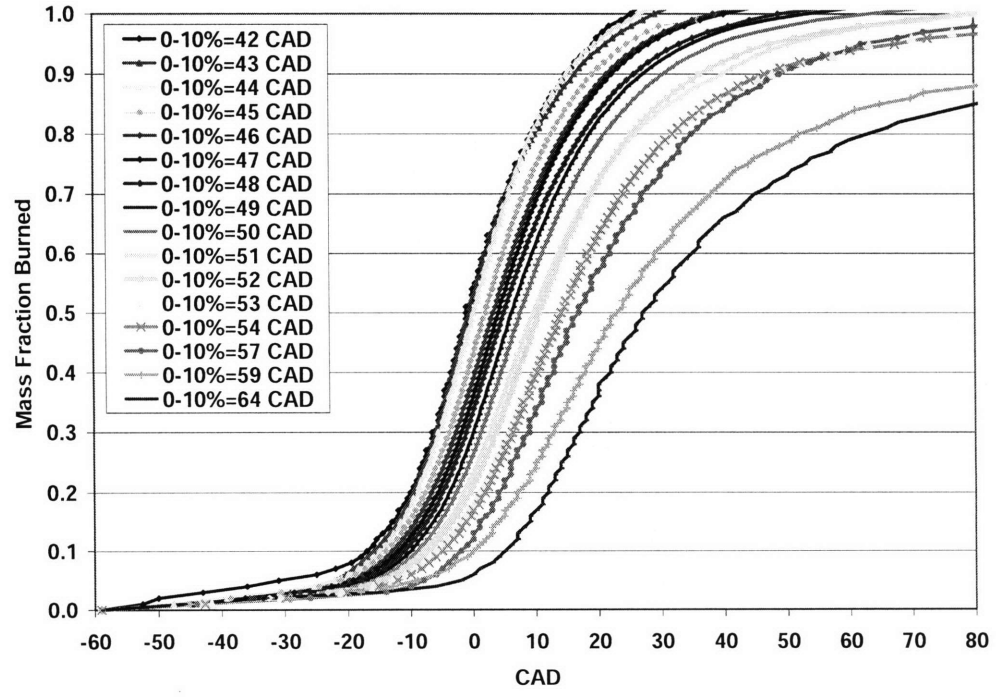

Figure 7-40 – Comparison of average burning profiles with different 0-10% burn duration; MBT timing, 1500 RPM, r_c=9.8:1, NIMEP = 3.5 bar, λ=1.7

7.9 Integrated Variability Simulation: Effect of Changes in Turbulence Intensity, Microscale, and Laminar Flame Speed

In the previous sections the variations in the eddy-burning time, the burn durations, and the NIMEP were correlated with the laminar flame speed. To fully understand the effect of variability, or changes, in each of the three model variables, the laminar flame speed (S_L), the turbulence intensity (u_t') or the turbulence microscale (λ_{micrsc}), on the NIMEP, a full simulation must be performed. This method will account for the full integrated effect of variable changes on the rates of mass entrainment and mass burning. This analysis also allows for a better quantification of the relative magnitude of each of the variable's fluctuations.

Figures 7-41, 7-42, and 7-43 demonstrate how variability in each of the three mentioned variables will affect the combustion process as defined by NIMEP, 0-10% burn duration, and 10-90% burn duration for a lean case (lambda=1.7, 3.5 bar NIMEP, Rc=9.8:1, 1500 rpm). Simulations were carried out by first establishing a baseline case, MBT timing for the specified conditions. Keeping everything else equal, each variable was perturbed, one at a time, and the corresponding changes in the combustion variables were then recorded. Rather than varying the laminar flame speed, the perturbed variable was the dilution, or relative air-fuel ratio for this case. This has the effect of perturbing the laminar flame speed, as well as creating the right thermodynamic conditions that are consistent with such laminar flame speed changes. Additionally, in real experiments it is more common and easier to assess fluctuations in relative air-fuel ratio, than fluctuations in the laminar flame speed.

Figure 7-41 shows how changes in the relative air-fuel ratio affect the NIMEP in a very asymmetric way. The effect on the 10-90% burn duration is also asymmetrical, seeing much larger changes when relative air-fuel ratio is positively perturbed. The 0-10% burn duration is not completely symmetric either, but the effect is much more subtle. The changes in the laminar flame speed are fairly linear and symmetric, justifying the use of the relative air-fuel ratio as the variable being directly perturbed. The asymmetric effect on the main combustion variables will further contribute to the asymmetric behavior observed for very lean case in the previous discussion of this chapter. The variable that is mostly affected is the NIMEP. A small change of approximately 2% in the relative air-fuel ratio already produces changes in the NIMEP that are close to the experimental average NIMEP variability for these conditions. The corresponding changes in the burn durations also agree with the average variability observed with such NIMEP

changes. Larger perturbations in $\lambda_{A/F}$, up to 6%, will even encompass the most extreme individual cycle-to-cycle NIMEP changes observed in the data. Thus, Figure 7-41 shows that variability in the laminar flame speed alone would be enough to account for the observed variability in the data. It should be noted that because the relative air-fuel ratio changes, the baseline MBT timing is no longer the optimum timing for the new conditions, contributing to the loss in the NIMEP. This is similar to what happens during variability in the real experiments.

Although cycle-to-cycle changes in the relative air-fuel ratio can not be easily measured, and were not measured for the experiments done for this research, published research shows that these fluctuations can range from +/-0.03 $\lambda_{A/F}$ to +/-0.08 $\lambda_{A/F}$ [44, 45]. For the experiments of this thesis, the limited methods to assess variations in $\lambda_{A/F}$ are studying the history of the calculated error in the average UEGO sensor measurement (which is compared to the $\lambda_{A/F}$ calculated from the calibrated air-flow and recorded weight of the consumed fuel), as well as monitoring the rapid fluctuations in the UEGO sensor reading. The calculated error ranged from 0.5% to up to 4-5% for highly lean cases. The small fluctuations in the UEGO measurements, observed while running experiments, varied from +/-0.005 $\lambda_{A/F}$ to +/-0.04 $\lambda_{A/F}$ for very lean cases. Calculations of the laminar flame speed using the Keck-Rhodes correlation, as a function of the measured cylinder pressure and the calculated adiabatic unburned gas temperature show fluctuations on the order of 6%. Based on Figure 7-41, this change in S_L would be caused by a perturbation of +/- 1% $\lambda_{A/F}$ which seems conservative, is within the observed and published fluctuations, and produces an NIMEP change of 2%, not quite the observed variability (3.5%), but close in magnitude. Additionally, there are still other variables that will contribute to the observed combustion variability, as discussed next.

The effect of perturbations in the turbulence intensity on combustion is shown in figure 7-42. While symmetric changes in u' do not cause symmetric changes in the other variables, the asymmetry is not nearly as large as observed with variations in $\lambda_{A/F}$. Another important observation is the large effect that u' changes will have on the turbulence microscale. For example, a change in u' of +/-5% will change the microscale by up to 15%. In order for fluctuations in the turbulent intensity alone to account for the observed average changes in NIMEP, u' would have to vary by more than +/-10%. In his turbulence experiments, Witze showed variability in the turbulence intensity close to +/- 10% relative to an average value [46].

His data is shown in the Appendix (Fig. A-6) for reference. Thus, the observed numbers in this analysis are sensible.

The corresponding analysis for changes in the size of the turbulence microscale is shown in figure 7-43. To account entirely for the observed experimental average NIMEP variability, the microscale needs to vary by 30-40%. This range seems large, but data from Wakisaka et. al. shows a similar magnitude for fluctuations in the microscale [47]. Their data is also included in the Appendix (Fig. A-7) for reference. However, smaller changes in the microscale combined with the already-mentioned modest changes in the laminar flame speed will be enough to cause significant changes in the eddy-burning time, leading to large changes in the NIMEP.

As a final point of this section, and to reinforce the conclusion from section 7-4, where it was shown how a small initial variability will be amplified as the dilution increases, figures 7-44, D5, and D6 compare the effect of the same three variables on NIMEP only, across three different dilution levels. The large/rapid increase in variability as dilution increases can be observed. For example, with a 20% perturbation in the size of the microscale, the NIMEP will vary by less than 0.2% for $\lambda_{A/F}$ =1.0, but it will vary by more than a factor of 10 (2.5%) for $\lambda_{A/F}$ =1.7. The same effect is seen with detrimental changes in the other two variables (u' and $\lambda_{A/F}$). When a change in the variable tends to enhance the combustion process (speeding up the burn durations and increasing the NIMEP), such as positive changes in the turbulence or negative changes in the relative air-fuel ratio, the differences across levels of dilution are not too significant.

An integrated analysis showing simultaneous changes in turbulence parameters and relative air-fuel ratio is described in section 7.10.

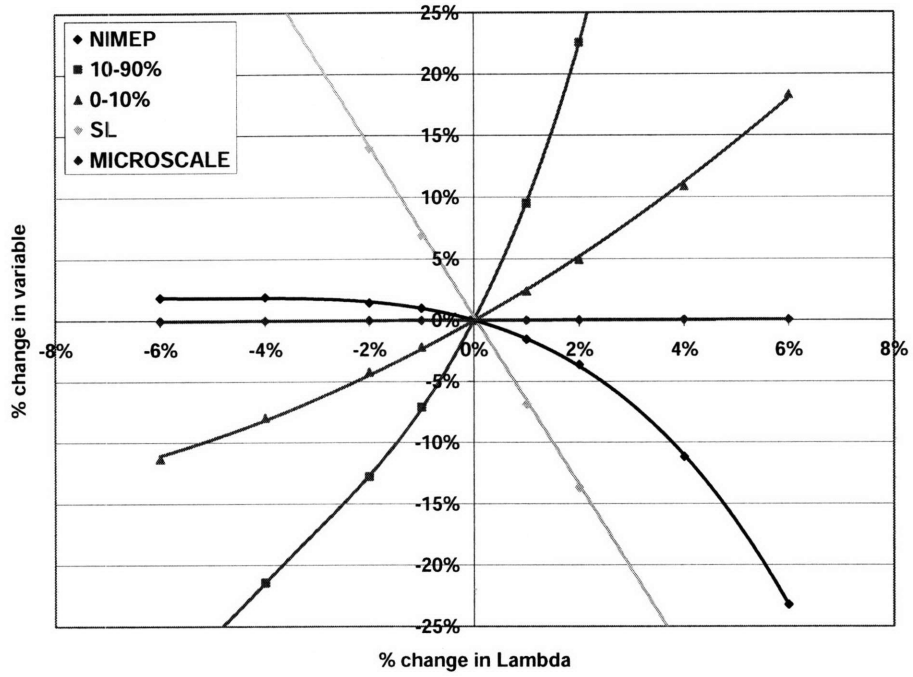

Figure 7-41 – Effect of variations in $\lambda_{A/F}$ on NIMEP, 10-90% burn duration, 0-10% burn duration, laminar flame speed, and λ_{micrsc}, relative to optimum MBT conditions (1500 RPM, r_c=9.8:1, NIMEP = 3.5 bar, λ=1.7)

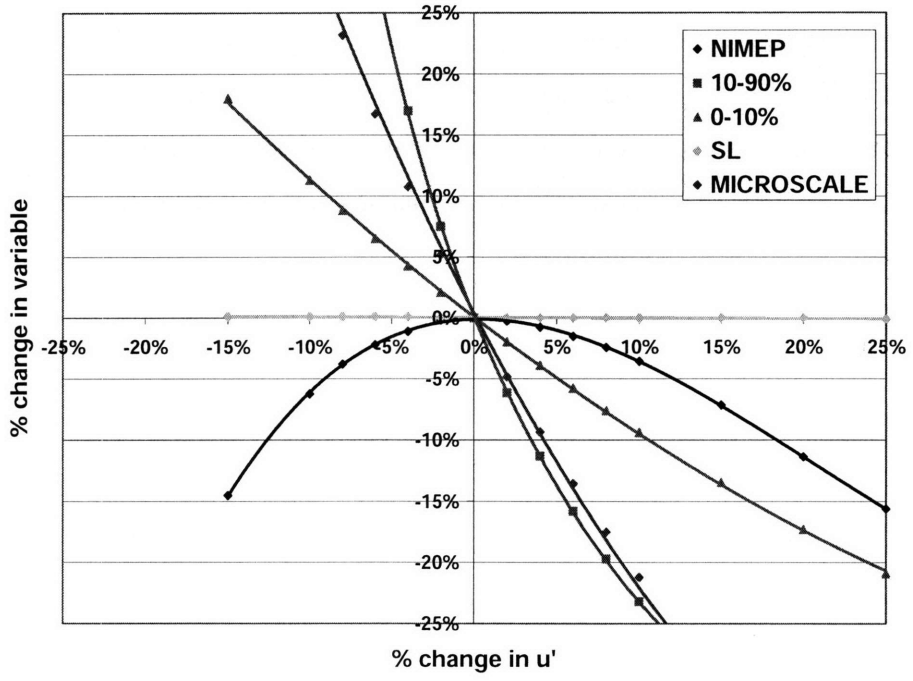

Figure 7-42 – Effect of variations in turbulence intensity on NIMEP, 10-90% burn duration, 0-10% burn duration, laminar flame speed, and λ_{micrsc}, relative to optimum MBT conditions (1500 RPM, r_c=9.8:1, NIMEP = 3.5 bar, λ=1.7)

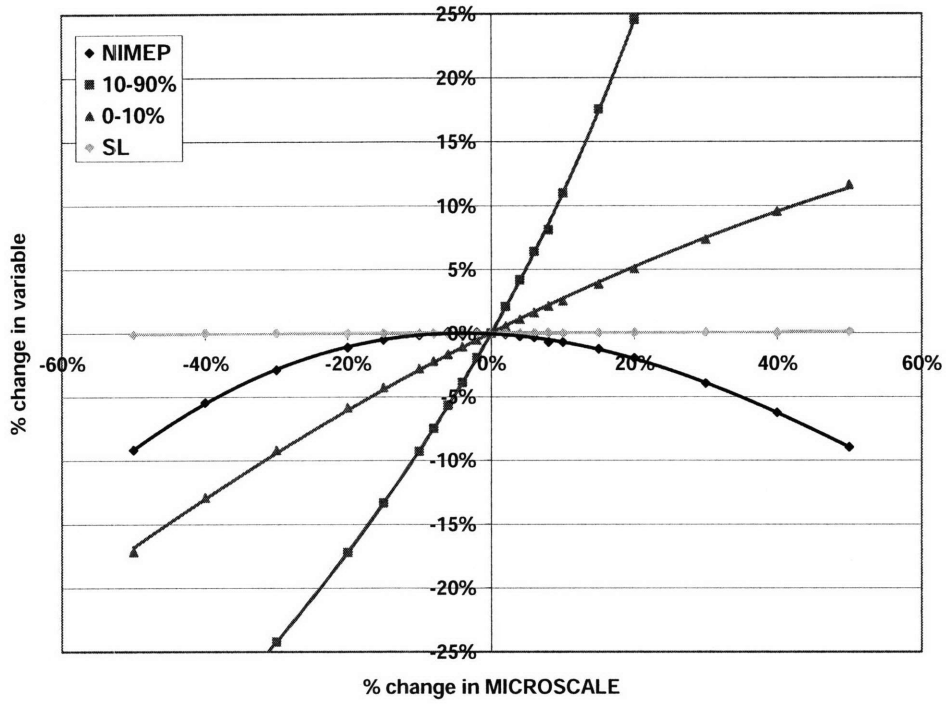

Figure 7-43 – Effect of variations in λ_{micrsc} on NIMEP, 10-90% burn duration, 0-10% burn duration, and laminar flame speed, relative to optimum MBT conditions (1500 RPM, r_c=9.8:1, NIMEP = 3.5 bar, λ=1.7)

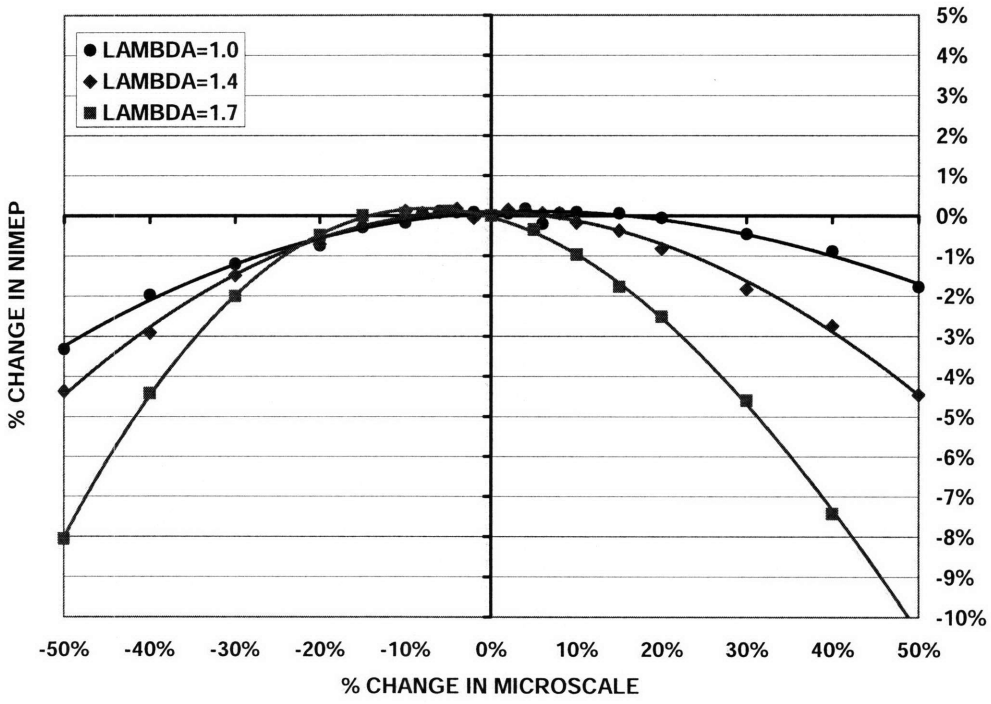

Figure 7-44 – Effect of variations in λ_{micrsc} on NIMEP, relative to optimum MBT conditions (1500 RPM, r_c=9.8:1, NIMEP = 3.5 bar), for $\lambda_{A/F}$=1.0, 1.4, 1.7

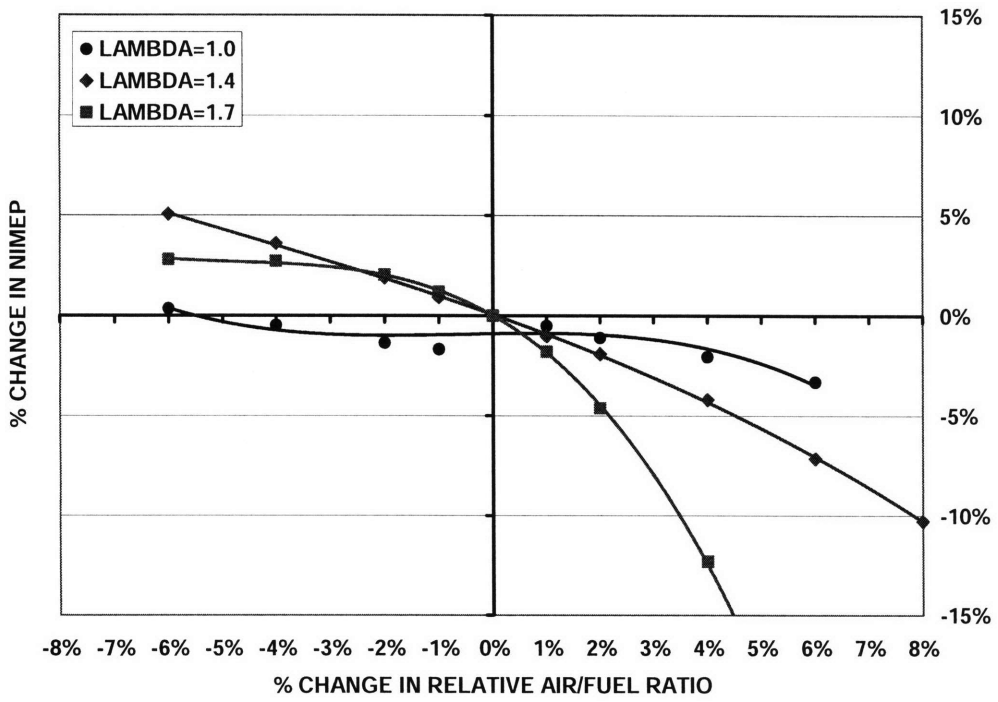

Figure 7-45 – Effect of variations in $\lambda_{A/F}$ on NIMEP, relative to optimum MBT conditions (1500 RPM, r_c=9.8:1, NIMEP = 3.5 bar), for $\lambda_{A/F}$=1.0, 1.4, 1.7

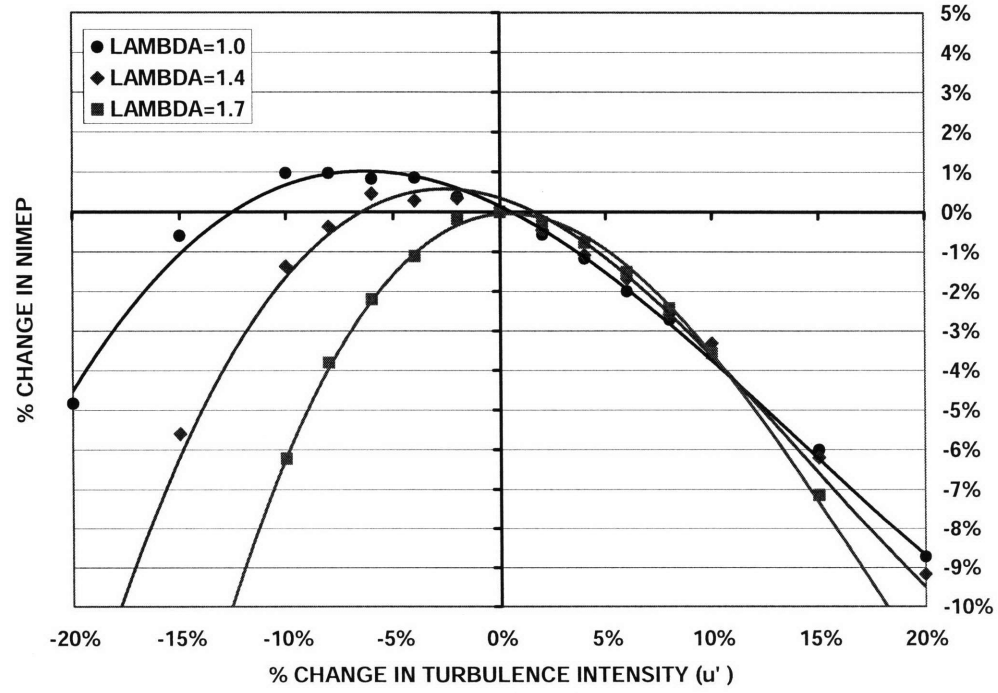

Figure 7-46 – Effect of variations in turbulence intensity on NIMEP, relative to optimum MBT conditions (1500 RPM, r_c=9.8:1, NIMEP = 3.5 bar), for $\lambda_{A/F}$=1.0, 1.4, 1.7

7.10 Effect of Turbulence on Variability

Having studied the independent effect of single variable perturbations on combustion, the next step is to perform integrated simulations with simultaneous perturbations across more than one variable. Two different cases are compared, a baseline case where only perturbations in the relative air-fuel ratio are incorporated (+/- 1% in $\lambda_{A/F}$), and a second case which adds perturbations in the microscale (+/- 1% in $\lambda_{A/F}$ plus +/-20% in microscale). These values were chosen as representative of real perturbations, based on the discussion from section 7.9.

This comparison confirms how a decreasing laminar flame speed will amplify the effect of the initial combustion variability. Turbulence intensity has remained constant for this analysis although it is important to note that because the microscale is greatly affected by the turbulence intensity, the conclusions from this analysis indirectly apply to changes in turbulence intensity as well. A symmetric distribution for the perturbations of each variable has been applied. For the first case, for example, $\lambda_{A/F}$ was perturbed by +/- 1%. All three results (2 perturbed cases plus 1 baseline case) where then averaged. The spread in the three points relative to the average was then calculated. The ratio of this number to the NIMEP was defined as the simulated variability in NIMEP. This methodology was followed to stay as consistent as possible with the COV of NIMEP definition. Similarly, for the second case, which includes simultaneous perturbations of the relative air-fuel ratio (+/- 1%) and of the microscale +/- 20%), 4 symmetric scenarios (2 x 2) plus the baseline case were averaged. Figure 7-47 shows the results. For each case the variability has been plotted. The first case, with the lower initial variability, extends out further in the relative-air-fuel ratio scale, compared to the second case, before the combustion variability rises rapidly. At a relative air-fuel ratio of 1.8, the variability in NIMEP for the first case has reached 2% of the average NIMEP value. The second case on the other hand, reaches 2% variability in NIMEP already at lambda of 1.6. Thus, keeping the same dilution conditions, including the same perturbation in dilution for both cases, will result in different lean limits, or different critical points where variability rises rapidly. This confirms how a decreasing laminar flame speed will amplify the initial combustion variability, as predicted by equation 7-5. As a result of this behavior, the case with a higher initial variability (case 2), will see a larger increase in variability as dilution is increased, compared to the lower initial variability case, where the amplified variability has a lower magnitude. The location of rapid variability increase is therefore not only dependant on the laminar flame speed, but also on the turbulence microscale.

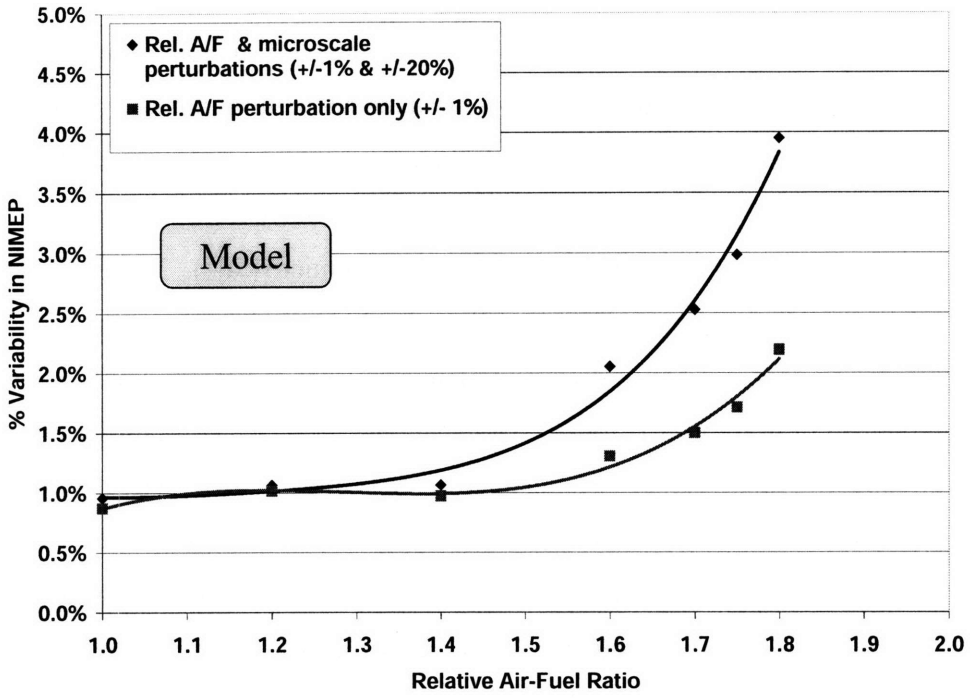

Figure 7-47 – Variability in NIMEP with relative air-fuel ratio for two sets of simulations: constant perturbations in $\lambda_{A/F}$ only (+/- 1% relative to MBT), and constant perturbations in both $\lambda_{A/F}$ and λ_{micrsc} (+/-1% and +/-20% relative to MBT); 1500 RPM, r_c=9.8:1, NIMEP = 3.5 bar

The most important point to follow from this analysis, is that variability can be controlled in two ways, increasing the laminar flame speed, as was extensively done throughout this research (see Chapter 4), or decreasing the microscale. This last variable is affected by the turbulence intensity, as shown in figure 7-42, and equation 6-17; the microscale size has also been correlated with valve lift [33]. Thus, a higher level of turbulence will not only speed up combustion but will also extend the location of the lean limit; this effect has been confirmed by past work at the Sloan Lab [14]. To stay consistent with the data shown throughout this research, engine combustion experiments with different turbulence characteristics, similar to the work done by Goldwitz, were repeated. These experiments vary the level of turbulence by introducing different restrictor plates and cones at the entrance of the inlet port as shown in Figs 2-3, 2-4, and 2-5 in Chapter 2.

Although not all the flow characteristics and fluid mechanics effects of the intake system have been studied in full rigorous detail (e.g. calculation of pressure drop across each section of intake system, Reynolds number, turbulence development length, viscous losses, etc.) all tested

configurations share the same intake system characteristics up to the location of the entrance to the inlet port; this is depicted in Chapter 2, figure 2-2, which shows a schematic of the complete inlet system, starting with the throttle valve, and continuing on to the intake valve. Additionally, two different cones which have the same inlet characteristics, differing only in the cross sectional area halfway through the cones, and at the cones' outlet, have been compared. These cones (Figs. 2-4 and 2-5), identified as deac (deactivation) and moderate (also swirl/turb), therefore share the same fluid mechanics characteristics from the throttle plate, all the way to the cone entrance, at least. This ensures that the observed relative changes between the cones, in terms of burn duration and variability during the combustion process, are caused by the differences in turbulence characteristics, caused by their nozzles (outlet), rather than by other potential fluid dynamics effects that might not have been analyzed. Goldwitz also performed careful bench experiments at Daimler Chrysler, showing the different turbulence characteristics among the various cones and plates tested. Figure 7-48 shows his data for the baseline plate used throughout this research as well as the two cones tested for this analysis.

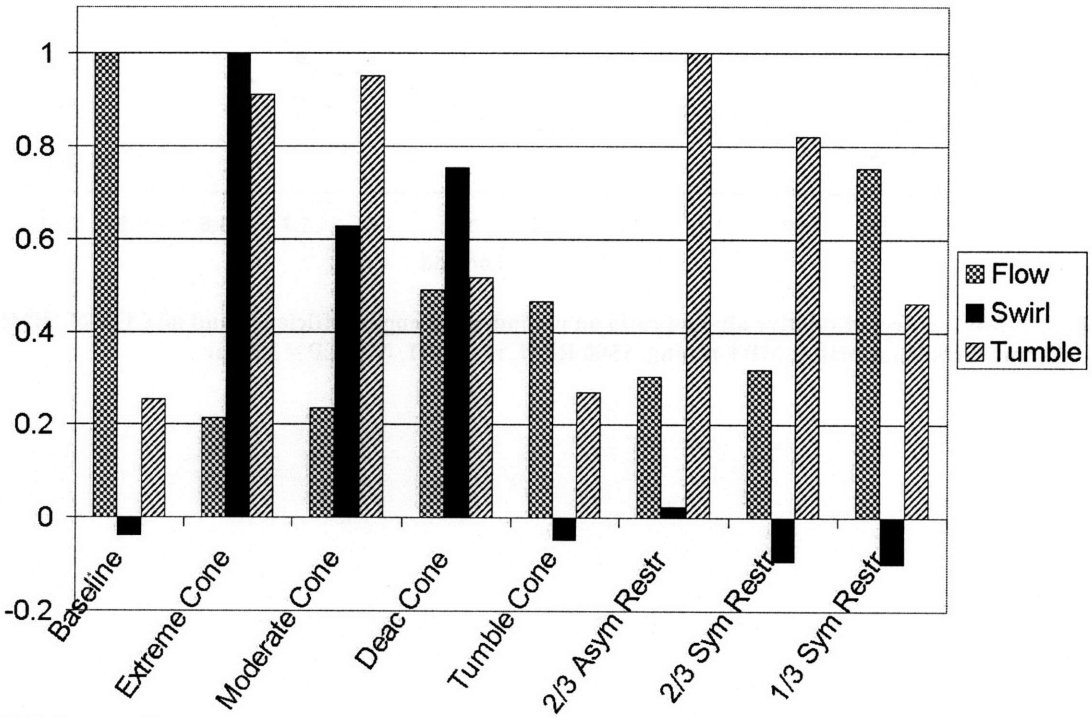

Figure 7-48, Inlet port flow rate, normalized (to flow rate) swirl torque, and tumble torque Moment plotted on a normalized scale for various inlet configurations (0.350 in Valve lift) [14]

Figure 7-49 shows the combustion results obtained with each of the two different cones mentioned. The swirl cone, which has the higher flow velocity and higher tumble moment relative to its flow, has lower burn durations (both 0-10% and 10-90%) and a higher extension of the lean limit, compared to the deactivation cone. Thus, with the lower turbulence cone, variability grows faster, and reaches the lean limit faster than the higher turbulence cone. This is consistent with a higher turbulence causing a smaller microscale, which reduces combustion variability as was just discussed.

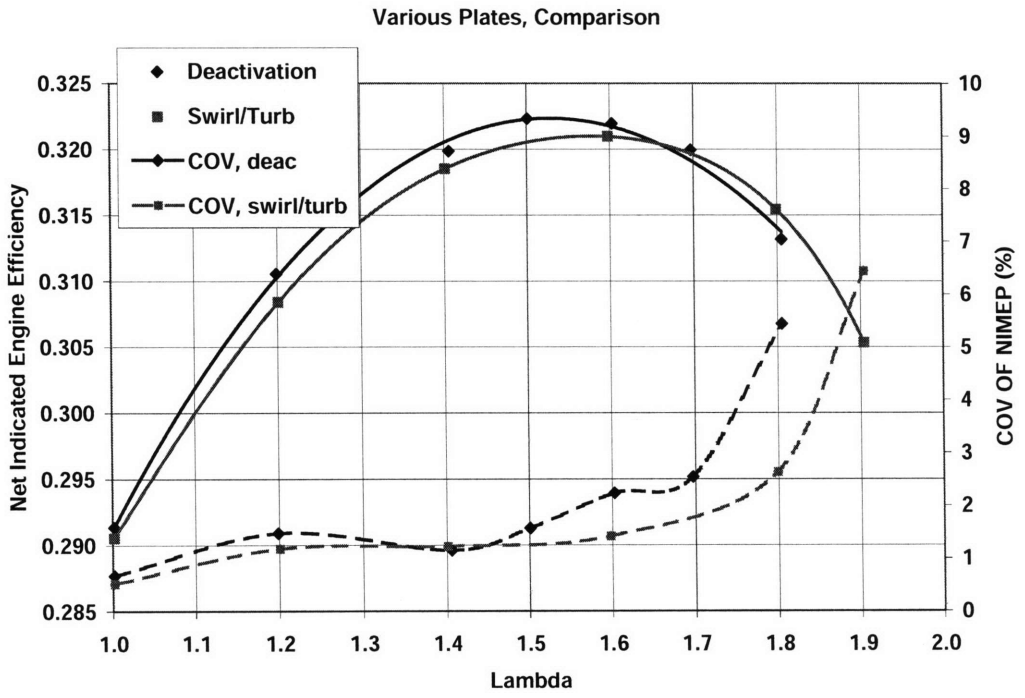

Figure 7-49 – Effect of relative air-fuel ratio on net indicated engine efficiency and on COV of NIMEP for two different turbulence plates; MBT timing, 1500 RPM, r_c=13.4:1, NIMEP = 3.5 bar

7.11 Dimensionless number at critical conditions

Section 7.4 identified a critical laminar flame speed at the onset of rapid combustion variability. The sudden rise in variability occurs because the variability in eddy burning time is proportional to $1/S_L$. Thus, with increasing dilution (i.e., decreasing laminar flame speed) an asymptotic behavior in variability is expected. Where this asymptote occurs however, depends on a combination of parameters. For example, figure 7-50 shows how the size of the microscale will affect the location of the sudden rise in eddy-burning time (ratio of λ_{micrsc} to S_L) and consequently the sudden rise in eddy-burning time variability (equation 7-5). At the given baseline conditions, and for a microscale of 0.05 cm, the sudden rise in variability occurs at a laminar flame speed of around 15 cm/sec. All else equal, when the microscale is doubled, the sudden rise in variability occurs at a laminar flame speed of 20 cm/sec. The exact location of the rapid rise in variability will thus be determined not only by $1/S_L$, but also by the other variables affecting equation 7-5 ($\lambda_{micrsc}, \Delta\lambda_{micrsc}, \Delta S_L$). This conclusion can be confirmed using real data. Figure 7-51 shows a comparison of two data curves at two different speeds (800 and 1500 rpm) and two different loads (2.0 bar and 3.5 bar NIMEP respectively). The slower engine speed curve reaches 2% COV in NIMEP earlier, at a lower dilution level, relative to the faster engine speed curve. This behavior is expected because at the lower engine speed, the microscale will be larger than at the higher engine speed (see equation 6-18). Thus, at the lower engine speed, initial eddy-burning time variability, as defined by equation 7-5, will be higher, reaching the COV in NIMEP earlier in terms of dilution.

In an attempt to understand when this rapid rise in variability occurs, and how it is affected with operating conditions, such as engine speed, a non-dimensional number is formulated. This number consists of normalizing the instant eddy-burning time by the combustion duration for a specified burn interval. Using 2% mass fraction burned as the normalizing time interval, there seems to be a critical value of approximately 0.57 for this non-dimensional number at the onset of rapid combustion variability:

$$\Theta_{critical} = \frac{\tau_{burn\_2\%\_mfb}}{\theta_{0-2\%}} = \frac{\lambda_{micrsc}}{S_L}\left(\frac{1}{t_{0-2\%}}\right) \approx 0.57 \qquad (7\text{-}7)$$

This number was obtained for the two different engine speeds and loads shown in figure 7-51. The laminar flame for equation 7-7 was calculated with the Rhodes-Keck correlation using experimental pressure and a calculated adiabatic unburned mixture temperature (see Fig. 7-52). The microscale and time interval were calculated with the MIT combustion model. A comparison of the model and data for 3.5 bar NIMEP and 1500 rpm was shown in Chapter 6. Figures 7-53 and 7-54 compare the model predictions against real data for the lower load (2 bar NIMEP), lower speed (800 rpm) case. The agreement between the model and the data is acceptable.

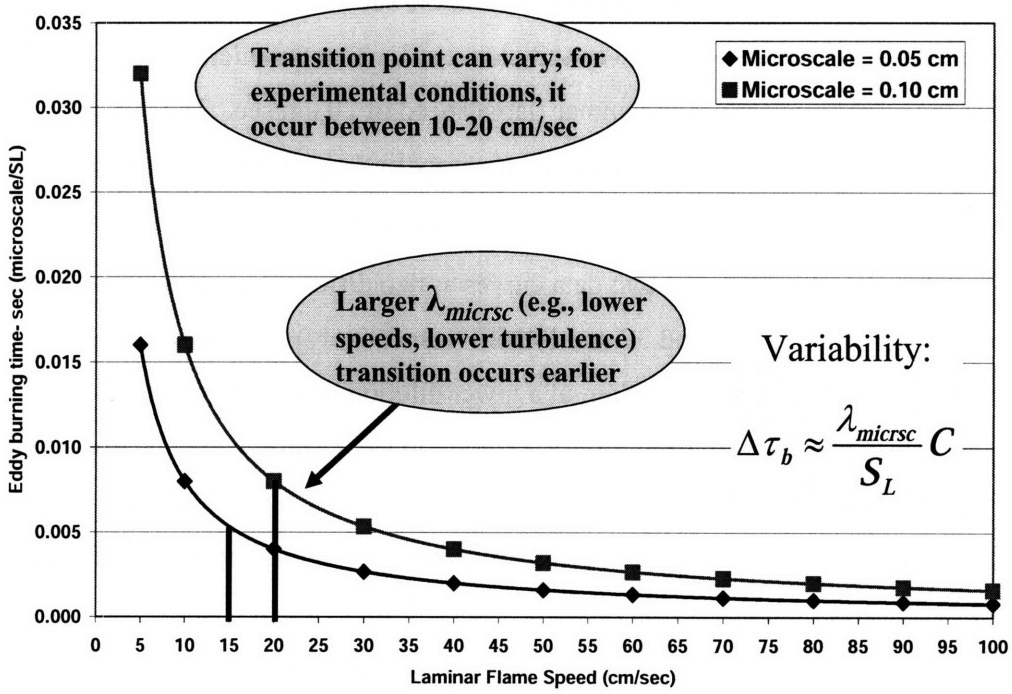

Figure 7-50 – Effect of microscale size on the exact location of the rapid increase in eddy burning time, and eddy-burning time variability, as the laminar flame speed decreases (simulation)

It is unclear based on model-predicted numbers, for equation 7-7, whether a common limiting non-dimensional number captures the physics. The predicted non-dimensional number decreases with dilution; however, as the engine speed increases, at constant dilution, the predicted number decreases as well. This would indicate that a critical value for the dimensionless number would be reached earlier for the higher speed, relative to the lower speed. This is the opposite behavior from what was shown with real data in figure 7-51. Further investigation is needed to draw

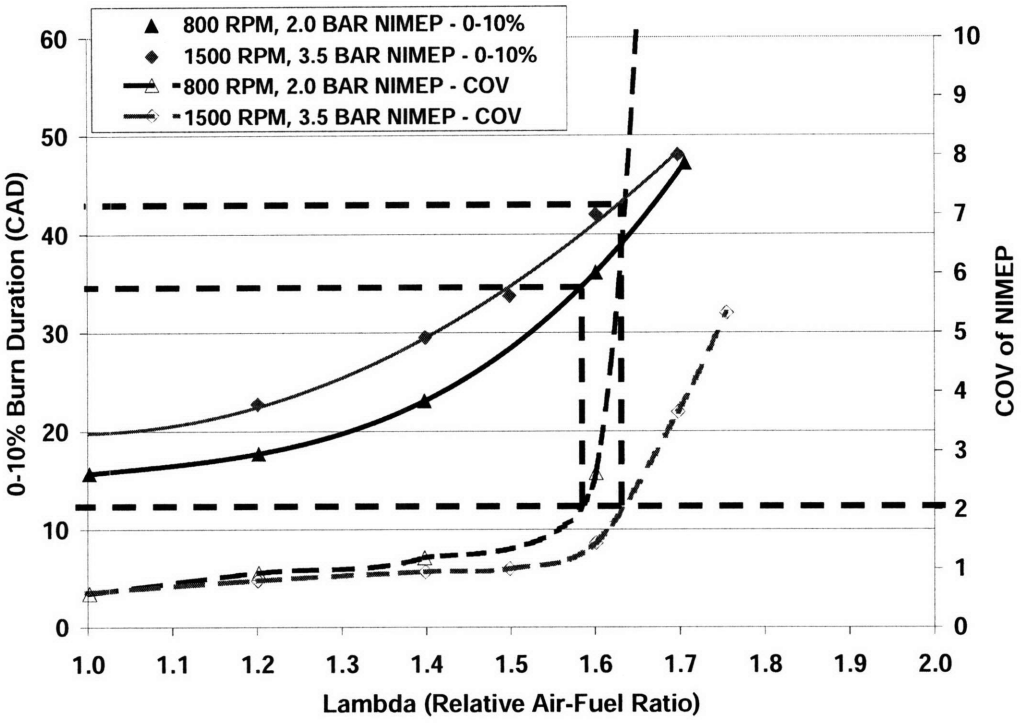

Figure 7-51 – Comparison of location of rapid increase in NIMEP variability with increasing dilution, for two cases with different engine speeds and loads

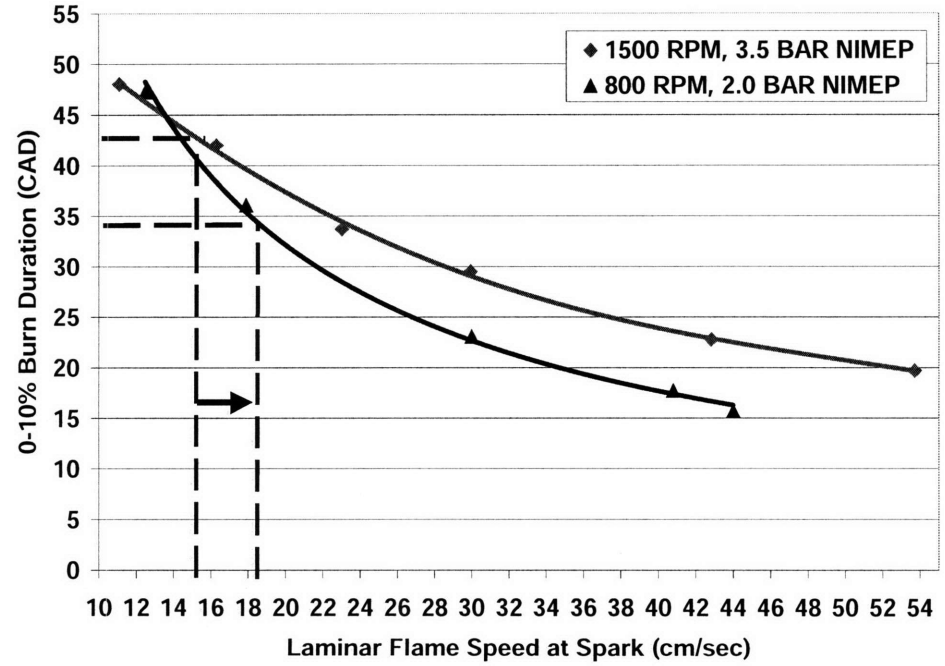

Figure 7-52 – Comparison of calculated laminar flame speed at the location of rapid rise in combustion variability for two cases with different engine speeds and loads

strong conclusions, and better formulate/validate a dimensionless number that can capture the conditions at the lean limit for various engine operating conditions.

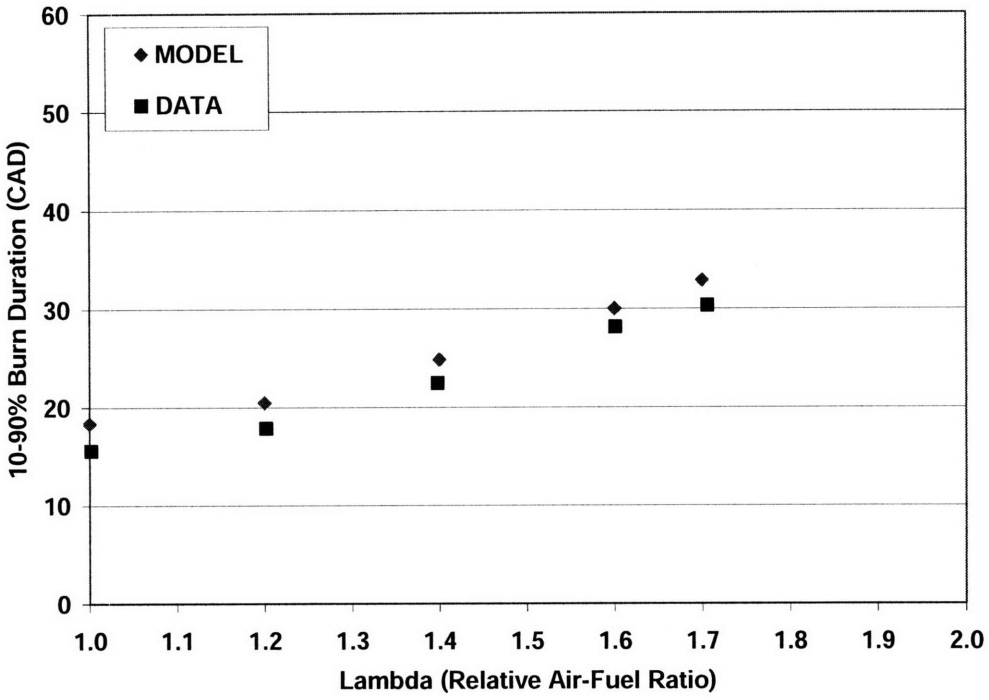

Figure 7-53 – Comparison of 10-90% burn duration model predictions and real data with increasing dilution for 800 rpm, 2.0 bar NIMEP, Rc=9.8:1

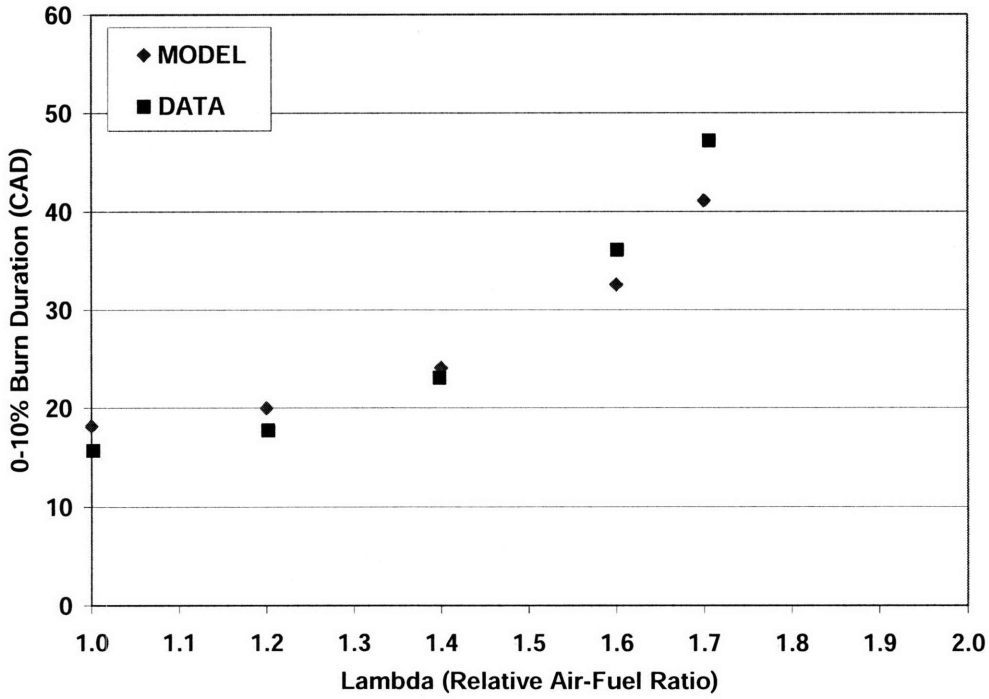

Figure 7-54 – Comparison of 0-10% burn duration model predictions and real data with increasing dilution for 800 rpm, 2.0 bar NIMEP, Rc=9.8:1

(this page was intentionally left blank)

Chapter 8 – HYDROGEN ENHANCEMENT, PRACTICAL CONSIDERATIONS

One of the goals of this research is to apply the fundamental understanding of lean combustion to the design of a hydrogen-enhanced engine. Chapter 5 already discussed results that serve this purpose. The effect of hydrogen enhancement was studied for air and EGR dilution, for different compression ratios, and for different loads. A comparison between the performance of pure hydrogen enhancement and plasmatron enhancement was also observed. The main conclusions from that chapter were that there are tradeoffs to using plasmatron enhancement with air vs. EGR, and that plasmatron enhancement has diminishing returns at high pressures. The reader is referred to Chapter 5, and in particular section 5.3 for a discussion of these conclusions. Other practical considerations of hydrogen-enhanced combustion using plasmatron include a previously observed diminishing returns effect at high levels of dilution, as well as other methods to decrease variability and extend the peak efficiency limit and the lean limit. These considerations are discussed in this Chapter.

8.1 Diminishing Returns of Hydrogen Enhancement at Leaner Baseline Peak Efficiency

During his research, Goldwitz identified a diminishing returns trend for the extension of peak efficiency. Goldwitz observed that as the $\lambda_{A/F}$ for baseline peak efficiency conditions increased (i.e., as efficiency peaked at leaner conditions), the effectiveness of the enhancement, in extending this location of peak efficiency, decreased. Figure 8-1 below shows this trend. The data includes experiments with different levels of enhancement, and different turbulence plates. Similar results were done during this research, with pure hydrogen enhancement, at MBT conditions, with a compression ratio of 13.4:1, and a load of 3.5 bar NIMEP. The results, shown in figure 8-2 are not easy to interpret, for they are subject to interpolation errors. The extension in peak efficiency, keeping the level of turbulence the same, seems about constant across different levels of pure hydrogen enhancement. However, a diminishing returns effect seems to appear as one compares across different levels of turbulence (figure 8-3), similar to Goldwitz' observations). To settle this issue, MIT's combustion model was used. Simulations were run for two different levels of turbulence. For one case, the baseline turbulence intensity multiplier was used, and for the second case the baseline turbulence intensity multiplier was scaled down by 80%. Figure 8-4 shows the efficiency and burn durations of these two cases as the relative air-

fuel ratio increases. The first point to notice from this chart is that the higher turbulence case has its peak efficiency at a higher relative air-fuel ratio compared to the lower turbulence case. As explained in Chapter 4, this is consistent with a lower 10-90% burn duration for the higher turbulence case.

In figure 8-5, hydrogen enhancement has been simulated by increasing the value of the laminar flame speed by 45%, and then doing a $\lambda_{A/F}$ sweep at MBT conditions, 1500 rpm, 3.5 bar NIMEP and compression ratio of 9.8:1. This yields an extension in the peak efficiency of approximately 0.08 lambdas. The same simulation is done for the higher turbulence case, as shown in figure 8-6. The improvement for this case is lower, approximately 0.05 lambdas. These results are again open to different interpretations depending on how the efficiency is interpolated. Different efficiency extensions will derive from different interpretations, but a diminishing returns effect will still be present, although perhaps smaller than what is shown in figure 8-7. This effect can be explained as follows: at higher dilutions, the absolute increase in the laminar flame speed with dilution will be lower than the absolute increase obtained with lower dilutions. Although the percent increase in laminar flame speed as enhancement is added under lean conditions might be the same as is achieved under less lean conditions, the absolute change is what is important for an absolute efficiency extension. The results are all consistent with the data.

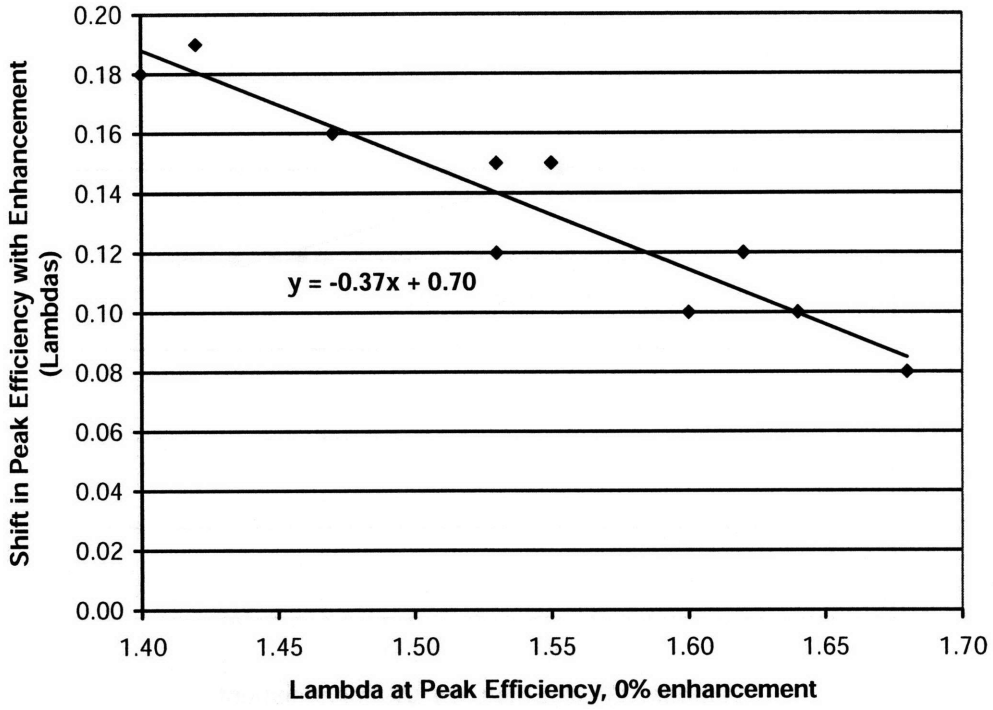

Figure 8-1 –Extension of peak efficiency with 20% plasmatron enhancement vs. baseline (non-enhanced) location of peak efficiency; MBT timing, 1500 RPM, r_c=9.8:1, constant fuel flow, various turbulence plates, various ignition systems, and various injectors (from Goldwitz thesis)

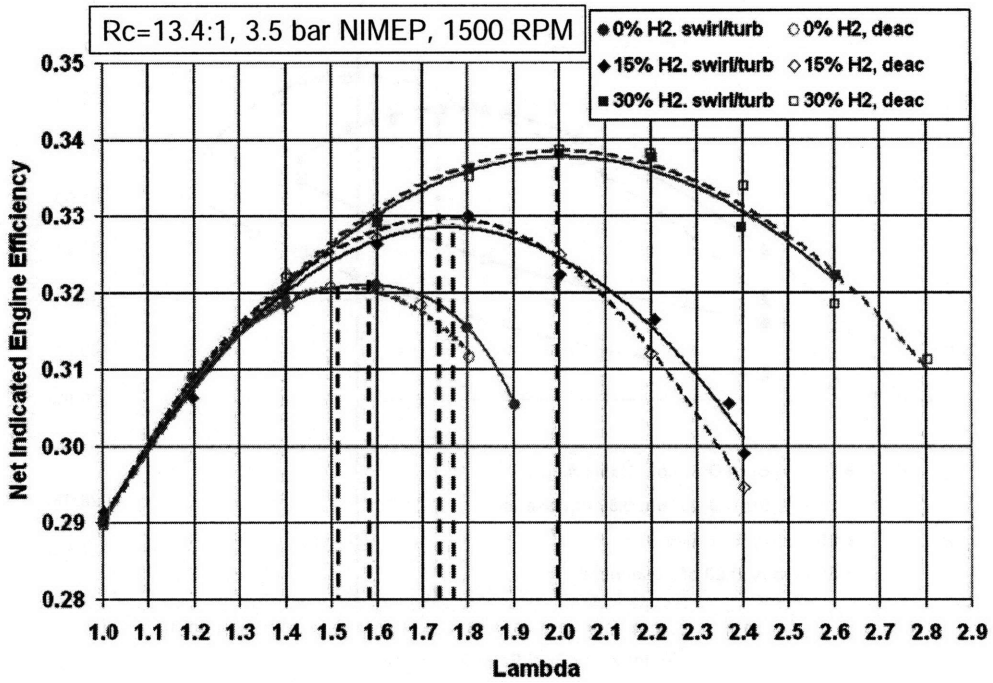

Figure 8-2 –Extension of peak efficiency with 15%, and 30% pure hydrogen enhancement vs. baseline (non-enhanced) location of peak efficiency for two levels of turbulence; MBT timing, 1500 RPM, r_c=13.4:1, 3.5 bar NIMEP, three turbulence cones, real data

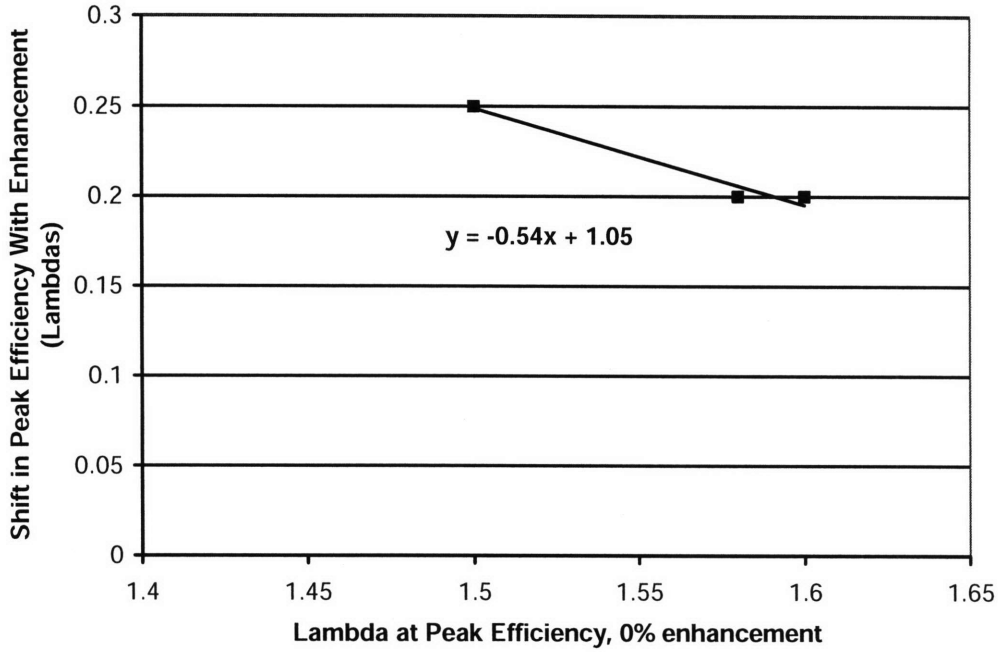

Figure 8-3 –Extension of peak efficiency with 15% pure hydrogen enhancement vs. baseline (non-enhanced) location of peak efficiency; MBT timing, 1500 RPM, r_c=13.4:1, 3.5 bar NIMEP, three turbulence cones, real data

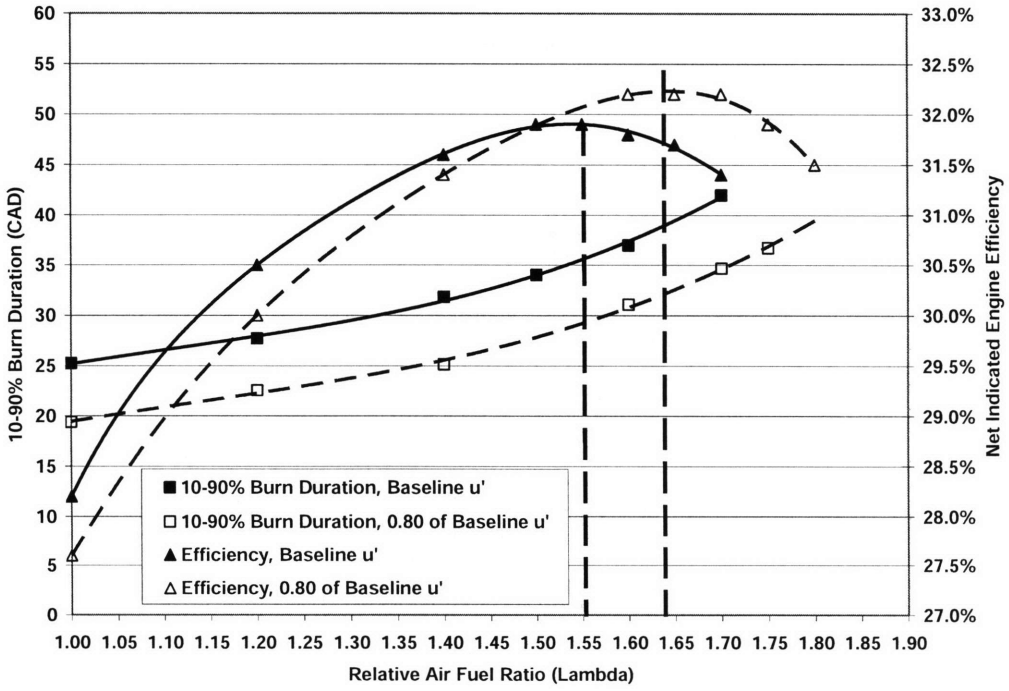

Figure 8-4 – Model comparison of net indicated engine efficiency, and 10-90% burn duration with relative air-fuel ratio for two turbulence levels (baseline u' and 80% u'); MBT timing, 1500 RPM, r_c=9.8:1, 3.5 bar NIMEP

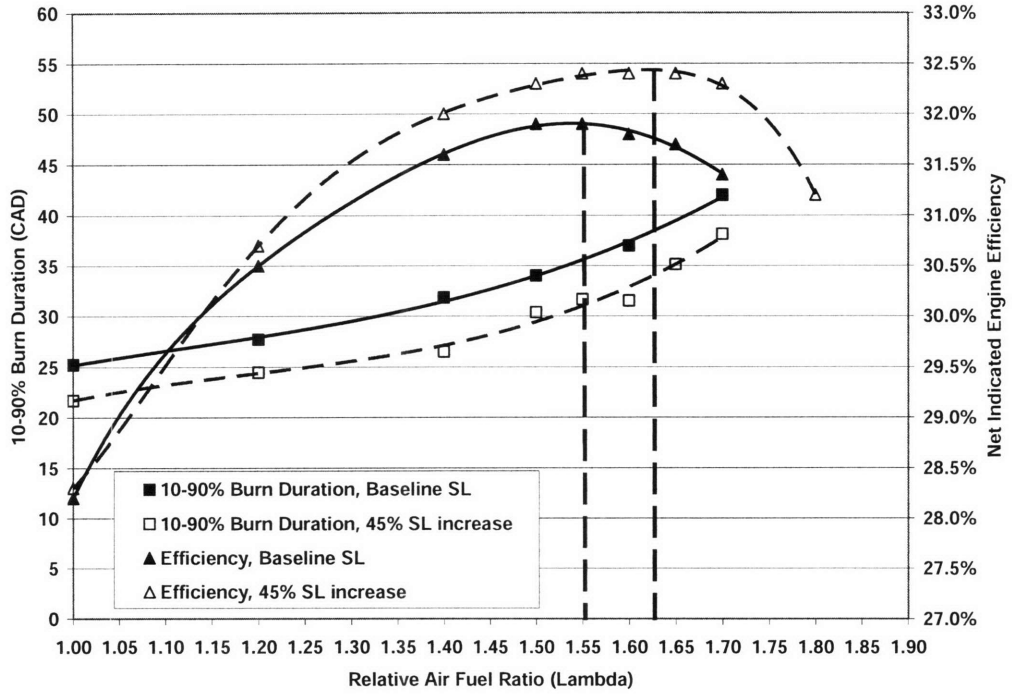

Figure 8-5 – Model comparison of net indicated engine efficiency, and 10-90% burn duration with relative air-fuel ratio for constant turbulence (baseline u') with simulated enhancement (baseline SL and 1.45 SL); MBT timing, 1500 RPM, r_c=9.8:1, 3.5 bar NIMEP

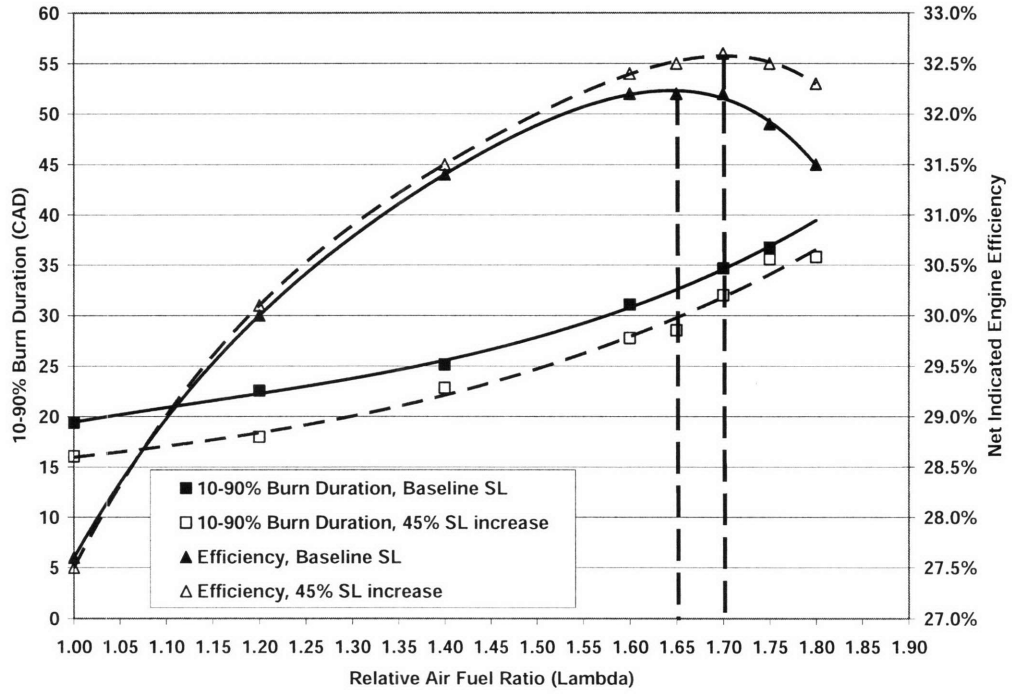

Figure 8-6 – Model comparison of net indicated engine efficiency, and 10-90% burn duration with relative air-fuel ratio for constant turbulence (0.80u') with simulated enhancement (baseline SL and 1.45 SL); MBT timing, 1500 RPM, r_c=9.8:1, 3.5 bar NIMEP

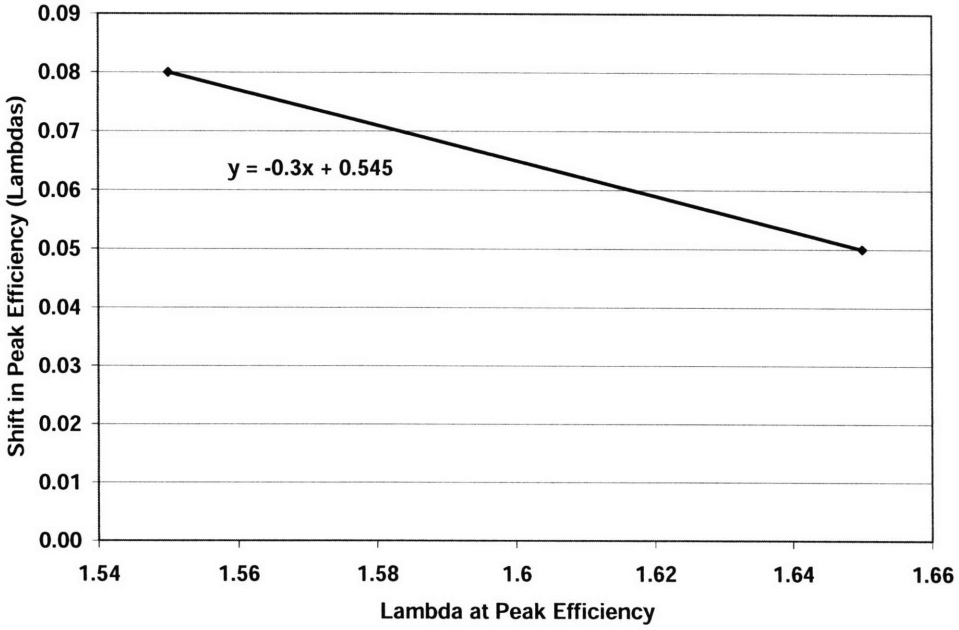

Figure 8-7 – Shift in peak efficiency with simulated enhancement vs. location of baseline (no enhancement) peak efficiency (results from figures 8-5 and 8-6); MBT timing, 1500 RPM, r_c=9.8:1, 3.5 bar NIMEP

Chapter 9 – SUMMARY AND CONCLUSIONS

9.1 Experimental Trends and Efficiency

- An extensive database of lean and hydrogen-enhanced SI engine combustion experiments was generated for a wide variety of operating conditions. The type of dilution, the amount and type of hydrogen enhancement, the compression ratio, and the load, were all varied.
- A framework was developed for analyzing the effects of air-fuel ratio on engine efficiency. These effects are lengthening burn duration, increasing ratio of specific heats (gamma/thermodynamic effect), decreasing pumping losses, and decreasing heat transfer losses. The summation of the individual process effects on efficiency in the framework gives good agreement with the data under a wide range of conditions. This indicates that the proposed framework is a useful tool that both provides fundamental knowledge about the variation of efficiency with air-fuel ratio, and predicts accurate results.
- With increasing air-fuel ratio, efficiency increases to a maximum value, and then decreases. A lengthening burn duration is the dominant detrimental effect on efficiency, and it determines the shape of the efficiency curve.
- As the air-fuel mixture becomes leaner/more diluted, a limiting 10-90% burn duration of 30 CAD was found at the location of peak efficiency, irrespective of operating conditions; this implies that the 10-90% burn duration "limits" efficiency, and that combustion deteriorates significantly beyond this 30 CAD, offsetting any efficiency gains from thermodynamic effects, reduced pumping work, or reduce heat transfer losses.
- As the air-fuel mixture becomes leaner/more diluted, a limiting 0-10% burn duration of 40 CAD was found at a 2% coefficient of variation (COV) of NIMEP; as explained in the fundamentals section, this is caused by a limiting laminar flame speed at the onset of rapid combustion variability.
- The 10-90% and 0-10% burn durations are well correlated: as the 0-10% burn duration increases, the 10-90% burn duration increases at a decreasing rate. The form of this correlation is rooted in the dependence of each of these burning intervals on the laminar flame speed and turbulence.

- Independent of combustion variability, the fundamental factor that determines the decrease in engine efficiency at high air-fuel ratio is a lengthening burn duration
- With increasing air-fuel ratio, combustion variability has no significant impact until after the location of peak efficiency. Beyond this point, it plays an increasing role.
- The maximum impact of variability on engine efficiency under lean conditions was found to be about 2-3%.

9.2 Fundamental Modeling and Variability

The mechanism to explain increasing combustion variability with increasing dilution has been developed:

- A flame entrainment combustion model, similar to the one originally developed by Blizard and Keck, was used and extended; the model has good agreement with the data, indicating that the physics are captured accurately.
- As combustion progresses, cycle-to-cycle burn duration variability increases due to combustion phasing differences, originating in the flame development stage (eddy-burning time variability). Slow burning (effectively retarded) cycles will continue to burn slowly, as the pressure and temperature increase at a slower rate. Faster burning (effectively advanced) cycles will continue to burn faster, as the pressure and temperature increase faster. Initial variability will grow, causing larger differences in the 10-90% burn duration and in the NIMEP.
- Symmetric fluctuations in the flame initiation process will cause asymmetric changes in later parts of the combustion process (i.e., in the 10-90% burn duration, and consequently, in NIMEP). The asymmetry is modest for small fluctuations and fast burning mixtures. However, for large but symmetric flame initiation spread, and slow burning mixtures, the asymmetry in the main burning angle (10-90% burn duration) will increase significantly.
- As a mixture burns slower (leaner/more dilute) and/or as the initial spread in the duration of the flame initiation grows, the variability in the 10-90% burn duration and NIMEP becomes increasingly asymmetric.

- The rapid rise in combustion variability as a mixture becomes leaner/more diluted is due to a decreasing laminar flame speed and the eddy burning time's inverse dependence on the laminar flame speed. With increasing dilution, this dependence will cause a steady and then rapid increase in the flame initiation variability. For the experimental engine, which operates at 1500 rpm, this limiting laminar flame speed, ~15 cm/sec, at the given level of turbulence, produced a 0-10% burn duration of close to 40 CAD
- At constant engine speed, the exact location of the sudden rise in variability will be affected by the size of the microscale, and the fluctuations in the microscale and the laminar flame speed.
- Preliminary analyses suggest that a dimensionless number, which incorporates engine speed and eddy-burning time, can be used to predict the location of the rapid rise in combustion variability. Further validation is required.

9.3 Plasmatron Concept and Practical Applications

- Under high pressures, hydrogen enhancement using plasmatron, has high rates of diminishing returns, compared to hydrogen enhancement using pure hydrogen. This comparison will be true on an equal percent of total energy provided by hydrogen. The added diluents are quite detrimental. Therefore, the benefits from plasmatron addition at high compression ratios and high loads will be marginal. At low pressures, the plasmatron enhanced experiments do not show signs of diminishing returns. There is a continuous decrease of the burn duration with increasing amounts of enhancement.
- All else equal, the absolute increase of laminar flame speed with enhancement will decrease with increasing dilution. This means that faster-burning engines that have peak efficiency at high lambdas, will see a lesser extension in the peak efficiency through plasmatron enhancement than slower-burning engines which peak at lower lambdas
- All else equal, a faster laminar flame speed will decrease combustion variability
- Engine variability for lean conditions with or without enhancement can be decreased by first decreasing the baseline variability of the engine running at stoichiometric conditions. This can be done in a few ways:
    - Increasing the level of turbulence. This will have the effect of decreasing the microscale structure which directly affects the variability of the engine

- Decreasing the lift. This will also have the effect of reducing the size of the microscale
- Design engines to run more homogeneous, reducing mixture and flow variability
- In the presence of normal non-homogeneities, injecting hydrogen near the spark plug, as suggested by Smaling [48], might be more effective at reducing the variability under lean conditions
- Other potential fixes, include adding a second spark plug, reducing the variability and the burning time

References

1. Noguchi, M., Sanda, S., and Nakamura, N., "Development of Toyota Lean burn Engine," SAE paper no. 760757, 1976.
2. Smaling, "High Efficiency Clean Combustion and Waste Heat Recovery for Internal Combustion Engines," Proposal to the U.S. Department of Energy, July 25, 2004.
3. Stein, R., Tachih, C., Lyjak, J., "The Combustion System of the Ford 5.4L 3-Valve Engine," Technical Paper presented at the September 2003, Powertrain Conference, Dearborn MI.
4. Ivanic, Z., Ayala, F., Goldwitz, J., Heywood, J., "Effects of Hydrogen Enhancement on Efficinecy and NOx emissions of Lean and EGR-Diluted mixtures in a SI Engine." SAE 2005-01-0253.
5. Green, J.B., Domingo, N., Storey, J.M.E., Wagner, R.M., J.S. Armfield, Bromberg, L., Cohn, D.R., Alexeev, N., "Experimental Evaluation of SI Engine Operation Supplemented by Hydrogen Rich Gas from a Compact Plasma Boosted Reformer." SAE paper 2000-01-2206.
6. Germane, G., Wood, C., "Lean Combustion in Spark-Ignited Internal "Combustion Engines – A Review" SAE paper no. 831694, 1983.
7. Notes from Professor James Keck, 2006
8. Chevron Phillips UTG-96, Certificate of Analysis.
9. Quader A. A., "What Limits Lean Operation in spark ignition engines, flame initiation or propagation?" SAE paper 760760.
10. Varde, K. S., "Combustion characteristics of small spark ignition engines using hydrogen supplemented fule mixtures." SAE paper 810921.
11. Arici, O., Tabaczynski, R. J., Arpaci, V. S., "A Model for the Lean Misfire Limit in Spark-Ignition Engines," Combustion Science and Technologies, 1983 Vol., 30 pp. 31-45.
12. Noguchi, M., Sanda, S., and Nakamura, N., "Development of Toyota Lean Burn Engine," SAE paper no. 760757, 1976.
13. Tully, E., Heywood, J., "Lean Burn Characteristics of a Gasoline Engine Enriched with Hydrogen form a Plasmatron Fuel Reformer." SAE 2003-01-0630.
14. Goldwitz, J., Heywood, J., "Combustion Optimization in a Hydrogen-Enhanced Lean Burn SI Engine." SAE 2005-01-0251.
15. Ayala, F.A., Gerty, M.D., Heywood, J.B., "Effects of Combustion Phasing, Relative Air-Fuel Ratio, Compression Ratio, and Load on SI Engine Efficiency," SAE 2006 World Congress, Detroit, MI, SAE paper 2006-01-0229.
16. Quader A., Kirwan J. E., James G. M., "Engine performance and emissions near the dilute limit with hydrogen enrichment using an on-board reforming strategy," SAE paper 2003-01-1356.
17. Rhodes, D.B., and Keck, J.C., "Laminar Burning Speed Measurements of Indolene-Air-Diluent Mixtures at High Pressures and Temperatures," SAE paper 850047, International Congress & Exposition, Detroit, MI, Feb. 25 – Mar. 1, SAE Trans., Vol. 95, 1985
18. Dai, W., Davis, G.C., Hall, M.J., Matthews, R.D., "Diluents and Lean Mixtures Combustion Modeling for SI Engines with a Quasi-Dimensional Model," SAE paper 952382.
19. Yu, G., Law, C.K., Wu, C.K., "Laminar Flame Speeds of Hydrocarbon Plus Air Mixtures with Hydrogen Addition," Combustion and Flame, Volume 63, Issue 3, March 1986, pages 339-347.
20. GRI Mech, 2.11 website: (http://diesel.me.berkeley.edu/~gri_mech/new21/version21/text21.html)
21. Poulos, S. G., and Heywood, J.B., "The Effect of Chamber Geometry on Spark Ignition Engine." SAE Paper 830587, 1983.
22. Heywood, J.B., Internal Combustion Engine Fundamentals, McGraw Hill, New York, 1988.
23. Cheng, W.K., Hamrin, D., Heywood, J.B., Hochgreb, S., Min, K, and Norris, M., "An Overview of Hydrocarbon Emissions Mechanisms in Spark-Ignition Engines," SAE paper 932708, presented at the SAE Fuels and Lubricants Meeting and Exposition, Philadelphia, PA, October 18-21, SAE Trans., Vol. 102, 1993.

24. Ozdor, N., Dulger, M., and Sher, E. "Cyclic Variability in Spark Ignition Engines: A Literature Survey," SAE paper 940987, 1994.
25. Muranaka, S., Takagi, Y., and Ishida, T., "Factors Limiting the Improvement in Thermal Efficiency of S.I. Engine at Higher Compression Ratio," SAE 870548.
26. Smaling, R.M., "System architecture selection in a multi-disciplinary system design optimization framework," Masters Thesis, Technology and Policy Program, MIT, 2003.
27. Blizard, N.C., Keck, J. C., "Experimental and Theoretical Investigation of Turbulent Burning Model for Internal Combustion Engines," SAE Paper 740191, SAE Automotive Engineering Congress, February 25 – March 1, 1974; SAE Transactions, Vol. 83, 1974.
28. Tabaczynski R. J., Trinker F. H., Shannon B. A. S., "Further refinement and validation of a turbulent flame propagation model for spark-ignition engines," *Combustion and Flame*, volume 29, Issue 2, October 1980, Pages 111-121.
29. Poulos, S.G., "The effect of combustion chamber geometry on S.I. engine combustion rats: a modeling study," Masters Thesis, Department of Mechanical Engineering, MIT, 1982.
30. Gerty, M.D., "Effects of operating conditions, compression ratio, and gasoline reformate on SI engine knock limits," Masters Thesis, Department of Mechancial Engineering, MIT, 2005
31. Keck, J.C., Heywood, J.B., and Noske, G., "Early Flame Development and Burning Rates in Spark Ignition Engines and Their Cyclic Variability," SAE paper 870164, 1987.
32. Wong, V.W., and Hoult, D.P., "Rapid Distortion Theory Applied to Turbulent Combustion," SAE paper 790357, SAE Congress & Exposition, Detroit, MI, February 26-March 2, 1979; SAE Transactions, Vol. 88 1979.
33. Keck, J.C., "Turbulent Flame Structure and Speed in Spark-Ignition Engines," Proceedings of Nineteenth Symposium (Int'l) on Combustion, The Combustion Institute, pp. 1451-1466, 1982.
34. Tennekes H., "A first course in turbulence," Cambridge, Mass., MIT Press 1972.
35. Tabaczynski, R.J., Ferguson, C.R., Radhakrishnan, K., "A turbulent Entrainment Model for Spark-Ignition Engine Combustion," SAE paper 770647.
36. Hires, S.D., Tabaczynski, R.J., Novak, J.M., "The prediction of ignition delay and combustion intervals for a homogeneous charge, spark ignition engine," SAE Paper 780232, SAE Transactions, Vol 87, 1978.
37. Fox, J.W., Cheng, W.K., Heywood, J.B., "A Model for Predicting Residual Gas Fraction in Spark-Ignition Engines," SAE paper 931025, SAE International Congress and Exposition, Detroit, MI, March 1-5, SAE Trans., vol. 102, 1993.
38. Beretta, G.P., Rashidi, M., Keck, J.C., "Thermodynamic Analysis of Turbulent Combustion in a Spark Ignition Engine. Experimental Evidence," Western States Section, The Combustion Institute, 1980 Spring Meeting, 21-22 April 1980.
39. Smith, J.R., "The Influence of Turbulence on Flame Structure in an Engine," Flows in Internal Combustion Engines, The Winter Annual Meeting of The American Society of Mechanical Engineers, Phoenix Arizona, November 14-19 1982.
40. Pischinger, S., and Heywood, J.B., "A Model for Flame Kernel Development in a Spark Ignition Engine," Twenty-Third Symposium (International) on Combustion, The Combustion Institute, pp. 1033-1040, 1990.
41. Pischinger, S., and Heywood, J.B., "How Heat Losses to the Spark Plug Affect Flame Kernel Development in an SI_Engine," SAE paper 900021, 1990.
42. Hill, P.G., "Cyclic Variations and turbulence Structure in Spark-Ignition Engines," *Combustion and Flame*, Vol. 72., pp. 73-89, 1988.
43. Hill, P.G., Kapil, A., "The Relationship Between Cyclic Variations in Spark-Ignition Engines and the Small Structures of Turbulence," Combustion and Flame, Vol 78., pp. 237-247, 1989.
44. Sohma K., Yukitake T., Azuhata S., "Application of Rapid Optical Measurement to Detect the Fluctuations of the Air-Fuel Ratio and Temperature of a Spark Ignition Engine," SAE Paper 910499.
45. Lee, K.H., Foster, D.E., "Cycle-by-Cycle Variations in Combustion and Mixture Concentration in the Vicinity of Spark Plug Gap," SAE paper 950814.

46. Witze, P.O., Martin, J.K., and Borgnakke, C., "Conditionally-Sampled Velocity and Turbulence Measurements in a Spark Ignition Engine," Comb. Sci. and Tech., vol. 36, pp. 301-317, 1984.
47. Wakisaka, T., Hamamoto, Y., Shimamoto, Y., "Turbulence Structure of Air Swirl in Reciprocating Engine Cylinders," Flows in Internal Combustion Engines, The Winter Annual Meeting of The American Society of Mechanical Engineers, Phoenix Arizona, November 14-19, 1982.
48. Notes from meeting with Rudy Smaling.

Appendix

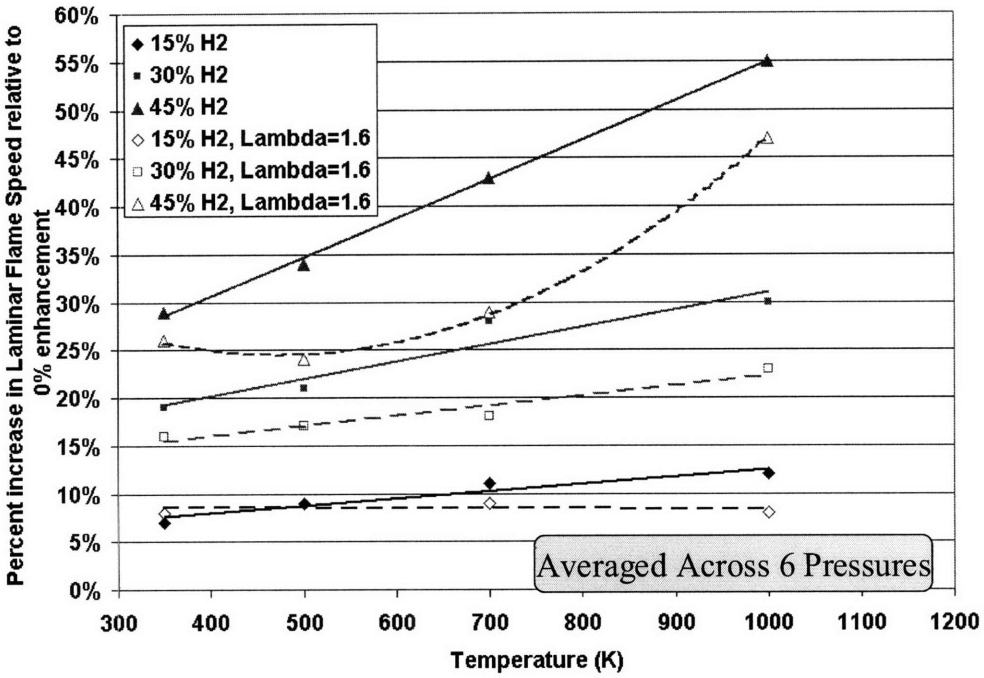

Figure A-1 – Percent increase in laminar flame speed, relative to baseline conditions, with temperature; Methane with various amounts of plasmatron enhancement, λ=1.0, and λ=1.6, averaged across six pressures

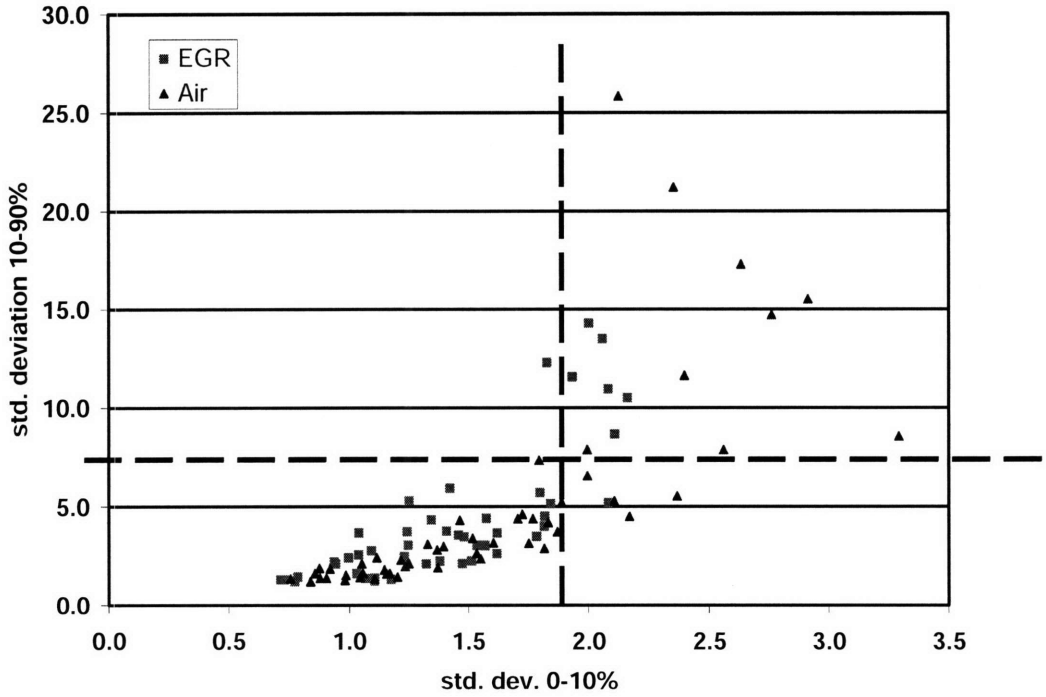

Figure A-2 – correlation of burn durations standard deviations. 10-90% standard deviation vs. 0-10% standard deviation

Thermal dilution parameter definition:

$$TDP = \frac{\Delta T_{stoichiometric}}{\Delta T}$$

where ΔT is defined as the chemical energy released during combustion per constant volume heat capacity of the unburned cylinder charge and thus represents thermal dilution of the mixture:

$$\Delta T = \frac{\sum_{i=1}^{5} m_{Xi} \cdot Q_{LHV,Xi}}{\sum_{j=1}^{9} m_{Xj} \cdot Cv_{Xj}}$$

with

$$\begin{cases} \chi_i \in (C_7H_{14}, H_2, CO, CH_4, C_2H_2) \\ \chi_j \in (H_2O, H_2, CO, CO_2, N_2, C_7H_{14}, C_2H_2, O_2, CH_4) \end{cases}$$

Since the change in specific heat of gases was ignored, ΔT only approximates the adiabatic constant volume temperature difference between the burned and unburned gas. In the analysis of experimental data, specific heats of all species were evaluated at a temperature of 600 degrees Kelvin, approximately the temperature at the time of spark. $\Delta T_{stoichiometric}$ was determined experimentally to be around 3040 degrees Kelvin for a baseline configuration with no hydrogen enhancement or dilution at stoichiometric air-fuel ratio. Many of the combustion related parameters scale well with the TDP since the flame speed is largely determined by the temperature rise across the flame [4].

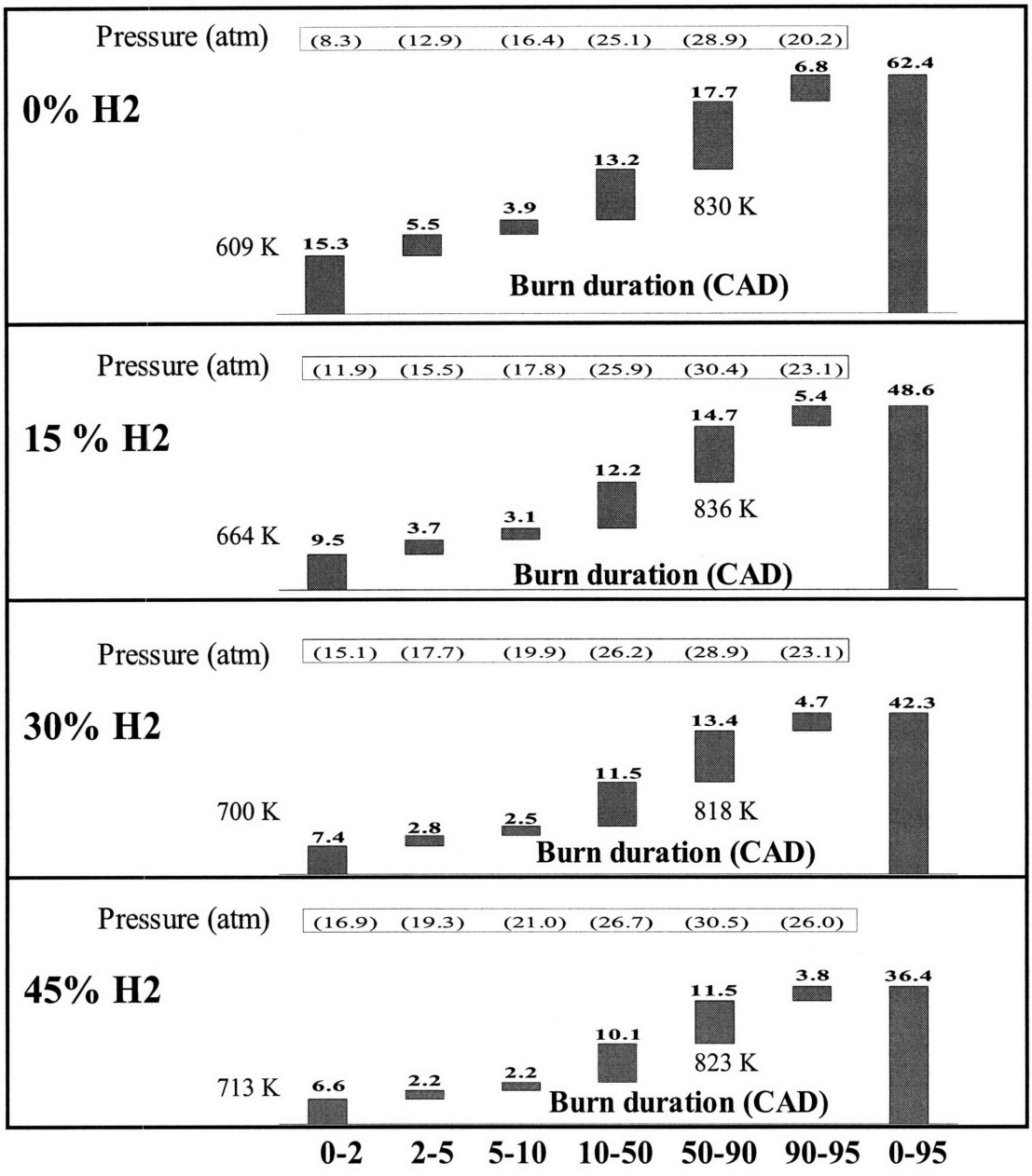

Figure A-3 – Comparison of pressure, temperature, and duration of mass burning intervals, for baseline conditions and 3 levels of pure hydrogen enhancement, near peak efficiency (λ=1.6); MBT timing, 1500 RPM, r_c=13.4:1, NIMEP = 3.5 bar

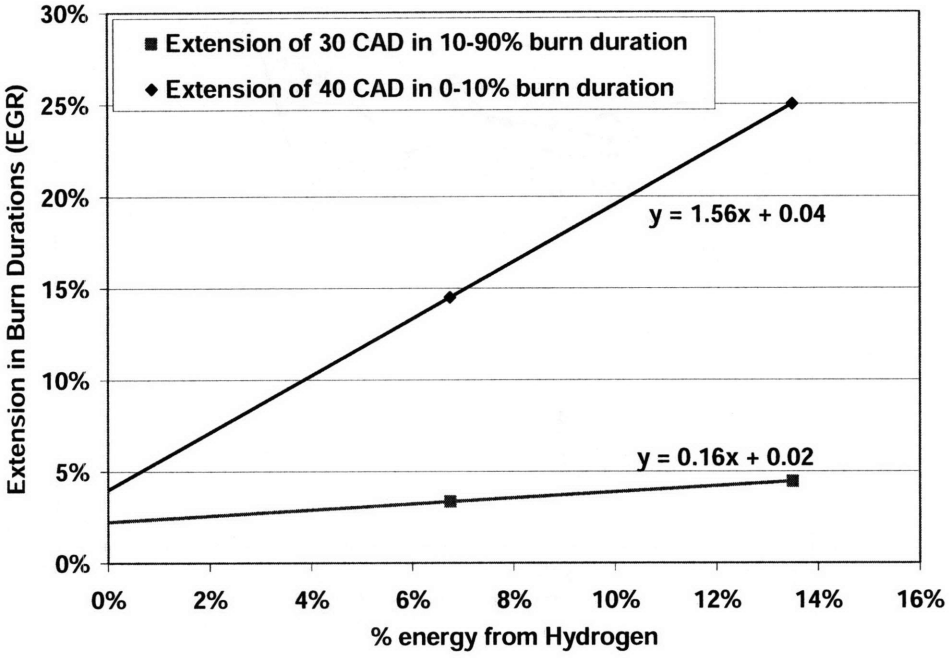

Figure A-4 Extension in the location of 30 CAD 10-90% burn duration and in location of 40 CAD 0-10% burn duration, as a function of the percent energy content provided by hydrogen, for pure hydrogen enhancement. Extension measured as absolute increase in %EGR; MBT timing, 1500 RPM, r_c=13.4:1, NIMEP = 3.5 bar

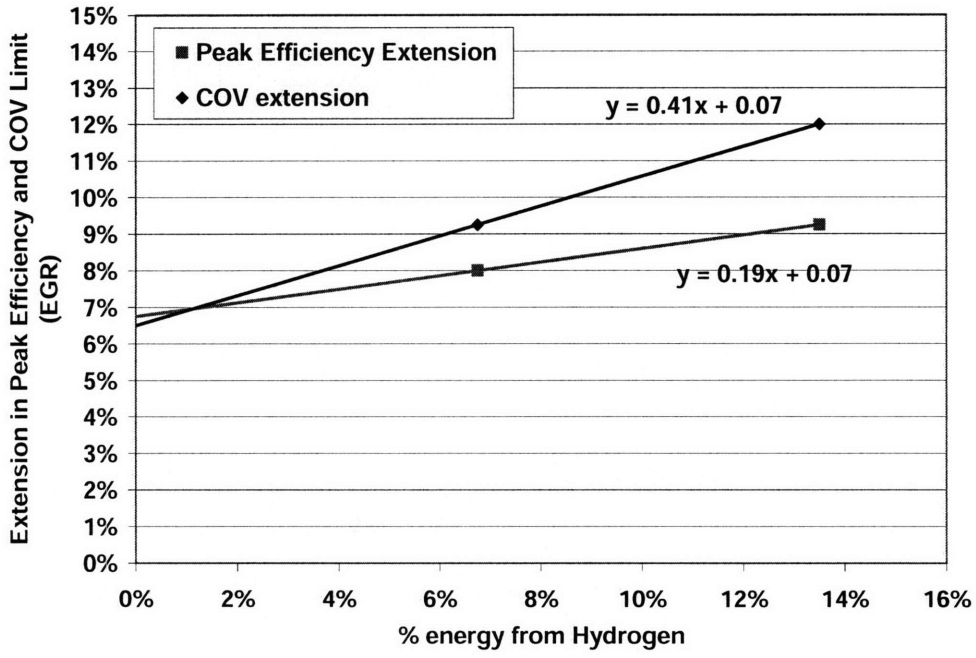

Figure A-5 Extension in the location of peak efficinecy and in location of COV limit as a function of the percent energy content provided by hydrogen, for pure hydrogen enhancement. Extension measured as absolute increase in %EGR; MBT timing, 1500 RPM, r_c=13.4:1, NIMEP = 3.5 bar

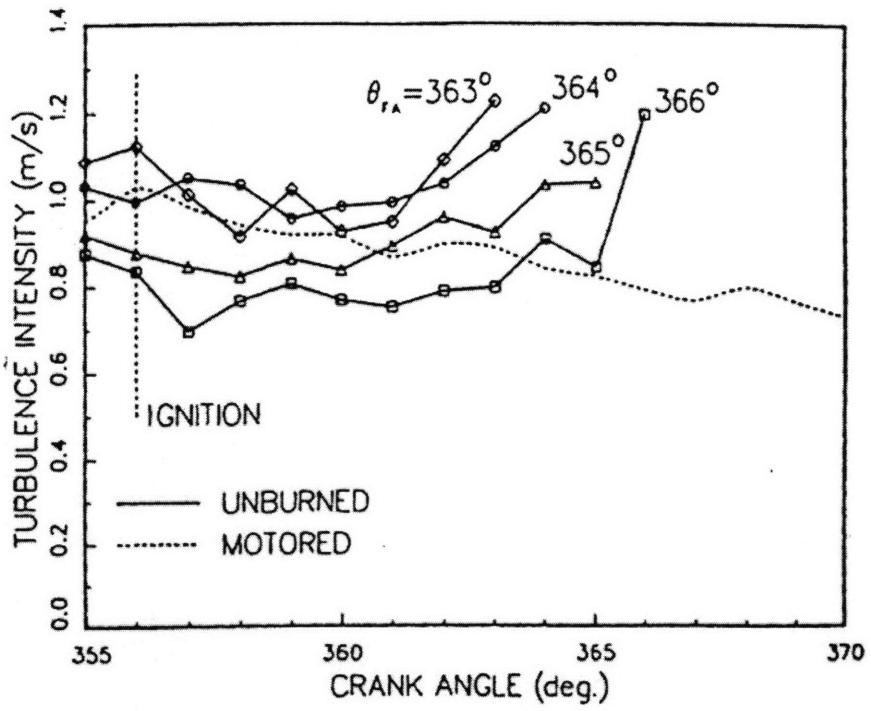

Figure A-6 Fluctuations in turbulence intensity with crank angle for identical conditions, different runs [46]

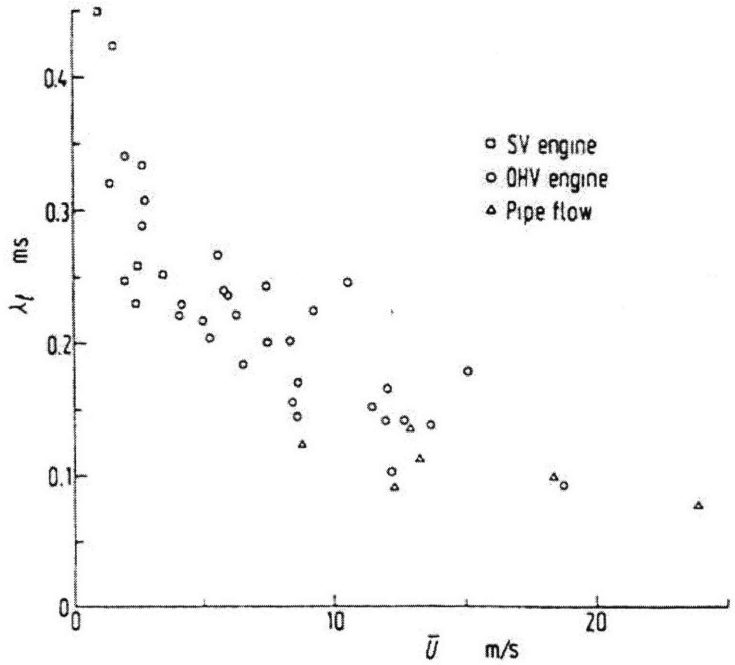

Fig.16(b) Plot of λt versus $\bar{U}$ (Engines and pipe flow)

Figure A-7 Fluctuations in temporal microscale with mean flow velocity [47]. To calculate spatial microscale multiply the temporal microscale by the mean flow velocity: $\lambda_{micrsc} = (\lambda_t)(U)$

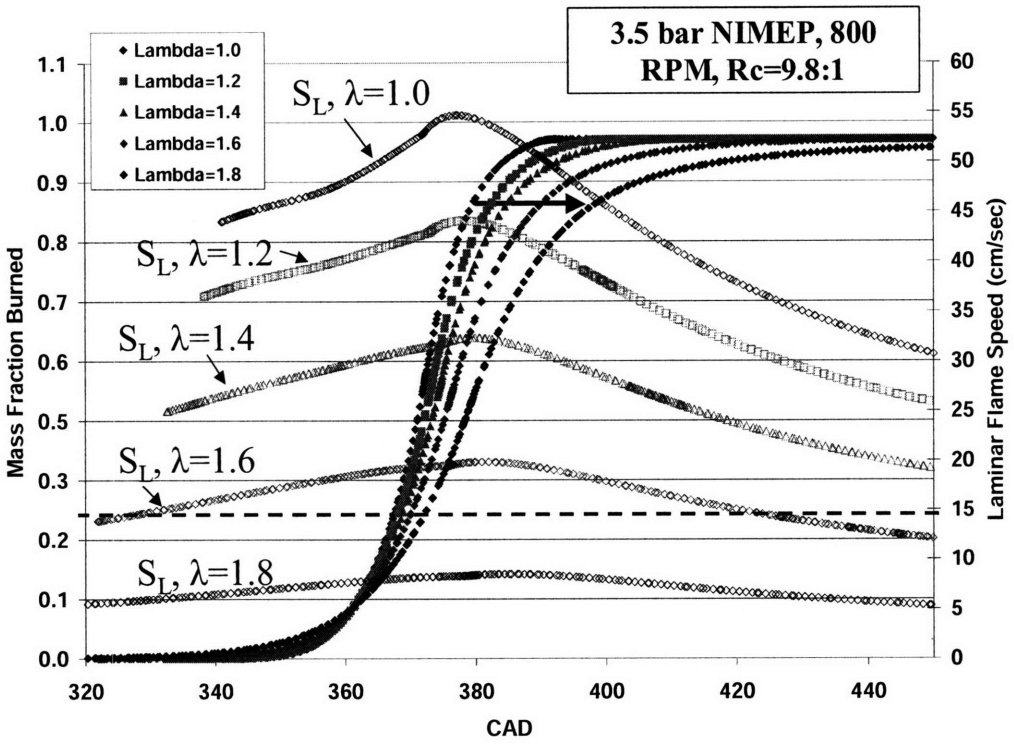

Figure A-8 Effect of increasing relative air-fuel ratio on mass fraction burned and laminar flame speed, as a function of engine crank angle degree

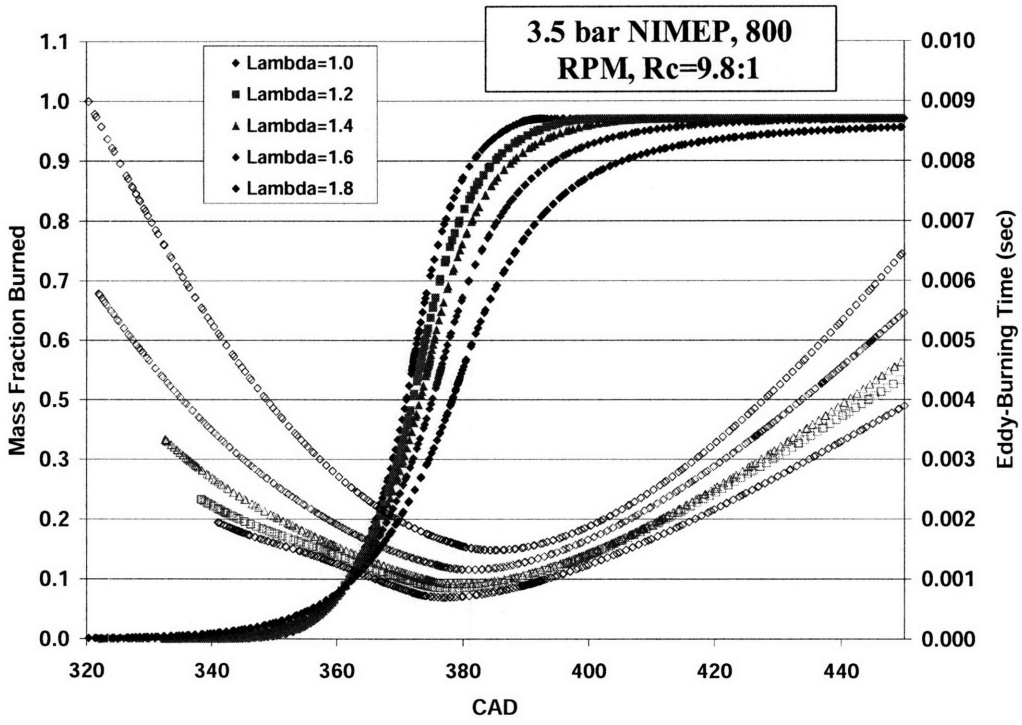

Figure A-9 Effect of increasing relative air-fuel ratio on mass fraction burned and eddy-burning time, as a function of engine crank angle degree